INSTITUTE FOR FUSION STUDIES

DOE/ET-53088-461 IFSR #461

Particle Simulation of Finite β Interchange Modes in a Sheared Magnetic Field (dissertation)

J.H. HAN
Institute for Fusion Studies
The University of Texas at Austin
Austin, Texas 78712

October 1990

THE UNIVERSITY OF TEXAS

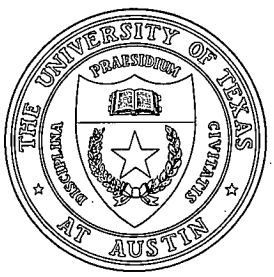

AUSTIN

PARTICLE SIMULATION OF FINITE β INTERCHANGE MODES IN A SHEARED MAGNETIC FIELD

APPROVED BY

SUPERVISORY COMMITTEE:

Robert L Bert

Patrick H Diamond

Lebow J

James W. VanDam

Wendell Horton

Edward J. Valeo

PARTICLE SIMULATION OF FINITE β INTERCHANGE MODES IN A SHEARED MAGNETIC FIELD

by

JUNG HOON HAN, M.S.

DISSERTATION

Presented to the Faculty of the Graduate School of

The University of Texas at Austin

in Partial Fulfillment

of the Requirements

for the Degree of

DOCTOR OF PHILOSOPHY

THE UNIVERSITY OF TEXAS AT AUSTIN

August, 1990

To

My Mother and Father

Acknowledgments

It has been a great pleasure and privilege to collaborate with and learn from my mentor, Dr. Jean Noel Leboeuf. Without his many helpful suggestions during numerous discussions, this dissertation would not have been possible. His patience, guidance, and knowledge are deeply appreciated and cherished.

I am very grateful to Prof. Marshall Rosenbluth, Prof. Herbert Berk, Prof. Patrick Diamond, Prof. Wendell Horton, Dr. James Van Dam, and Prof. Ethan Vishniac for their invaluable instruction, support, and encouragement and for serving as my thesis committee members. I also deeply appreciate the support and extensive assistance received from Dr. Benjamin Carreras and Dr. Robert Dory at Oak Ridge National Laboratory.

I wish to thank Dr. Gyung-Su Lee, Dr. Nicolas Dominguez, and Dr. Doug-Kyo Lee for their encouragement and help during my stays in the ORNL Fusion Energy Division.

I also wish to express my gratitude to Suzy Crumley, Dawn East, Joyce Patton, Saralyn Stewart, and Carolyn Valentine at the IFS; Marsha Correira and Norma Kotz in The University of Texas Physics Department; and Dorothy Tate and Malinda Hutchinson at ORNL for their kind assistance.

It is a great pleasure to acknowledge pleasant collegiate relationships with Drs. G. Craddock, S. Eways, T.S.Hahm, B.G. Hong, D.J. Kim, Y.J. Kim, H.T. Kook, M. Kwon, O.J. Kwon, P.M. Lyster, J.J. Paik, and H. Ouroua during my time in the IFS and at ORNL.

Finally I would like to express my indebtedness and gratitude to my parents and my family for their support and understanding during these years.

JUNG HOON HAN

The University of Texas at Austin

August, 1990

PARTICLE SIMULATION OF FINITE β INTERCHANGE MODES IN A SHEARED MAGNETIC FIELD

Publication No. _____

Jung Hoon Han, Ph.D.
The University of Texas at Austin, 1990

Supervising Professors: Jean Noel Leboeuf
Herbert L. Berk

Particle simulations of ideal and resistive interchange modes driven by density gradient and magnetic field curvature in finite β plasmas and sheared slab geometry have been performed. A 2-1/2D bounded magneto-inductive guiding center electron particle code, which accurately follows the perturbed magnetic field in the shear Alfvén limits has been implemented and used. To simulate effective collisions between electrons and ions in the guiding center electron plasma, an accurate algorithm for the Lorentz collision operator has been constructed and used for resistive interchange modes. With the particle code, linear and quasilinear behaviors of interchange modes in finite β plasmas have been investigated along with their electrostatic limit as a reference for both collisionless and collisional regimes. Salient features of the results are good agreement between kinetic linear theory and simulations for the linear phase of the interchange instability, and verification of the Suydam's criterion for stability in finite β sheared slab geometry. Analytical estimates from quasi-linear theory are also in agreement with the measured electrostatic potential and radial magnetic field fluctuation levels at saturation. Nonlinear features of particle simulations include mode cascadings in wave number space at sat-

uration in electrostatic collisional plasmas and a significant amount of parallel ion temperature profile modification associated with quasilinear density profile modification in finite β collisional plasmas.

Table of Contents

List of Figures

Chapter 1

Introduction

Self-consistent electromagnetic turbulence phenomena observed in the vast varieties of plasmas existing in nature, from solar plasmas to present day experimental fusion plasma devices, are still not well understood. Due to their nonlinear and self-consistent nature, a definitive analytical model of the phenomena has not been, and most likely, cannot be given. In spite of these difficulties, there is great motivation to understand the dynamics of self-consistent electromagnetic turbulence. In particular, in magnetic fusion plasmas, when the thermal energy density of the particles is a significant fraction of the magnetic field energy density, in other words when the plasma β value is finite, collective microinstabilities produce substantial magnetic fluctuations due to the oscillating particle currents. These magnetic fluctuations in turn cause a significant anomalous radial thermal electron transport in toroidal fusion devices. A simple heuristic picture of the self-consistent cycle of the electromagnetic perturbations which eventually cause anomalous radial thermal electron transport is as follows. In the electromagnetic regime in which magnetic perturbations are no longer negligible, when a perturbed perpendicular magnetic field is added to the ambient magnetic field, the parallel electron motion, defined by the direction of the total magnetic field, is impeded by the radial component of the perturbed magnetic field. Its direction is also altered to the radial direction since the radial velocity component adds to the original parallel velocity

and forces the electrons to move radially inward or outward. This cause the electrons to carry heat from the hot core region of the toroidal fusion device to the cold edge region or vice versa, and thus results in anomalous radial thermal transport. The newly defined perturbed parallel electron velocities due to the perpendicular magnetic fluctuations determine new parallel oscillating electron currents, which in turn induce new perturbed magnetic fields.

When densely packed multi-rational surfaces are introduced, magnetic islands due to perpendicular magnetic fluctuations overlap each other. If the overlap becomes large enough to cause severe 'magnetic braiding', then magnetic surfaces are eventually destroyed[1] and field lines become stochastic and cause enhanced radial transport, as was proposed by Stix[2]. Rechester and Rosenbluth[3] have proposed a model for radial electron heat transport based on test particle diffusion in the stochastic magnetic field lines. Another approach was adopted by Kadomtsev and Pogutse[4], using a fluid model instead of a test particle one. Later on, a comprehensive study of stochastic magnetic field transport was given by Krommes, Oberman, and Kleva[5]. All of these calculations assumed stochastic magnetic field lines and also assumed static perturbed magnetic fields instead of self-consistent magnetic fluctuations. Thus the effects of the magnetic fluctuations on the underlying instabilities were not included. The experimental evidence[6,7,8] shows that the predictions based on these models with the measured magnetic fluctuation levels still cannot explain the observed electron thermal losses. Thus a more complete analytical model including self-consistent effects is required to explain the anomalous electron thermal losses. Particle simulations, which define the position of charged particles in the electromagnetic field in a self-consistent manner, are in principle an ideal methodology to investigate the dynamics of the low frequency electromagnetic turbulence induced by numerous microinstabilities covering wide physical

parameter spaces. Therefore particle simulations can possibly contribute to improved understanding of anomalous radial electron heat transport.

One approach to obtain a dynamical picture of the low frequency self-consistent electromagnetic turbulence in sheared magnetic fields with many mode rational surfaces in toroidal plasma fusion devices, would be a full three dimensional multi-helicity particle simulation code that defines the perturbed magnetic field self-consistently. However, the application of such a code is a formidable task if one considers the present day computational resources which we can afford in practice. This was also the case with electrostatic particle codes when the task of the low frequency electrostatic turbulence was faced a decade ago. Because modern development of supercomputing facilities has led to nearly exponential growth in processing and memory as each new generation of supercomputers has become available, progress in overcoming this difficult challenge may occur on a relatively short time scale. Besides this technological limitation, even if we can somehow provide the computational environment to proceed with this task, there exists at present no established definitive self-consistent electromagnetic turbulence theory that can provide predictable parameter ranges for the physics of interest to be incorporated in the proposed extra large scale computations. Also, experimental databases that are being accumulated for these low frequency electromagnetic turbulence phenomena are somewhat limited in their description of electromagnetic turbulence phenomena. As a first step in gaining a glimpse or an insight for understanding the dynamics of the self-consistent low frequency electromagnetic phenomena and their impact on anomalous transport, it is reasonable to begin with the better understood electrostatic mode and then progressively add finite β (electromagnetic) effects in order to see their influence on the turbulent state. The work in this dissertation work has proceeded in this spirit. By taking ad-

vantage of the well known electrostatic nature of resistive interchange modes, we can attempt to isolate effects for self-consistent electromagnetic turbulence phenomena when we test this mode in parameter regimes for which magnetic perturbations are significant.

Low frequency resistive interchange modes or resistive g-modes are driven by pressure gradients with unfavorable average magnetic field curvature in low β plasmas. The low frequency resistive g-mode has been exhaustively studied[9–13] since the early pioneering work of Furth, Killeen, and Rosenbluth[14] in sheared slab geometry and the subsequent work of Coppi, Greene, and Johnson[15] in cylindrical geometry. Nowadays, it is well understood as an electrostatic mode in both the linear phase and fully turbulent stage, in terms of the fluid turbulence model. In electrostatic fluid turbulence, in which the equilibrium magnetic field is constant (which implies constant pressure), plasma transport in the regime of low frequency microinstabilities is dominated by $E \times B$ pressure convection. The fluid turbulence approach[16] which adopts a pressure convection model has been successfully implemented in a full 3D magneto-hydrodynamic code to predict the behavior of particle and thermal transport induced by the pressure gradient driven mode.

Under the present day computational situation, we have developed and used for the initial study of the self-consistent electromagnetic turbulence a $2-1/2\mathrm{D}(x, y, v_x, v_y, v_z)$ magneto-inductive particle code that follows the low frequency shear Alfvén dynamics[17] in sheared slab geometry, with a single mode rational surface. With only one mode rational surface, at which the plasma and the field lines are decoupled due to a small amount of resistivity, interchange modes become unstable and are localized around the mode rational surface. Thus, the nonlinear behavior of finite β interchange modes in sheared slab

geometry belongs to the quasilinear weak turbulence regime, instead of the strong turbulence regime, which is produced by the overlapping of unstable eigenmodes for the case of the densely packed multi-mode rational surfaces in 3D confugurations. It is, therefore, premature to provide the quantitative measurements related to thermal electron transport coefficient such as the electron thermal diffusivity coefficient χ_e. The work presented here is the very necessary first step in a search for the dynamical mechanism of self consistent magnetic turbulence. It provides clues to understand the anomalous transport observed in present day toroidal fusion devices.

The organization of the remaining chapters of this thesis is as follows. In Chapter 2, the simulation model and algorithm are developed. The 2−1/2D magneto-inductive particle model is implemented in sheared slab geometry. To follow perturbed magnetic fields precisely, magnetic fields are defined at each step for the time advancing of the electrons and ions . An elaborate iterative field solver for the transverse electric field is implemented which characterizes the magneto-inductive model.

Both guiding center electrons particle codes (Lee and Okuda)[18,19]and Darwin[20] or magneto-inductive models [21,22]have been used for many years to simulate plasma phenomena. While the guiding center electrons models are able to describe the low frequencies and long space scales of interest here they have been mostly limited to an electrostatic description of the plasma. Because the displacement current is neglected in the Darwin model, electromagnetic modes with frequencies lower than those of light waves can be followed without resorting to the excruciatingly small time step an electromagnetic code would require. However, most Darwin models include a full dynamics treatment of both electrons and ions and as such are better suited to frequencies on the

order of the plasma frequency and higher. Recently, a few models have surfaced which attempt to merge the two descriptions. Our model is one of the newer ones of this type and as such as benefitted greatly from previous developments. It does include guiding center electrons, full ion dynamics, but only the shear Alfven component of the low frequency electromagnetic fluctuations. The main difference between the present model and the one proposed by Lee *etal.*[23] resides in the incorporation of the ion source terms in the solution for the transverse electric field and of the ion current in Ampere's law. Our model is a shear Alfvén branch of the model of Geary *et.al.*[24], which also includes compressional Alfven waves. The difference here is that particle motions and field components parallel and perpendicular to the magnetic field are more accurately defined by including the fluctuating magnetic fields in the relevant projection operators and particle velocities. A more sophisticated iterative procedure has alo been implemented in our model to solve for the transverse electric field. It is of the Concus-Golub type[25], with the shift constant chosen so as to optimize convergence for the sharp plasma density profiles used. Chebyshev acceleration has also been included to speed-up convergence and accuracy. Moreover, great care has been taken to properly time-center the evolution equations for fields and particles. These developments result in a more accurate and reliable performance with the large time steps required to make the calculations presented here feasible. Our most significant accomplishment is perhaps the implementation of an efficient and accurate Lorentz collision operator for guiding center electrons dynamics. This treatment has proven equally beneficial in the electrostatic and magneto-inductive versions of our model.

As a test of the magneto-inductive model, simulations are carried out for Bernstein waves, shear Alfvén waves, and ordinary ion cyclotron waves, and the results are compared with the linear kinetic theory results.

In Chapter 3, as a reference, particle simulations of the electrostatic interchange modes are performed for both collisionless and collisional regimes along with the corresponding linear analyses. Linear eigenmode equations are derived from the drift-kinetic equation and the gyro-kinetic equation for the low frequency electron and ion responses, respectively, and from the quasi-neutrality condition. Linear analyses of the electrostatic interchange modes with kinetic effects such as finite gyroradius effects, diamagnetic drift frequency effects, and electron and ion wave particle interactions are carried out with a second order shooting code. Prominent features such as growth rate scalings for the relevant parameters, mode widths, and mode structures are obtained and compared with the fluid limit calculations in both regimes. In the nonlinear stages, saturation levels for the field and particle quantities are measured and compared with mixing length estimates. Also, phase relationships between field fluctuation quantities and particle fluctuation quantities are measured in both linear and nonlinear phases. Quasilinear effects such as plateau formation in the density profiles, along with parallel temperature profile modifications, are observed. Specific nonlinear phenomena, which the particle code can deliver uniquely, such as low wave number condensation of resistive interchange modes at the saturation phase, are observed.

In Chapter 4, finite β interchange mode simulations are performed after extensive linear kinetic analyses are carried out to provide an affordable parameter set for both collisionless and collisional regimes. As a first step, coupled linear eigenmode equations are derived from the quasineutrality condition and parallel Ampére's law, with perturbed densities and currents obtained from moments of the electron drift-kinetic equation and the ion gyro-kinetic equation. The coupled eigenmode equations are solved by a fourth-order shooting code scheme. As a benchmark, this coupled eigenmode shooting code scheme is

applied to finite β drift waves and produces results identical to those of Tsang *et.al.*[26] Then, extensive radial eigenmode analyses are carried out for finite-β interchange modes in both collisionless and collisional regimes. Growth rate scaling studies are performed for relevant parameters in both regimes. The radial eigenmode structures for the electrostatic potential ϕ and the parallel electromagnetic vector potential $A_{||}$ are also obtained. In collisionless simulations, the Suydam criterion is tested with stable and unstable parameters. Scaling studies of linear quantities are carried out for relevant parameters and compared with the results of linear analyses. Field and particle fluctuation levels are measured and compared with quasilinear theory and mixing length estimates. The relative phases and spatial mode structures of perturbed field and particle quantities are measured at specific times in the field energy evolution. Density profile modifications accompanied by parallel temperature profile modifications are observed. Also, magnetic island widths at the saturated phase under variation of the relevant parameters are measured. In collisional plasmas, similar analyses as for the collisionless case are carried out. Significant parallel ion temperature profile modification, along with quasilinear density plateau formation for both species, are observed and elaborate diagnostics are performed to isolate the physics of interest.

In Chapter 5, a summary and conclusions are given, along with suggestions for future work.

Chapter 2

Simulation Model and Algorithm

2.1 Particle equations

Particle motion for the electrons is governed by the guiding center electron model[18,19] in which the electron gyro-radius ρ_e is taken to be zero. For the ions full particle dynamics which maintain a finite ion gyro-radius ρ_i are adopted. The equations of motion for the electrons and ions are described by the Newton-Lorentz equations which are separated into parallel and perpendicular directions with respect to the ambient magnetic field **B**. The equation of motion for the parallel electron dynamics is

$$\frac{dv_{\parallel}}{dt} = -\frac{|e|}{m_e} E_{\parallel} \tag{2.1}$$

Perpendicular to the magnetic field, electrons do not gyrate but only move across the field lines with the drift velocity

$$\mathbf{v}_{\perp} = c\frac{\mathbf{E}_{\perp} \times \mathbf{B}}{|B|^2} - \frac{c}{|e|}\frac{\boldsymbol{g}_e \times \mathbf{B}}{|B|^2} \tag{2.2}$$

where $|\boldsymbol{g}_e| = T_e/L_c$ is the centrifugal curvature force felt by the electrons, which is often regarded as an effective gravity in slab geometry. T_e is the electron temperature, and L_c is the curvature scale length. Ion motion with finite ion gyro-radius ρ_i follows the dynamics with full three dimensional velocities, described by

$$\frac{d\mathbf{v}_i}{dt} = \frac{|e|}{m_i}\left(\mathbf{E} + \frac{\mathbf{v}\times\mathbf{B}}{c}\right) + \frac{\boldsymbol{g}_i}{m_i} \tag{2.3}$$

,where $|\boldsymbol{g}_i| = T_i/L_c$ is the curvature drift force on the ions and T_i is the ion temperature.

To advance the particles in time and in space according to the prescribed equations of motion for the electrons and ions, two different particle pushing schemes are employed : the "leap-frog" scheme[27] for the ions and the predictor-corrector scheme for the guiding center electrons. Ion positions and velocities are alternatingly defined at the time steps $n+1/2$ and $n+1$, so they are "leap-frog" advancing between two parallel time arrays of position and velocity. The leap-frog particle pusher which carries the 3-D ion dynamics is

$$\begin{aligned}\mathbf{v}^{n+1} &= \mathbf{v}^n + \Delta t\frac{|e|}{m_i}\left[\mathbf{E}^{n+1/2} + \frac{1}{c}\frac{(\mathbf{v}^{n+1}+\mathbf{v}^n)}{2}\times\mathbf{B}^{n+1/2}\right] \\ &\quad + \Delta t\frac{\boldsymbol{g}_i}{m_i}\end{aligned} \tag{2.4}$$

$$\mathbf{x}^{n+3/2} = \mathbf{x}^{n+1/2} + \Delta t\mathbf{v}^{n+1} \tag{2.5}$$

In this scheme, time centering between ion positions and fields should be observed; i.e., fields and their ion source positions are defined at the same time step.

This time centering property of the leap-frog scheme is no longer valid for the guiding center electrons since their perpendicular drift velocity at the $n+1$ step,viz., $\mathbf{v}_\perp^{n+1}$, which is combined with their parallel velocity at the $n+1$ step,viz.,$v_\parallel^{n+1}$, and which is used to push the particle position to the $n+3/2$ step, is defined instantaneously from the field quantities, i.e.,

$$\mathbf{v}_\perp^{n+1} = c\left(\frac{\mathbf{E}_\perp\times\mathbf{B}}{B^2}\right)^{n+1} - \frac{c}{|e|}\frac{\boldsymbol{g}\times\mathbf{B}^{n+1}}{(B^{n+1})^2}. \tag{2.6}$$

Therefore field quantities at the $n+1$ step, which are not defined on the particle position at the $n+1$ step, are required.

The predictor-corrector scheme[18,19] is designed to satisfy the time centering condition in the advancement of the guiding center electrons by having perpendicular velocities at the $n+1$ step be defined from the fields, which are defined on the particle positions at the $n+1/2$ step and the fields, defined on the temporary predicted positions at the $n+3/2$ step, instead of defining fields at the $n+1$ step. This scheme enables us to have accurate time centering between electron particle positions and field quantities in the velocity advancement. The particle pushing steps used in the predictor-corrector scheme are described briefly in the following equations, along with the parallel electron velocity advancement which is time centered:

$$v_{\|}^{n+1} = v_{\|}^{n} - \Delta t \frac{|e|}{m_e} E_{\|}^{n+1/2}(x^{n+1/2}) \tag{2.7}$$

$$x_{\|}^{n+3/2} = (x_{\|}^{n-1/2} + \Delta t v_{\|}^{n}) + \Delta t v_{\|}^{n+1} \tag{2.8}$$

$$\mathbf{v}_{\perp_{pred}}^{n+1/2} = c\frac{\mathbf{E}(\mathbf{x}^{n+1/2}) \times \mathbf{B}(\mathbf{x}^{n+1/2})}{|\mathbf{B}(\mathbf{x}^{n+1/2})|^2} - \frac{c}{|e|}\frac{\boldsymbol{g} \times \mathbf{B}(\mathbf{x}^{n+1/2})}{|\mathbf{B}(\mathbf{x}^{n+1/2})|^2} \tag{2.9}$$

$$\mathbf{x}_{\perp_{pred}}^{n+3/2} = \mathbf{x}_{\perp}^{n-1/2} + 2\Delta t \mathbf{v}_{\perp}^{n+1/2} \tag{2.10}$$

$$\mathbf{x}_{pred}^{n+3/2} = \mathbf{x}_{\perp_{pred}}^{n+3/2} + x_{\|}^{n+3/2}\hat{\mathbf{b}} \tag{2.11}$$

$$\mathbf{x}_{pred}^{n+3/2} = \mathbf{x}^{n-1/2} + 2\Delta t \left[\mathbf{v}_{\perp}^{n+1/2} + \left(\frac{v_{\|}^{n} + v_{\|}^{n+1}}{2}\right)\hat{\mathbf{b}}\right] \tag{2.12}$$

$$\mathbf{v}_{\perp_{pred}}^{n+3/2} = c\frac{\mathbf{E}(\mathbf{x}^{n+3/2}) \times \mathbf{B}(\mathbf{x}^{n+3/2})}{|\mathbf{B}(\mathbf{x}^{n+3/2})|^2} - \frac{c}{|e|}\frac{\boldsymbol{g} \times \mathbf{B}(\mathbf{x}^{n+3/2})}{|\mathbf{B}(\mathbf{x}^{n+3/2})|^2} \tag{2.13}$$

$$\mathbf{v}_{\perp_{corr}}^{n+1} = \frac{1}{2}\left[\mathbf{v}_{\perp_{pred}}^{n+3/2} + \mathbf{v}_{\perp}^{n+1/2}\right] \tag{2.14}$$

$$\mathbf{x}_{corr}^{n+3/2} = \mathbf{x}^{n+1/2} + \Delta t \left[v_{\parallel}^{n+1} \hat{\mathbf{b}} + \left(\frac{\mathbf{v}_{\perp}^{n+3/2} + \mathbf{v}_{\perp}^{n+1/2}}{2} \right) \right] \tag{2.15}$$

The details of the time stepping of all the field and particle quantities are described in Section 2.3.

2.2 Field Equations

The field quantities which advance the particle positions and velocities through the Newton-Lorentz equations of motion are calculated in the magneto-inductive shear Alfvén model. This is obtained from the full electromagnetic model by the elimination of two branches which are not compatible with the underlying physics. Since what we are looking for is the low frequency electromagnetic mode, whose frequency is one or two orders of magnitude smaller than the ion gyro-frequency and also is in the low β limit, modes with frequencies above this range and a branch which is negligible in low beta plasmas should be removed in order to see the phenomena of interest without interference from high frequency phenomena. The first step is done by neglecting the radiation term, which generates high frequency electromagnetic waves, in Maxwell's equations:

$$\nabla \cdot \mathbf{E}_L = 4\pi\rho \tag{2.16}$$

$$\nabla \cdot \mathbf{B} = 0 \tag{2.17}$$

$$\nabla \times \mathbf{B}_T = \frac{4\pi}{c} \mathbf{J}_T \tag{2.18}$$

$$\nabla \times \mathbf{E}_T = -\frac{1}{c} \frac{\partial \mathbf{B}_T}{\partial t} \tag{2.19}$$

The time derivative term in Ampére's law has been deleted. The second simplification is done by neglecting the compressional Alfvén branch which is dom-

inant in the high β regime. We retain only the perpendicular magnetic perturbation $\delta B_\perp$ (from the parallel component of the vector potential $A_{||}$), or shear Alfvén mode, and neglect the parallel magnetic perturbation, or compressional Alfvén mode $\delta B_{||}$ (from $A_\perp$), with respect to the ambient magnetic field. This magneto-inductive shear Alfvén model is implemented in the $2\frac{1}{2}$ dimensional ; (x, y, v_x, v_y, v_z) sheared-slab geometry. The field quantities to be calculated are the longitudinal electrostatic fields E_L^x and E_L^y and the transverse electromagnetic fields B_T^x, B_T^y, and E_T^z. In the compressional Alfvén model[24], the field quantities B_T^z, E_T^x, and E_T^y should be included. This particle simulation model follows the reduced MHD equations, which represent low frequency shear Alfvén dynamics[17], yet retains kinetic ingredients such as finite gyro-radius effects, ω_e^* efffects, and particle-wave interactions.

To calculate the field quantities in the particle simulations, two numerical prerequisites are necessary. One is the finite size particle (FSP)[27] effect which accompanies each field variable and source quantity, and the other is the Fast Fourier Transform (FFT) field solver[28] which performs field calculations with given sources quantities defined on the finite spatial grid. The role of the FSP is such that with a much smaller number of finite size particles ($10^3 \sim 10^6$) than in a real plasma ($\sim 10^{12}$), one can describe the collective behavior of the plasma without having the numerically generated collisional effects due to the small number of particles in the simulation model. A commonly used FSP in particle simulations is the 2D Gaussian shaped particle :

$$S(\mathbf{x} - \mathbf{x}_j) = \frac{1}{2\pi a_x a_y} \exp\left[-\frac{(x - x_j)^2}{2a_x^2} - \frac{(y - y_j)^2}{2a_y^2}\right]. \qquad (2.20)$$

The general form of this Gaussian particle is

$$S(\mathbf{x}-\mathbf{x}_j) = \frac{\exp\{-(\mathbf{x}-\mathbf{x}_j)^2/2a_0^2\}}{2\pi^{n/2}a_0^n} \tag{2.21}$$

where a_0 is the scale length of the Gaussian particle. The quantity $S(\mathbf{x})$ is normalized such that

$$\int S(\mathbf{x})d^n\mathbf{x} = 1. \tag{2.22}$$

With finite size particles(FSP), charge densities and current densities are defined as

$$\rho(\mathbf{x}) = \sum_\alpha q_\alpha \sum_j S(\mathbf{x}-\mathbf{x}_{j\alpha}) \tag{2.23}$$

$$\mathbf{J}(\mathbf{x}) = \sum_\alpha q_\alpha \sum_j \mathbf{v}_{j\alpha} S(\mathbf{x}-\mathbf{x}_{j\alpha}), \tag{2.24}$$

where α and j are indicies which represent particle species and positions respectively. Each FSP is assigned and averaged on top of each grid point. A rather simple but accurate averaging procedure is the substracted dipole(SUD)scheme[29], which is a truncated multipole expansion of the source quantities at each grid point. For each particle species α, the charge densities accumulated on each grid point by SUD are given by

$$\rho(\mathbf{x}) \simeq \sum_g [Q(\mathbf{x}_g)S(\mathbf{x}-\mathbf{x}_g) + D(\mathbf{x}_g)\cdot\nabla_g S(\mathbf{x}-\mathbf{x}_g)] \tag{2.25}$$

with

$$Q(\mathbf{x}_g) = \sum_{j\epsilon g} q_j$$

$$D(\mathbf{x}_g) = \sum_{j\epsilon g} q_j(\mathbf{x}_j-\mathbf{x}_g), \tag{2.26}$$

where $Q(\mathbf{x}_g)$ and $D(\mathbf{x}_g)$ represent the monopole moment and the dipole moment of the charge distribution. Current densities are also accumulated in the same

way as charge densities and are expressed as

$$\mathbf{J}(\mathbf{x}) \simeq \sum_g \mathbf{J}_M(\mathbf{x}_g) S(\mathbf{x}-\mathbf{x}_g) + \mathbf{J}_D(\mathbf{x}_g)\cdot\nabla_g S(\mathbf{x}-\mathbf{x}_g) \tag{2.27}$$

with the following definitions of monopole and dipole currents

$$\begin{aligned}\mathbf{J}_M(\mathbf{x}_g) &= \sum_{j\epsilon g} q_j \mathbf{v}_j \\ \mathbf{J}_D(\mathbf{x}_g) &= \sum_{j\epsilon g} q_j \mathbf{v}_j (\mathbf{x}_j - \mathbf{x}_g)\end{aligned} \tag{2.28}$$

The source quantities defined on the finite grid points enable us to use a rapid field solver FFT on the finite spatial grid. In two dimensional grid space, the FFT is defined as

$$F(\mathbf{x}) = \sum_{m,n} F(k_m, k_n)\exp(i\mathbf{k}\cdot\mathbf{x}_g) \tag{2.29}$$

$$k_m = \frac{2\pi m}{L_x} \quad , \quad k_n = \frac{2\pi n}{L_y}$$

$$\begin{aligned}F(k_m,k_n) &= \frac{1}{L_x L_y}\int_0^{L_x} dx \int_0^{L_y} dy\, f(\mathbf{x}_g)\exp(-i\mathbf{k}\cdot\mathbf{x}_g) \\ &= \frac{1}{MN}\sum_{m=0}^{M-1}\sum_{n=0}^{N-1} f(\mathbf{x}_g)\exp(-i\mathbf{k}\cdot\mathbf{x}_g),\end{aligned} \tag{2.30}$$

where $L_x = M\Delta_x$ and $L_y = N\Delta_y$ are the system lengths, M and N are the number of grid in the x and y directions, respectively, and Δ is the unit grid spacing. With FSP and FFT, the E and B fields are defined and calculated at each grid point according to

$$\mathbf{E}(\mathbf{x}_g) = \int d^2\mathbf{x}\ \mathbf{E}(\mathbf{x})\ S(\mathbf{x}-\mathbf{x}_g) \tag{2.31}$$

$$\mathbf{B}(\mathbf{x}_g) = \int d^2\mathbf{x}\ \mathbf{B}(\mathbf{x})\ S(\mathbf{x}-\mathbf{x}_g) \tag{2.32}$$

In k space, the fields are transformed through FFT as follows

$$\mathbf{E}(\mathrm{k}) = L_x L_y\ S(-\mathrm{k})\mathbf{E}(\mathrm{k}) \tag{2.33}$$

$$\mathbf{B}(\mathrm{k}) = L_x L_y\ S(-\mathrm{k})\mathbf{B}(\mathrm{k}) \tag{2.34}$$

In discrete Fourier space, the longitudinal electrostatic fields and transverse magnetic fields are calculated at each source which is accumulated on the grid point via Maxwell's equations, as follows :

• Longitudinal electric field field

$$\begin{aligned}\nabla \cdot \mathbf{E}_L &= 4\pi\rho \\ &= 4\pi \sum_\alpha q_\alpha \sum_g S(\mathbf{x}-\mathbf{x}_g) n_\alpha(\mathbf{x}_g)\end{aligned} \tag{2.35}$$

in k space

$$\mathbf{E}_L(\mathrm{k}) = -4\pi i \frac{\mathrm{k}}{k^2} S(\mathrm{k}) \sum_\alpha n_\alpha(\mathrm{k}) q_\alpha \tag{2.36}$$

• Transverse magnetic field

$$\begin{aligned}\nabla \times \mathbf{B}_T &= \frac{4\pi}{c}\mathbf{J}_T \\ &= \frac{4\pi}{c} \sum_\alpha q_\alpha \sum_g S(\mathbf{x}-\mathbf{x}_g)\mathbf{v}_\alpha(\mathbf{x}_g)\end{aligned} \tag{2.37}$$

in k space

$$\begin{aligned}\mathbf{B}_T(\mathrm{k}) &= \frac{4\pi i}{c} \frac{\mathrm{k} \times \mathbf{J}_T(k)}{k^2} \\ &= \frac{4\pi i}{c} S(\mathrm{k}) \frac{\mathrm{k} \times \sum_\alpha q_\alpha \mathbf{v}_\alpha(\mathrm{k})}{k^2}\end{aligned} \tag{2.38}$$

To solve for the transverse electric field E_T^z directly from

$$\nabla \times \mathbf{E}_T = -\frac{1}{c}\frac{\partial \mathbf{B}_T}{\partial t}$$

results in a numerical instability caused by the time advancement of the field quantities. Since only source quantities are advanced in time, and since field quantities are defined instantaneously from the source quantities, we do not have radiation in our model. Direct time integration of $\mathbf{B}_T$ breaks the time centering of the algorithm and is also counter to the magneto-inductive formulation[22]. This problem is resolved by combining Faraday's law,

$$\nabla \times \mathbf{E}_T = -\frac{1}{c}\frac{\partial \mathbf{B}_T}{\partial t},$$

and Ampére's law,

$$\nabla \times \mathbf{B}_T = \frac{4\pi}{c}\mathbf{J}_T,$$

into

$$\nabla^2 \mathbf{E}_T = \frac{4\pi}{c^2}\left(\frac{\partial \mathbf{J}}{\partial t}\right)_T, \tag{2.39}$$

which has a time derivative only on the source current. In this way we recover a time centered algorithm. Equation(2-40), given below, is solved by iteration and FFT. Details of this calculation are as follows:

• Transverse electromagnetic field $\mathbf{E}_T^z$ Solver

$$\begin{aligned}\nabla^2 \mathbf{E}_T &= \frac{4\pi}{c^2}\left(\frac{\partial \mathbf{J}}{\partial t}\right)_T \\ &= \frac{4\pi}{c^2}\left[\left(\frac{\partial \mathbf{J}_e}{\partial t}\right)_T + \left(\frac{\partial \mathbf{J}_i}{\partial t}\right)_T\right]\end{aligned} \tag{2.40}$$

Source terms are separated into ion sources and electron sources due to their different dynamical characteristics in the electron guiding center model. The electron current $\mathbf{J}_e$ is separated into perpendicular and parallel components with respect to the magnetic field $\mathbf{B} = \mathbf{B}_0 + \delta\mathbf{B}$, where $\mathbf{B}_0$ is the equilibrium sheared magnetic field and $\delta\mathbf{B}$ is the perturbed magnetic field.

The electron source term is calculated in the following manner :

$$\mathbf{J}_e = J_{e\|}\hat{\mathbf{b}} + \mathbf{J}_{e\perp} \tag{2.41}$$

$$\begin{aligned}
\frac{\partial \mathbf{J}_e}{\partial t} &= \frac{\partial J_{e\|}}{\partial t}\hat{\mathbf{b}} + \frac{\partial \mathbf{J}_{e\perp}}{\partial t} \\
&= \sum_j q_j \frac{\partial v_{\|j}}{\partial t} S(\mathbf{x} - \mathbf{x}_j)\hat{\mathbf{b}} \\
&\quad + \sum_j q_j v_{\|j} \frac{\partial S(\mathbf{x} - \mathbf{x}_j)}{\partial t}\hat{\mathbf{b}} \\
&\quad + \sum_j q_j \frac{\partial \mathbf{v}_{\perp j}}{\partial t} S(\mathbf{x} - \mathbf{x}_j) \\
&\quad + \sum_j q_j \mathbf{v}_{\perp j} \frac{\partial S(\mathbf{x} - \mathbf{x}_j)}{\partial t},
\end{aligned} \tag{2.42}$$

where the time derivative of $\mathbf{v}_{\perp j}$, in the fourth row of Eq.(2-42), is zero since guiding center electrons have no acceleration in the perpendicular direction. By converting the last term of Eq.(2-42) as follows,

$$\begin{aligned}
\frac{\partial S(\mathbf{x} - \mathbf{x}_j)}{\partial t} &= \frac{\partial S(\mathbf{x} - \mathbf{x}_j)}{\partial \mathbf{x}_j}\frac{\partial \mathbf{x}_j}{\partial t} \\
&= -\frac{\partial S(\mathbf{x} - \mathbf{x}_j)}{\partial \mathbf{x}}\frac{\partial \mathbf{x}_j}{\partial t}
\end{aligned} \tag{2.43}$$

and with the definitions

$$\frac{\partial v_{\|j}}{\partial t} = \frac{q_j}{m}\mathbf{E}_{\|}(\mathbf{x}_j)$$

$$\mathbf{v}_{\perp j} = v_{\|j}\hat{\mathbf{b}} + \mathbf{v}_{\perp j}, \tag{2.44}$$

the electron source term can be expressed as

$$\frac{\partial \mathbf{J}_e}{\partial t} = \sum_j \frac{q_j^2}{m} \mathbf{E}_{\|}(\mathbf{x}_j) S(\mathbf{x} - \mathbf{x}_j) - \sum_j q_j \mathbf{v}_j (\mathbf{v}_j \cdot \nabla S). \tag{2.45}$$

The averaged form of the electron source term over FSP is

$$\frac{\partial \langle \mathbf{J}_e \rangle}{\partial t} = \frac{|e|^2}{m_e} n_e \mathbf{E}_{\|} + \nabla \cdot \langle |e| \mathbf{v}_e \mathbf{v}_e \rangle. \tag{2.46}$$

By a similar procedure, the ion source term can be written in averaged form as

$$\frac{\partial \langle \mathbf{J}_i \rangle}{\partial t} = \frac{|e|^2}{m_i} n_i \mathbf{E} + \frac{|e|}{m_i c} (\mathbf{J}_i \times \mathbf{B}) - \nabla \cdot \langle |e| \mathbf{v}_i \mathbf{v}_i \rangle. \tag{2.47}$$

By substituting Eq.(2-46) and Eq.(2-47) into Eq.(2-40) we have the equation to be solved for the transverse electric field:

$$\begin{aligned} \nabla^2 \mathbf{E}_T &= \frac{4\pi}{c^2} \left[\frac{|e|^2}{m_e} n_e \mathbf{E}_{\|} + \frac{|e|^2}{m_i} n_i \mathbf{E} \right]_T \\ &\quad + \frac{4\pi}{c^2} \left[\frac{|e|}{m_i c} (\mathbf{J}_i \times \mathbf{B}) + \nabla \cdot \langle |e| \mathbf{v}_e \mathbf{v}_e \rangle \right. \\ &\quad \left. - \nabla \cdot \langle |e| \mathbf{v}_i \mathbf{v}_i \rangle \right]_T . \end{aligned} \tag{2.48}$$

We separate the field terms from the source terms as a first step towards an iteration scheme for $\mathbf{E}_T$:

$$\nabla^2 \mathbf{E}_T = [E]_T + [R]_T \tag{2.49}$$

Here $[E]_T$ and $[R]_T$ are defined as

$$[E]_T = \frac{4\pi}{c^2} \left[\frac{|e|^2}{m_e} n_e \mathbf{E}_{\|} + \frac{|e|^2}{m_i} n_i \mathbf{E} \right]_T \tag{2.50}$$

$$\begin{aligned} [R]_T &= \frac{4\pi}{c^2} \left[\frac{|e|^2}{m_i c} (\mathbf{J}_i \times \mathbf{B}) \right. \\ &\quad \left. + \nabla \cdot \langle |e| \mathbf{v}_e \mathbf{v}_e \rangle - \nabla \cdot \langle |e| \mathbf{v}_i \mathbf{v}_i \rangle \right]_T \end{aligned} \tag{2.51}$$

Eq.(2-49) is transformed by means of FFT into

$$\mathbf{E}_T(\mathbf{k}) = -\frac{1}{k^2} FFT\left\{[E]_T + [R]_T\right\} \tag{2.52}$$

and solved iteratively in k space. The transverse components of the source terms are defined in k space as

$$[R]_T = \mathbf{I}\cdot\mathbf{R}(\mathbf{k}) - \frac{\mathbf{k}}{k^2}(\mathbf{k}\cdot\mathbf{R}(\mathbf{k})), \tag{2.53}$$

where $\mathbf{I}$ is the unit tensor. Since in the shear Alfvén slab model, only the z component of transverse electric field $\mathbf{E}_T$ exists and also since in our two dimensional k space we have $k_z = 0$ by definition , the z component of Eq. (2-33) becomes

$$\begin{aligned}[R]_T^z &= [\mathbf{I}\cdot\mathbf{R}]_z - \frac{k_z}{k^2}[\mathbf{k}\cdot\mathbf{R}(\mathbf{k})] \\ &= R_z \end{aligned} \tag{2.54}$$

and therefore operations in k space are much simplified.

As a second step to complete the iteration scheme, the longitudinal electric field, embedded in the parallel electric field in $[E]_T$, should be filtered out and added to the source term R_T. The parallel electric field is therefore decomposed into its longitudinal part $\mathbf{E}_L$ and transverse part $\mathbf{E}_T$:

$$\begin{aligned} E_{\|} &= \frac{\mathbf{E}_L\cdot\mathbf{B}}{B} + \frac{\mathbf{E}_T\cdot\mathbf{B}}{B} \\ &= \left(\frac{E_L^x B_x + B_L^y B_y}{B}\right) + \frac{E_T^z B_z}{B}, \end{aligned} \tag{2.55}$$

where the magnetic field is the total field $B = |\mathbf{B}| = |\mathbf{B_0} + \delta\mathbf{B}|$.

After these two procedures, Eq. (2.48) can be written in terms of electron and ion plasma frequencies, ω_{pe} and ω_{pi} respectively, as follows:

$$\begin{aligned} \nabla^2 E_T^z &= \left(\frac{\omega_{pe}^2}{c^2}\frac{n_e}{n_0}\frac{B_z^2}{B^2} + \frac{\omega_{pi}^2}{c^2}\frac{n_i}{n_0}\right) E_T^z \\ &\quad + \frac{\omega_{pe}^2}{c^2}\frac{n_e}{n_0}\left(\frac{E_L^x B_x + E_L^y B_y}{B}\right)\frac{B_z}{B} + R_z. \end{aligned} \tag{2.56}$$

As a final step for the completion of the numerical scheme for E_T^z, the number density n_0 is substracted from both sides of the Eq. (2.56). This substraction minimizes the number of iterations and thus speeds up the iteration to find the solution. The completed iteration scheme can then be written as follows :

$$\begin{aligned} \left[\nabla^2 - \left(\frac{\omega_{pe}^2 + \omega_{pi}^2}{c^2}\right)\right] E_T^z &= \frac{\omega_{pe}^2}{c^2}\left[\frac{n_e\left(\frac{B_z}{B}\right)^2 - n_0}{n_0}\right] E_T^z \\ &\quad + \frac{\omega_{pi}^2}{c^2}\left(\frac{n_i - n_0}{n_0}\right) E_T^z \\ &\quad + S_z \end{aligned} \tag{2.57}$$

where

$$S_z = \frac{\omega_{pe}^2}{c^2}\frac{n_e}{n_0}\left(\frac{E_L^x B_x + E_L^y B_y}{B}\right)\frac{B_z}{B} + R_z \tag{2.58}$$

$$R_z = R_T^z \tag{2.59}$$

Eq. (2.57) is iterated in k space and yields E_T^z.

2.3 Time Stepping

In this section, the source and field quantities calculated by the methods described in sections 2.2 and 2.3 are displayed in time sequential order. Sources and fields are calculated self-consistently. The following procedures will show these calculations step by step. All steps are performed at one time step, and this time step is repeated in a time loop until the physical phenomena of interest are observed.

Initial Step

Define initial conditions for particle positions, velocities, and field quantities:

$$\begin{array}{l} \mathbf{v}^n,\ \mathbf{x}^{n+1/2},\ \mathbf{B}_T^{n-1},\ \mathbf{E}_T^{n-1},\ \mathbf{E}_L^{n-1/2} \\ \quad \mathbf{x}^{n+1/2},\ \mathbf{E}_T^n,\quad \mathbf{E}_T^n, \end{array}$$

Time Loop Starts

Step 1. Define positions and source quantities :

$$\begin{array}{l} \mathbf{x}_n^* = \mathbf{x}^{n+1/2} - \frac{1}{2}\Delta t \mathbf{v}^n \longrightarrow n_e^n,\ \ n_i^n,\ \mathbf{J}_e^n,\ \mathbf{J}_i^n \\ \qquad\qquad\qquad\qquad\qquad\qquad\quad \mathbf{F}_{ve}^n,\ \mathbf{F}_{vi}^n \\ \mathbf{x}^{n+1/2} \longrightarrow \rho^{n+1/2} \end{array}$$

where $\mathbf{F}_{ve}^n$ and $\mathbf{F}_{vi}^n$ are the electron and ion velocity fluxes defined in Eq.(2.49) respectively.

Step 2. Define fields at the n and the $n+1/2$ time steps :

$$\mathbf{E}_L^{n+1/2} : \nabla \cdot \mathbf{E}_L^{n+1/2} = 4\pi\rho^{n+1/2} \longrightarrow \mathbf{E}_L^n = \frac{1}{2}\left(\mathbf{E}_L^{n+1/2} + \mathbf{E}_L^{n-1/2}\right)$$

$$\mathbf{B}_T^n : \nabla \times \mathbf{B}_T^n = \frac{4\pi}{c}\mathbf{J}^n$$

$$\mathbf{E}_T^n : \nabla^2 \mathbf{E}_T^n = \frac{4\pi}{c^2}\left(\frac{\partial \mathbf{J}}{\partial t}\right)^n \text{ ; By } \textbf{Iteration}$$

$$\mathbf{B}_T^{n+1/2} : \mathbf{B}_T^{n+1/2} = \frac{3}{2}\mathbf{B}_T^n - \frac{1}{2}\mathbf{B}_T^{n-1}$$

$$\mathbf{E}_T^{n+1/2} : \mathbf{E}_T^{n+1/2} = \frac{3}{2}\mathbf{E}_T^n - \frac{1}{2}\mathbf{E}_T^{n-1}$$

Step 3. Ion pusher :

$$\mathbf{v}_i^{n+1} \quad : \quad \mathbf{v}_i^{n+1} = \mathbf{v}_i^n + \Delta t \frac{|e|}{m_i}\left(\mathbf{E}_L^{n+1/2} + \mathbf{E}_T^{n+1/2}\right)$$

$$+\Delta t \frac{|e|}{m_i c}\left[\frac{\left(\mathbf{v}_i^{n+1} + \mathbf{v}_i^n\right)}{2} \times \left(\mathbf{B}_0 + \mathbf{B}_T\right)^{n+1/2}\right]$$

By matrix inversion find $\mathbf{v}_i^{n+1}$:

$$\left(\mathbf{x}_i^{n+1}\right)^* : \mathbf{x}_i^{n+1^*} + \frac{1}{2}\Delta t \mathbf{v}_i^{n+1} \longrightarrow n_i^{n+1} \ , \ \mathbf{J}_i^{n+1} \ , \ \mathbf{F}_{vi}^{n+1}$$

$\rho_i^{n+3/2}$ is defined at $\mathbf{x}_i^{n+3/2} = \mathbf{x}_i^{n+1/2} + \Delta t \ \mathbf{v}_i^{n+1}$

Step 4. Electron predictor pusher :

$$v_{\|}^{n+1} : v_{\|}^{n+1} = v_{\|}^{n} - \Delta t \frac{|e|}{m_e} E_{\|}^{n+1/2}$$

$$\mathbf{B}^{n+1/2} : \mathbf{B}^{n+1/2} = \mathbf{B}_0 + \mathbf{B}_T^{n+1/2}$$

$$E_{\|}^{n+1/2} : E_{\|}^{n+1/2} = \left(\mathbf{E}_L^{n+1/2} + \mathbf{E}_T^{n+1/2}\right) \cdot \left(\hat{\mathbf{b}}\right)^{n+1/2}$$

$$\mathbf{v}_{\perp}^{n+1/2} : \mathbf{v}_{\perp}^{n+1/2} = c \left(\frac{\mathbf{E} \times \mathbf{B}}{B^2}\right)^{n+1/2} - \frac{c}{|e|} \frac{\boldsymbol{g} \times \mathbf{B}^{n+1/2}}{(B^{n+1/2})^2}.$$

$$v_{\|}^{n+1/2} : v_{\|}^{n+1/2} = \frac{1}{2}\left[v_{\|}^{n+1} + \mathbf{v}^{n} \cdot \left(\hat{\mathbf{b}}\right)^{n}\right]$$

$$\mathbf{v}^{n+1/2} : \mathbf{v}^{n+1/2} = v_{\|}^{n+1/2} \left(\hat{\mathbf{b}}\right)^{n+1/2} + \mathbf{v}_{\perp}^{n+1/2}$$

$$\mathbf{x}_p^{n+3/2} : \mathbf{x}_p^{n+3/2} = \mathbf{x}^{n-1/2} + 2\Delta t \ \mathbf{v}^{n+1/2}$$

$$\rho_{ep}^{n+3/2} : \text{at } \mathbf{x}_p^{n+3/2}, \rho_{ep}^{n+3/2} \text{ is defined}$$

Step 5. Electron corrector pusher

$$\mathbf{E}_{Lp}^{n+3/2} : \nabla \cdot \mathbf{E}_{LP}^{n+3/2} = 4\pi \left(\rho_{ep}^{n+3/2} + \rho_i^{n+3/2}\right)$$

$$\mathbf{E}_{Lp}^{n+1} : \mathbf{E}_{Lp}^{n+1} = \frac{1}{2}\left(\mathbf{E}_{Lp}^{n+3/2} + \mathbf{E}_L^{n+1/2}\right)$$

$$\mathbf{E}_T^{n+1^*} : \left(\mathbf{E}_T^{n+1}\right)^* = 2\mathbf{E}_T^{n} - \mathbf{E}_T^{n-1}$$

$$\mathbf{B}_T^{n+1^*} : \left(\mathbf{B}_T^{n+1}\right)^* = 2\mathbf{B}_T^n - \mathbf{B}_T^{n-1}$$

$$\mathbf{v}_p^{n+1^*} : \left(\mathbf{v}^{n+1}\right)^* = v_{\|}^{n+1}\left(\hat{\mathbf{b}}\right)^{n+1} + c\left(\frac{\mathbf{E}\times\mathbf{B}}{|B|^2}\right)^{n+1} - \frac{c}{|e|}\frac{\boldsymbol{g}\times\mathbf{B}^{n+1}}{(B^{n+1})^2}.$$

$$\mathbf{x}_p^{n+1^*} : \left(\mathbf{x}_p^{n+1}\right)^* = \mathbf{x}^{n-1/2} + \frac{3}{2}\Delta t\ \mathbf{v}^{n+1/2}$$

$$\left(\mathbf{x}_p^{n+1}\right)^* \text{ defines } \left(\mathbf{J}_e^{n+1}\right)^* \ , \ \left(n_e^{n+1}\right)^*$$

$$\mathbf{B}_T^{n+1} : \nabla\times\mathbf{B}_T^{n+1} = \frac{4\pi}{c}\left(\mathbf{J}^{n+1}\right)^*$$

$$\mathbf{E}_T^{n+1} : \nabla^2\mathbf{E}_T^{n+1} = \frac{4\pi}{c^2}\left[\left(\frac{\partial\mathbf{J}}{\partial t}\right)^{n+1}\right]^* \ ; \text{ By Iteration}$$

$$\mathbf{B}_T^{n+3/2} : \mathbf{B}_T^{n+3/2} = \frac{3}{2}\mathbf{B}_T^{n+1} - \frac{1}{2}\mathbf{B}_T^n$$

$$\mathbf{E}_T^{n+3/2} : \mathbf{E}_T^{n+3/2} = \frac{3}{2}\mathbf{E}_T^{n+1} - \frac{1}{2}\mathbf{E}_T^n$$

$$\mathbf{v}_\perp^{n+3/2} : \mathbf{v}_\perp^{n+3/2} = c\left(\frac{\mathbf{E}\times\mathbf{B}}{B^2}\right)^{n+3/2} - \frac{c}{|e|}\frac{\boldsymbol{g}\times\mathbf{B}^{n+3/2}}{(B^{n+3/2})^2}.$$

$$\mathbf{v}^{n+1} : \mathbf{v}^{n+1} = v_{\|}^{n+1}\left(\hat{\mathbf{b}}\right)^{n+1} + \frac{1}{2}\left[\mathbf{v}_\perp^{n+1/2} + \mathbf{v}_\perp^{n+3/2}\right]$$

$$\mathbf{x}_c^{n+1} : \mathbf{x}_c^{n+1} = \mathbf{x}^{n+1/2} + \frac{1}{2}\Delta t\mathbf{v}^{n+1}$$

$$\mathbf{x}_c^{n+3/2} : \mathbf{x}_c^{n+3/2} = \mathbf{x}^{n+1/2} + \Delta t\mathbf{v}^{n+1}$$

At $\mathbf{x}_c^{n+3/2}$ and at $\mathbf{x}_c^{n+1}$, the quantities $\rho_{ep}^{n+3/2}$ and $\mathbf{J}_{ec}^{n+1}$ are defined .

Time Loop Ends

In the time loop, subscripts p and c identify quantities which are defined at the predictor and corrector steps respectively, and $\hat{\mathbf{b}}$ is the unit vector for the total

magnetic field **B** which is defined at each different time step. Also quantities marked with an asterisk subscript * are not stored, in order to save memory size but are used only temporarily. The entire time loop is repeated at each time step until the expected physical phenomena are established.

2.4 Boundary Treatment

2.4.1 Boundary conditions at the walls

To model the bounded slab, boundary conditions are adopted, which translate into conducting wall boundaries in the $x-$direction and periodic boundaries in the $y-$direction. The conducting wall boundary condition[30] uses the image charge method, which makes the appropriate charge and current densities and fields to be zero at the conducting walls. To implement this boundary condition, we assume the conducting walls are located at $x = 0$ and $x = L_x$ and place a test charge at the arbitrary point x_0 and then double the system to accomodate the image charge located at $2L_x - x_0$. This configuration is shown in Fig. (2.1). With the image charge method, the conducting wall boundaries are satisfied by the relationship between test charge density and image charge density,

$$\rho(2L_x - x) = -\rho(x), \tag{2.60}$$

and by the field quantity $\phi(x)$, which is defined through Poisson's equation with image charges as the source quantities, so that

$$\phi(2L_x - x) = -\phi(x). \tag{2.61}$$

From these relationship, we can see that there exist definite parities for both source and field quantities with respect to the walls. Charge density $\rho(x)$ and

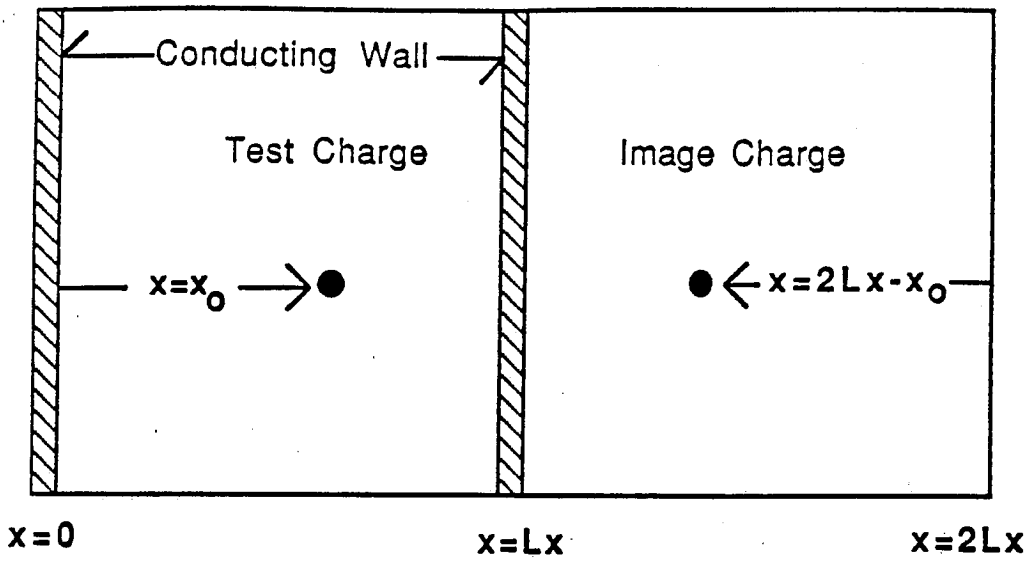

Figure 2.1: Conducting wall boundaries using image charge method.

elctrostatic potential $\phi(x)$ have the same odd parity with respect to the wall. Parity relationships between source and field quantities are discussed in the next subsection.

2.4.2 Parity conservation for source and field quantities

The parities of $\rho(x)$ and $\phi(x)$ due to the conducting wall boundary condition propagate to all source and field quantities through the density equation and Maxwell's equations. For example, $E_x = -\frac{\partial \phi}{\partial x}$ will have an even parity with respect to the walls, whereas $\phi(x)$ is odd :

$$E_x(2L_x - x) = -\frac{\partial \phi(2L_x - x)}{\partial(2L_x - x)} = -\frac{\partial \phi}{\partial x}$$
$$= E_x(x). \qquad (2.62)$$

From the density equation,

$$\frac{\partial \rho}{\partial t} + \nabla \cdot \mathbf{J} = 0,$$

and the field equations,

$$\nabla \times \mathbf{B} = \frac{4\pi}{c}\mathbf{J}$$

$$\nabla \times \mathbf{B} = \mathbf{A}$$

$$\nabla^2 E_T^z = -\frac{4\pi}{c^2} J_T^z,$$

one can induce all symmetry properties of source and field quantities with respect to the walls by conserving the parities in the above equations. The parities for all sources and fields are shown in the follwoing table.

Source and Field Parities for Boundaries

Odd	*Even*
ρ	
J_y, J_z	J_x
ϕ	
A_z	
E_L^y	E_L^x
E_T^z	
B_T^x	B_T^y

These parities with respect to the walls should be distinguished from the parities of eigenmodes which are imposed at a rational surface, e.g., interchange parity when ϕ is even and $A_{||}$ is odd, or tearing parity when ϕ is odd and $A_{||}$ is even. Interchange parity with respect to a rational surface is handled by keeping only odd mode numbers for $A_{||}$ and only even mode numbers for ϕ, respectively.

2.5 Particle Simulation Model of the Lorentz Collision Operator in Guiding-Center Plasmas

2.5.1 Introduction

In particle simulations of low frequency plasma instabilities, guiding-center electron plasma models[18,19] are used to eliminate unnecessary high frequency electron cyclotron oscillations. This means that only the thermal velocity along the ambient magnetic field is kept for the electrons in the simulation model, instead of the full three-directional thermal velocities as is done in conventional particle codes. In guiding-center electron models, the perpendicular electron velocities only come in as particle drift velocities, such as $\mathbf{E} \times \mathbf{B}$, $\boldsymbol{g} \times \mathbf{B}$, or diamagnetic drifts due to pressure gradients. These perpendicular electron velocities due to particle drifts are also much smaller than the electron thermal velocity for relevant simulation parameters.

The guiding-center electron model uses the predictor-corrector method[2] to accurately advance the electron velocities and positions in time. This is necessary since the electrons respond instantaneously to the electric field in the perpendicular direction, while parallel electron acceleration is retained. The ions are pushed by means of the standard leapfrog scheme with full three-directional velocities and Lorentz force, thus allowing for finite ion gyro-radius effects.

When collisionality is introduced in this guiding-center electron plasma model by adopting the Lorentz gas model for the collision operator,[31,32] we face a mismatch between these two models. The Lorentz collision operator allows the particles to do small pitch-angle scattering in three-dimensional velocity space, conserving each particle's energy but not its momentum. The particle velocity vector changes its direction after each small pitch-angle scattering pro-

cess while preserving its magnitude. The Lorentz collision model requires three velocities which are the same order of magnitude in order to perform the right amount of scattering. On the other hand, the guiding-center electron model only evolves the parallel electron thermal velocity and neglects perpendicular thermal velocities which would generate high frequency electron cyclotron waves.

Several consecutive pitch-angle scattering processes with only one significant velocity component will cause a significant loss of its magnitude. Therefore particle energy conservation during the collisional process, which is the character of the Lorentz collision operator, cannot be maintained in the guiding-center electron plasma model. As a cure for this problem, making use of conservation of the magnetic moment μ, we introduce during the collisional process two perpendicular pseudo-thermal electron velocity components in addition to the parallel electron thermal velocity component. However, we retain only that same parallel electron thermal velocity after collision and the two perpendicular velocity components due to particle drifts in the dynamical part of the simulation procedure. In this way we can achieve particle energy conservation for the collisional parallel electron dynamics and also retain the low frequency character of the guiding-center electron plasma model.

We have applied this collisional model to the case of low frequency electrostatic resistive interchange modes in sheared slab geometry. A $2-\frac{1}{2}$D electrostatic particle code with this particular implementation of the Lorentz collision operator is used to simulate these modes. Agreement between simulation and theory is good in terms of linear growth rates and linear eigenmode widths. In subsection 2.5.2 we discuss the implementation of the Lorentz collision operator. In subsection 2.5.3 we apply it to study resistive interchange

mode in sheared slab. Our conclusions are given in subsection 2.5.4.

2.5.2 Implementation of the Lorentz Collision Operator in Guiding-Center Electron Plasma Models

The Lorentz collision operator, which conserves particle energy and number density, is defined by

$$C(g_e) = \frac{\nu_{ei}}{\sin\theta}\frac{\partial}{\partial\theta}\left[\sin\theta\left(\frac{\partial g_e}{\partial\theta}\right)\right] \tag{2.63}$$

where g_e is the adiabatic part of the electron distribution function. Other definitions are :

$$\theta = \cos^{-1}\left(\frac{v_{||}}{(v_{||}^2 + v_{\perp}^2)^{1/2}}\right) : \quad \text{pitch angle}$$

$$\nu_{ei} = 2\pi n_0 e^4 \ln\Lambda/(m_e^2 v_{Te}^3) : \quad \text{collision frequency}$$

It is clear that this collision operator cannot be implemented straightforwardly in the guiding-center electron model which has only one electron thermal velocity component parallel to the sheared equlibrium magnetic field,

$$\mathbf{B}_0 = B_{eq}\left[\hat{\mathbf{z}} + \left(\frac{x - x_0}{L_s}\right)\hat{\mathbf{y}}\right],$$

where B_{eq} is equiribrium magnetic field strength and L_s is the magnetic shear scale length. Since the electron parallel velocity at $t = \Delta t$, after a small pitch-angle scattering process, is given by

$$v_{||}(\Delta t) = v_{||}(t = 0) \times \cos\theta, \tag{2.64}$$

after n time steps ($t = n\Delta t$) the electron parallel velocity begins to lose most of its magnitude due to this scattering:

$$v_{||}(n\Delta t) = v_{||}(t = 0) \times (\cos\theta)^n \ll 1\ . \tag{2.65}$$

Therefore, if the Lorentz collision operator is implemented in a guiding-center particle code without considering the conservation of particle energy, the parallel electron Maxwellian velocity distribution rapidly becomes a cold electron beam due to the scattering process of Eq. (2.65) as shown in Fig. 2.2. However, the gains or losses in magnitude by the perpendicular velocities are not propagated by the dynamics, since these are recalculated from the appropriate particle drifts at each time step.

To resolve the problems caused by this parallel guiding-center electron velocity loss in the Lorentz collision model, two pseudo-thermal perpendicular electron velocities, which are randomly generated from a Maxwellian (at $t = 0$), are introduced to conserve the electron energy E in the electrostatic limit :

$$E = \frac{1}{2} m_e v_{\|}^2 + \mu B_0 + e\phi_0$$

Here the electrostatic potential energy $e\phi_0$ is zero if a dc electric field does not exist, and the electron magnetic moment μ, which is an adiabatic invariant for the guiding-center electrons, is given by

$$\mu = \frac{m_e v_{\perp}^2}{2B_0} .$$

These two electron pseudo-thermal perpendicular velocities are used only in the scattering process and do not propagate into the perpendicular electron dynamics. By performing the collisional procedure in the manner detailed next, we recover the conservation of parallel guiding-center electron energy during the collision (see also Fig. 2.3).

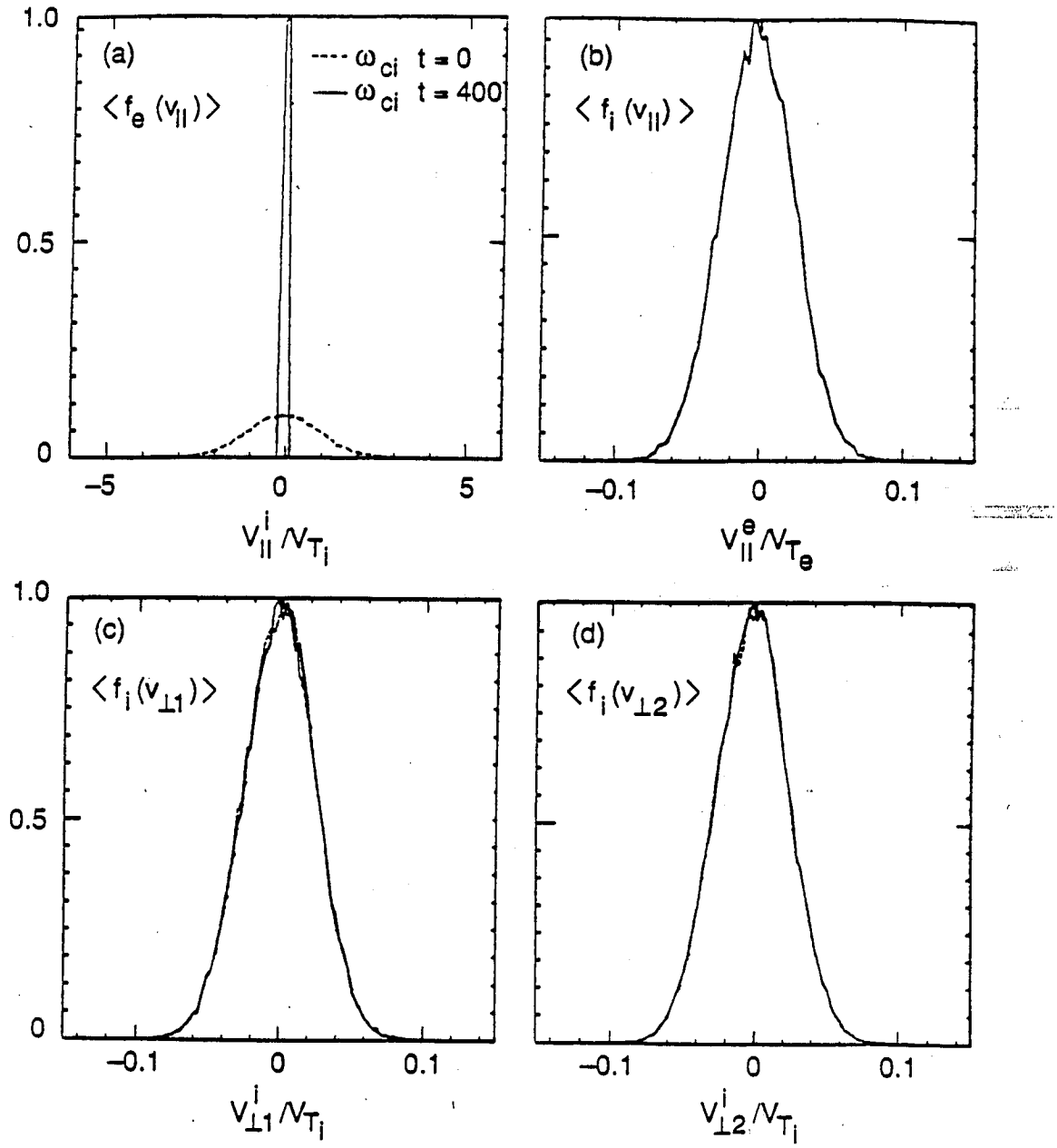

Figure 2.2: Parallel velocity distribution of guiding-center electrons in case of the plainly implemented Lorentz collision operator.

At t = 0

Guiding-center electrons having

$$E = \frac{1}{2} m_e v_{\|}^2 + \mu B_0 + e\phi_0 = \text{ const. },$$

$$\mu = m_e v_{\perp}^2 / 2B_0 = \text{ const.}$$

are loaded and three thermal electron velocities

$$\left(v_{\|}, v_{\perp 1}, v_{\perp 2}\right)$$

are defined with $v_{\perp}^2 = v_{\perp 1}^2 + v_{\perp 2}^2$.

Scattering by Lorentz Collision Operator at each time step

The scattered angle of the jth electron in velocity space is defined by

$$\Delta\theta_j = \left[-4\nu_{ei} \left(\frac{v_{Te}}{(v_{\|}^2 + v_{\perp}^2)^{1/2}} \right)^3 \Delta t \, \ln(1 - r_j) \right]^{1/2}$$

r_j = random number between $(0, 1)$

Δt = time step

At t = Δt:

The gains or losses in velocity generated by the collisional process are

$$(\Delta v_{\|}, \Delta v_{\perp 1}, \Delta v_{\perp 2}) \, .$$

These velocity increments are added to the old velocity set before scattering

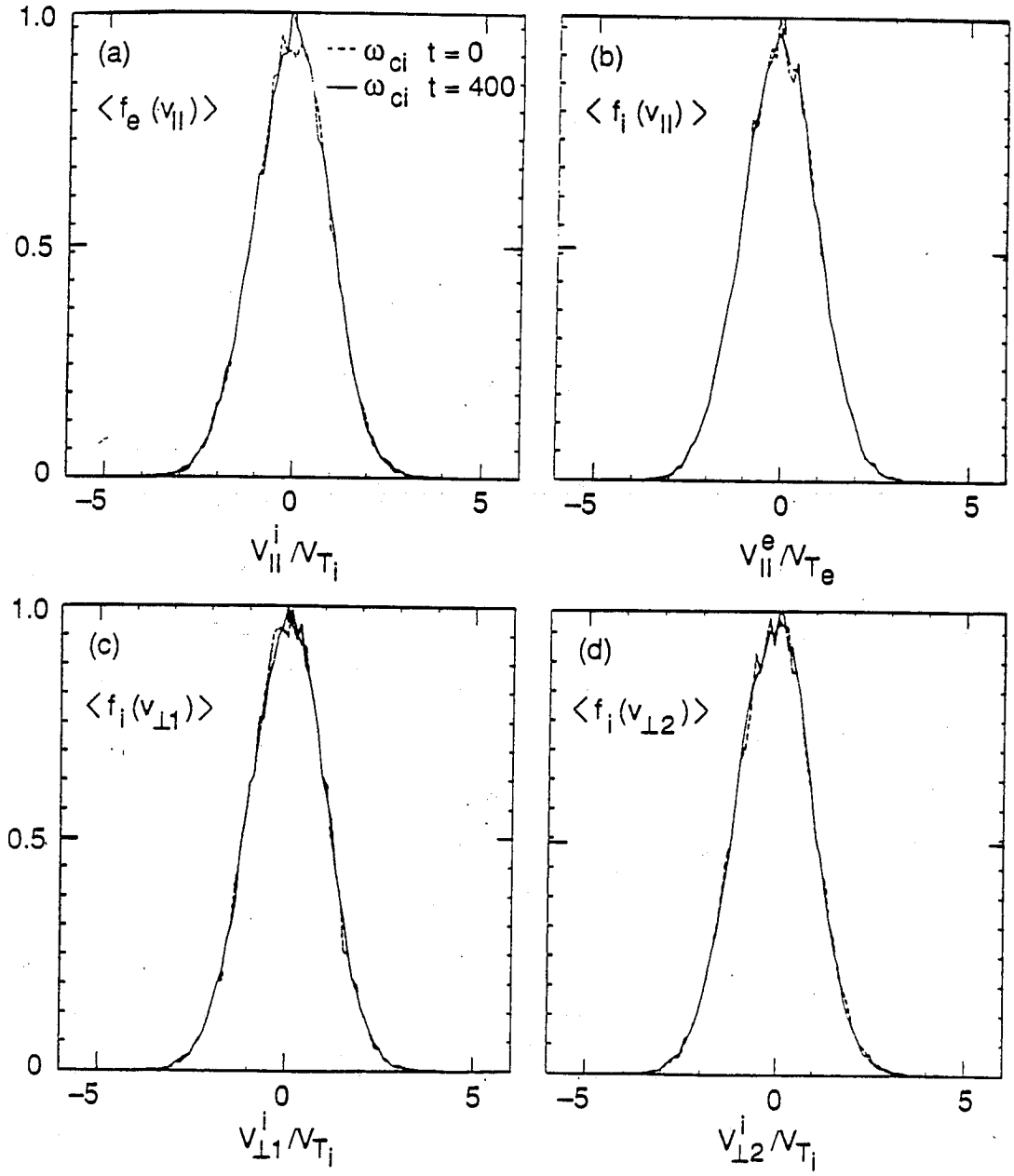

Figure 2.3: Parallel electron and ion velocity distributions with the implemented collisional procedure with the same parameters as those of Fig.2.2.

and are updated as a new velocity set which will be used as the input for the electron thermal velocities at the next time step :

$$v_{\|}^{\text{new}} = v_{\|}^{\text{old}} + \Delta v_{\|}$$

$$v_{\perp 1}^{\text{new}} = v_{\perp 1}^{\text{old}} + \Delta v_{\perp 1}$$

$$v_{\perp 2}^{\text{new}} = v_{\perp 2}^{\text{old}} + \Delta v_{\perp 2} \ .$$

The expressions for the Δv's are explicitly given in Ref. 33.

2.6 Test of the Simulation Model and Algorithm

To check the validity and integrity of the simulation model and the algorithm described in the preceding sections, several tests were performed for plasma waves, whose dispersion relations are relatively well known also whose frequency spectra can be reproduced by a simplified version of the model. Tests were carried out for Bernstein waves, shear Alfvén waves and ordinary ion cyclotron waves. The test code used was a $2-1/2$D periodic version of the magneto-inductive particle code. The configuration of the test model is illustrated in Fig. 2.4. An external magnetic field, $\mathbf{B}_0 = B_0(\text{Cos}\theta\ \hat{\mathbf{z}} + \text{Sin}\theta\ \hat{\mathbf{y}})$, was imposed on the simulation system. Test parameters vary slightly for each test case and depend on the characteristics of wave propagation. However, the parameters which set the properties of the thermal magnetized plasma are common to all cases. Simulation results are compared with linear Vlasov theory which gives the dispersion relation for each mode. The dispersion relation from simulations is obtained by measuring the power spectrum for each mode. Agreement between simulation and the linear kinetic theory for each mode is excellent.

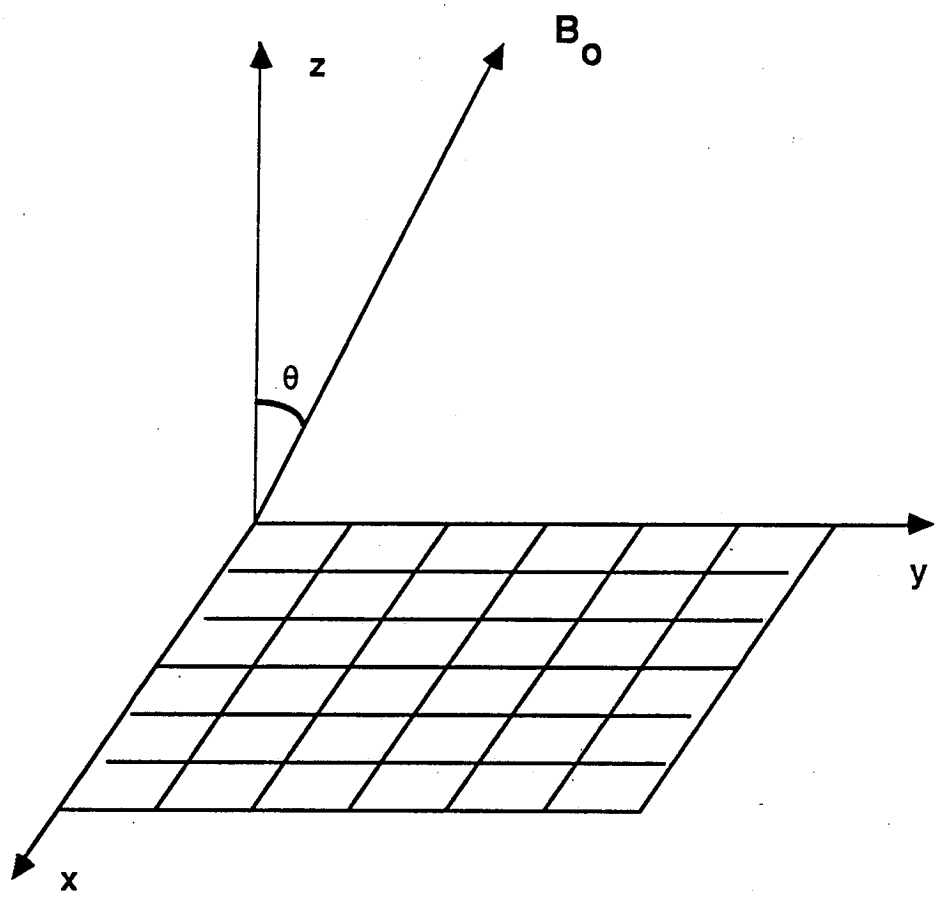

Figure 2.4: Configuration of test model. Imposed external magnetic field is $\mathbf{B}_0 = B_0(\mathrm{Cos}\theta\ \hat{\mathbf{z}} + \mathrm{Sin}\theta\ \hat{\mathbf{y}})$

2.6.1 Bernstein Mode Test

The Bernstein mode[34,35] is an electrostatic mode and is categorized as a linear Vlasov wave. This mode propagates perpendicular to the external magnetic field and has frequencies close to the harmonics $n\omega_{c\alpha}$ of the cyclotron frequency, where α denotes the particle species. From the linearized Vlasov equation, the dispersion relation for Bernstein modes may be obtained and written as

$$\epsilon(k_\perp,\omega) = 1 - \frac{1}{k_\perp^2\lambda_{de}^2}\sum_n e^{-b_e} I_n(b_e)\frac{n\omega_{ce}}{\omega - n\omega_{ce}} - \frac{1}{k_\perp^2\lambda_{di}^2}\sum_n e^{-b_i} I_n(b_i)\frac{n\omega_{ci}}{\omega - n\omega_{ci}} \tag{2.66}$$

For strongly magnetized plasmas such that $\omega \ll \omega_{ce}$, the dispersion relation becomes

$$\epsilon(k_\perp,\omega) = 1 + \frac{1}{k_\perp^2\lambda_d e^2}\sum_n e^{b_e} I_n(b_e) - \frac{1}{k_\perp^2\lambda_{di}^2}\sum_n e^{-b_i} I_n(b_i)\frac{n\omega_{ci}}{\omega - n\omega_{ci}} \tag{2.67}$$

For the guiding center electron plasma model with ρ_e=0, the dispersion relation to be compared with simulation can be written as

$$\begin{aligned}\epsilon(k_\perp,\omega) &= 1 + \frac{1}{k_\perp^2\lambda_{de}^2} - \frac{1}{k_\perp^2\lambda_{di}^2}\sum_n e^{-b_i} I_n(b_i)\frac{n\omega_{ci}}{\omega - n\omega_{ci}} \\ &= 0\end{aligned} \tag{2.68}$$

The comparison of this dispersion relation calculation with the simulation results shows excellent agreement, as demonstrated in Fig. 2.5. Simulation

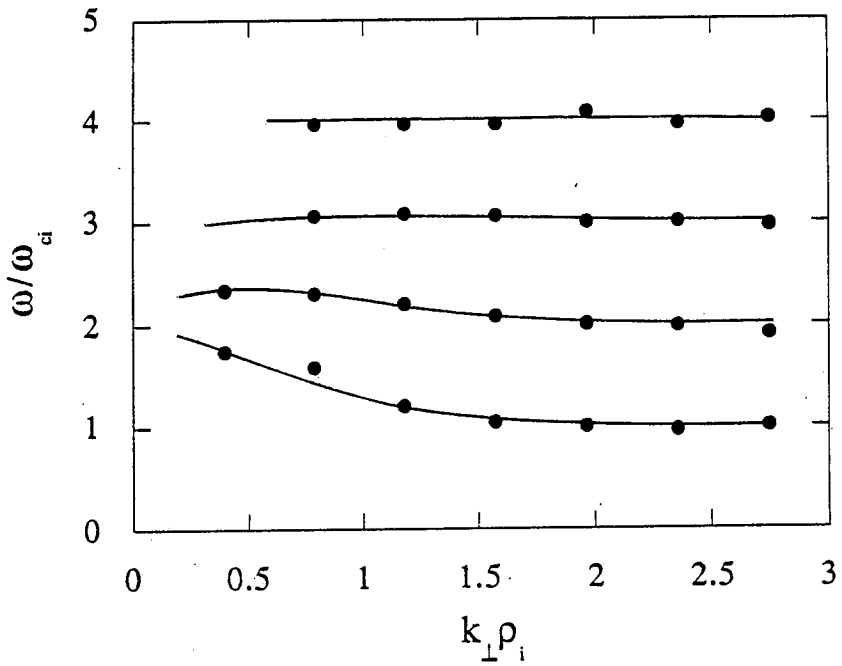

Figure 2.5: Bernstein mode dispersion relation comparison between simulation and theory calculation.

parameters used are $L_x \times L_y = 64\Delta \times 64\Delta$, $n_0 = 4/\Delta^2$, $m_i/m_e = 100$, $T_e/T_i = 1$, $\lambda_{de} = 1\Delta$, $\rho_i = 2\Delta$, particle size $a_x = a_y = 1.5\Delta$, $\omega_{pe}\Delta t = 4.0$, and the total run time is $\omega_{ci}\Delta t = 300$. Another measurement obtained from the simulation is the frequency spectrum of the Bernstein modes. Fig. 2.5 shows us the harmonics of ω_{ci} which are the resonances of the dispersion relation Eq. (2.68).

2.6.2 Shear Alfvén Wave Test

The shear Alfvén wave[36] is an electromagnetic wave that has a $\delta B_\perp$ perturbation with respect to the external magnetic field B_0 which is along the z direction and that propagates parallel to the external magnetic field. Its dispersion relation, with $k_{||}$ only, also comes from the linearized Vlasov equation

and may be written as

$$\epsilon(k_{||},\omega) = 1 - \frac{c^2 k_{||}^2}{\omega^2} + \frac{\omega_{pe}^2}{\omega^2}\frac{\omega}{\sqrt{2}k_{||}v_e} Z\left(\frac{\omega+\omega_{ce}}{\sqrt{2}k_{||}v_e}\right) + \frac{\omega_{pi}^2}{\omega^2}\frac{\omega}{\sqrt{2}k_{||}v_i} Z\left(\frac{\omega+\omega_{ci}}{\sqrt{2}k_{||}v_i}\right). \quad (2.69)$$

For strongly magnetized plasmas $\omega \ll \omega_{ce}$, and with $\xi_e \gg 1$ so that $Z(\xi_e) \sim -1/\xi_e$, we obtain

$$\epsilon(k_{||},\omega) = 1 - \frac{k_{||}^2 c^2}{\omega^2} - \frac{\omega_{pe}^2}{\omega\omega_{ce}} + \frac{\omega_{pi}^2}{\omega^2}\frac{\omega}{\sqrt{2}k_{||}v_i} Z\left(\frac{\omega-\omega_{ci}}{\sqrt{2}k_{||}v_i}\right). \quad (2.70)$$

In the Darwin model limit, $k_{||}^2 c^2/\omega^2 \gg 1$, the dispersion relation to be compared with simulation becomes

$$\epsilon(k_{||},\omega) = -\frac{k_{||}^2 c^2}{\omega^2} - \frac{\omega_{pe}^2}{\omega\omega_{ce}} + \frac{\omega_{pi}^2}{\omega^2}\frac{\omega}{\sqrt{2}k_{||}v_i} Z\left(\frac{\omega-\omega_{ci}}{\sqrt{2}k_{||}v_i}\right) = 0. \quad (2.71)$$

Simulation parameters remain the same as in the case of the Bernstein modes except that $\theta = 5°$, in order to have a $k_{||}$ component in our 2D **k** space, and $L_x \times L_y = 32\Delta \times 128\Delta$. L_y is extended to 128Δ to have $k_{||}v_A \ll \omega_{ci}$ ($v_A = 2.5v_{Te}, \omega_{ci} = 0.05\omega_{pe}$). A comparison of the simulation results with the dispersion relation of theory is plotted in Fig. 2.6 and shows good agreement.

2.6.3 Ordinary Ion Cyclotron Wave Test

As a final test of the kinetic waves in homogeneous warm magnetized plasmas, the ordinary ion cyclotron wave[37] is followed. This wave is an electromagnetic wave which propagates perpendicular to the equilibrium magnetic

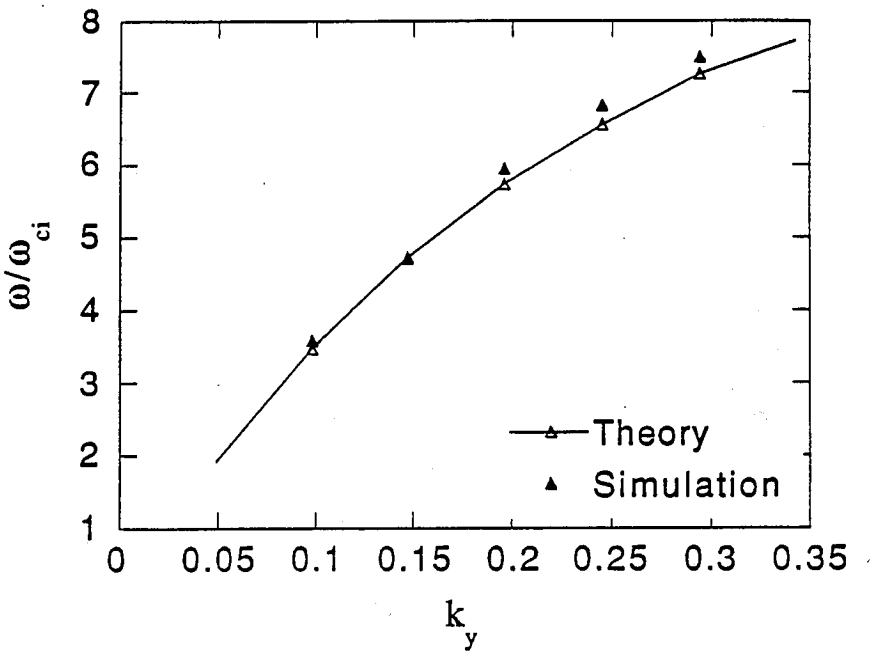

Figure 2.6: Shear Alfvén wave dispersion relation comparison between simulation and theory.

field $\mathbf{B_0}$, with a transverse electric field perturbation $\mathbf{E}_T$ along $\mathbf{B_0}$. In the simulation configuration, these translate into $\mathbf{B_0} = B_0\hat{\mathbf{z}}, \mathbf{k} = k_\perp\hat{\mathbf{x}}$, and $\mathbf{E}_T = E_T\hat{\mathbf{z}}$. The dispersion relation for these waves is

$$\begin{aligned}\epsilon(k_\perp,\omega) &= 1 - \frac{c^2k_\perp^2}{\omega^2} - \sum_j \frac{\omega_{pj}^2}{\omega^2} \\ &\quad + \sum_j \frac{\omega_{pj}^2}{\omega^2} \sum_{n=-\infty}^{\infty} \int d^3v \frac{n\omega_{cj}J_n^2(b_j)}{\omega - n\omega_{cj}} \frac{v_z^2}{\mathbf{v}_\perp} \frac{\partial F_{j0}}{\partial \mathbf{v}_\perp} \\ &= 0 \end{aligned} \tag{2.72}$$

where

$$b_j = k_\perp\rho_j \quad , \quad \omega_{pj}^2 = \frac{4\pi n_0 e_j^2}{m_j}$$

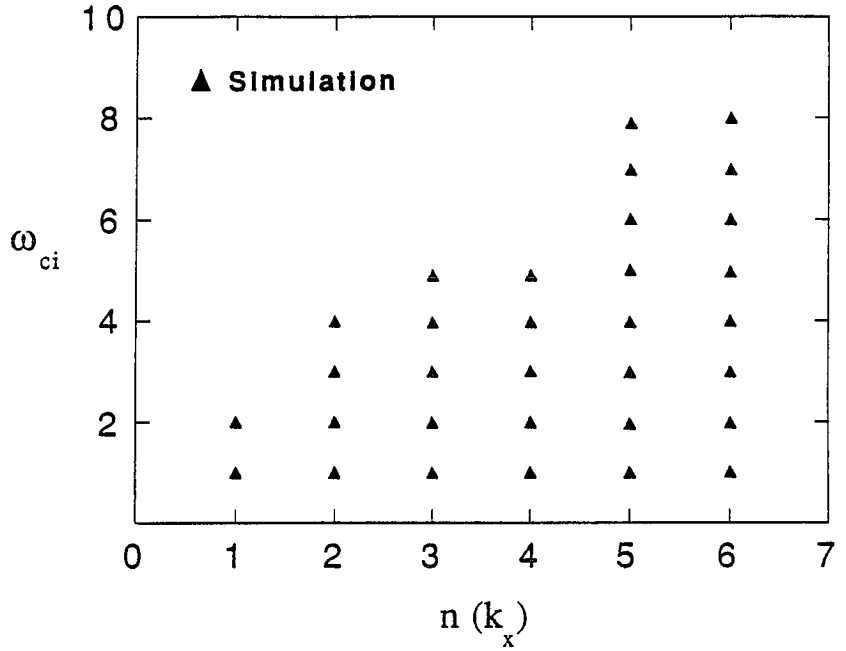

Figure 2.7: Ordinary Ion Cyclotron Wave dispersion relation comparison between theory and simulation. Each points are multiple of $\omega_{ci} = 0.05\omega_{pe}$.

.

For frequencies near the cyclotron harmonics with $k_\perp \rho_i < 1$, $\omega_{ci} \gg \omega_{ce}$, and ρ_e=0, the dispersion relation is simplified to

$$\omega \simeq n\omega_{ci}\left[1 + \frac{\omega_{pi}^2}{k_\perp^2 c^2}(k_\perp \rho_i)^{2n}\right]$$

$$\simeq n\omega_{ci} \tag{2.73}$$

Simulation parameters used to verify this wave are $L_x \times L_y = 32\Delta \times 128\Delta$, $a_x = a_y = 1.0\Delta$, $T_e/T_i = 1.0$, m_e/m_i =0.01, $\omega_{ci} = 0.05\omega_{pe}, \theta = 5°$, ρ_i=2.0Δ, and total run time = 300 ω_{ci}^{-1} with time step, $\Delta t = 4\omega_{pe}^{-1}$. Fig.2.7 shows excellent agreement in the dispersion relation between theory and simulation .

Chapter 3

Particle Simulation of Electrostatic Interchange Modes

3.1 Introduction

Electrostatic interchange modes, which are basically MHD modes in toroidal geometry, can be put into two categories. One is the fast interchange mode and the other is the slow interchange mode[15]. Both are driven by pressure gradients and bad average magnetic field curvature and are radially localized at the mode rational surfaces. These modes are different from the gravitational interchange modes in which the electron drift due to the gravitational force is cut down by the mass ratio m_e/m_i compared to the ion drift, whereas curvature driven modes depend upon the temperature ratio T_e/T_i. Thus the dynamical behavior of the electrons in curvature driven modes is not the same as in the case of gravitational interchange modes.

The key factors distinguishing these two curvature driven modes in MHD analyses are the resistivity η and the azimuthal(poloidal) mode number m in cylindrical(toroidal) geometry which corresponds to the magnitude of k_y in slab geometry. Fast interchange modes, having a characteristic growth rate of

$$\gamma \sim \left(\frac{T_e + T_i}{m_i L_n L_c}\right)^{1/2},$$

with no dependence on resitivity, are basically ideal MHD modes with high m number following the Alfvén time scale of $\tau_A \sim R/v_A$. On the other hand, the

slow interchange mode is a resistive MHD mode with finite resistivity η and with low m number following the slow resistive time scale of $\tau_R \sim a^2/\eta$. The prominent characteristic of resistive interchange modes is that the growth rate follows $\gamma \sim \eta^{1/3}$ scaling[14,15].

Kinetic modifications of these two modes are studied here with the inclusion of diamagnetic drift frequency and finite Lamor radius effects[12,13] in sheared slab geometry. Since these two modes are strongly localized radially, the slab approximation is the simplest and the most affordable model both in theory and in simulation. The eigenmode equation is derived from the drift-kinetic equation for the guiding center electron response and from the gyro-kinetic equation for the gyro-phase averaged ion response with finite ion gyro-radius ρ_i. A second order shooting code scheme is used to solve the radial eigenmode equation and gives the linear eigenfrequency and the linear mode width.

Linear analyses were carried out in the following way. As a preliminary step, finite gyro-radius effects on unstable interchange modes, which evolved from shear stabilized drift waves by increasing the curvature drift, were studied to obtain the optimum k_y value at which fast and slow interchange modes can be identified. Secondly, with zero resistivity and with larger k_y, which corresponds to high m number, linear eigenmode analyses for the collsionless fast interchange modes were performed by solving the linear radial eigenmode equation. As a next step, with finite resistivity and with relatively low m number, which is equivalent to the smallest affordable k_y in the simulation system, analyses for the slow interchange mode were carried out.

The behavior of the kinetic eigenmodes is studied by comparing a calculation in fluid limit with the particle simulation results in the linear phase.

The linear and nonlinear behavior of these modes is studied with respect to phase relations, saturation levels of the fluctuations, and density profile modification for each particle species. Saturated fluctuation levels are compared with mixing length theory estimates.

3.2 Derivation of Linear Eigenmode Equation

The linear eigenmode equation for electrostatic interchange modes is derived from the linearized drift-kinetic equation[38] for the guiding-center electrons,

$$(\omega - \omega_{de} - k_{\|} v_{\|e}) g_e - i\, C(g_e) = -\left(\frac{|e|}{T_e}\right) F_e^M (\omega - \omega_e^*)\phi \,, \tag{3.1}$$

where ϕ is the perturbed electrostatic potential and

$$\omega_{de} = \frac{cT_e}{eB_0}\frac{k_y}{L_c} \quad , \qquad \omega_e^* = \frac{cT_e}{eB_0}\frac{k_y}{L_n} \,. \tag{3.2}$$

Also,

$$C(g_e) = -\nu_{ei}\left[g_e - \frac{F_e^M}{n_0}\int d^3v\, g_e\right] \tag{3.3}$$

is the number-conserving Krook collision operator[39, 40]. The perturbed electron distribution function is separated into adiabatic and non-adiabatic pieces

$$f_e = \frac{|e|}{T_e}\phi\, F_e^M + g_e \,. \tag{3.4}$$

where F_e^M is an electron Maxwellian distribution function

$$F_e^M = \frac{n_0(x)}{(2\pi v_T^2)^{3/2}} \exp(-\frac{v^2}{2v_T^2}) \quad , \quad T = m v_T^2$$

To model collisions we use the particle number conserving Krook collision operator for simplicity. Other operators like the Lorentz collision operator produce equivalent results for interchange modes[40]. The linearized gyro-kinetic equation[38,41] is used to describe the behavior of the ions with finite Larmor radius ρ_i

$$(\omega - \omega_{di} - k_{\|} v_{\|i}) g_i = \left(\frac{|e|}{T_i}\right) F_i^M (\omega - \omega_i^*) J_0(k_\perp \rho_i) \phi \tag{3.5}$$

where

$$f_i = \left(\frac{|e|}{T_i}\right) \phi F_i^M + g_i e^{-iL}, \; L = k_\perp \rho_i \cos\varphi \tag{3.6}$$

$$\tau = T_e/T_i, \quad \omega_{di} = -\omega_{de}/\tau, \quad \omega_i^* = -\omega_e^*/\tau. \tag{3.7}$$

The standard averaging procedure over velocity space for f_e and f_i yields the following perturbed density n_e and n_i.

$$n_e = \frac{|e| n_0}{T_e}\phi + \frac{|e| n_0}{T_e}\left(\frac{\omega - \omega_e^*}{\sqrt{2} k_{\|} v_e}\right) \frac{Z_e}{\left[1 + \frac{i\nu_{ei}}{\sqrt{2} k_{\|} v_e} Z_e\right]} \phi \tag{3.8}$$

$$n_i = -\frac{|e| n_0}{T_i}\left[\phi + \frac{(\omega - \omega_i^*)}{\sqrt{2} k_{\|} v_i} Z_i \Gamma_0 \phi\right] \tag{3.9}$$

By invoking quasi-neutrality $n_e \sim n_i$, we obtain the eigenmode equation for the perturbed electrostatic potential ϕ :

$$\left[1 + \tau + \left(\frac{\tau\omega + \omega_e^*}{\sqrt{2}\, k_{\|} v_{Ti}}\right) Z_i \left(\Gamma_0 - \rho_i^2 \frac{d\Gamma_0}{db} \frac{\partial^2}{\partial x^2}\right)\right.$$

$$+\left(\frac{\omega-\omega_e^*}{\sqrt{2}\,k_{||}v_{Te}}\right)Z_e\Big/\left(1+i\left[\frac{\nu_{ei}\,Z_e}{\sqrt{2}\,k_{||}v_{Te}}\right]\right)\Bigg]\phi=0 \qquad (3.10)$$

$$Z_e=Z_e(\xi_e),\xi_e=\frac{\omega-\omega_{de}+i\nu_{ei}}{\sqrt{2}\,k_{||}v_{Te}}$$

$$Z_i=Z_i(\xi_i),\xi_i=\frac{\omega-\omega_{di}}{\sqrt{2}\,k_{||}v_{Ti}}\ , \qquad \Gamma_0=e^{-b}\,I_0(b)\ ,\ b=k_\perp^2\,\rho_i^2\ .$$

In this equation, the electron curvature drive, ω_{de}, and the ion curvature drive,ω_{di}, are embedded in the arguments ξ_e and ξ_i of the electron and ion plasma dispersion functions[42] Z_e and Z_i, respectively. The eigenmode equation, Eq. (3.9), is solved with a second order shooting code, in terms of the scaling with normalizations $x=x/\rho_i$ and $\omega=\omega/\omega_e^*$.

3.3 Linear Analyses of Electrostatic Interchange Mode

3.3.1 Finite Gyro-radius Effect

Before we perform the separate analyses of the electrostatic interchange mode in two separate regimes i.e., fast and slow interchange modes, we need to carry out preliminary analyses for one key parameter. Since one of the key factors differentiating fast and slow modes in slab geometry is k_y(the m number) and since this parameter is directly linked with finite Larmor radius effects for kinetic modes, we first look at the behavior of the eigenmode for different values of $k_y\rho_i$ with fixed ρ_i . Analysis is carried out by varying $k_y\rho_i$ with a trial value of $L_n/L_c=0.286$, which yields typical unstable interchange mode structures with a rather strong growth rate. Available minimum and maximum values of k_y which the particle simulation scheme can accomodate to possibly distinguish fast and slow interchange modes are $2\pi/128\Delta=0.049$

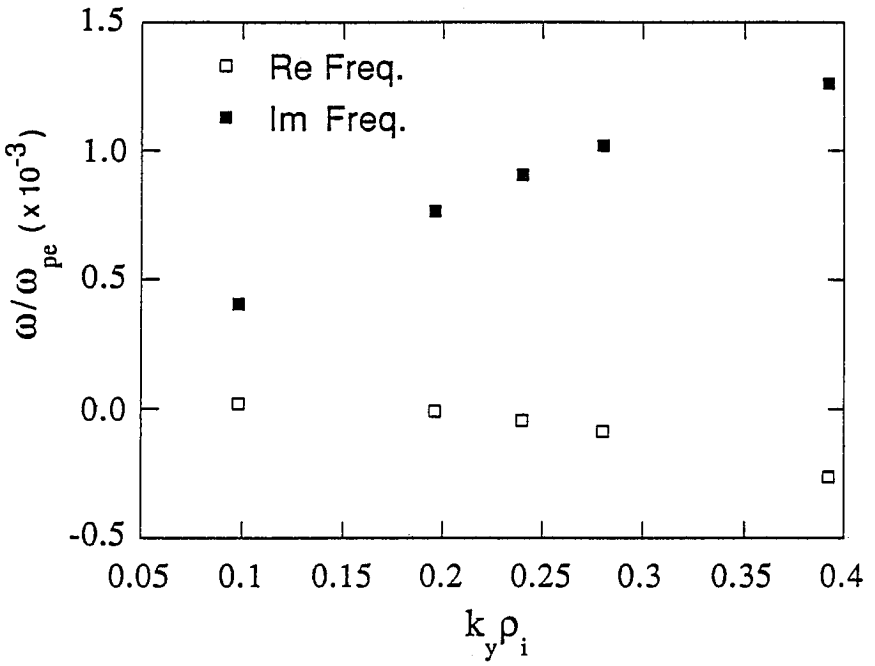

Figure 3.1: Eigenmode spectrum of electrostatic interchange mode under the variation of $k_y\rho_i$ with $L_n/L_c = 0.286$

and $2\pi/32\Delta = 0.196$, respectively. Here Δ is the unit grid spacing. The rest of the parameters in the simulation are L_s/L_n =14, m_e/m_i =0.01, T_e/T_i =1, and $\omega_{ci} = 0.05\omega_{pe}$. The results from the numerical analysis results are shown in Fig. 3-1. It is seen that eigenmodes with $k_y\rho_i$ less than 0.2 behave nearly the same as the resistive MHD interchange mode with almost zero real frequency. With $k_y\rho_i$ larger than 0.2, they become kinetic interchange modes with negative real frequencies which are mainly caused by the ω_i^* effect as in the case of flute modes and with growth rates approaching ω_e^* . The associated eigenmode structures with $k_y\rho_i$=0.098, 0.196, and 0.392 for fixed ρ_i=2 are shown in Fig. 3-2.

3.3.2 Linear Analyses of Fast Interchange Mode

To find unstable eigenmodes solely due to the curvature drive, we started from the electrostatic drift waves which are already stabilized by the magnetic shear. Then by increasing the magnetic curvature drift frequency ω_{de} , which in our normalization is measured in terms of the ratio $\omega_{de}/\omega_e^* = L_n/L_c$, the stable drift wave becomes an unstable drift-interchange mode. The transition from stable drift wave to unstable drift-interchange mode as the value of L_n/L_c is varied shown in Fig. 3.3 in terms of the real and imaginary parts of the eigen-frequency. The accompanying eigenmode structure and electrostatic potential structure for this transition are shown in Fig. 3.4 and in Fig. 3.5, respectively. As the value of L_n/L_c increases, the mode structure becomes more localized at the mode rational surface, which is located the radial position at $x = 0$, and it exhibits a typical g-mode structure. After the curvature drive L_n/L_c exceeds the value of $L_n/L_c = 0.2$, the real eigenfrequency becomes negative and becomes close to ω_i^* . In the stage of drift-interchange modes, the eigenmode structures broadens slightly as L_n/L_c is increased. To see this mode broadening behavior, we take the fluid limit of Eq. (3.9). Expanding the plasma dispersion functions Z_e and Z_i in the large-argument fluid limit $\xi_e \gg 1$ and $\xi_i \gg 1$, viz.,

$$Z(\xi_e) \simeq -\frac{1}{\xi_e}\left(1+\frac{1}{2\xi_e^2}\right) \quad , \quad Z(\xi_i) \simeq -\frac{1}{\xi_i} \tag{3.11}$$

and taking the frequency orderings $\omega_e^* > \omega_{de}$, $\omega > \omega_{de}$, $\omega_i^* > \omega_{di}$, and $\omega > \omega_{di}$, and also in long wave length limit $k_y^2\rho_s^2 \ll 1$, we have

$$\left[\rho_s^2\frac{\partial^2}{\partial x^2} - k_y^2\rho_s^2\right]\phi + \left[\frac{\omega_e^*(\omega_{di}-\omega_{de})}{\omega^2}\right.$$

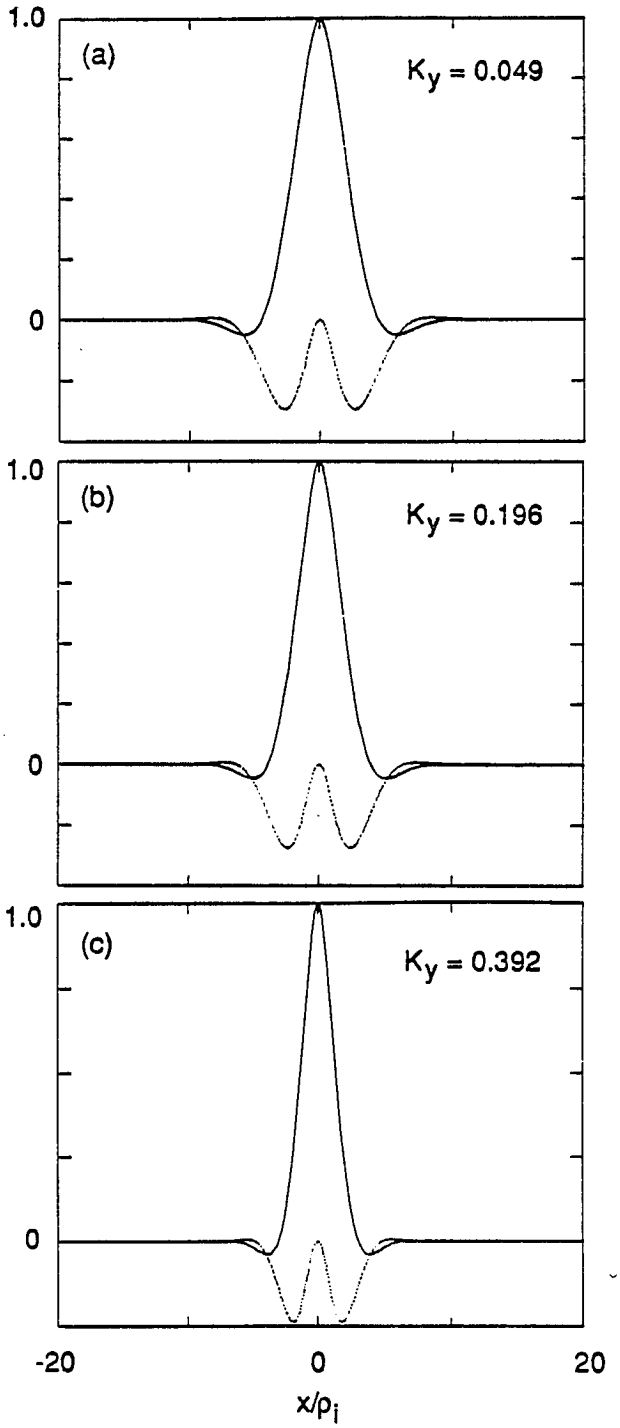

Figure 3.2: Mode structures of $k_y\rho_i$=0.098, 0.196, and 0.392 for $L_n/L_c = 0.286$

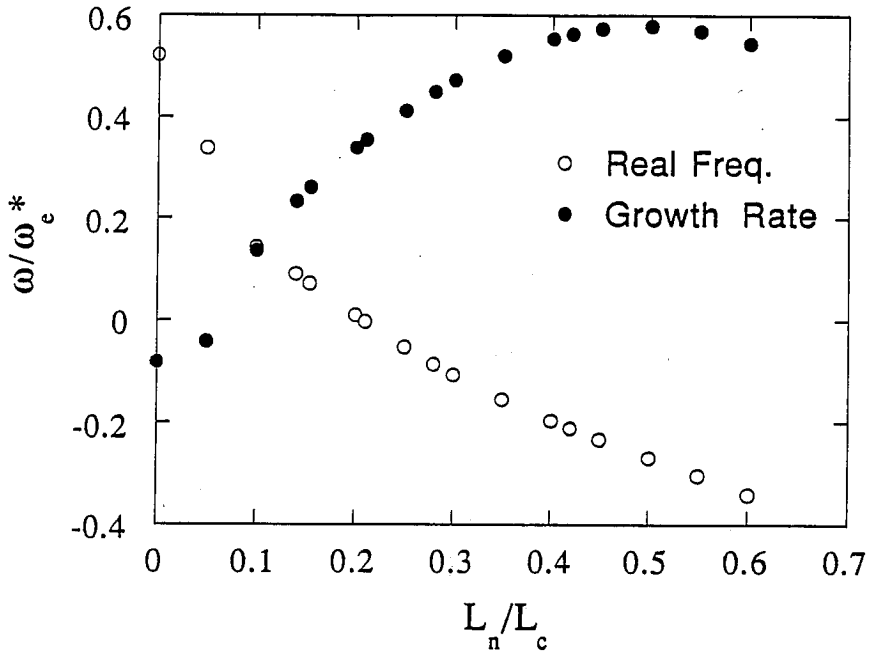

Figure 3.3: Eigenmode spectrum with variation of L_n/L_c. Other parameters are T_e/T_i =1.0, m_e/m_i =0.01, L_s/L_n =14, $k_y\rho_i$=0.392

$$+\left(\frac{\omega-\omega_e^*+i\nu_{ei}}{\omega-\omega_{de}}\right)\frac{k_y^2v_{Te}^2|x|^2}{\left(\omega-\omega_{de}+i\nu_{ei}\right)^2L_s^2}\Bigg]\phi=0 \quad (3.12)$$

where the first two terms represent the ion polarization drift, the third term represents the instability driving term, and the fourth term represents line bending plus field line diffusion in the presence of resistivity. We use a trial eigenfunction[43] given by

$$\phi_l = e^{-x^2/2\Delta^2}H_l(x/\Delta), l=0,1,2,\ldots \quad (3.13)$$

where the H_l are Hermite polynomials of order l. By solving Eq. (3.11) in the fluid limit in which $\omega \sim i\gamma$ and $\nu_{ei}=0.0$, we obtain expressions for the growth rate and the linear mode width of the collisionless electrostatic interchange mode, which are nearly in the fluid regime,

$$\gamma/\omega_e^* = -\gamma_s + \left[\gamma_s^2+\gamma_0^2\right]^{1/2} \quad (3.14)$$

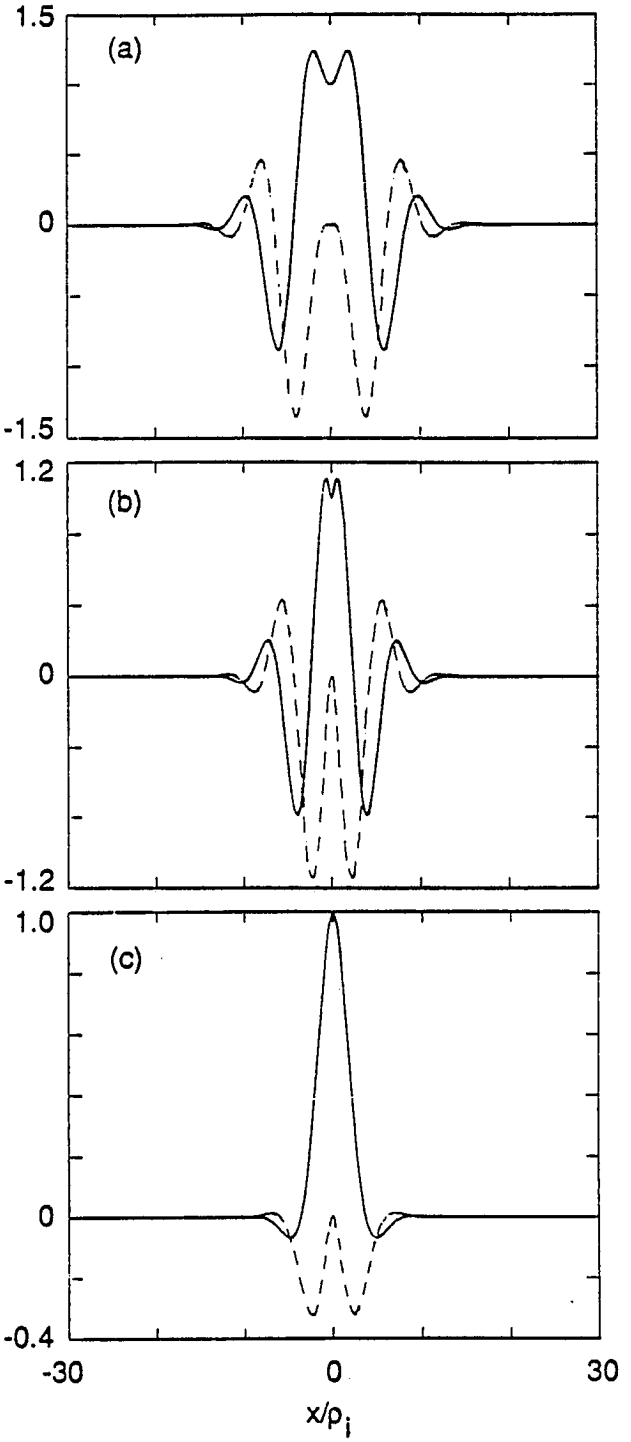

Figure 3.4: Eigenmodes of L_n/L_c=0.0, 0.0714, 0.25. Rest of parameters are the same as in Fig.3-3

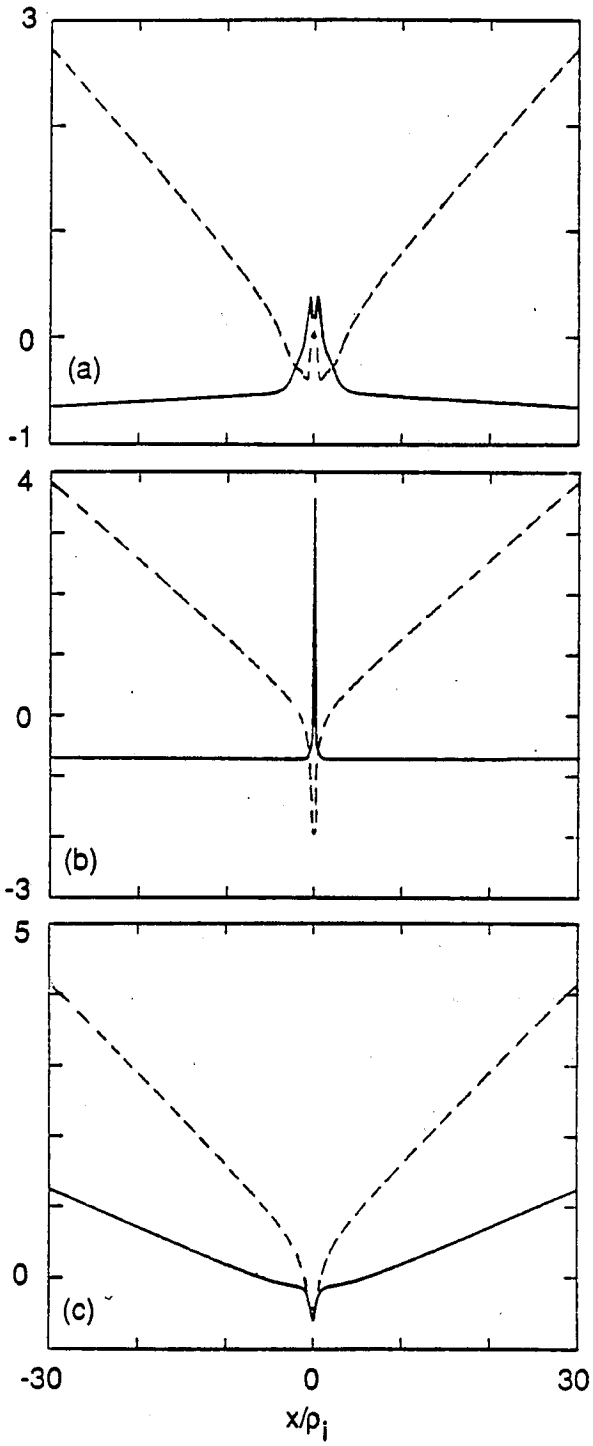

Figure 3.5: Corresponding electrostatic potential ϕ of eigenmodes of Fig.3-5

where

$$\gamma_s = \frac{1}{2}\left(\frac{m_i}{m_e}\right)^{1/2}\left(\frac{L_n}{L_s}\right)\frac{1}{k_y^2\rho_s^2} \quad , \quad \gamma_0 = \left[\frac{1}{k_y^2\rho_s^2}\frac{(1+\tau)}{\tau}\frac{L_n}{L_c}\right]^{1/2} \tag{3.15}$$

Here γ_s includes the stabilizing effect of the magnetic shear, and γ_0 is the growth rate of the fast interchange mode in the absence of magnetic shear. The linear eigenmode width can be obtained from Eq. (3.11) by use of the trial eigenfunction ϕ_l, which yields

$$\Delta^2 = \frac{\gamma\rho_s L_s}{k_y v_{Te}.} \tag{3.16}$$

The resulting linear eigenmode width from this relation can be written as

$$\frac{\Delta}{\rho_s} = \frac{1}{\sqrt{2}k_y\rho_s}\left\{-1+\left[1+\frac{4(1+\tau)k_y^2\rho_s^2}{\tau}\left(\frac{m_e}{m_i}\right)\left(\frac{L_n}{L_c}\right)\left(\frac{L_s}{L_n}\right)^2\right]^{1/2}\right\}^{1/2} \tag{3.17}$$

In this expression we can see that the mode width has a weak dependence on L_n/L_c and a rather strong dependence on $k_y\rho_i$. The eigenmode width and the growth rate, calculated with the second order shooting code and compared with the results from Eq. (3.13) and Eq. (3.16), are plotted in Figs. 3.6 and 3.7 as a function of L_n/L_c and $k_y\rho_i$, respectively.

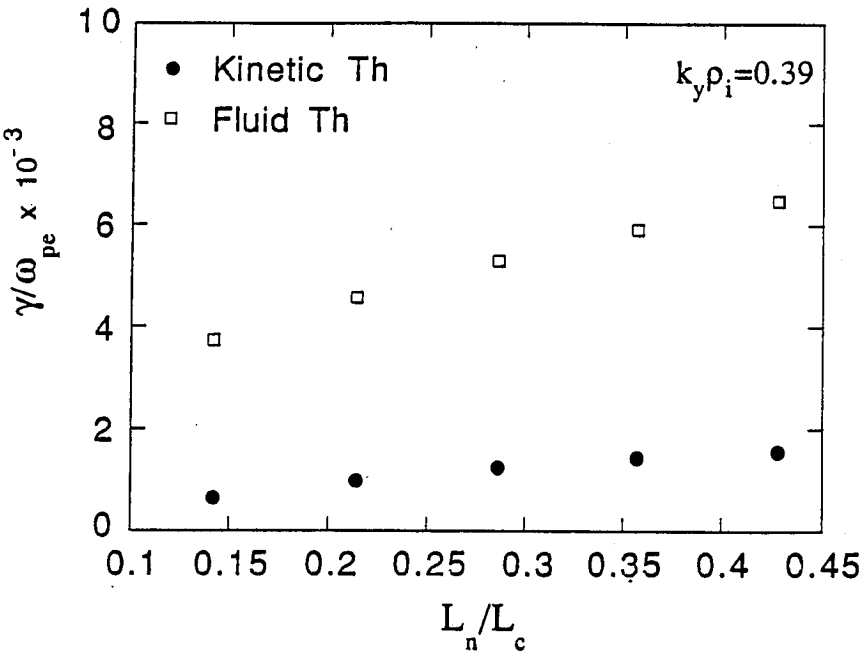

Figure 3.6: Growth comparison between fluid and kinetic mode under the variation of L_n/L_c .

The trend in the variation of the growth rate and the mode width is similar for both the kinetic mode and the fluid mode. In Fig. 3.6, the growth rate of the interchange mode in the fluid limit is higher than that of the kinetic mode. This is due to the kinetic effects such as electron or ion Landau damping which is inherent to kinetic theory and finite Larmor radius effect. In Fig. 3.7 the kinetic eigenmode width is broader than the eigenmode calculated in the fluid limit. Also we can see that the width of the low m mode is broader than that of the high m mode.

As a summary of subsections 3.3.1 and 3.3.2, we show in Fig. 3.8 the behavior of the electrostatic interchange modes having two extremum values of k_y, which would be affordable in the particle simulation, with fixed $\rho_i = 2\Delta$ for the same variation of L_n/L_c . In Fig. 3.8, for all L_n/L_c values, note that $k_y\rho_i$=0.39 has a larger growth rate and a more negative real frequency which

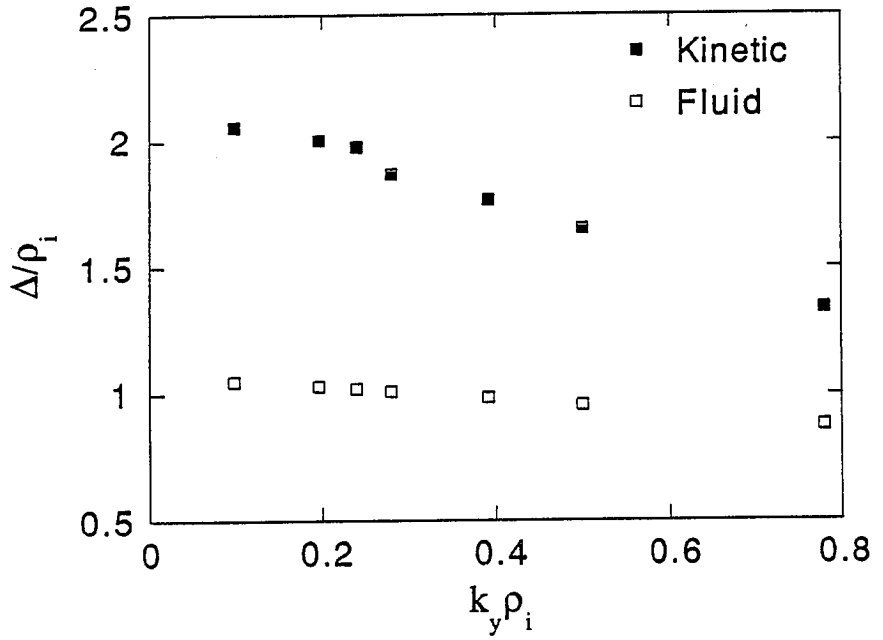

Figure 3.7: Mode width comparison between fluid and kinetic mode under the variation of $k_y\rho_i$ ($\rho_i = 2\Delta$).

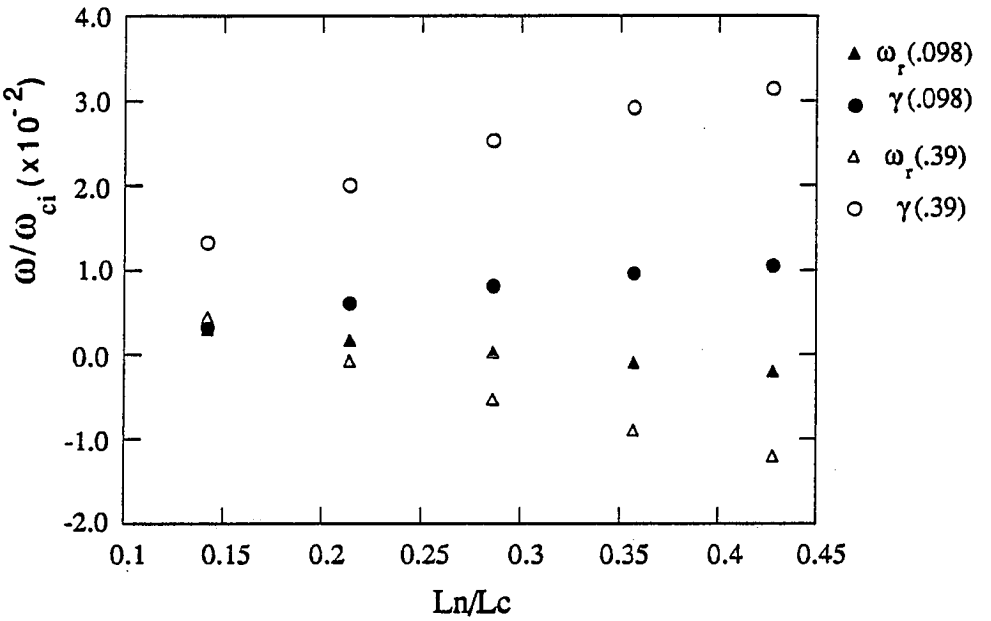

Figure 3.8: Curvature drift $\omega_{de}/\ \omega_e^*= L_n/L_c$variation with $k_y\rho_i$=0.098, 0.39 and L_s/L_n =14.,m_e/m_i =0.01, T_e/T_i =1.,ω_{ci} = 0.05

is mainly due to ω_i^* effects as for the case of flute modes. The eigenmode with $k_y\rho_i$=0.098 follows the same trend as that for the $k_y\rho_i$=0.39 case, but shows less ω_i^* effects, with a smaller growth rate and a real frequency close to zero. Thus in the linear phase, the eigenmode with high m number grows faster than the low m number mode and also has a larger negative frequency due to ω_i^* .

3.3.3 Linear Analyses of Slow Interchange Mode

For the slow interchange mode with smaller k_y, which corresponds to lower m numbers, we follow a procedure similar to that for the fast interchange mode calculation, except that

$$k_y^2\rho_s^2 \ll \rho_s^2\frac{\partial^2}{\partial x^2} \quad , \quad k_y \ll 1 \tag{3.18}$$

Neglecting the second term in Eq. 3.9, we have an expression for the growth rate of the low m number, slow interchange mode,

$$\gamma/\omega_e^* = (\nu_{ei}/\omega_e^*)^{1/3}\,(m_e/m_i)^{1/3}\,(L_s/L_n)^{2/3}\,(L_n/L_c)^{2/3}\,(1+T_i/T_e)^{2/3} \tag{3.19}$$

and for the linear eigenmode width

$$\Delta/\rho_s = (\nu_{ei}/\omega_e^*)^{1/3}\,(m_e/m_i)^{1/3}\,(L_s/L_n)^{2/3}\,(L_n/L_c)^{1/6}\,(1+T_i/T_e)^{2/3} \tag{3.20}$$

which are valid for the resistive mode in the fluid limit. The $\nu_{ei}^{1/3}$ scaling of the growth rate and mode width are well- known major features of resistive interchange modes in the fluid regime. These characteristic features are also obtained by solving the linear kinetic eigenmode equation Eq. (3.9). For each m mode, the spectra of real and imaginary eigenfrequencies versus collision frequency are shown in Figs. 3.9 and 3.10. The typical $\nu_{ei}^{1/3}$ scaling of the fluid approximation is recovered in Fig. 3.11.

The physics of kinetic resistive interchange modes can be understood in the following way. Unstable interchange modes driven by the pressure gradient with unfavorable magnetic field curvature can be stabilized by the sheared magnetic field. In the presence of the sheared magnetic field, the adiabatic electrons zip along the field lines, neutralizing the charge separation due to the particle drifts. In a resistive plasma, this charge neuralization by the adiabatic electrons is blocked by electron-ion collisions, and therefore instabilities are localized at the mode rational surface at $k_{\|} = k_y(x - x_0)/L_s = 0$, where the field lines and the plasma are decoupled. As collisionality increases, the unstable region become broader due to increased blocking. As a result mode broadening occurs around mode rational surfaces, and instability persists further with increased growth rate. This physical picture is in quantitative agreement with Eq. (3.18) and with Eq. (3.19) for the fluid approximation. The resistive interchange eigenmode can be constructed from the shear-stabilized collisionless interchange mode with low m numbers. By increasing the electron-ion collision frequency ν_{ei} continuously, the eigenmode transforms from a stable drift wave-like mode to an unstable mode which is radially localized around the mode rational surface, and then becomes broadened as we further increase the collision frequency.

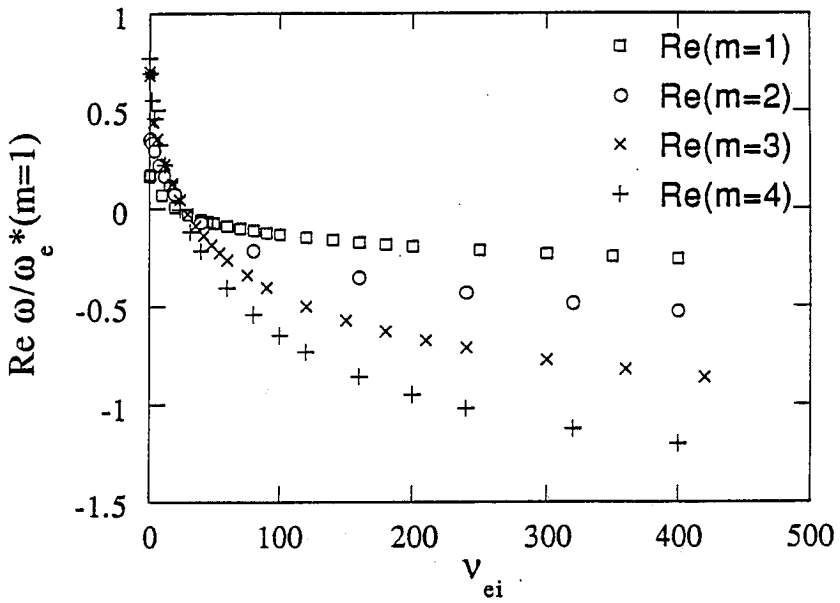

Figure 3.9: Real frequency vs. ν_{ei}

Parameters used in this analysis are $T_e/T_i = 1.0$, $m_i/m_e = 400$, $k_y \rho_i = 0.098$, $L_s/L_n = 14$, $L_n/L_c = 0.134$, $\omega_e^* = 3.436 \times 10^{-4}\ \omega_{pe}$ for m=1 mode, and $\omega_{ci} = 0.05\omega_{pe}$. The collision frequency ν_{ei} is varied from zero up to values for which the growth rates follow the typical resistive scaling. For each m mode, the frequency spectrum is calculated, showing that high m modes are growing faster than low m modes. This picture is consistent with the result of the preceding subsection and also can be understood by looking at the driving term in Eq.(3.11) which has a couping of $\omega_e^* = k_y cT_e/eBL_n$ and ω_{de} $= k_y cT_e/eBL_c$. Both quantities contain an m dependence through k_y ; thus the mode with larger m has the stronger drive and, as a result, has a larger growth rate.

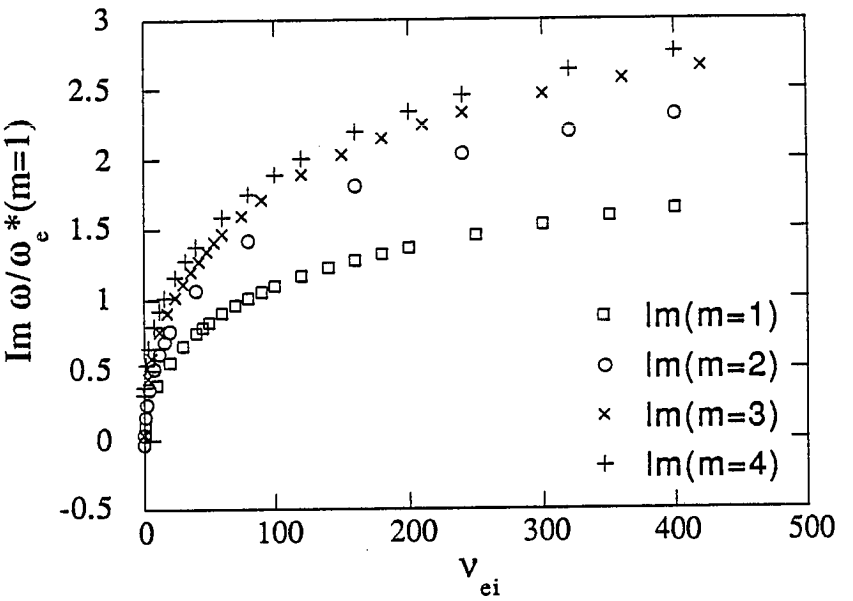

Figure 3.10: Imaginary frequency vs. ν_{ei}

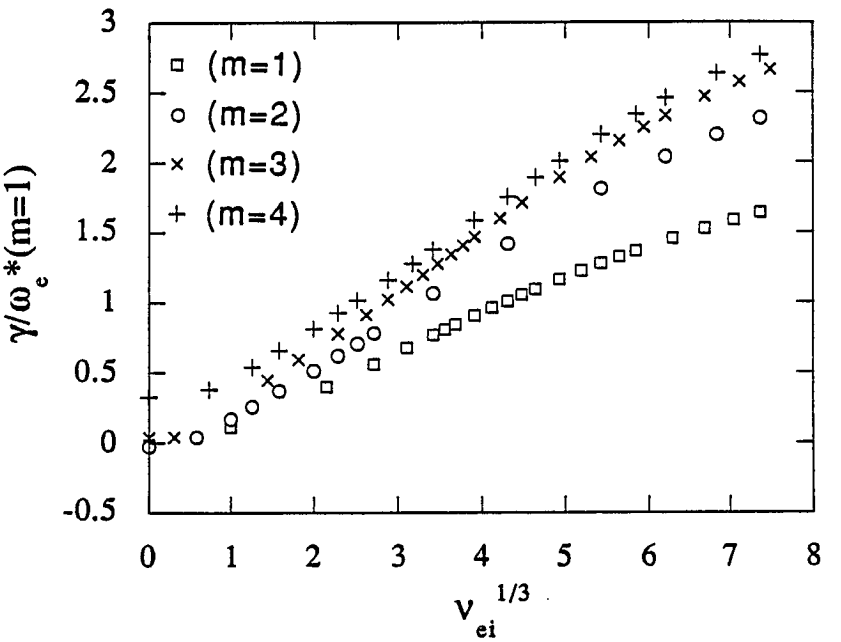

Figure 3.11: Growth rate vs. $\nu_{ei}^{1/3}$ scaling

3.4 Electrostatic Interchange Mode Simulation

3.4.1 Simulation Configulation and Parameters

A $2-\frac{1}{2}$D bounded, electrostatic, guiding-center electron particle model[44,45] is used for the simulations. The configuration for this model is shown in Fig. 3.12. A single mode rational surface is located at x_0 in the middle of the sheared slab, which is extended in the (x,y)-plane with conducting wall boundaries in the x-direction and periodic boundaries in the y-direction. An equilibrium sheared magnetic field is imposed on the (y,z) plane :

$$\mathbf{B_0} = (0, B_0(x-x_0)/L_s, B_0). \tag{3.21}$$

The parallel wave number $k_{||}$ associated with this magnetic field is defined as

$$k_{||} = \mathbf{k}\cdot\mathbf{B}/B = k_y(x-x_0)/L_s \tag{3.22}$$

$$k_y = 2\pi m/L_y, \quad m = 0, \pm 1, ..., \pm L_y/2$$

A density gradient is initially defined and imposed in the x direction,

$$n(x) = -n_0\frac{L_x}{L_n}\left[\exp(-x)/(1-\exp(L_x/L_n))\right], \tag{3.23}$$

and is allowed to relax. Magnetic curvature drift forces are introduced in the direction opposite to the direction of the density gradient,

$$\mathbf{F_c} = \frac{T_j}{L_c}\hat{\mathbf{x}} \tag{3.24}$$

where L_c is the curvature scale length, and T_j stands for the temperature of each particle species. Interchange parity, in which the electrostatic potential ϕ has even parity, is maintained at the mode rational surface. The method-II reflecting boundary scheme of Naitou *et al.*[46] is used to handle the particles

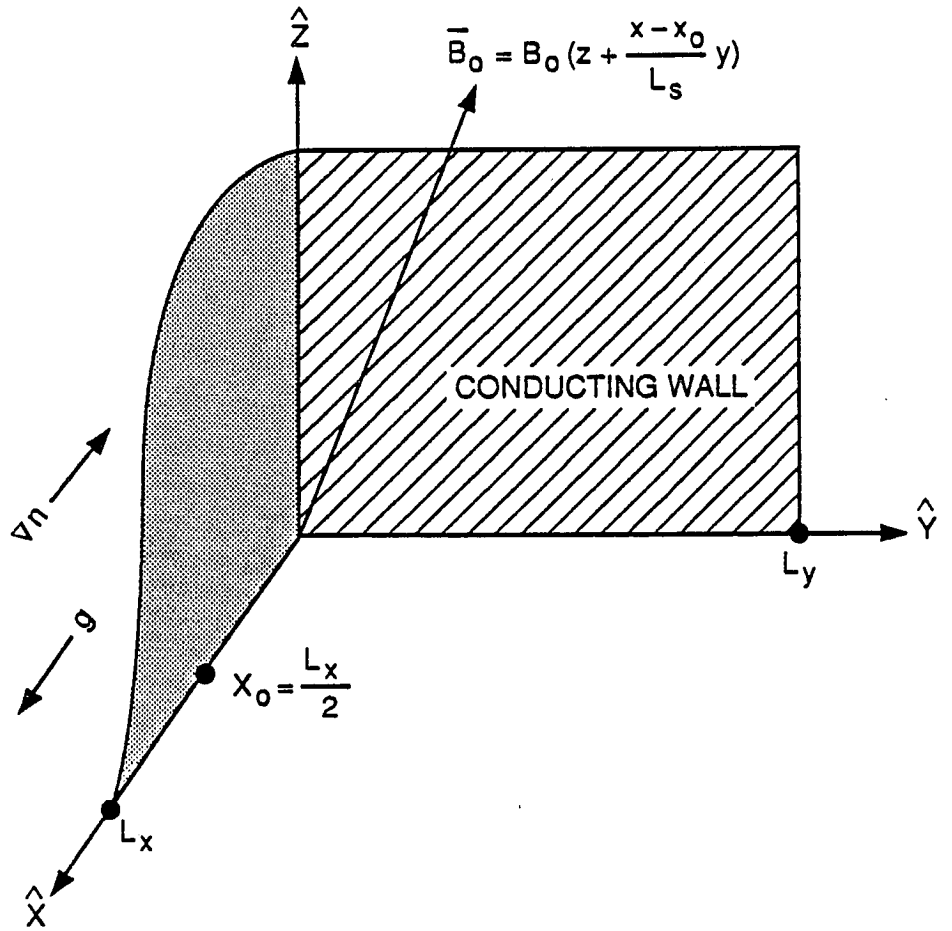

Figure 3.12: Bounded $2 - \frac{1}{2}$D sheared slab model for simulation. Density gradient is in the negative x-direction and centrifugal force F_c is in the positive x-direction in sheared slab. The mode rational surface is located in the middle of the system at $x_0 = L_x/2$.

at the boundaries. Simulations are performed with emphasis on two particular features.

The first point is a scaling study of field and particle quantities through measurements at the linear and nonlinear phase with respect to the most relevant parameter which drives instabilities most visibly. Measurements of the growth rate and eigenmode width in the linear phase are carried out with the most relevant parameter variations which affect linear instabilities and are compared with the results of linear kinetic theory. In the nonlinear phase, the saturation levels of the density perturbations n_e and n_i and of the electrostatic potential ϕ are measured and compared with mixing length estimates with respect to the parameter variation.

The second point concerns measurements related to the quasilinear and nonlinear behavior of particle and field quantities, which particle simulations can readily deliver. The dynamical behavior of field and particle quantities is observed and measured with respect to phase relations between particle and field fluctuations in the linear and nonlinear phases. Also the time variation of the mode spectrum is measured. Details of relevant measurements, observations, and related physical pictures will be discussed in the following subsections.

3.4.2 Simulation of Fast Interchange Mode

Scaling studies for the linear growth rates with respect to the curvature drive parameter L_n/L_c are carried out and compared with the predictions of linear kinetic theory. The simulation parameters used are $L_x \times L_y = 64\Delta \times 32\Delta$, T_e/T_i =1.0, ρ_i=2.0, ω_{ci} = 0.05, m_e/m_i =0.01, L_s/L_n =14, $k_y\rho_i$=0.39m, and ω_e^*=2.748 $\times$ $10^{-3}m\omega_{pe}$. The total run time is $n\Delta t = 400\omega_{ci}^{-1}$, and L_n/L_c

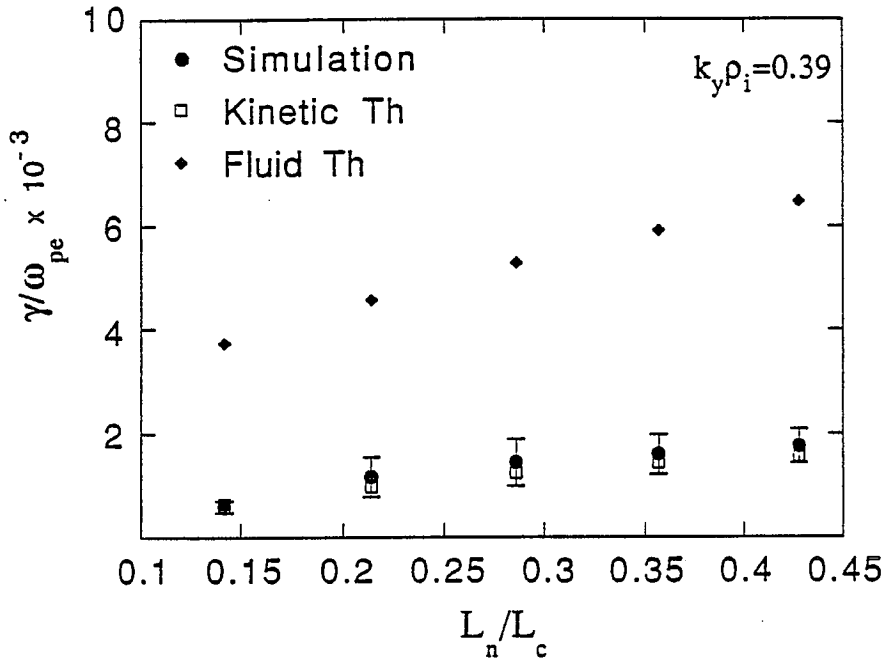

Figure 3.13: Growth rate comparison between theory and simulation. Also fluid calculation results are compared.

is varied from zero to the value which gives maximum growth rate in the linear kinetic theory. The L_n/L_c values are 0.1428, 0.2143, 0.2857, 0.3571, and 0.4286. The number of modes introduced in the simulation system is 5 m modes optimized for the system size ($L_y = 32\Delta$). Mode numbers larger than this m number are affected by the finite size particle effect, due to $\exp(-k_y^2 a_y^2)$, and information about these modes would be inaccurate and negligible.

Measurements of the linear growth rate of the most unstable modes in the simulation are compared with the predictions from linear kinetic theory and linear fluid theory. Agreement between simulation and linear kinetic theory is excellent as shown by Fig. 3.13. The discrepancy with linear fluid theory is due to kinetic effects such as linear ion Landau damping and finite Larmor radius effect[47], which are not included in the fluid calculation. Fluid estimates of the growth rate without any dissipation mechanisms show an order of mag-

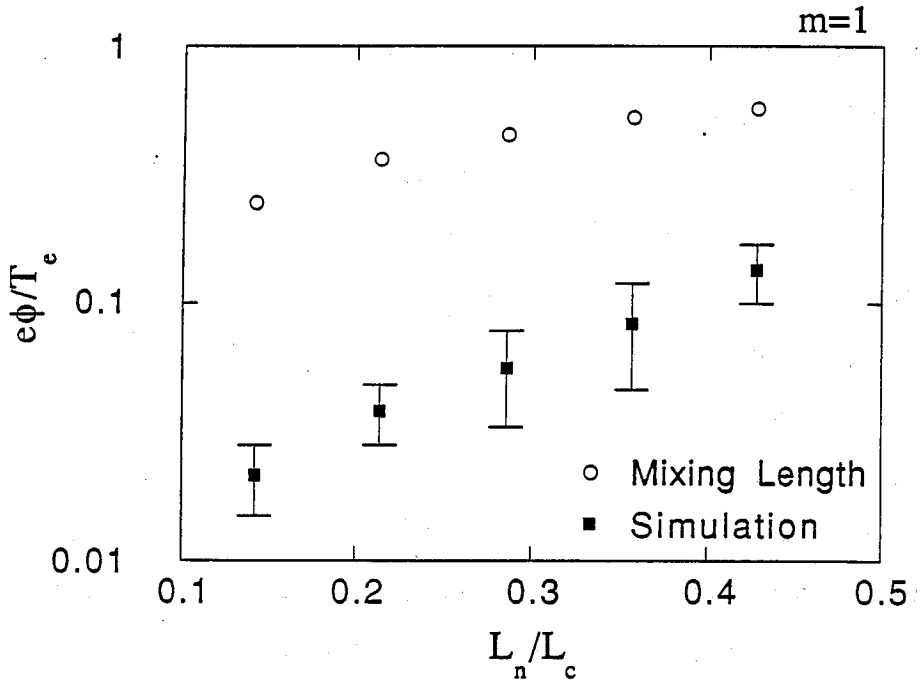

Figure 3.14: Measured saturation level of $m = 1$ mode compared with mixing length theory.

nitude discrepancy with the kinetic calculation. The amount of discrepancy corresponds to the dissipation due to ion Landau damping and FLR effect. Mode widths in the linear phase are also measured and show the same trend as in linear theory. In the nonlinear phase, the scaling of the ϕ saturation levels as the value of L_n/L_c is varied is measured and compared with mixing length theory estimates[44] (Fig. 3.14). There is an order of magnitude discrepancy in absolute magnitude between theory and simulation but both show a similar trend. In Fig. 3.15, the time evolution of the electrostatic field energy $E^2 = k^2\phi^2$ and the potential field energy ϕ^2 are shown. After an initial transient phase, the linear stage holds till $t = 120\omega_{ci}^{-1}$, and saturation occurs after $t = 120\omega_{ci}^{-1}$, with damping starting at $t = 160\omega_{ci}^{-1}$. Both field energies saturate in a similar manner. In the saturated phase, several relevant measurements and observations, which are mainly quasilinear effects, are made. The first

one is the density gradient profile flattening[48] associated with pressure convection. Quasilinear plateau formation in the electron density profile starts at the initial saturation phase. In the fully saturated phase, the electron density profile has a fully developed plateau, whose extent corresponds to the nonlinearly broadened eigenmode width, while ions exhibit a negligible change in density profile (Fig. 3.16). As L_n/L_c increases, quasilinear flattening of the electron density gradient is observed, commensurate with the broader mode width. Parallel electron temperature profile modification starts in the saturation phase at $t = 140\omega_{ci}^{-1}$ and accompanies the electron density profile modification. On the dense side of the electron density gradient, which is to the left of the mode rational surface, parallel electron temperature heating occurs, while at the right side, electron temperature cooling is observed (Fig. 3.17). The peak heating point is approximately 3.5 ρ_i away from the mode rational surface. These heating and cooling regions become diffused radially when steady state saturation is achieved. Parallel electron temperature profile modifications can be seen more clearly through parallel electron velocity distribution contours. At the first occurence of saturation, there is a clear deformation of the parallel electron velocity distribution, and later on this deformation reaches a diffusive state (Fig. 3.17). By contrast, the parallel ion temperature profile remains almost unchanged. Also there is no noticeable velocity deformation of the ion parallel (Fig. 3.18).

Second, phase relations[49] between the particle species and the associated field quantities are measured and compared in both linear and nonlinear phases. The phase relationship between perturbed electron density and electrostatic potential is measured in both the initial linear phase and the saturated phase. In the beginning of the linear phase, there is a clearly visible phase difference between n_e and ϕ . Contour plots of n_e and ϕ given in Fig. 3.19

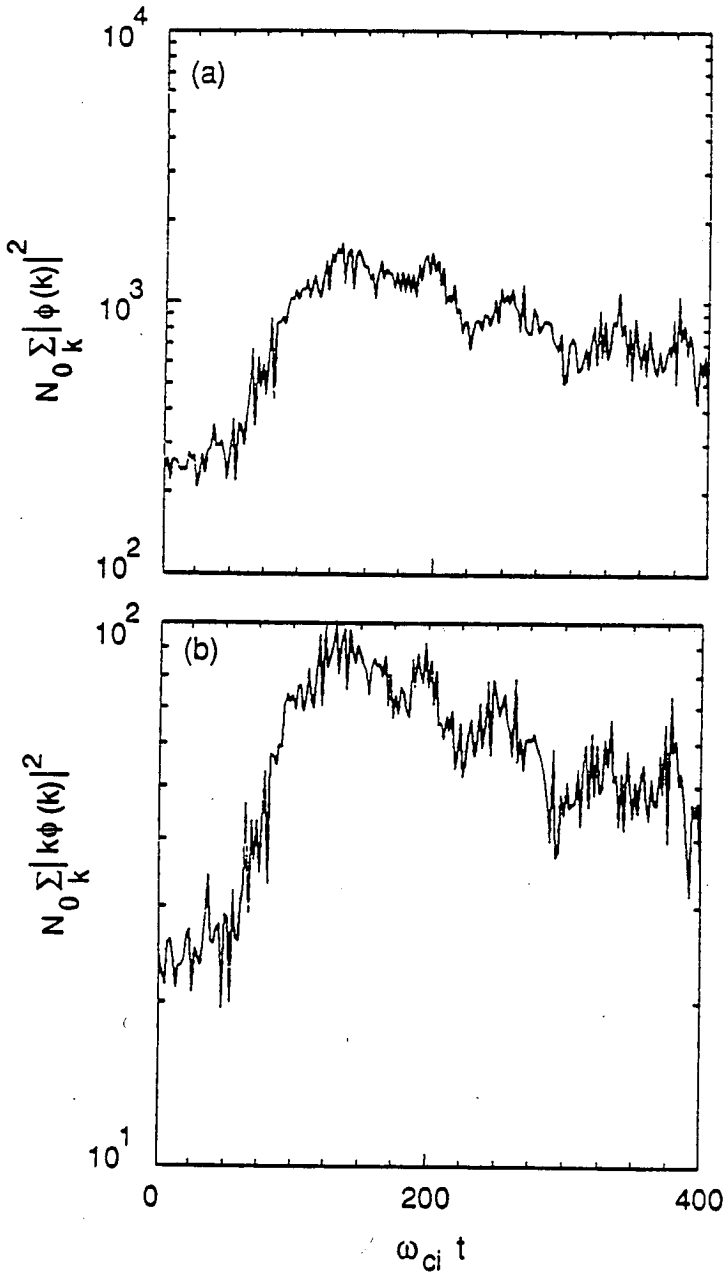

Figure 3.15: Time evolution of electrostatic field energy and potential energy. Both field energies are saturated in a similar fashion. N_O is the total number of particles in the simulation system.

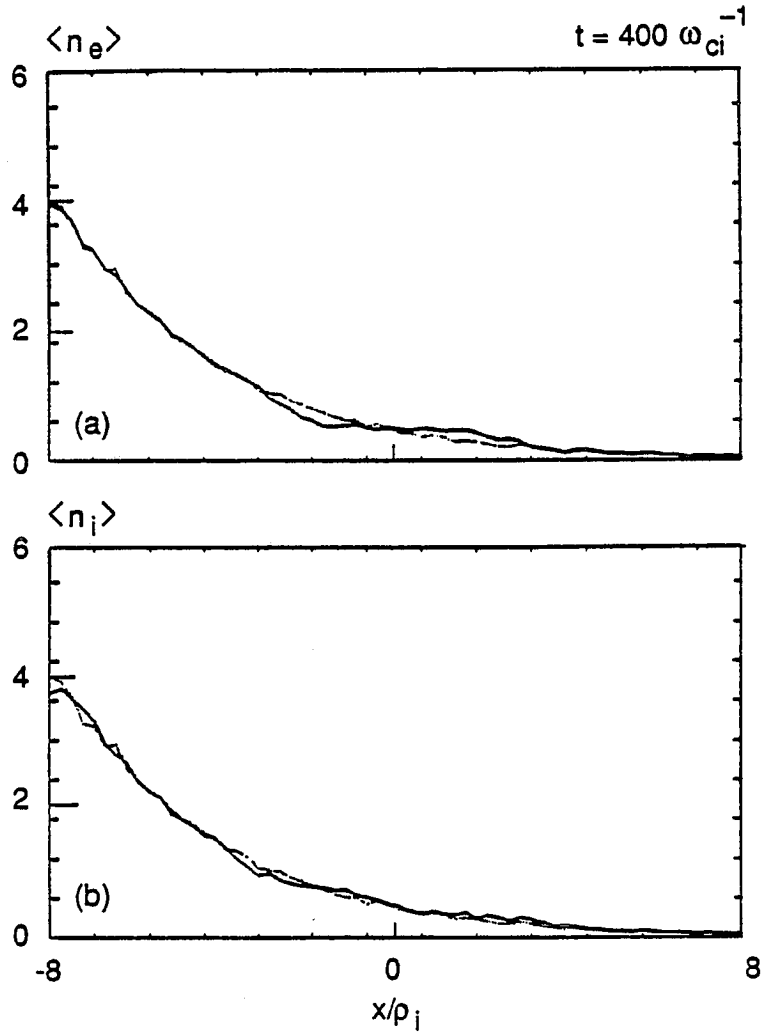

Figure 3.16: Electron and ion density profile at $t = 400\omega_{ci}^{-1}$

show that at $t = 60\omega_{ci}^{-1}$, the phase difference is near $\pi/2$. At the final saturated phase, the phase difference is close to zero. This phase relationship between n_e and ϕ is also shown by the snapshots of the n_e, n_i, and ϕ spatial structures observed in the simulation (Fig. 3.20). At the strongly growing linear phase $t = 120\omega_{ci}^{-1}$, a phase difference of approximately $\pi/4$ is observed from the spatial mode structures of n_e and ϕ . At the fully saturated phase, n_e and ϕ are nearly in phase. One interesting point is that in this fully saturated phase, n_i and ϕ have similar spatial structures whereas the n_e spatial structure shows more fluctuations (Fig. 3.21). The saturation levels of ϕ , n_e, and n_i are shown in Fig. 3.22. Another observation is that n_i and ϕ have similar time correlation spectra. From the spatial structures of n_i and ϕ in the saturation phase shown in Fig. 3.21 and the shape of the correlation spectrum shown in Fig. 3.22, n_i and ϕ are well correlated in the saturated phase whereas n_e and ϕ are less correlated.

3.4.3 Simulation of Slow Interchange Mode

Linear scaling studies of the growth rate and the mode width are performed in the our simulations, which include the algorithm for the Lorentz collision operator, described in Chapter 2, with respect to the electron-ion collision frequency ν_{ei} . The linear growth rate and eigenmode width measured from the simulations are compared with linear kinetic theory. The simulation parameters used for the scaling studies are the same as for the linear theory calculation with system sizes $L_x = 64\Delta$ and $L_y = 128\Delta$, particle sizes $a_x = a_y = 1.5\Delta$, $\rho_i = 2\Delta$, $n_0 = 16/\Delta^2$, with unit grid spacing Δ, $\rho_i/L_n = 0.14$, $\rho_i/L_c = 1.876 \times 10^{-2}$,$\omega_{ci} = 0.025\omega_{pe}$, ω_e^*=$3.436 \times 10^{-4} m\omega_{pe}$ and run time $(n\Delta t) = 4000 \times 4\omega_{pe}^{-1} = 400\omega_{ci}^{-1}$. The number of modes inserted in the simula-

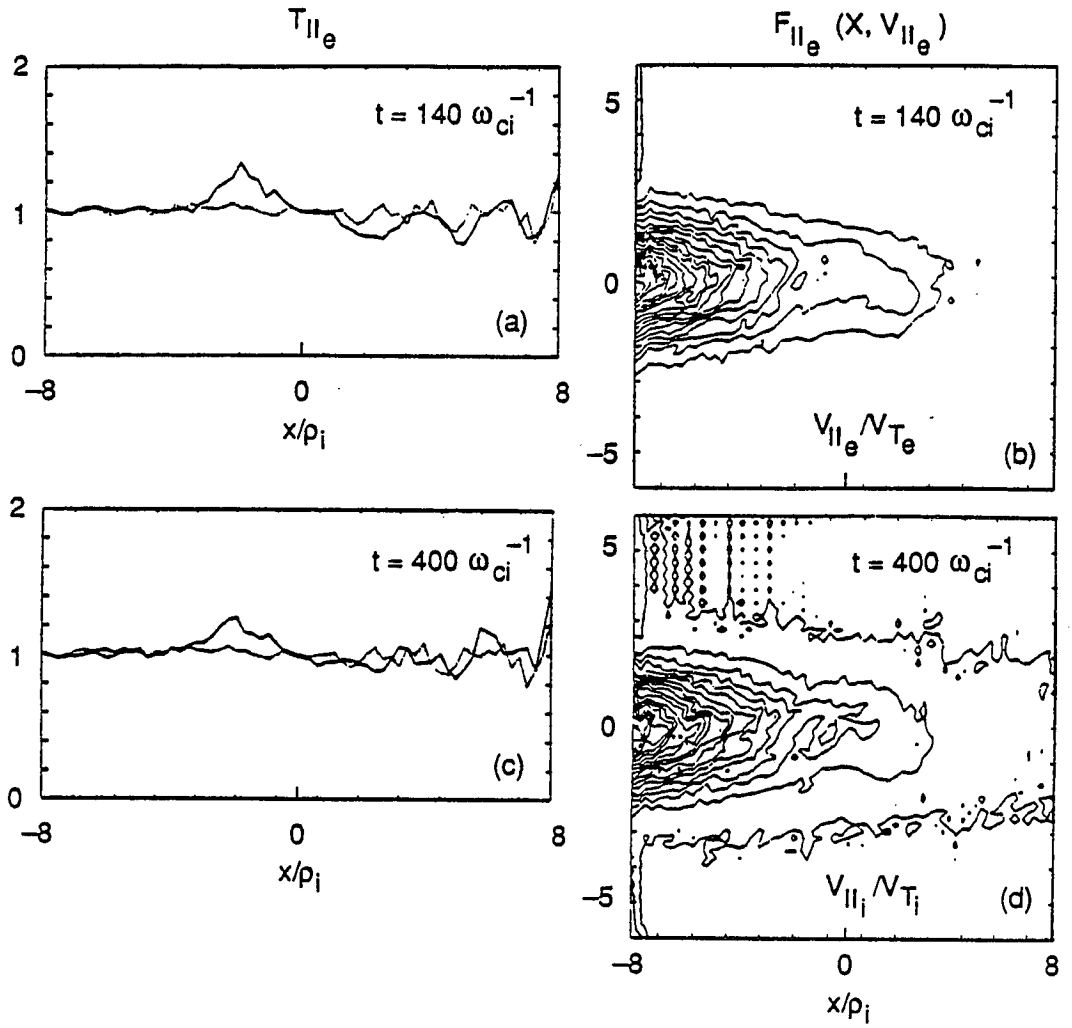

Figure 3.17: Parallel electron temperature profile modification and corresponding velocity distribution contour at $t = 140\omega_{ci}^{-1}$ and $t = 400\omega_{ci}^{-1}$.

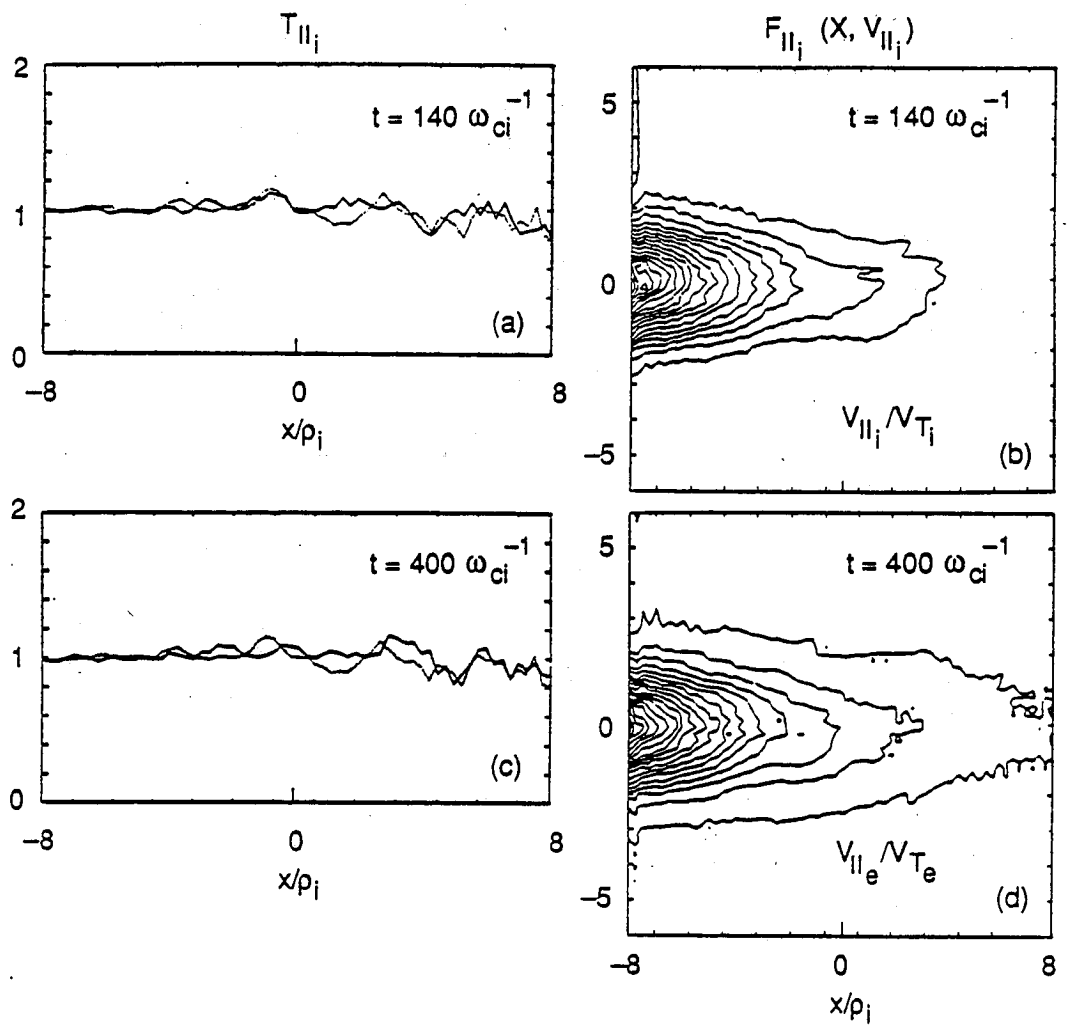

Figure 3.18: Parallel ion temperature profile modification and corresponding velocity distribution contour at $t = 140\omega_{ci}^{-1}$ and $t = 400\omega_{ci}^{-1}$.

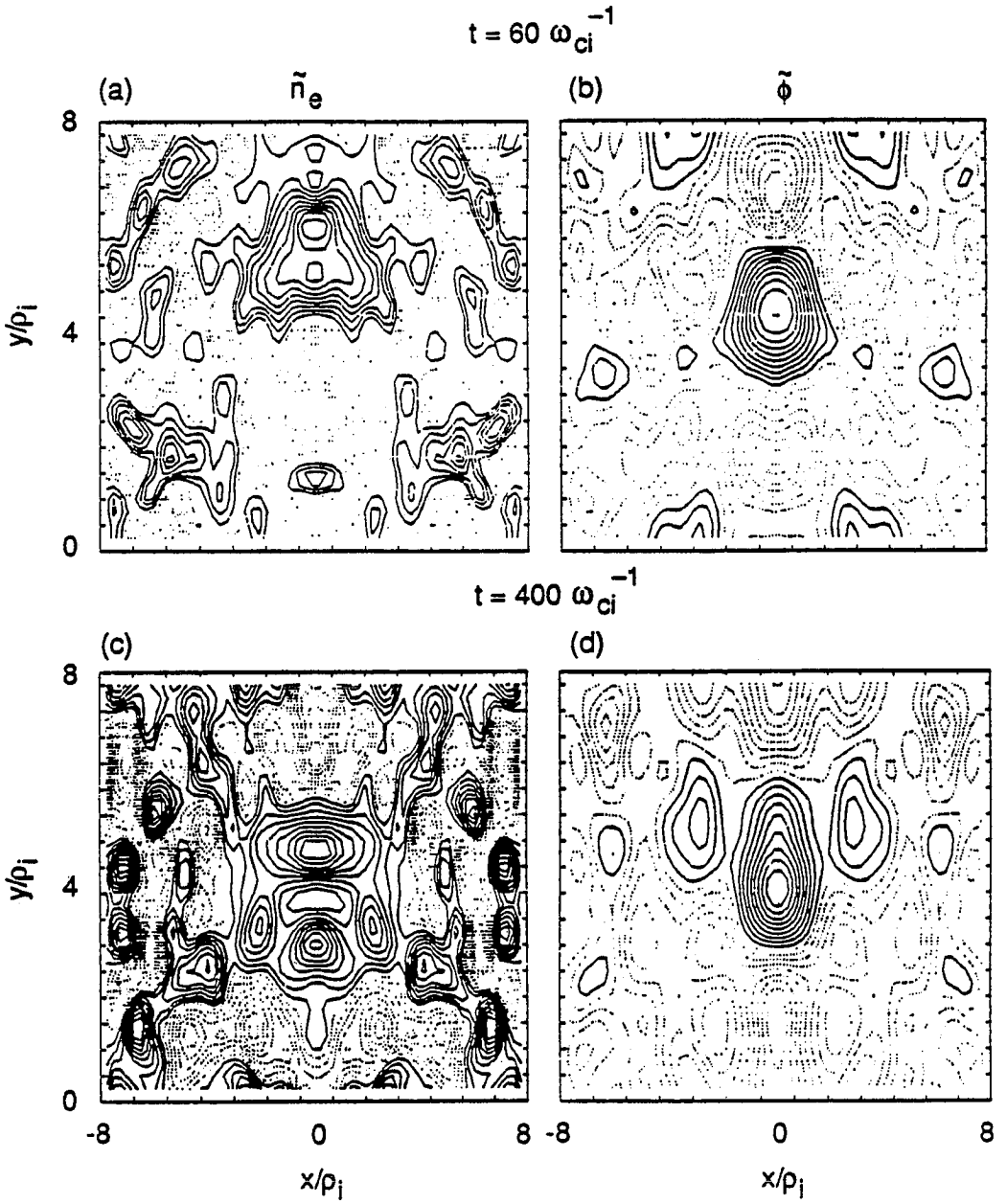

Figure 3.19: Electrostatic potentialϕ contour and elctron density n_e contour at $t = 60\omega_{ci}^{-1}$ with phase difference of $\pi/2$ and $t = 400\omega_{ci}^{-1}$ with phase difference of near zero.

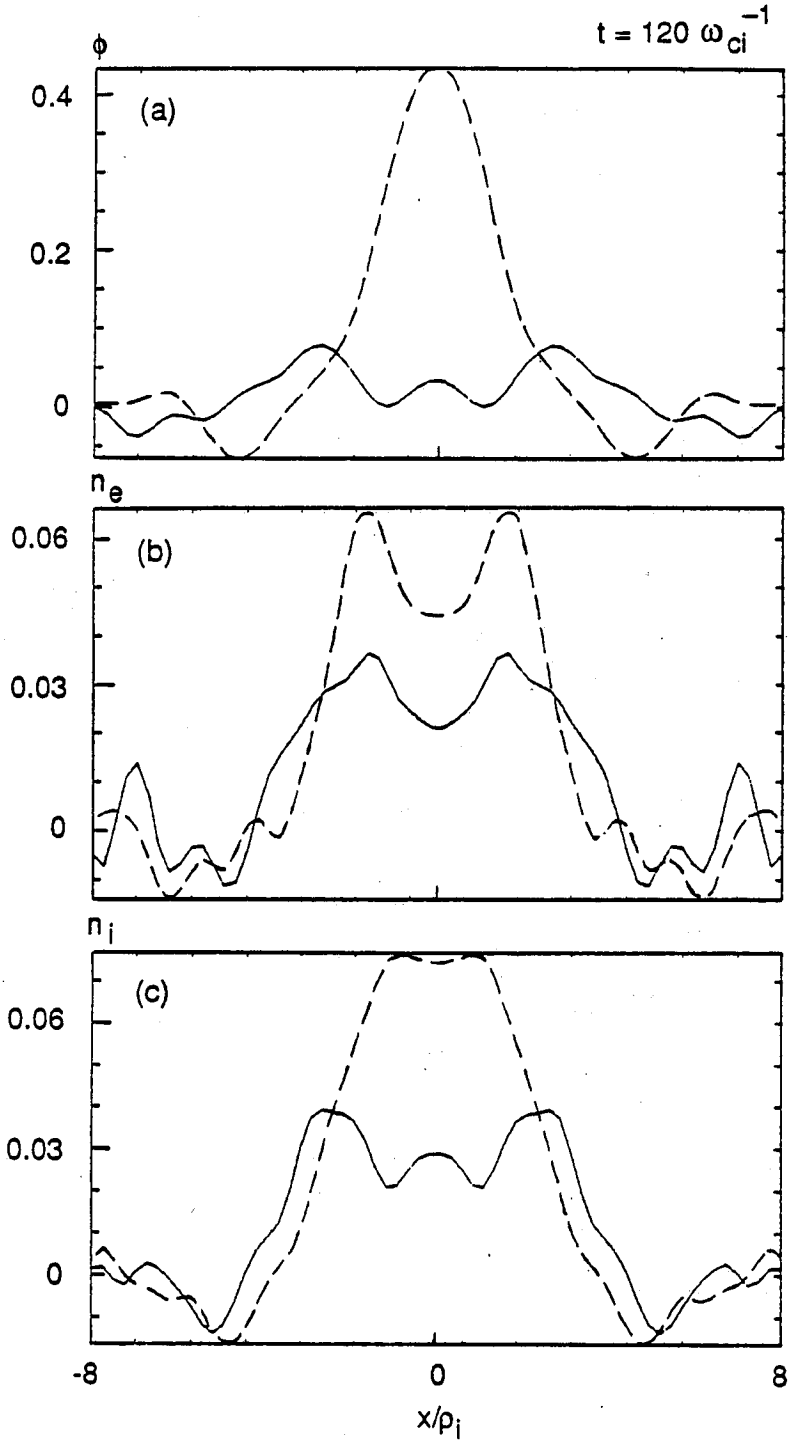

Figure 3.20: Snap shot of the eigenmode ϕ , n_e and n_i at $t = 120\omega_{ci}^{-1}$. Solid line is real part and dotted line is imaginary part.

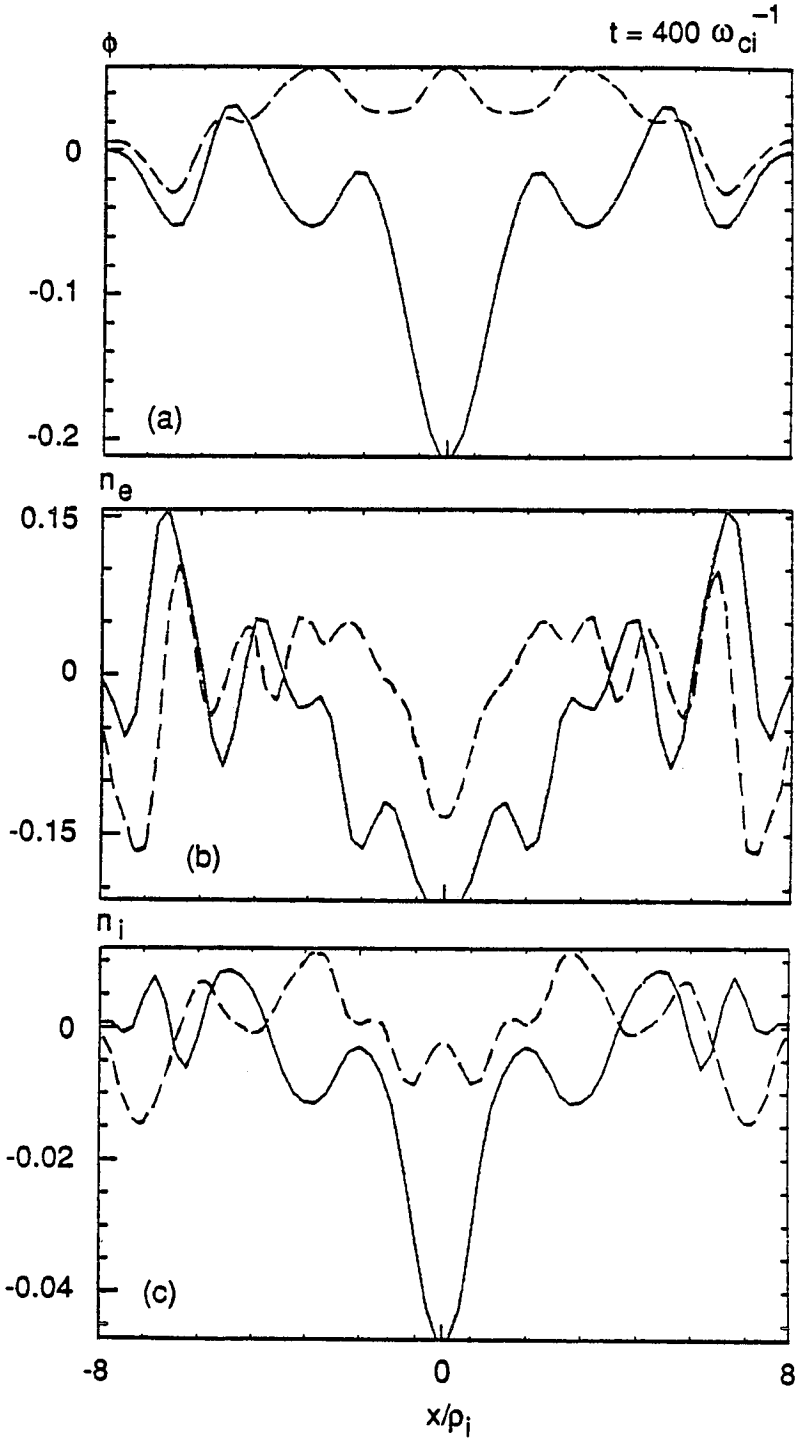

Figure 3.21: Snapshot of the spatial structure ϕ , n_e and n_i at $t = 400\omega_{ci}^{-1}$. The three of them are in phase.

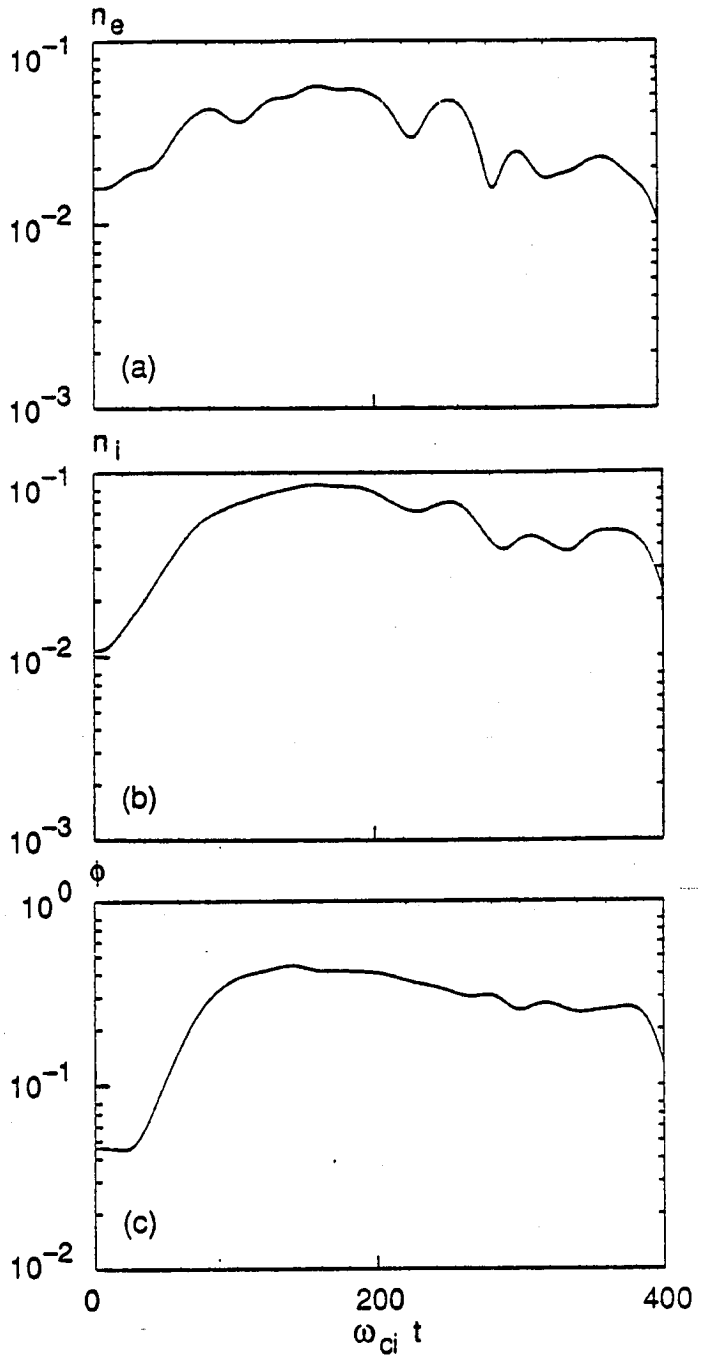

Figure 3.22: ϕ , n_e and n_i time correlation spectrum.

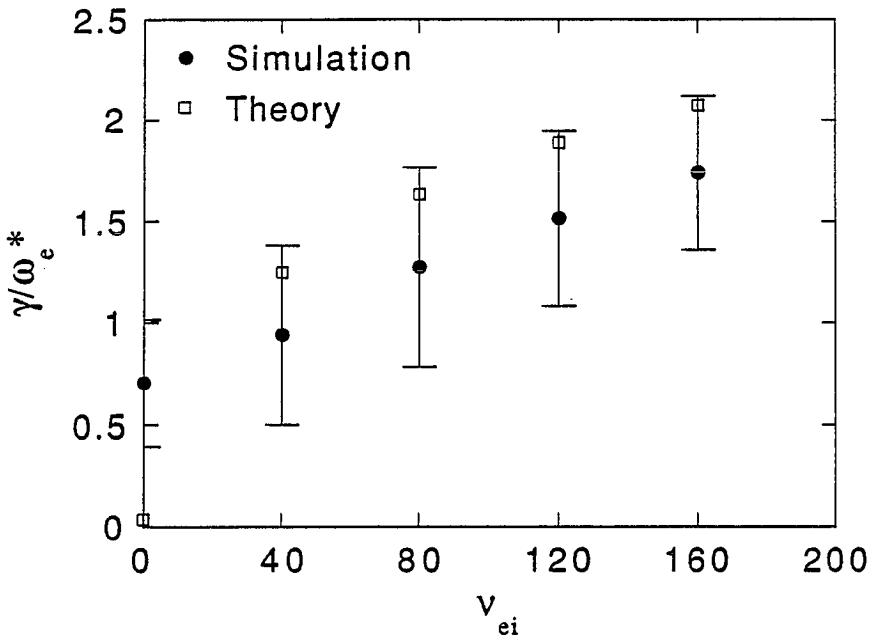

Figure 3.23: Comparison of linear growth rate between simulation and kinetic theory for the $m = 3$ mode, which is the most dominant mode in simulation. Higher wave numbers above $m = 3$ are affected by finite size particle effects and are less dominant.

modes. The collision frequency ν_{ei} is varied from 0 to $160\omega_e^*$, which puts the growth rate in the $\gamma \sim \nu_{ei}^{1/3}$ scaling range as shown in Fig. 4. We find that there is excellent agreement between simulation and theory, as may be seen in Fig. 3.23 and Fig. 3.24 for linear growth rate and for linear eigenmode width.

Although simulation and linear theory use different collision operators, namely, the Lorentz collision operator and the Krook collision operator, respectively, the degree of agreement is well inside the error bars expected from the (shearless) linear theory results of Ref. 7 over the range of $\nu_{ei}/k_{\|}v_{Te}$ values that were used. As the resistivity increases, quasilinear flattening of the density gradient is observed, commensurate with the broader mode width (Fig.3.25). The global electrostatic energy and its saturation level increase as the instability drive due to resistivity is increased as shown by Fig. 3.25. The measured

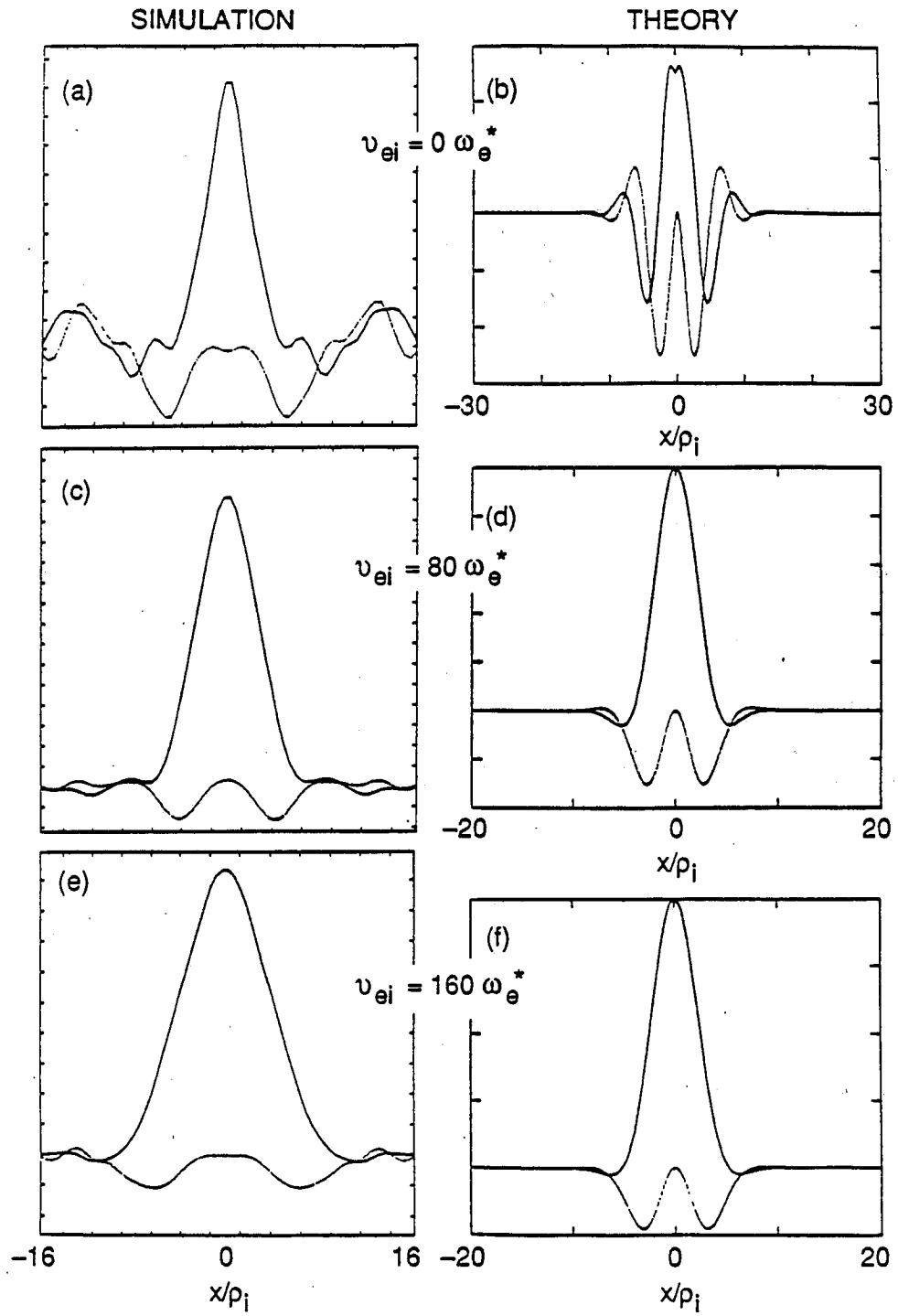

Figure 3.24: Mode structure comparison between simulation and theory. Simulation grids length is 16 ρ_i from the mode rational surface. Theory grid extend up to 30 ρ_i to provide necessary shooting length.

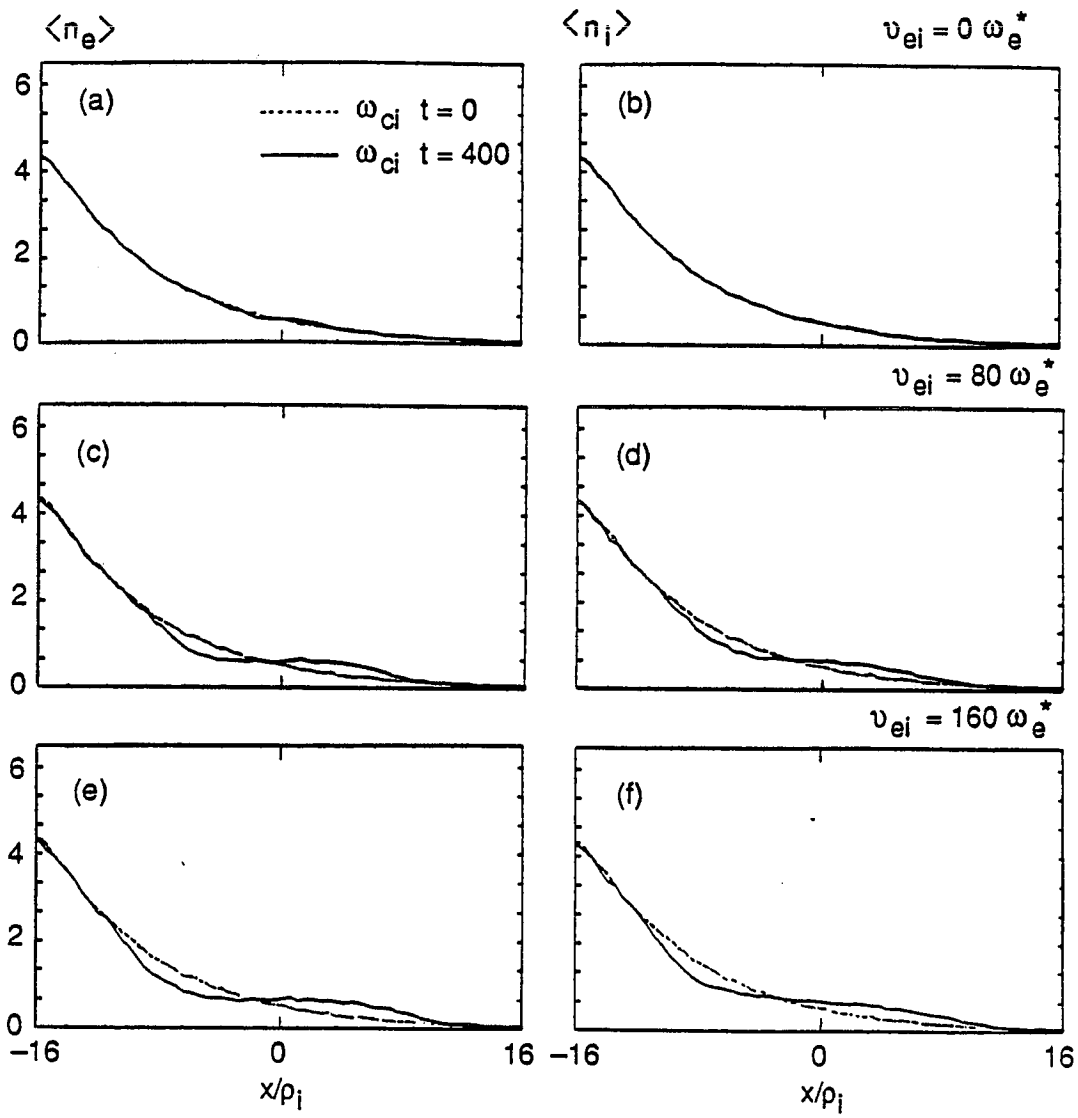

Figure 3.25: Electron and ion density profiles in the saturated state for the cases with $\nu_{ei} = 0$, 80 and $160\omega_e^*$.

ity drive due to resistivity is increased as shown by Fig. 3.25. The measured ϕ saturation level is compared with mixing length theory and shows a similar trend as the value of ν_{ei} is varied (Fig.3.27).

3.4.4 The Spectral Evolution of the Reistive interchange Mode

To understand the dynamical aspect of resistive interchange modes, another simulation is performed with the parameter set of $m_e/m_i = 0.01$, L_n/L_c= 0.286 ($\rho_i/L_c = 4.004 \times 10^{-2}$), $\omega_{ci} = 0.05\omega_{pe}$, ω_e^*=$6.872 \times 10^{-4} m\ \omega_{pe}$, collision frequency ν_{ei}=20 ω_e^* and run time is $(n\Delta t) = 4000 \times 4\omega_{pe}^{-1} = 400\omega_{ci}^{-1}$. The other parameters are the same as the parameters used for the scaling studies. The number of modes launched in the simulation system is 10 m modes. The time evolution of the electrostatic field energy $|E(k)|^2/4\pi n_0 T_e$ and the electrostatic potential energy $|e\phi/T_e|^2$ are shown in Fig. 3.28. Although the electrostatic field energy shows saturation, the potential energy increases at the end of the saturated phase. This phenomenon can be understood in terms of the mode condensation from high m numbers to low m numbers. To study this, snapshots of the perturbed ϕ and E_y wave functions along with n_e and n_i, in the (x, y) plane at particular times are used. For each sampled snapshot, phase relations between ϕ , n_e, and n_i are also measured and observed. In the middle of the initial linear stage, viz. $t = 80\omega_{ci}^{-1}$, a well established linear eigenmode structure is observed (Fig.3.29). At this linear stage, contour plots of ϕ , n_e, n_i and E_y are shown in Fig. 3.30. The quasineutrality condition holds well between n_e and n_i. A phase difference of approximately $\pi/2$ between ϕ and n_e is observed in Fig.3.30. From ϕ contours, we see that the instability occurs for mode $m = 4$. The same mode number is measured in the contour plot of E_y. At $t = 480\omega_{ci}^{-1}$ which is the second saturation stage in the time

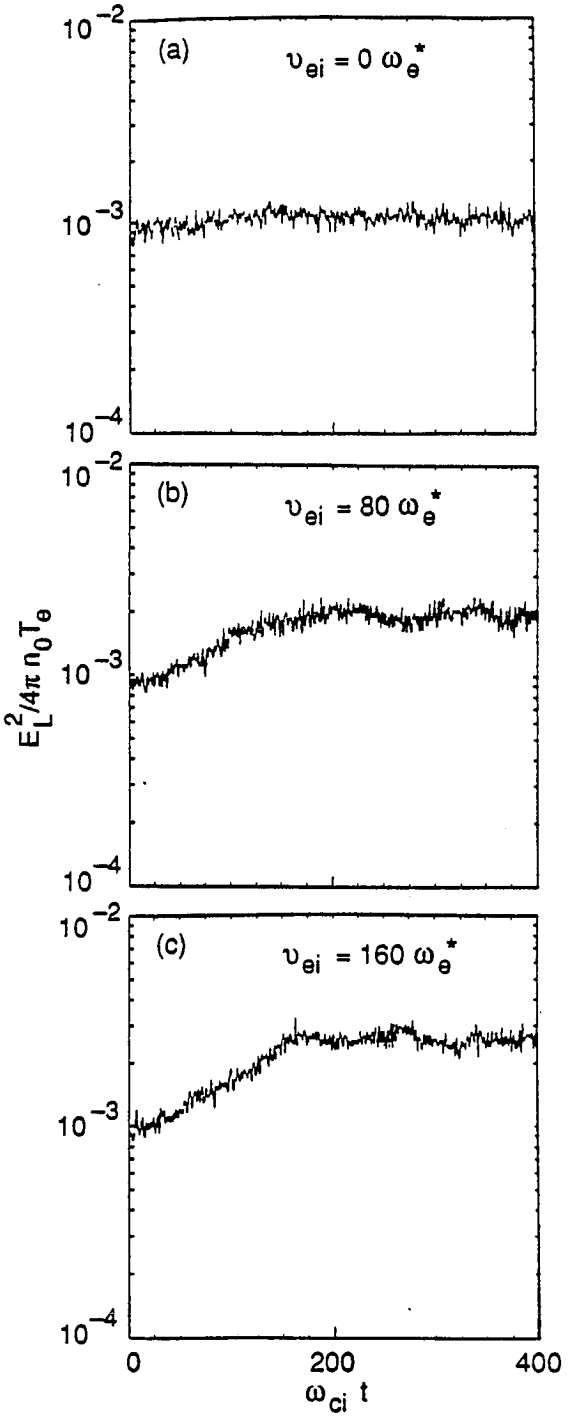

Figure 3.26: Global electrostatic energy, $|E(k)_L|^2 = \sum_k k^2 |\Phi_k|^2$ normalized by electron kinetic energy $4\pi n_0 T_e$ versus time for the same cases as in Fig.3-24.

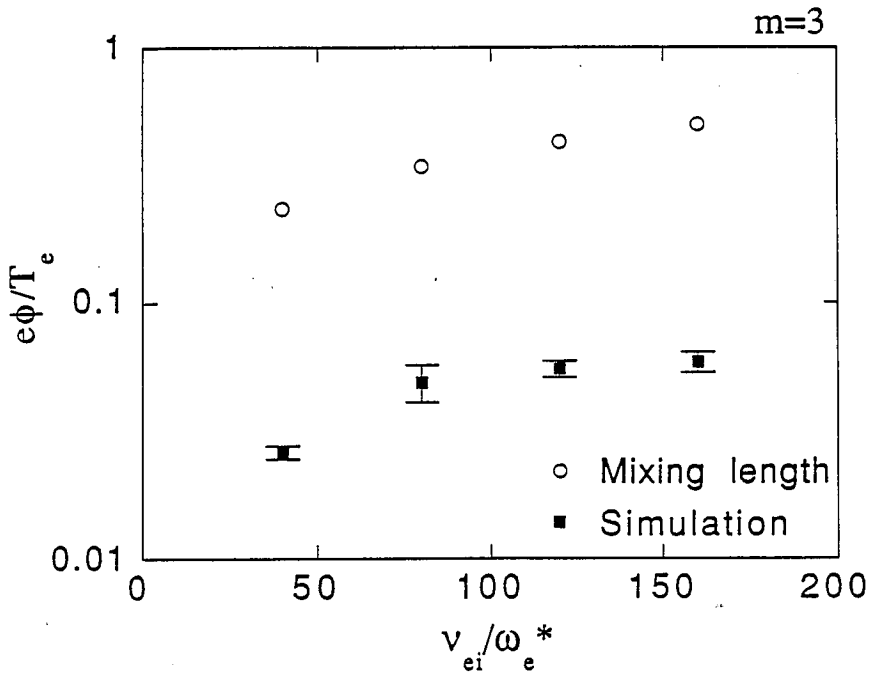

Figure 3.27: ϕ saturation level comparison between simulation and mixing length theory with parameter ν_{ei} variation.

history, the driving mode in ϕ has changed from $m = 4$ to $m = 1$ (Fig. 3.31). At this time n_e, n_i, and ϕ are compeletely in phase. The E_y contour plot shows that the mode with $m = 2$ and $m = 3$ modes are the excited modes. At the final stage, viz. $t = 800\omega_{ci}^{-1}$, the contour plot of ϕ shows that the dominant mode number is $m = 1$ (Fig. 3.32). The contour plot of $E_y = -k_y\phi$ shows that energy is carried to the $m = 5 \sim m = 6$ modes. Meanwhile n_e, n_i, and ϕ are still in phase. The observations made at the three stages in the time evolution of $|\phi|^2$ and $|E_y|^2$ reveal the following facts. The $m = 4$ mode, which has the highest linear growth rate, acts as a driver in the linear stage of the field energy evolution. However, the lowest m mode , even though it has a smaller linear growth rate than that of the higher m modes, continues to grow at a high rate due to its larger mode width. At the final stage of the evolution, a significant amount of energy is carried out to the high m modes. Therefore, the energy

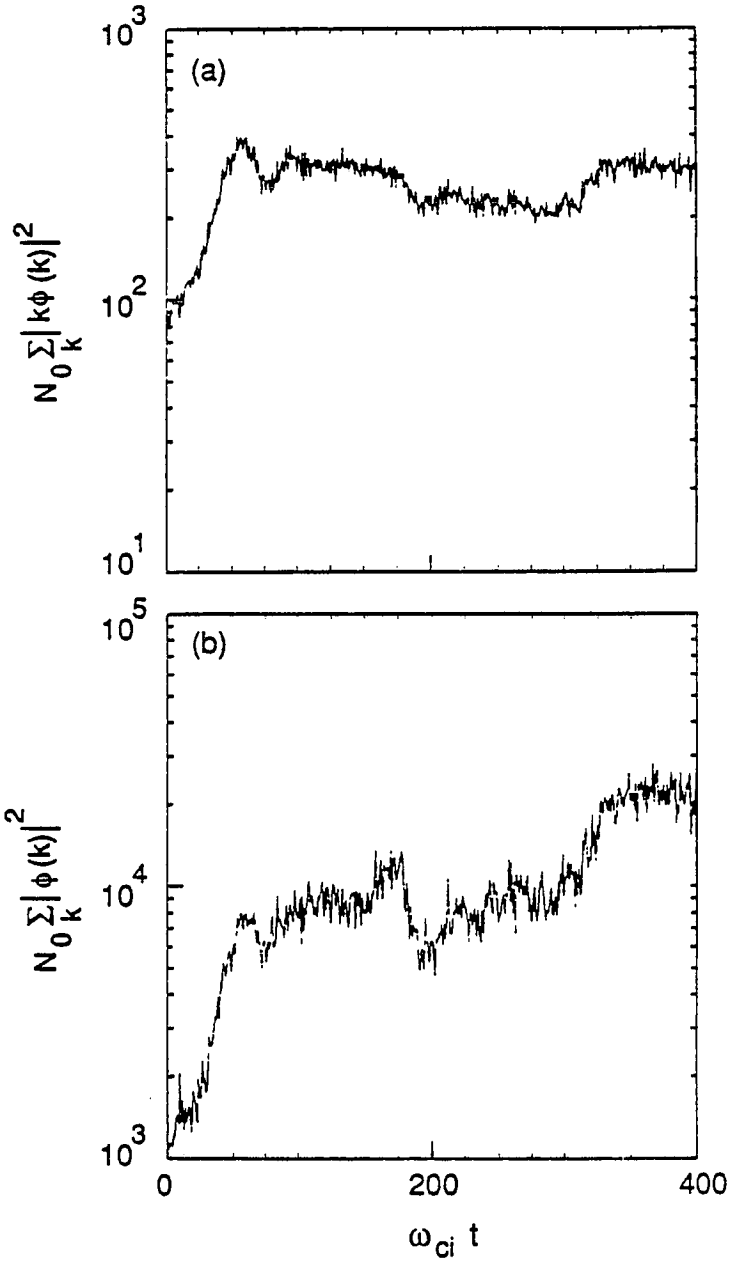

Figure 3.28: Time evolution of electrostatic field and potential energy. N_o is total number of particles in the simulation system.

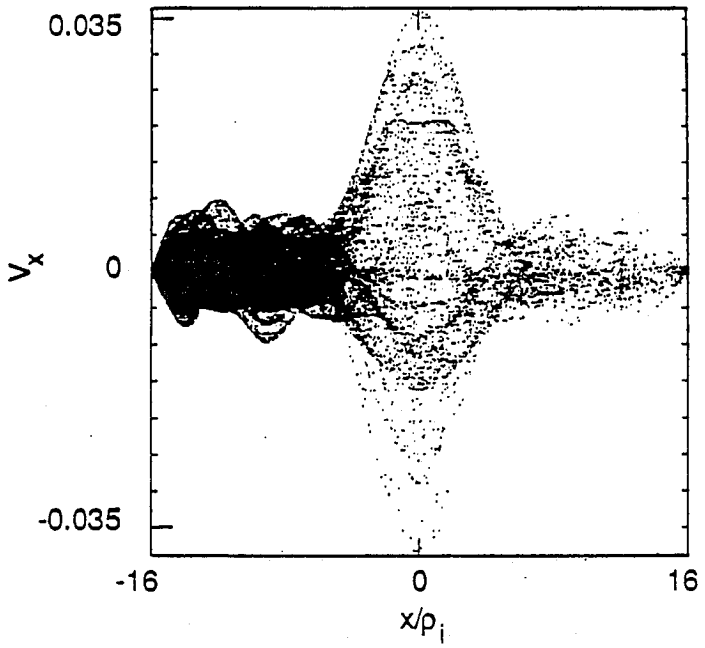

Figure 3.29: Snapshot of eigenmode observed at $t = 80\omega_{ci}^{-1}$ in the simulation.

input to the system through the low m modes is balanced by the dissipation of high m modes through the nonlinear energy transfer mechanism, which excites high m modes at the final stage of the saturation. The energy input, which is driven by the m mode of the highest growth rate at the initial linearly growing stage, is driven by the low m mode at the nonlinear saturation stage. Thus low m mode condensation occurs at the final saturation stage of the resistive interchange mode.

For the three stages mentioned before, we also observe the time evolution of the quasilinear density profile modification and the parallel temperature profile modification. At the middle of the linear stage, when $t = 80\omega_{ci}^{-1}$, electron density profile modification has already begun, whereas the ion density profile is only slightly modified (Fig. 3.33). Also there are no noticeable temperature profile modifications for electrons and ions (Figs.3 .34,35). At $t = 240\omega_{ci}^{-1}$,

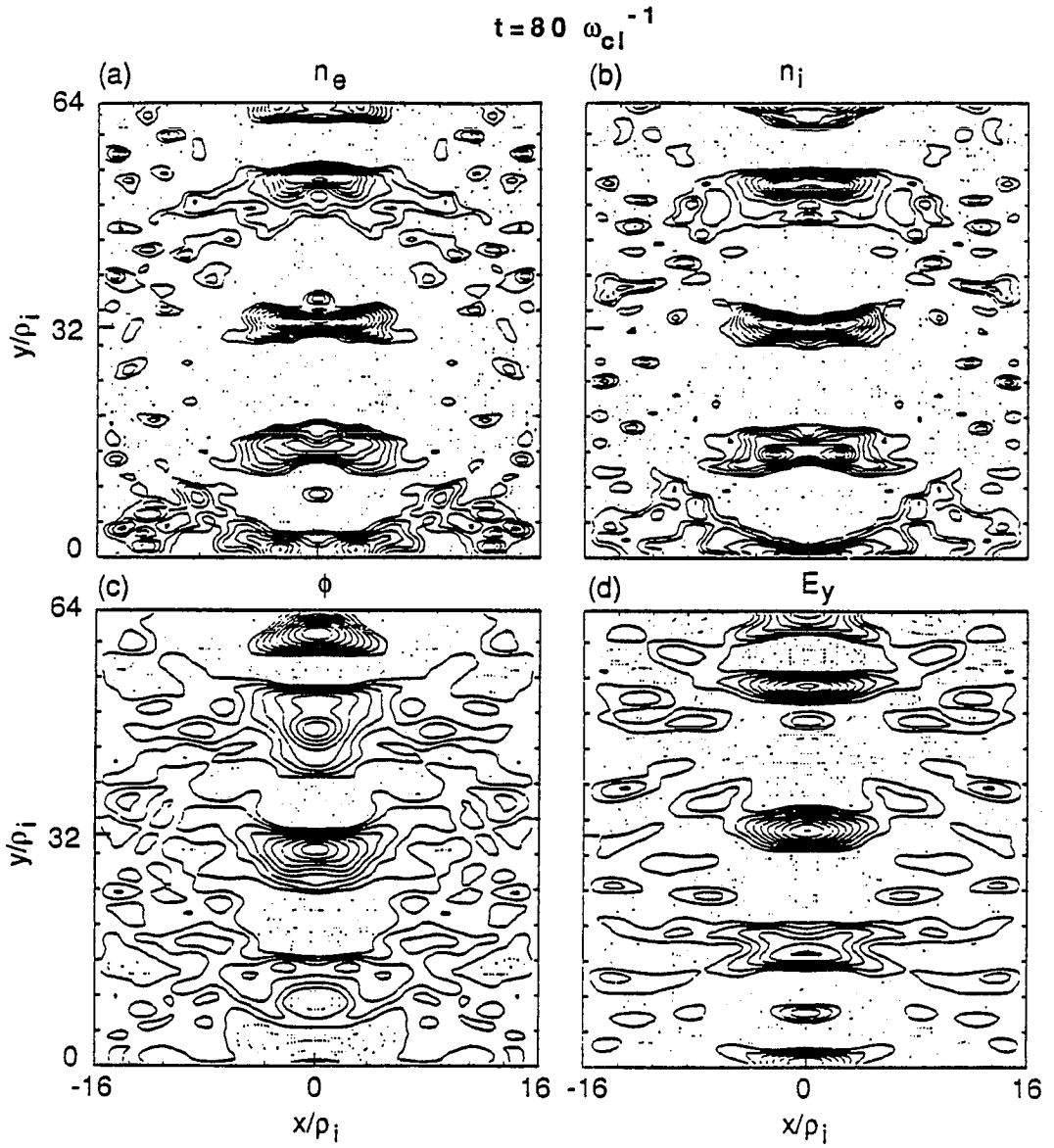

Figure 3.30: Snapshot of ϕ , n_e, n_i and E_y observed at $t = 80\omega_{ci}^{-1}$ in the simulation.

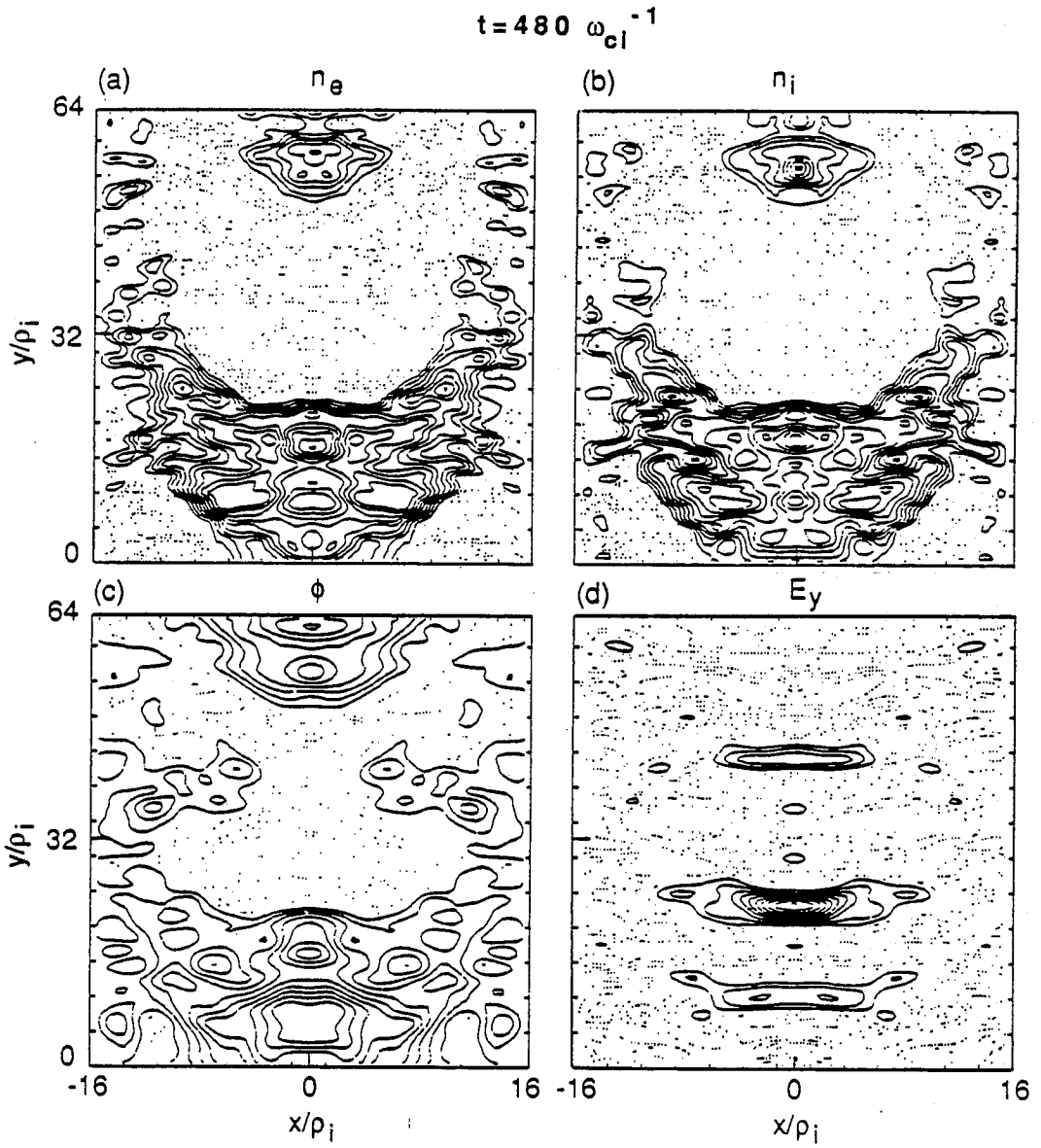

Figure 3.31: Snapshot of ϕ , n_e, n_i and E_y observed at $t = 480\omega_{ci}^{-1}$ in the simulation.

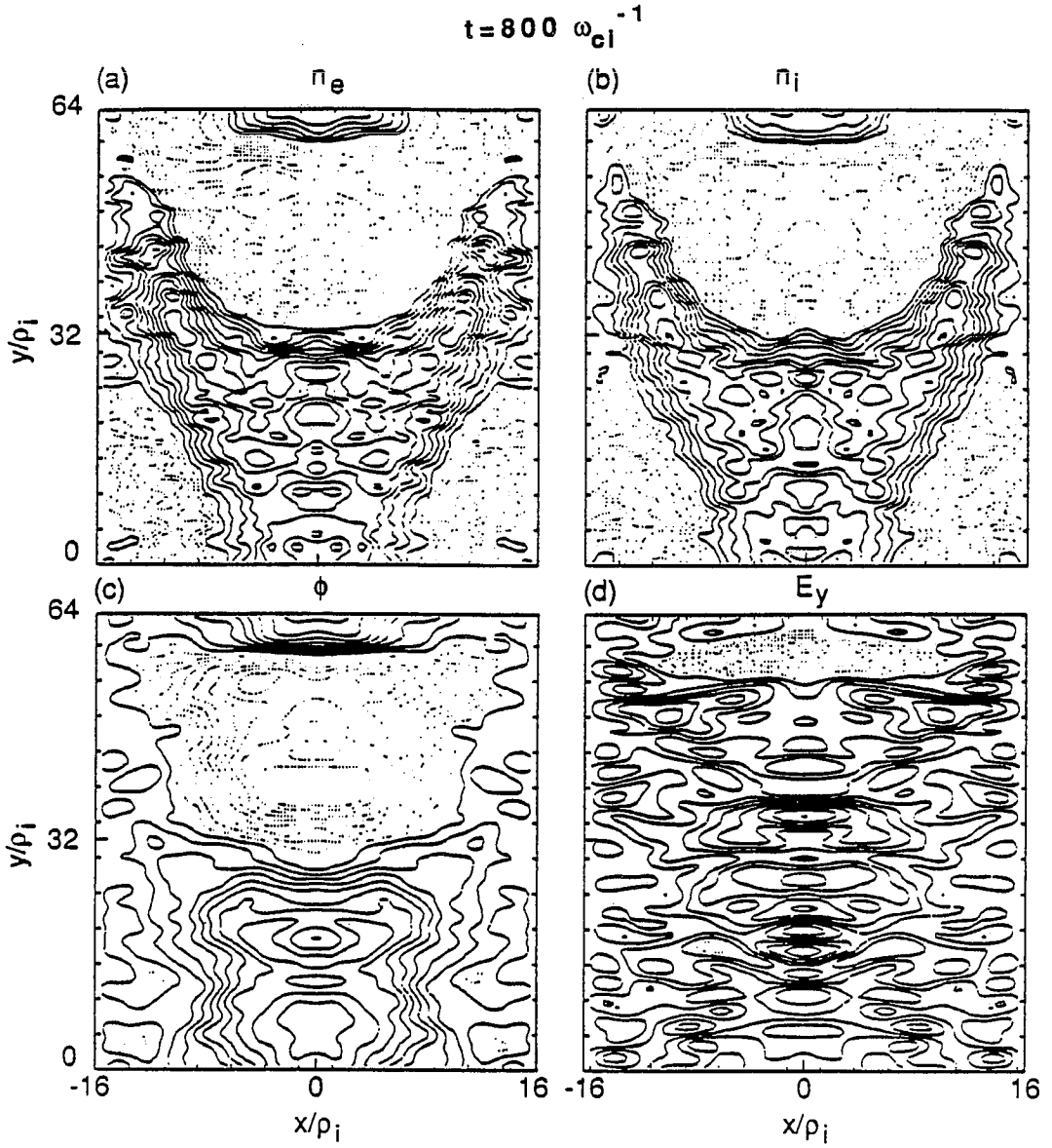

Figure 3.32: Snapshot of ϕ , n_e, n_i and E_y observed at $t = 800\omega_{ci}^{-1}$ in the simulation.

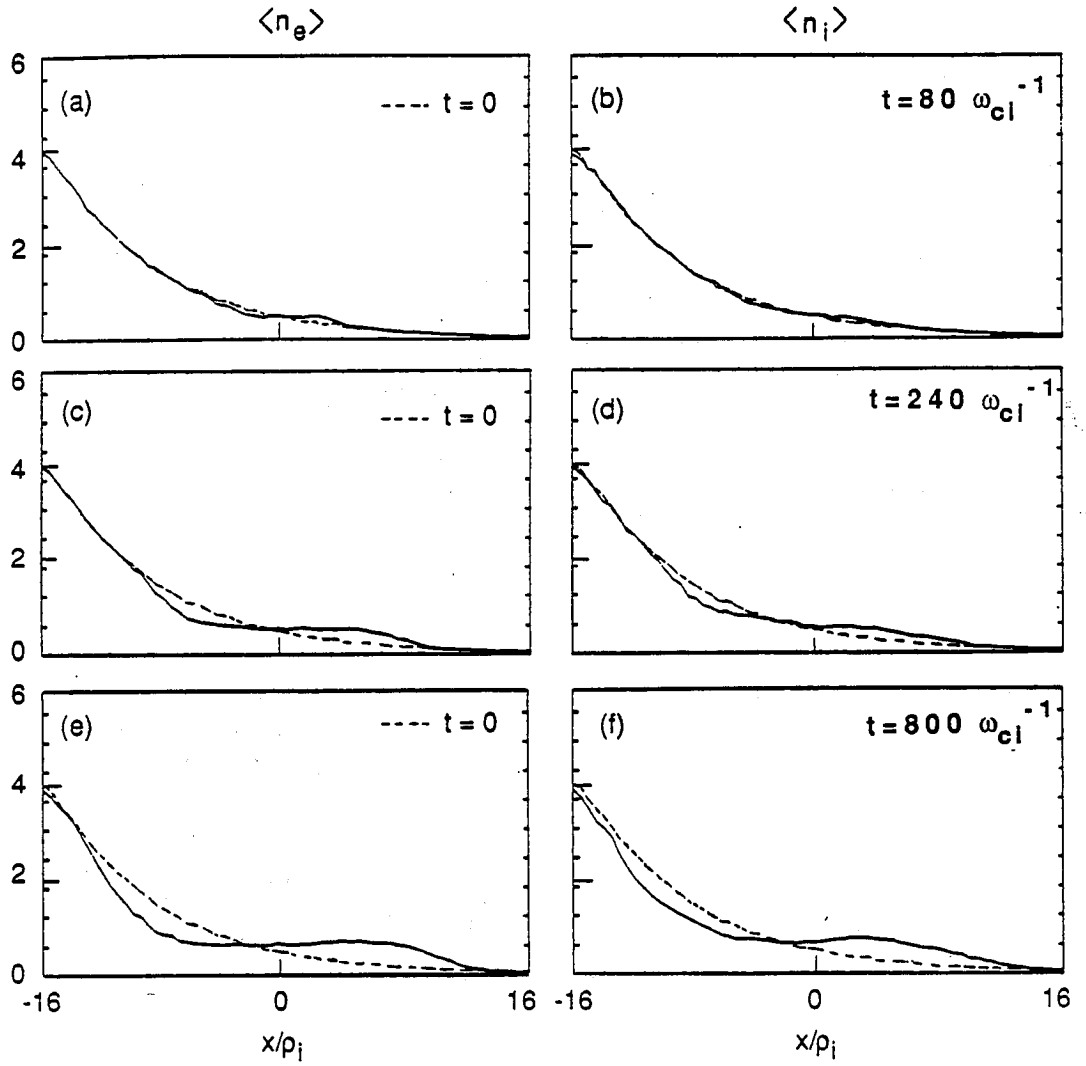

Figure 3.33: Electron and ion density profile evolution at $t = 80, 240, 800\omega_{ci}^{-1}$

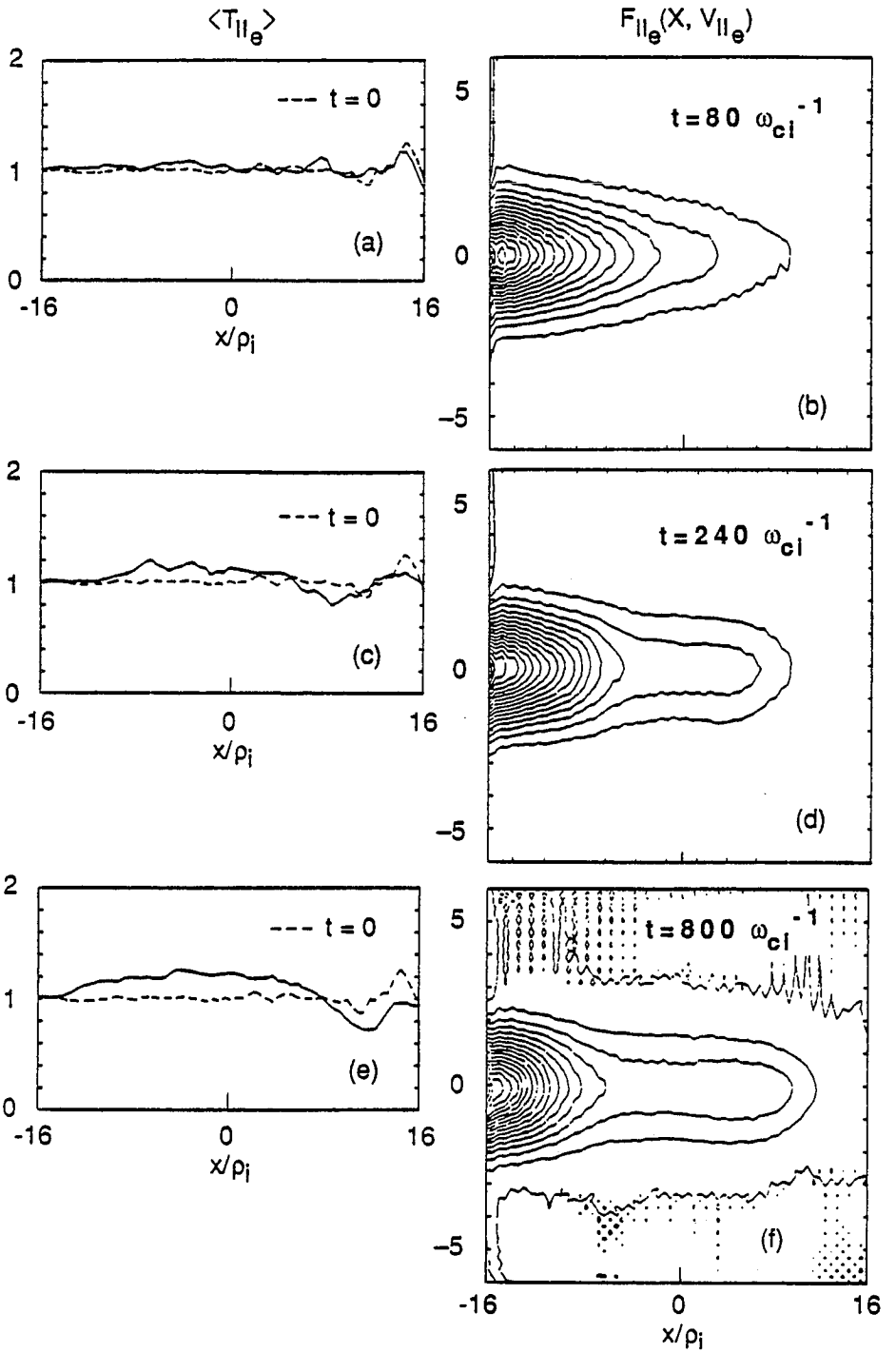

Figure 3.34: Parallel electron temperature profile evolution at $t = 80,\ 240,\ 800\omega_{ci}^{-1}$

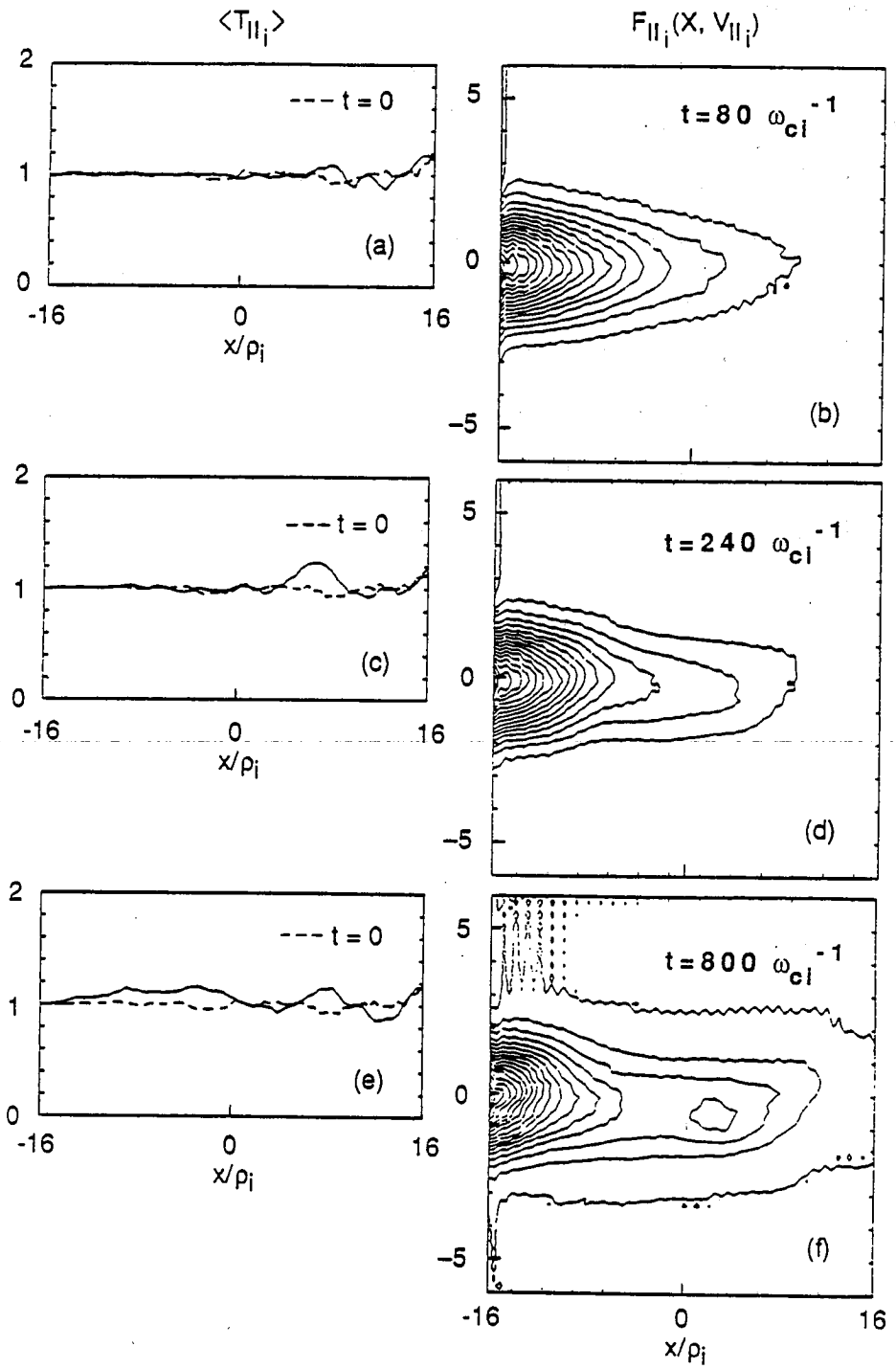

Figure 3.35: Parallel ion temperature profile evolution at $t = 80, 240, 800\omega_{ci}^{-1}$

which is in the middle of the second saturation stage, quasilinear plateau formation in the electron density profile around the mode rational surface is clearly observed. Also, a comparable amount of ion density profile modification is observed. Parallel electron and ion temperature profile modification is noticeable. At the final stage of saturation, $t = 800\omega_{ci}^{-1}$, severe density and temperature profile modifications are observed. The amount of density profile flattening is comparable to the broadened mode width. Around the mode rational surface, electron heating is observed, and on the low density side of the density profile, temperature cooling is also observed. A comparable amount of parallel ion temperature profile modification has occured.

Chapter 4

Particle Simulation of Electromagnetic Interchange Modes

4.1 Introduction

When the thermal energy of the plasma is significant compared to the magnetic field energy, i.e., $\beta \leq m_e/m_i$, the perpendicular magnetic fluctuation $B_\perp$ due to the oscillating parallel current $J_{||}$, which is induced by the small inductive electric field along the magnetic field, is no longer negligible. This perpendicular magnetic fluctuation, $B_\perp$(or $A_{||}$), is coupled with the electrostatic potential ϕ through the parameter β_i , which is the square of the ratio of ion thermal velocity to Alfvén velocity, $\beta_i = v_i^2/v_A^2$. In terms of β_i , the total β is defined as $\beta = (1+\tau)\ \beta_i$,where $\tau = T_e/T_i$ is the temperature ratio.

To describe this perpendicular magnetic fluctuation $B_\perp$, the parallel component of Ampére's law should be included in the dynamics, in addition to the quasi-neutrality condition which is used to describe low frequency electrostatic perturbations. With these finite β considerations[51,52], a set of two coupled 1−D radial eigenmode equations for ϕ and $A_{||}$ are derived for the electromagnetic interchange mode in sheared slab geometry. These coupled eigenmode equations, derived in Section 4-1 and normalized by ρ_i for the spatial scale and by ω_e^* for the inverse time scales, are solved by a 4th-order shooting code scheme.

Before tackling the electromagnetic interchange mode, we apply this

eigenmode scheme to the collisionless electromagnetic drift waves which are coupled to shear Alfvén waves, in order to see the transition from drift waves to interchange modes in finite beta plasmas. This transition for finite beta cases is compared with the result in the electrostatic limit. By following numerical procedures similar to those of Tsang *et.al.*[26,53], both the stable finite beta drift wave branch and the stable shear Alfvén wave branch are recovered separately.

4.2 Derivation of Linear Eigenmode Equations

The linear kinetic eigenmode equations for the collisionless and collisional electromagnetic interchange modes in sheared slab geometry are derived in a manner similar to the case of the electrostatic interchange mode. For low beta plasmas with $m_e/m_i \leq \beta \ll 1$ in a sheared slab with equilibrium magnetic field $\mathbf{B_0} = B_0(\hat{\mathbf{z}} + x/L_s\hat{\mathbf{y}})$, we have both a perturbed electrostatic potential ϕ and a perturbed electromagnetic potential $A_{||}$. In this regime compressional magnetic field fluctuations $B_{||}$(or $A_{\perp}$) are neglected. Low frequency, long wave length kinetic modes, which have finite $\rho_i \ll L_0$, where L_0 is the shortest equilibrium system length in the regime of $\omega \ll \omega_{ci}$ and $k_{||} \ll k_{\perp}$, can be described by the drift kinetic equation for the electron response with $\rho_e = 0$ and by the ion gyro-kinetic equation for the ion response with finite ρ_i . The linearized drift-kinetic equation for the electron response to finite beta interchange modes, with the electron perturbed distribution function f_e separated into an adiabatic piece and a non-adiabatic piece g_e,

$$f_e = \frac{|e|\phi}{T_e} F_e^M + g_e$$

where F_e^M is an electron Maxwellian distribution function

$$F_{me} = \frac{n_0(x)}{(2\pi v_T^2)^{3/2}} \exp(-\frac{v^2}{2v_T^2}) \quad , \quad T = m v_T^2,$$

can be written as

$$(\omega - \omega_{de} - k_{\|} v_{\|e}) g_e - iC(g_e)$$

$$= -\frac{|e|}{T_e} F_e^M (\omega - \omega_e^*)(\phi - \frac{v_{\|e}}{c} A_{\|}). \tag{4.1}$$

Here $\omega_{de} = k_\perp v_{de}$, with v_{de} is the drift velocity due to the magnetic field curvature, and $C(g_e)$ is a number conserving Krook collision operator[39,40]

$$C(g_e) = -\nu_{ei} \left[g_e - \frac{F_e^M}{n_{ce}} \int d^3 v g_e \right]$$

with electron-ion collision frequency ν_{ei}. With the following abbreviation for the non-adiabatic electron response integrated over velocity space,

$$\langle g_e \rangle = \int d^3 v g_e$$

Eq. (4.1) can be written as

$$\left(\omega - \omega_{de} - k_{\|} v_{\|e} + i\nu_{ei}\right) g_e - i\nu_{ei} \frac{F_{me}}{n_{e0}} \langle g_e \rangle$$

$$= -\frac{|e|}{T_e} (\omega - \omega_e^*) \left(\phi - \frac{v_{\|e}}{c} A_{\|} \right) F_e^M \tag{4.2}$$

When Eq.(4-2) is integrated over velocity, $\langle g_e \rangle$ becomes

$$\langle g_e \rangle = -\frac{|e|}{T_e} (\omega - \omega_e^*) \left[\int \frac{(\phi - \frac{v_{\|e}}{c} A_{\|}) F_{me}}{(\omega - \omega_{de} - k_{\|} v_{\|e} + i\nu_{ei})} d^3 v \right]$$

$$\Big/ \left[1 - i \frac{\nu_{ei}}{n_o e} \int \frac{F_{me}}{(\omega - \omega_{de} - k_{\|} v_{\|e} + i\nu_{ei})} d^3 v \right]. \tag{4.3}$$

By the standard integration procedures, we obtain

$$\langle g_e \rangle = \frac{|e|n_0}{T_e}\left(\frac{\omega-\omega_e^*}{\sqrt{2}k_{||}v_e}\right)\frac{\left[Z(\xi_e)\phi-\sqrt{2}\left(\frac{v_e}{c}\right)(1+\xi_e Z_e)A_{||}\right]}{\left[1+\frac{i\nu_{ei}}{\sqrt{2}k_{||}v_e}Z_e\right]}. \tag{4.4}$$

By taking the zeroth order moment of $\langle g_e \rangle$ in velocity space, we obtain the electron density response for finite beta interchange modes :

$$n_e = \frac{|e|n_0}{T_e}\phi + \frac{|e|n_0}{T_e}\left(\frac{\omega-\omega_e^*}{\sqrt{2}k_{||}v_e}\right)\frac{\left[Z_e\phi-\sqrt{2}\left(\frac{v_e}{c}\right)(1+\xi_e Z_e)A_{||}\right]}{\left[1+\frac{i\nu_{ei}}{\sqrt{2}k_{||}v_e}Z_e\right]}, \tag{4.5}$$

where Z_e is the electron plasma dispersion function with argument

$$\xi_e = \frac{\omega-\omega_{de}+i\nu_{ei}}{\sqrt{2}k_{||}v_e}.$$

The ion response is obtained from the linearized gyrokinetic equation

$$(\omega-\omega_{di}-k_{||}v_{||i})g_i = \frac{|e|}{T_i}F_{m_i}(\omega-\omega_i^*)J_0(k_\perp\rho_i)(\phi-\frac{v_{||i}}{c}A_{||}) \tag{4.6}$$

with the ordering $k_{||}v_{||i} \ll \omega \sim \omega_i^* \sim \omega_{di}$. The ion response f_i is also separated into an adiabatic piece and a non-adiabatic piece with a gyro averaging factor :

$$f_i = -\frac{|e|\phi}{T_i}F_i^M + g_i e^{-iL}$$

where

$$L = \frac{\mathbf{k}_\perp \cdot \hat{b}\times\mathbf{v}_i}{\Omega_i} \quad , \quad \mathbf{k}_\perp = k_y\hat{y} - i\hat{x}\frac{\partial}{\partial x}$$

$$= k_\perp\rho_i\cos\varphi \tag{4.7}$$

and φ is the gyro-angle around the equilibrium magnetic field. With g_i defined in Eq. (4-6) and by means of the Bessel function identity

$$\exp\left[-i\frac{kv_\perp}{\Omega_i}\cos\varphi\right] = \sum_l (-i)^l J_l(b) e^{il\varphi} \quad , \quad b = \frac{k_\perp v_\perp}{\Omega_i} \tag{4.8}$$

we obtain the perturbed ion density n_i by averaging f_i over velocity space :

$$n_i = -\frac{|e|n_0}{T_i}\left[\phi + \frac{(\omega-\omega_i^*)}{\sqrt{2}k_\parallel v_i}\left\{Z_i\Gamma_0\phi - \sqrt{2}\left(\frac{v_i}{c}\right)(1+\xi_i Z_i)\Gamma_0 A_\parallel\right\}\right]. \tag{4.9}$$

Here Z_i is the ion dispersion function with argument given by

$$\xi_i = \left(\frac{\omega-\omega_{di}}{\sqrt{2}k_\parallel v_i}\right)$$

and

$$\Gamma_0(b) = e^{-b} I_0(b) \tag{4.10}$$

$$b = k_\perp^2\rho_i^2 = \left(k_y^2 - \frac{\partial^2}{\partial x^2}\right)\rho_i^2, \tag{4.11}$$

where $I_0(b)$ is the zeroth order modified Bessel function. One should note that in a sheared magnetic field, $\Gamma_0(b)$ should be regarded as an operator. In the limit $k_x\rho_i < 1$, and $k_\parallel v_i/\omega < 1$, we expand $\Gamma_0(b)$ about $b = b_0$ as

$$\begin{aligned}\Gamma_0(b) &= \Gamma_0(b_0) + \left.\frac{d\Gamma_0}{db}\right|_{b=b_0}(b-b_0) \\ &= \Gamma(b_0) - \left.\frac{d\Gamma_0}{db}\right|_{b=b_0}\rho_i^2\frac{\partial^2}{\partial x^2},\end{aligned} \tag{4.12}$$

where $b_0=(k_y\rho_i)^2$. By invoking quasi-neutrality $n_e \sim n_i$ and inserting Eq.

(4.12) into Eq.(4.9) we obtain

$$
\begin{aligned}
&(1+\tau)\phi + \left(\frac{\tau\omega+\omega_e^*}{\sqrt{2}k_\parallel v_i}\right) Z_i \left(\Gamma_0 - \rho_i^2 \frac{d\Gamma_0}{db}\frac{\partial^2}{\partial x^2}\right)\phi \\
&\quad - \left(\frac{\tau\omega+\omega_e^*}{k_\parallel c}\right)(1+\xi_i Z_i)\left(\Gamma_0 - \rho_i^2 \frac{d\Gamma_0}{db}\frac{\partial^2}{\partial x^2}\right) A_\parallel \\
&\quad + \left(\frac{\omega-\omega_e^*}{\sqrt{2}k_\parallel v_e}\right) \frac{Z_e}{\left(1+\frac{i\nu_{ei}}{\sqrt{2}k_\parallel v_e} Z_e\right)}\phi \\
&\quad - \left(\frac{\omega-\omega_e^*}{k_\parallel c}\right) \frac{(1+\xi_e Z_e)}{\left(1+\frac{i\nu_{ei}}{\sqrt{2}k_\parallel v_e} Z_e\right)} A_\parallel \\
&= 0
\end{aligned}
\tag{4.13}
$$

The other equation for ϕ and $A_\parallel$, which gives us two coupled eigenmode equations, comes from the parallel component of Ampére's Law,

$$
\begin{aligned}
\nabla_\perp^2 A_\parallel &= \frac{4\pi}{c}|e|\left[\int f_e v_\parallel d^3v - \int f_i v_\parallel d^3v\right] \\
&\doteq \frac{4\pi}{c} J_\parallel
\end{aligned}
\tag{4.14}
$$

After the integrals over velocity space in Eq. (4.14) are performed by the standard procedure, we have

$$
\begin{aligned}
\left[\frac{\partial^2}{\partial x^2} - k_y^2\right] A_\parallel \quad = \quad & \frac{1}{\lambda_d e^2}\left\{\left(\frac{\tau\omega+\omega_e^*}{k_\parallel}\right)(1+\xi_i Z_i)\left(\Gamma_0 - \rho_i^2 \frac{d\Gamma_0}{db}\frac{\partial^2}{\partial x^2}\right)\phi \right. \\
& \left. + \left(\frac{\omega-\omega_e^*}{k_\parallel}\right)(1+\xi_e Z_e)\phi \right.
\end{aligned}
$$

$$- \sqrt{2} v_i \xi_i \left(\frac{\tau\omega + \omega_e^*}{k_\| c} \right) (1 + \xi_i Z_i) \left(\Gamma_0 - \rho_i^2 \frac{d\Gamma_0}{db} \frac{\partial^2}{\partial x^2} \right) A_\|$$

$$- \sqrt{2} v_e \xi_e \left(\frac{\omega - \omega_e^*}{k_\| c} \right) (1 + \xi_e Z_e) A_\|$$

$$+ \frac{i\nu_{ei}}{k_\|} \left(\frac{\omega - \omega_e^*}{k_\| c} \right) (1 + \xi_e Z_e) A_\| \Bigg\} \qquad (4.15)$$

Eq. (4-13) and Eq. (4-15) are the two coupled equations for ϕ and $A_\|$.

After normalization of the time scale by ω_e^* and of the space scale by ρ_i and using the normalized quantities

$$\frac{x}{\rho_i} \equiv x \ , \ \frac{\omega}{\omega_e^*} \equiv \omega \ , \ \frac{\nu_{ei}}{\omega_e^*} \equiv \nu_{ei} \ , \ \frac{\omega_{de}}{\omega_e^*} \equiv \omega_{de} = \frac{L_n}{L_c} \ ,$$

$$\frac{\omega_{di}}{\omega_e^*} \equiv \omega_{di} \ = \ -\tau \frac{L_n}{L_c} \ , k_y \rho_i \ \equiv \ k_y, \text{ and } \tau = \frac{T_e}{T_i}, \qquad (4.16)$$

we obtain the following set of normalized equations, to be solved by a fourth order shooting code are :

Quasi-neutrality condition

$$\frac{d^2\Phi}{dx^2} + \frac{1}{D} \Bigg\{ [1 - \Gamma_0 + \Lambda] - \omega_{di} \left(\frac{1 + \tau}{\tau\omega^2 + 1} \right)$$

$$+ \left(\frac{\omega_{de} - \omega_{di}}{\omega - \omega_{de} + \mu} \right) \left(\frac{\omega - 1}{\tau\omega + 1} \right) \xi_e Z_e \Bigg\} \Phi$$

$$= \frac{\Lambda}{D} \left\{ \left(\frac{\omega - \omega_{di}}{x} \right) \left(\frac{L_s}{L_n} \right) \tau \right\} \chi \qquad (4.17)$$

Parallel Ampére's Law

$$\begin{aligned}
\frac{\partial^2\chi}{\partial x^2} &- \left\{k_y^2 + \frac{\sigma\Lambda}{D}\left(\frac{\omega-\omega_{di}}{w}\right)\left(\frac{L_s}{L_n}\right)\tau\right. \\
&+ \sigma\left(\frac{\omega-1}{\tau\omega+1}\right)\left(\frac{1+\xi_e Z_e}{\Gamma_0-\Gamma_1}\right)\left[\left(\frac{\omega-\omega_{di}}{x}\right)\left(\frac{\omega-\omega_{de}+i\nu_{ei}}{\omega-\omega_{de}+\mu}\right)\right. \\
&- \left.\left.\left(\frac{\omega-\omega_{de}}{x}\right)\right]\left(\frac{L_s}{L_n}\right)\tau\right\}\chi \\
&= -\sigma\left\{\frac{(\Lambda+1-\Gamma_0)}{D} + \left(\frac{1-\Gamma_0}{\Gamma_0-\Gamma_1}\right) - \left(\frac{\omega-1}{\tau\omega^2+1}\right)\left(\frac{\mu}{\omega-\omega_{de}+\mu}\right)\xi_e Z_e\right. \\
&+ \left.\frac{(1+\xi_i Z_i)}{D}\left[\left(\frac{\omega-1}{\tau\omega+1}\right)\left(\frac{\omega_{de}-\omega_{di}}{\omega-\omega_{de}+\mu}\right)\xi_e Z_e - \left(\frac{1+\tau}{\tau\omega+1}\right)\omega_{di}\right]\right\}\Phi
\end{aligned} \tag{4.18}$$

The following definitions have been employed

$$\begin{aligned}
\sigma &= \beta_i\left(\frac{\tau\omega+1}{x}\right)\left(\frac{L_s}{L_n}\right)(\Gamma_0-\Gamma_1) \\
D &= (\Gamma_0-\Gamma_1)\xi_i Z_i \\
\mu &= i\nu_{ei}(1+\xi_e Z_e) \\
\Lambda &= \gamma_0(1+\xi_i Z_i) \\
&\quad + \left(\frac{\omega^2-1}{\tau\omega+1}\right)\left[1+\left(\frac{\omega-\omega_{de}}{\omega-\omega_{de}+\mu}\right)\xi_e Z_e\right] \\
\Phi &= \frac{e\phi}{T_e} \\
\chi &= \frac{v_i}{c}A_{\|}
\end{aligned}$$

Equations (4.17) and (4.18) are solved by a fourth order shooting code scheme described briefly as follows. Rewrite Eq. (4.17) and Eq. (4.18) as

$$\frac{d^2\phi}{dx^2} + R(x,\omega)\Phi = S(x,\omega)\chi \tag{4.19}$$

$$\frac{d^2\chi}{dx^2} - P(x,\omega)\chi = -Q(x,\omega)\Phi \tag{4.20}$$

where P, Q, R, and S are the complex potentials. With the definitions of $F_1 = \Phi, F_2 = \Phi', F_3 = \chi$, and $F_4 = \chi'$ Eqs. (4-19) and (4-20) are turned into matrix equations for F_1, F_2, F_3, F_4,

$$\frac{d}{dx}\begin{pmatrix} F_1 \\ F_2 \\ F_3 \\ F_4 \end{pmatrix} = \begin{pmatrix} 0 & 1 & 0 & 0 \\ -R & 0 & S & 0 \\ 0 & 0 & 0 & 1 \\ -Q & 0 & P & 0 \end{pmatrix}\begin{pmatrix} F_1 \\ F_2 \\ F_3 \\ F_4 \end{pmatrix} \tag{4.21}$$

and then solved iteratively.

4.3 Linear Analysis of Collisionless Electromagnetic Interchange Mode

Linear eigenmode analyses are carried out by solving the two coupled eigenmode equations for ϕ and $A_{||}$ that were derived in Section 4.2. As the numerical scheme, a fourth-order shooting method is used to obtain the eigenvalues. To test the numerical scheme and the eigenmode system, a trial analysis for drift-Alfvén waves[53,54] is carried out with the same parameter set as in the work of Tsang *et.al.*[26] Parameters used in this analysis are T_e/T_i =1.0, m_e/m_i =1/1836, L_s/L_n =16, $k_y\rho_i$ = 0.25, accompanied by a variation of β_i . Identical results with respect to eigenvalues and mode structures are recovered by treating the numerical examples of Tsang et. al. The eigenmode structures for finite β drift wavesand shear Alfvén waves are shown in Figs. 4-1 and 4-2

along with the associated potentials. In the next subsection the features of drift-Alfvén waves will be discussed in detail.

4.3.1 Finite β effect on Drift-Alfvén Waves

Finite beta effects have an additional stabilizing influence over drift waves which are already stabilized by the magnetic shear. With inclusion of finite beta effects, drift waves are coupled to shear Alfvén waves and acquire an electromagnetic component. In the presence of magnetic shear, we have an effective potential which is symmetric in the radial direction with respect to the mode rational surface and thus allows its eigenmodes of ϕ and $A_{||}$ to possess parities. We follow even parity ϕ and odd parity $A_{||}$ eigenmodes for finite beta drift wave branches since in the future we are going to look at the transition from drift waves to drift-interchange modes, which are most unstable when they have even parity for ϕ in the electrostatic limit.

Finite beta stabilization of drift waves in sheared magnetic field can be explained by the following arguments. The effective potential induced by magnetic shear localizes the interaction zone of drift waves with resonant particles[55] ($\mathrm{x}_e < \mathrm{x}$), where x_e is the point where drift waves resonate with electrons,

$$\mathrm{x}_e = \frac{L_s|\omega_r|}{k_y v_{Te}}, \tag{4.22}$$

with ω_r the real part of the eigen-frequency. For $\mathrm{x} < \mathrm{x}_e$ there are nonresonant electrons which damp out the drift waves. Finite beta effects allow the existence of shear Alfvén waves with phase velocity v_A, which is comparable to the thermal electron velocity v_{Te} when β_i is greater than m_e/m_i . At the resonant point x_A , defined by

$$\mathrm{x}_A = \frac{L_s|\omega_r|}{k_y v_A} \tag{4.23}$$

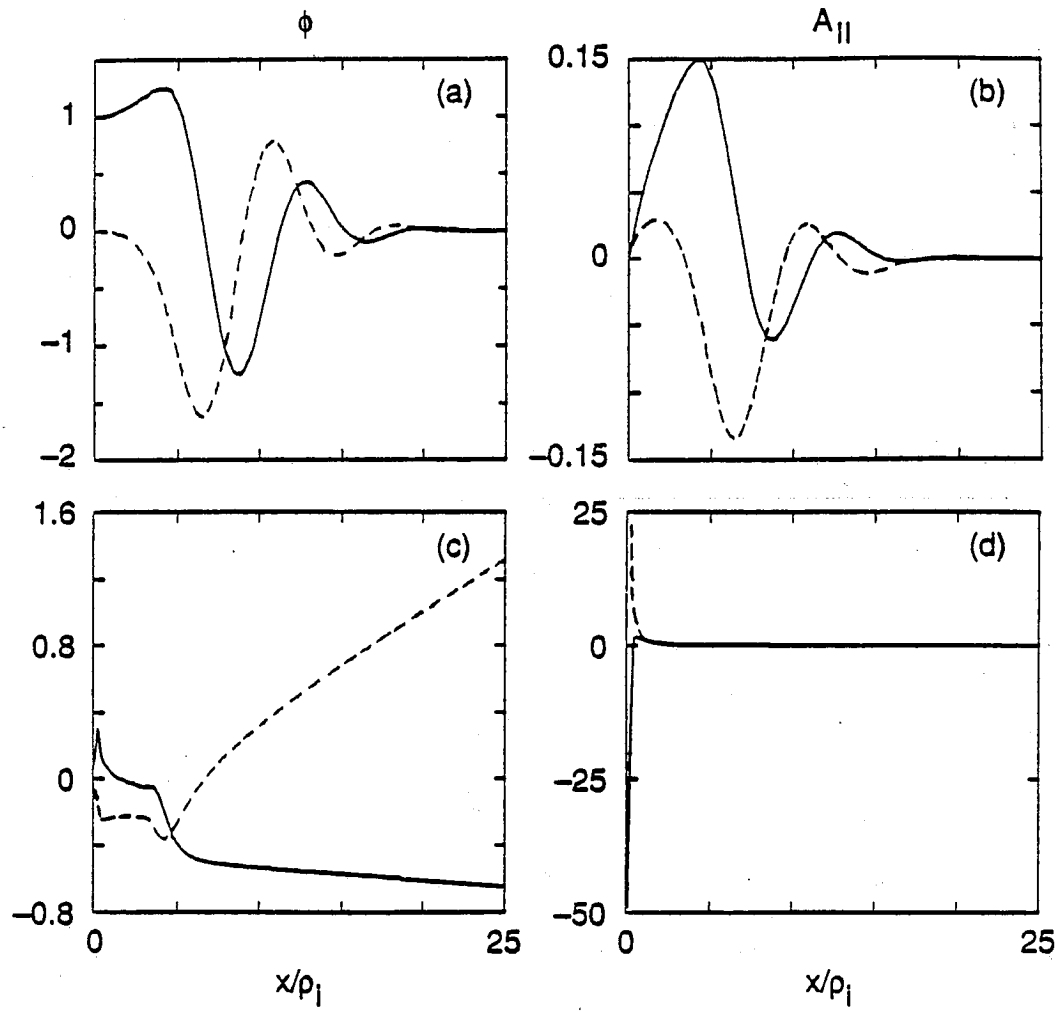

Figure 4.1: Finite beta drift wave mode structures with parity of even ϕ and odd $A_{||}$, which is identical to the result of Tsang et. al and its potentials structures. Parameter used are $k_y\rho_i$=0.25, β_i=0.02, L_s/L_n =16., m_e/m_i =1/1836, T_e/T_i =1.

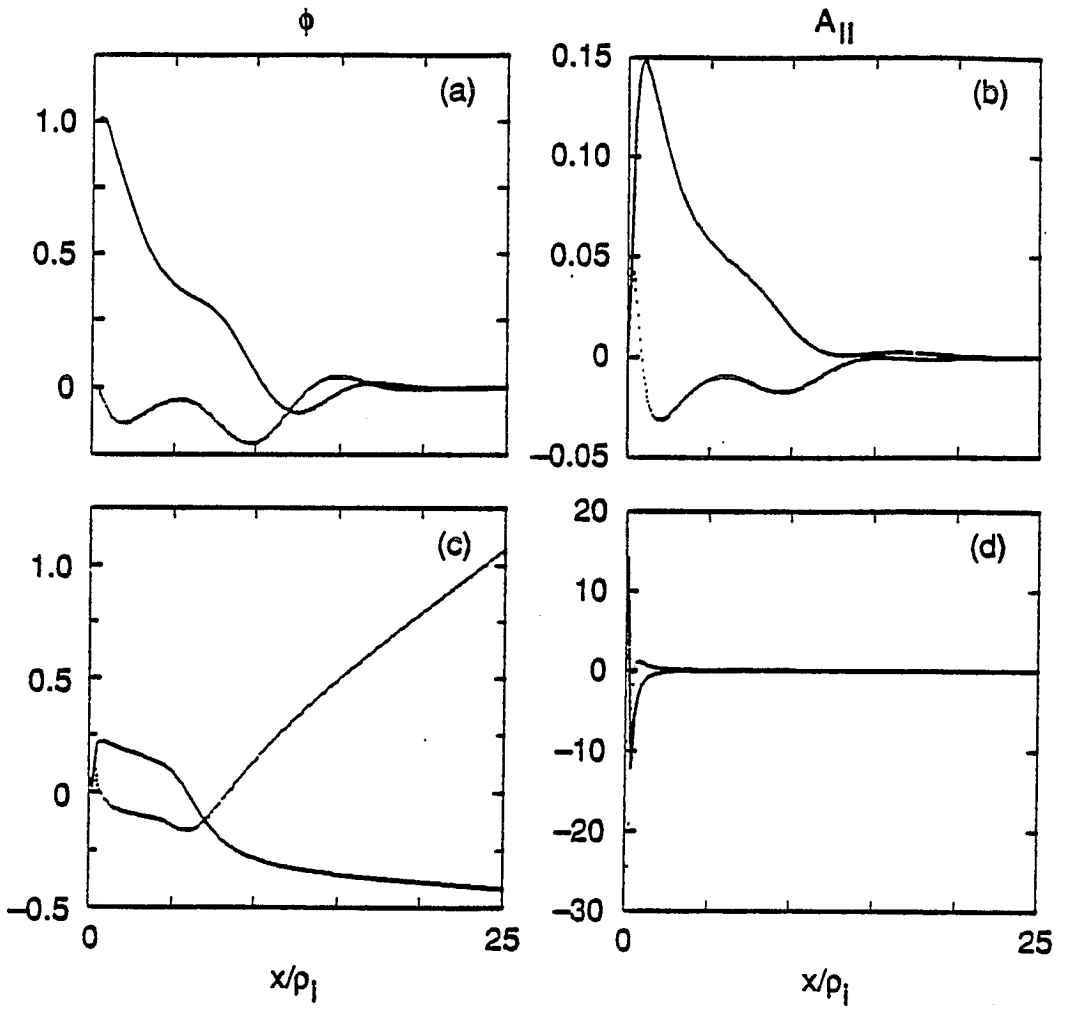

Figure 4.2: Shear Alfvén mode structures with parity of even ϕ and odd $A_{||}$ along with its potentials structures. Same parameters in Fig.4-1 are used

shear Alfvén waves are strongly coupled with drift waves which are interacting with the resonant thermal electrons. In our normalization x_e and x_A can be rewritten as

$$x_e = \left(\frac{L_s}{L_n}\right)\left(\frac{T_e}{T_i}\right)^{1/2}\left(\frac{m_e}{m_i}\right)^{1/2}|\omega_r| \tag{4.24}$$

$$x_A = \left(\frac{L_s}{L_n}\right)\left(\frac{T_e}{T_i}\right)\sqrt{\beta_i}|\omega_r| \tag{4.25}$$

As β_i increases, x_A is moving away from the mode rational surface ($x = 0$) and exceeds x_e so that $x_e < x_A$. Therefore, the interaction region of the drift waves with the resonant electrons is reduced from $x_e < x < x_T$ to $x_A < x < x_T$, where x_T is the radial turning point for drift waves, obtained from the outgoing wave boundary conditions. This picture of the stable influence of finite beta effect on drift waves attributed to the reduction of their interaction range with resonant electrons is shown in Figs. 4.3 and 4.4. While stable drift waves are stabilized further by finite beta effects, stable shear Alfvén waves are less damped as β_i is increased[26,56] (Fig. 4.5). This tendency of shear Alfvén waves to become less damped can be understood using a similar picture as for the drift waves. By tracking the shear Alfvén branch through careful increments of β_i , the corresponding eigenvalues show, via Eq. (4.22), that x_e moves inward for the case of shear Alfvén waves, whereas x_e remains almost constant for the case of drift waves (Fig.4-6). Thus the region where nonresonant electrons damp out the shear Alfvén waves is reduced and the shear Alfvén waves become less damped but yet remain stable in sheared slab geometry. Fig.4-6 also tells us that the shear Alfvén wave is electromagnetic wave in nature, since the shear Alfvén branch does not exist when β_i is below m_e/m_i .

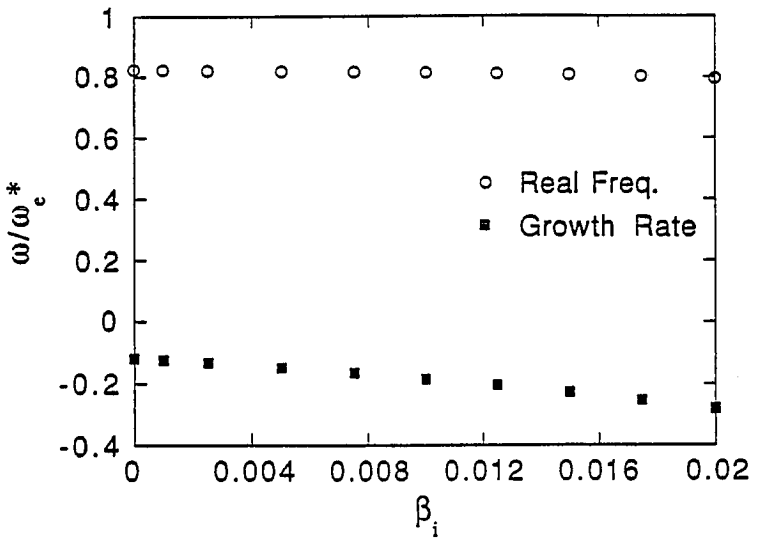

Figure 4.3: Finite β drift wave with parameter set of $k_y\rho_i$=0.25, L_s/L_n =16, m_e/m_i =1/1836, T_e/T_i =1

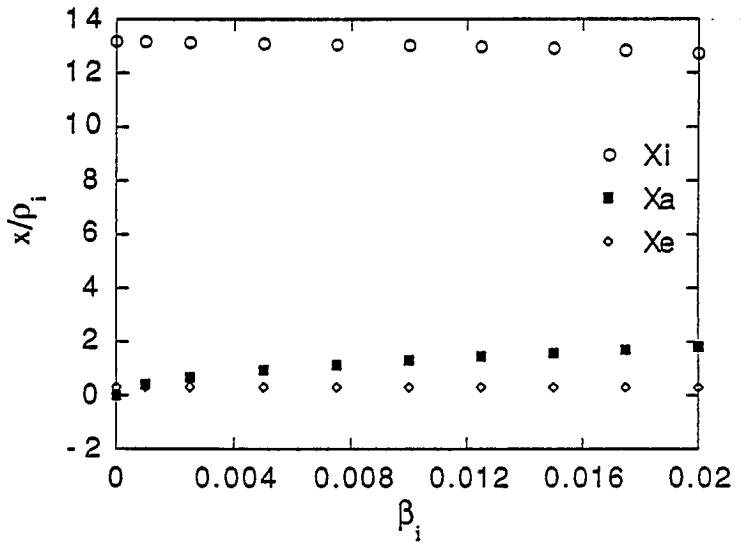

Figure 4.4: x_e, x_A, x_i of finite β drift wave under the variation of β_i

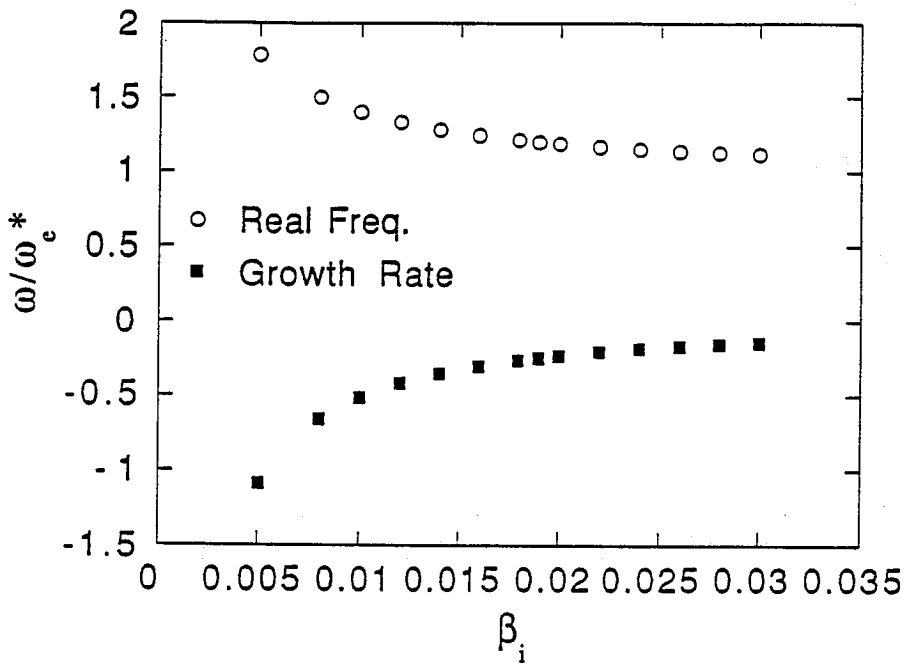

Figure 4.5: Shear Alfvén wave eigenmode spectrum with respect to β_i , parameter used are the same as the finite beta drift waves in Fig.4-3.

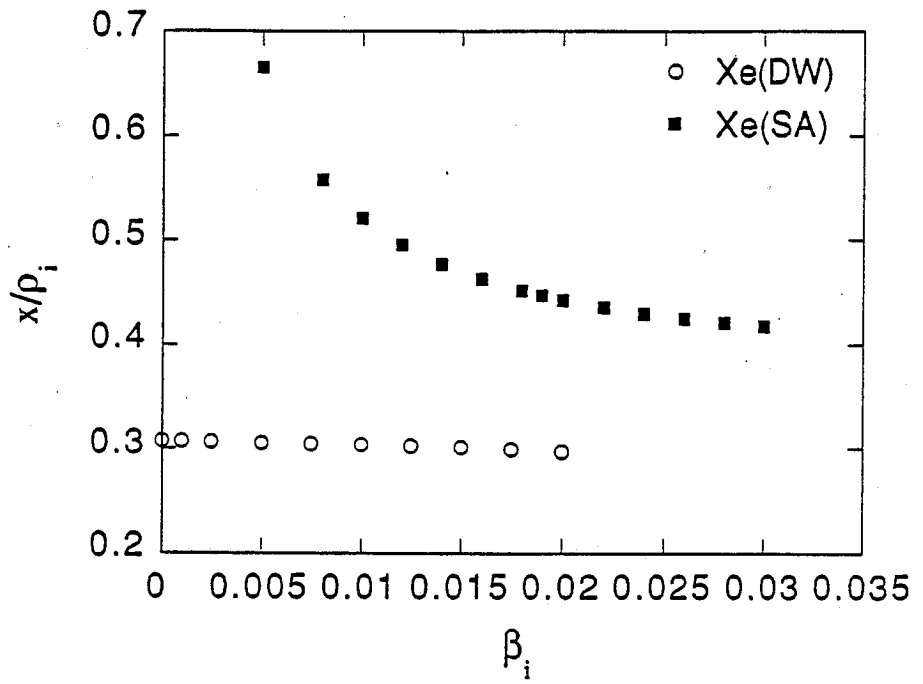

Figure 4.6: x_e of finite beta drift wave and shear Alfvén wave under variation of β_i .

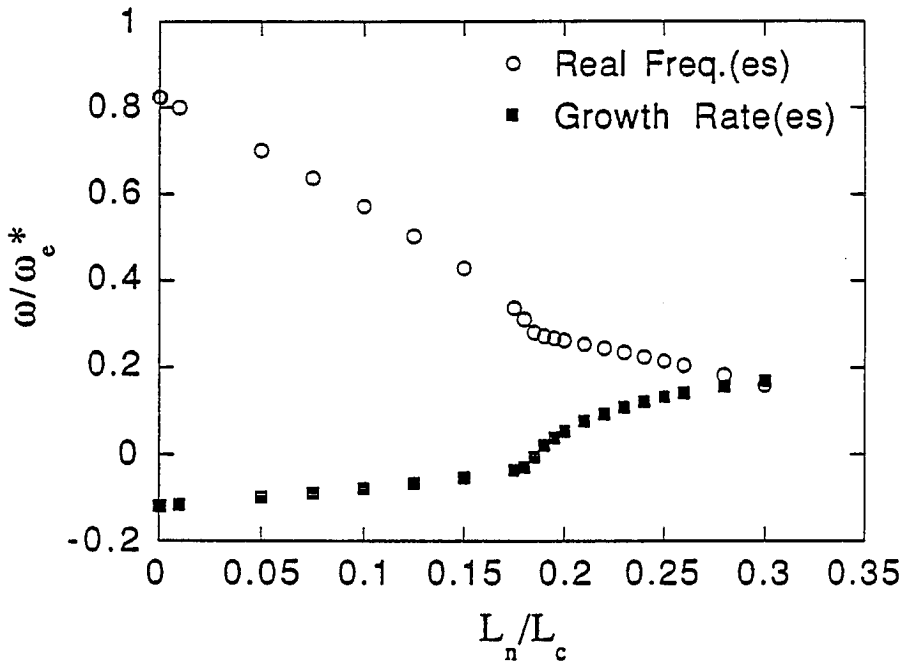

Figure 4.7: Transition of drift wave to drift-interchange mode with the increment of L_n/L_c . Parameter used are the same of the finite beta drift waves except that β_i=0.0.

4.3.2 Transition from Drift waves to Drift Interchange Modes

Linear eigenmode studies for drift-Alfvén waves show that both drift waves and shear Alfvén waves are stable in sheared slab geometry. Therefore, we studied the evolution of drift waves to drift-interchange modes in finite beta plasmas by increasing the curvature drive which is parametrized by $\omega_{de}/\omega_e^*=L_n/L_c$ in our normalization. In addition to this transition, we also investigated the behavior of the shear Alfvén branch with the same set of parameters. In the analysis of the evolution of drift waves to drift-interchange modes, we first tested electrostatic modes (β_i=0.0) with the same parameter set as for finite beta drift waves (Fig.4.7). In this transition, there exists a threshold of $(L_n/L_c)_c$=0.175 which divides stable and unstable modes. Both real and imaginary eigenfrequencies evolved into different branches after pass-

ing the threshold value $(L_n/L_c)_c$. When L_n/L_c is less than $(L_n/L_c)_c$, the mode structure is close to the one for stable drift waves (Fig.4-8). After passing the threshold $(L_n/L_c)_{crit}$ the mode becomes unstable and strongly localized at the mode rational surface.

Finite β effects on this transition are distinctive, as shown in Fig. 4.9. While the electrostatic mode has a smooth transition from a stable drift mode to an unstable interchange mode as the curvature drive L_n/L_c is varied, the electromagnetic mode has an abrupt transition in growth rate. With an increment of L_n/L_c , the finite beta drift mode becomes more stable till L_n/L_c reaches 0.15. After passing this value there is a sudden jump to an unstable mode which becomes more unstable as L_n/L_c increases. In contrast to the imaginary eigenfrequency behavior, the real parts have similar transitions in the electrostatic and electromagnetic cases when L_n/L_c varies. As shown by Fig. 4.9, finite β effects slightly reduce the real frequency under variation of L_n/L_c , yet the tendency of the electrostatic transition is retained. Finite β effects on this transition are effective with β_i values of $0 < \beta_i < m_e/m_i$ (Fig.4.9). In the presence of β_i , the amount of curvature drift L_n/L_c determines whether the mode is of the drift type or of the interchange type. This picture is shown in Fig.4-10 in which modes having L_n/L_c larger than $(L_n/L_c)_c$ become more unstable and modes with L_n/L_c less than $(L_n/L_c)_{crit}$ become less unstable as β_i increases.

4.3.3 Local Analysis of Finite β Drift-Interchange Mode

Finite beta effects on stable drift waves and unstable drift-interchange modes have different outcomes. Drift waves become more stable and drift-interchange modes become unstable when L_n/L_c surpasses the threshold value

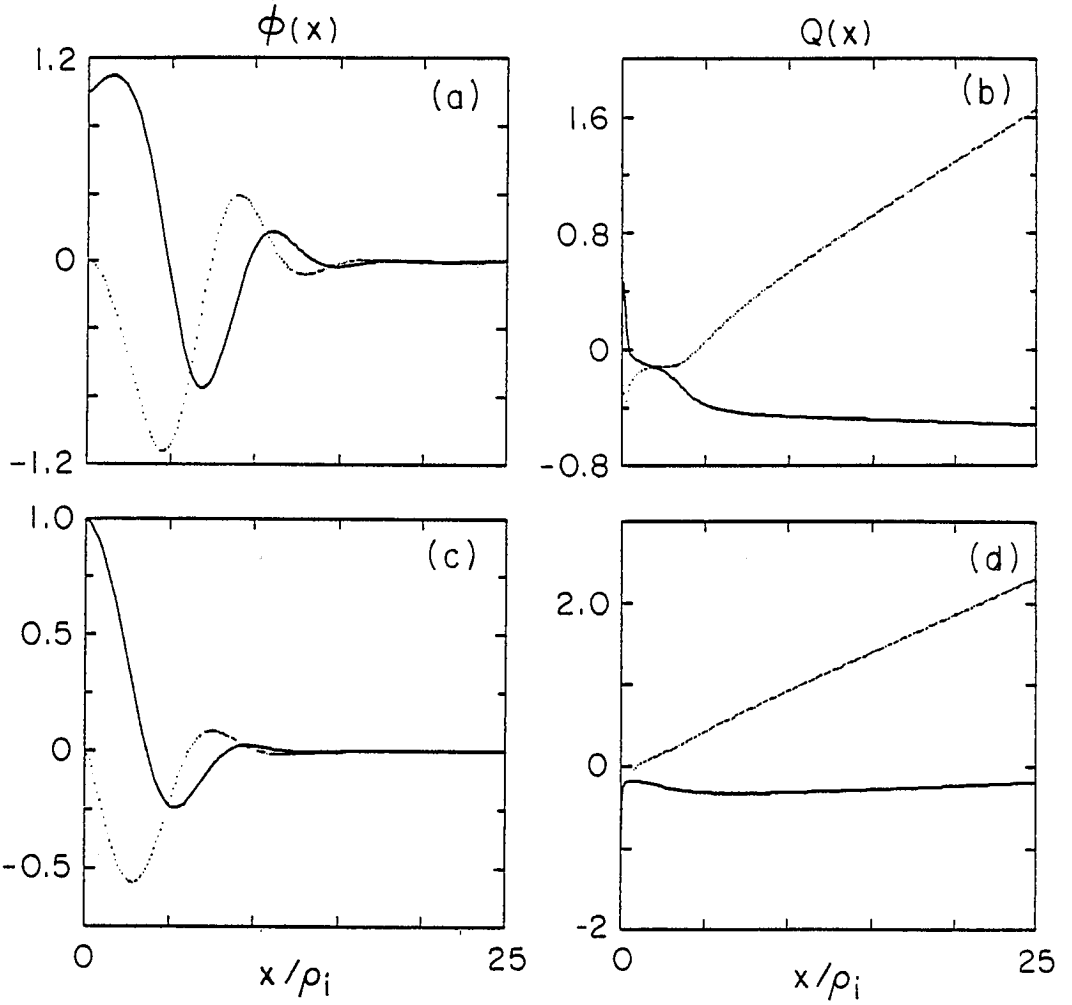

Figure 4.8: Mode structures of stable drift wave and unstable drift-interchange mode for L_n/L_c =0.1 and 0.26. Corresponding eigenvalues are (0.57, −0.07) ω_e^* and (0.20,0.14) ω_e^* .

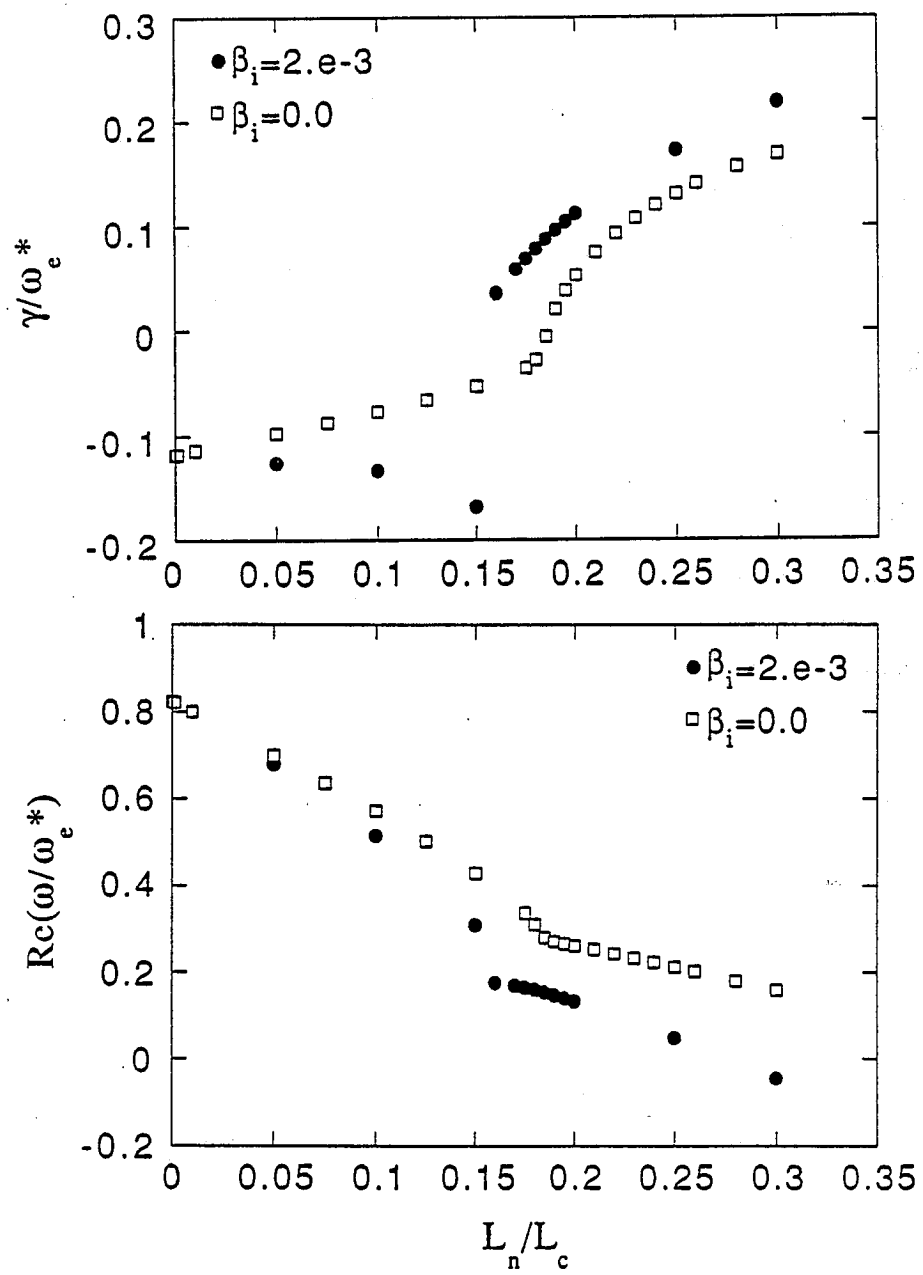

Figure 4.9: Eigenmode spectrum for the case of the transition of drift wave to drift-interchange mode with the increment of L_n/L_c for β_i=0.0 and 0.002.

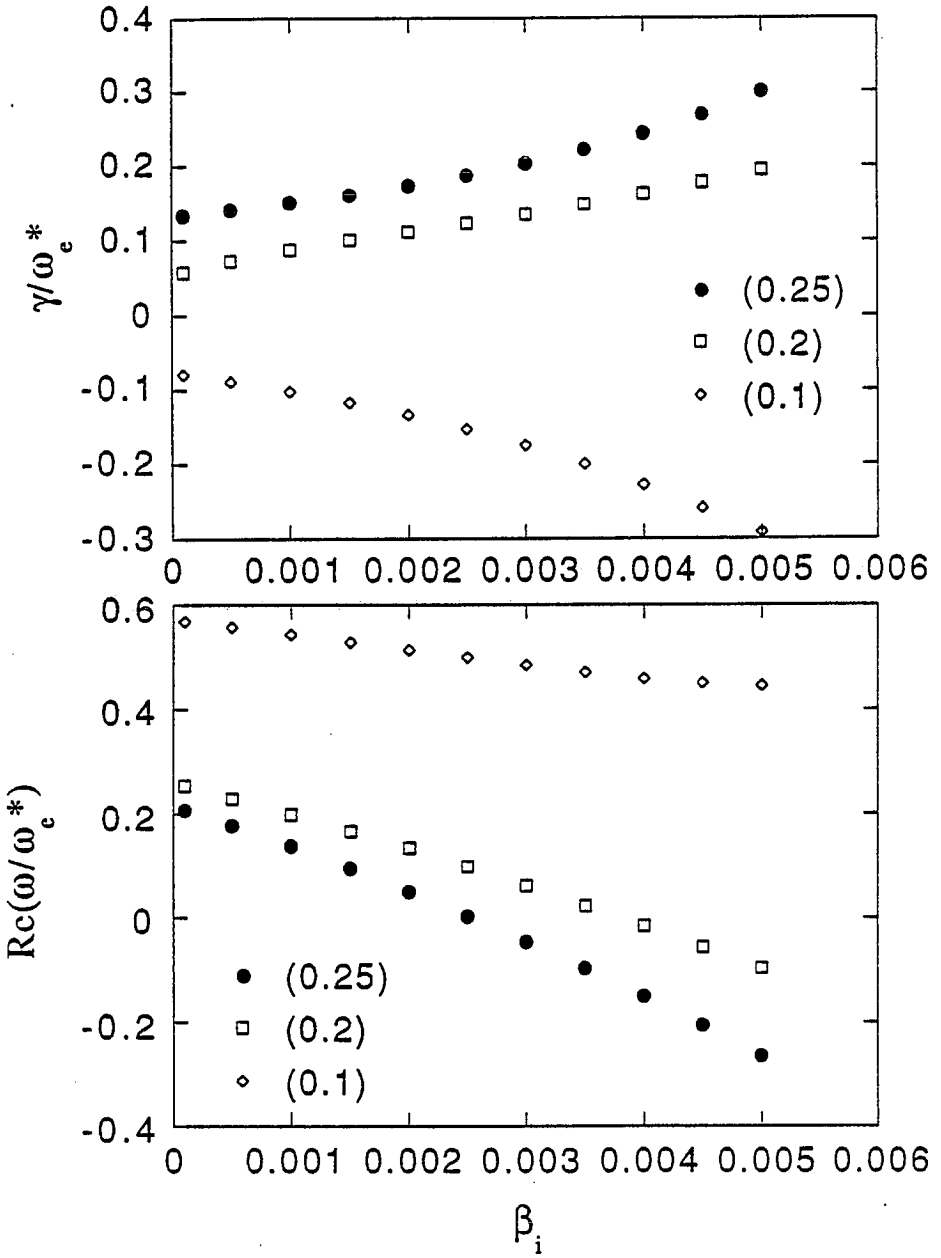

Figure 4.10: Eigenmode spectrum for the case of drift wave and drift-interchange mode under the variation of β_i .

$(L_n/L_c)_c$. A physical explanation can be given for these different tendencies. By turning on finite β , we have a magnetic potential which is accompanied by shear Alfvén waves propagating along the field lines at the expense of the free energy source given by the density gradient. Thus, drift waves driven solely by this free energy source become more stable when β_i is turned on, due to the dissipation by $k_{\|}v_A$. While finite beta effect play a role as an energy sink in drift waves, they affect both the energy source and the sink for the drift-interchange modes. Magnetic curvature drifts combined with the density gradient are the free energy source for the interchange mode. Since curvature drifts are driven by finite beta through the temperature, which turns into pressure in combination with the density, the amount of free energy provided by increasing the beta value exceeds the loss from the generation of shear Alfvén waves, and hence the interchange mode becomes more unstable. Shearless local analyses in which $k_{\|}$ is a continuous variable are carried out to confirm this picture. The local dispersion relation is obtained by combining the two coupled radial eigenmode equations in the shearless limit, so that

$$
\begin{aligned}
D(k,\omega) = & \left[\left(\frac{\omega-\omega_e^*}{k_{\|}c}\right)(1+\xi_e Z_e)+\tau\left(\frac{\omega-\omega_i^*}{k_{\|}c}\right)(1+\xi_i Z_i)\Gamma_0\right]^2 \\
& +\left[k_\perp^2\lambda_{De}^2-\left(\frac{\omega-\omega_e^*}{k_{\|}c}\right)\sqrt{2}\left(\frac{v_e}{c}\right)\xi_e(1+\xi_e Z_e)\right. \\
& \left.-\tau\left(\frac{\omega-\omega_i^*}{k_{\|}c}\right)\sqrt{2}\left(\frac{v_i}{c}\right)\xi_i(1+\xi_i Z_i)\Gamma_0\right] \\
& \times\left[1+\tau+\left(\frac{\omega-\omega_e^*}{\sqrt{2}k_{\|}v_e}\right)Z_e+\tau\left(\frac{\omega-\omega_i^*}{k_{\|}c}\right)Z_i\Gamma_0\right] \\
= & \, 0
\end{aligned}
\tag{4.26}
$$

where $k_{||} = k_y \sin\theta$ and θ is the angle between the wave vector $\mathbf{k}$ and the ambient magnetic field $\mathbf{B}_0$. Equation (4.26) is normalized in terms of ω_{ci} for the time scale and ρ_i for the space scale, since in the local analysis ω_e^* , which does have a k_y dependence, is also a continuous variable and cannot be used as a proper time unit, unlike in the global analysis in which ω_e^* is fixed. With this normalization, the dispersion relation can be written as

$$
\begin{aligned}
D(k,\omega) = \Big[k_y^2 - \beta_i \frac{\sqrt{2}}{\tau}\Big[& \left(\frac{\omega-\omega_e^*}{k_y \sin\theta}\right) \xi_e(1+\xi_e Z_e) \left(\frac{v_e}{v_i}\right) \\
& + \tau \left(\frac{\omega-\omega_i^*}{k_y \sin\theta}\right) \xi_i(1+\xi_i Z_i)\Gamma_0\Big]\Big] \\
& \times \left[1+\tau+\frac{1}{\sqrt{2}}\left(\frac{\omega-\omega_e^*}{k_y \sin\theta}\right)\left(\frac{v_e}{v_i}\right) Z_e + \frac{\tau}{\sqrt{2}}\left(\frac{\omega-\omega_i^*}{k_y \sin\theta}\right) Z_i\Gamma_0\right] \\
& + \frac{\beta_i}{\tau}\left[\left(\frac{\omega-\omega_e^*}{k_y \sin\theta}\right)(1+\xi_e Z_e) + \tau\left(\frac{\omega-\omega_i^*}{k_y \sin\theta}\right)(1+\xi_i Z_i)\Gamma_0\right]^2 \\
= 0 & \qquad (4.27)
\end{aligned}
$$

By solving this dispersion relation that involves full electron and ion Z-functions with the use of a root-finder dispersion solver, we find the same tendency of finite beta effects on both drift waves and interchange modes as shown by the global analysis (Figs.4-11, 4-12). For the case in which the mass ratio m_e/m_i =0.01 and $k_y\rho_i$=0.39 (which correspond to k_y=0.185 in the horizontal axis of dispersion relation) and with the vertical axis in units of ω/ω_{ci}, the growth rate is reduced as β_i increases for the case of drift waves. This tendency holds as long as L_n/L_c is less than 0.11. For L_n/L_c=0.11 or larger, and for $k_y\rho_i$ less than 0.4, the growth rate increases as β_i increases.

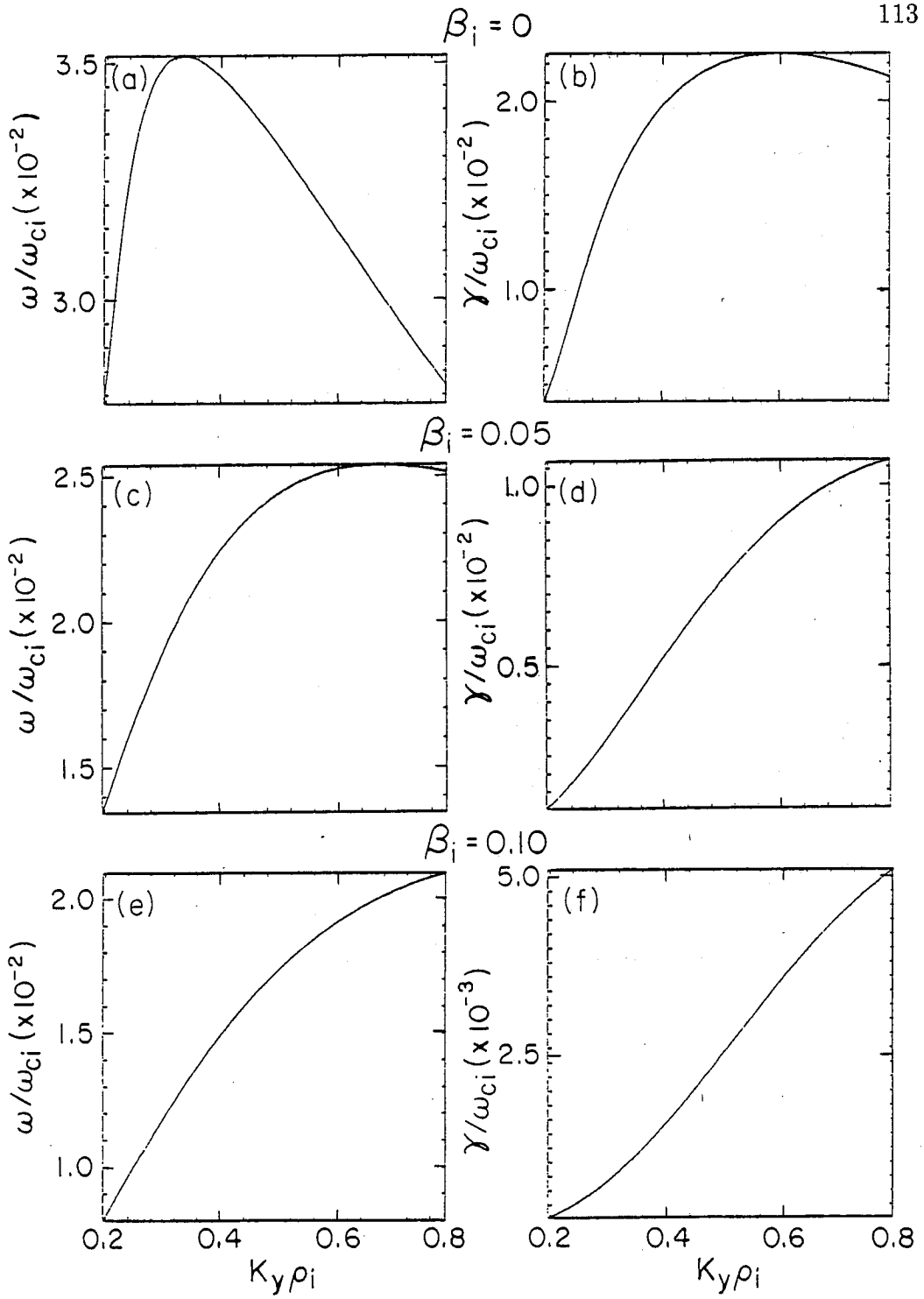

Figure 4.11: Local dispersion relation of finite beta drift waves. Parameter used are T_e/T_i =1.0, m_e/m_i =0.01, $\Delta/L_n = 0.07, \theta = 0.5°, \omega_i = 0.05$, ρ_i=2.

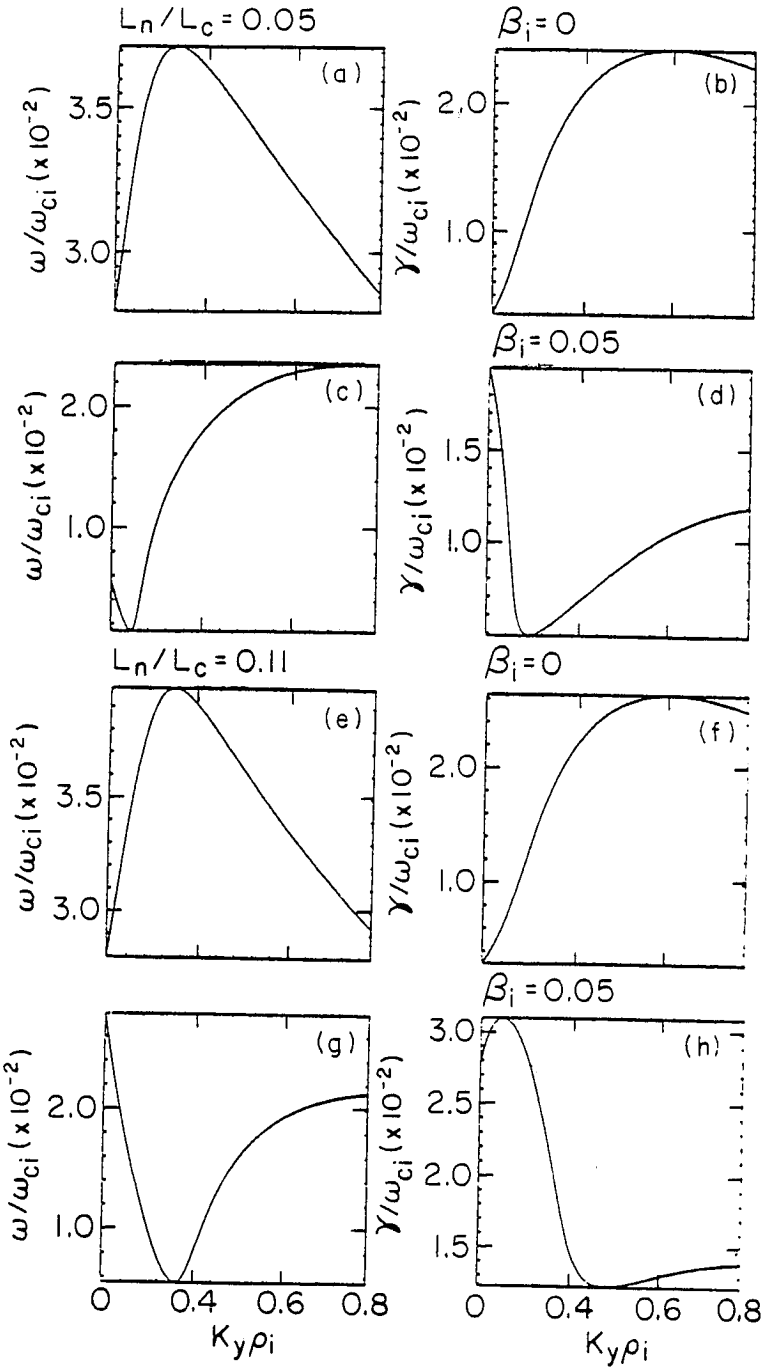

Figure 4.12: Local dispersion relation of finite beta drift interchange mode. Parameter used are the same as drift waves in Fig.4-11.

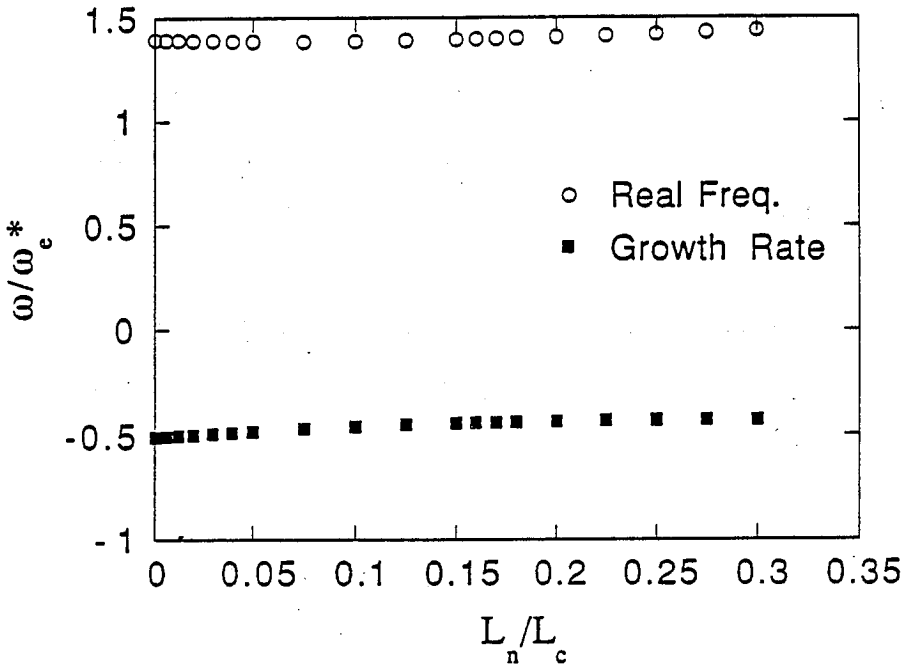

Figure 4.13: Eigenmode spectrum of the shear Alfvén wave under the variation of L_n/L_c . Rest of parameter used are the same as the case of finite beta drift waves in Fig.4-7.

4.3.4 Effect of Curvature Drift on Shear Alfvén Waves

Shear Alfvén waves exist only when β_i is above a certain beta value, for which magnetic fluctuations are no longer negligible. In our analysis, this beta value is 5.0×10^{-3} for the set of parameters T_e/T_i =1, m_e/m_i =1/1836, L_s/L_n =16, and $k_y\rho_i$=0.25, which is the same as in the case of drift waves. For the same variation of the curvature drive L_n/L_c as in the case of finite β drift waves, the shear Alfvén waves have real eigen-frequencies slightly above ω_e^* and show no dependence on the curvature drive. In Fig.4-13 shear Alfvén waves with β_i=0.01, which is well above the mass ratio, show almost no response as L_n/L_c is varied.

4.3.5 Suydam's Criterion

The analyses in the past two subsections show that the drift-interchange mode, which is a kinetic deviation from the fluid interchange mode, becomes more unstable as β_i increases, whereas the stability of the shear Alfvén wave is indifferent to the influence of the curvature drive L_n/L_c . These two pictures are related and can be visualized heuristically in terms of the fluid descrption of finite β interchange modes in the shearless limit. From a one–fluid MHD formulation, the growth rate is obtained as

$$\gamma = \left[\gamma_0^2 - k_\parallel^2 v_A^2\right]^{1/2} \tag{4.28}$$

$$\gamma_0^2 = \frac{T_e + T_i}{m_i L_n L_c} \tag{4.29}$$

In terms of our normalization, the growth rate in Eq. (4-28) can be rewritten as

$$\left(\frac{\gamma}{\omega_e^*}\right)^2 = \left(\frac{L_n}{L_c}\right)\left(\frac{1}{k_\perp^2 \rho_i^2}\right)\left[\frac{1+\tau}{\tau^2}\right] - \frac{1}{\beta_i}\left(\frac{k_\parallel}{k_\perp}\right)^2\left(\frac{L_n}{\rho_i}\right)^2\left(\frac{1}{\tau}\right)^2 \tag{4.30}$$

Eq.(4-30) shows that growth rate of the finite β interchange mode is determined by the competition between the instability due to the curvature drive L_n/L_c and the dissipation accompanied by the coupling to the stable shear Alfvén waves $k_\parallel v_A$ which exist only above a certain β_i in the sheared magnetic field case. In Eq.(4-30), as β_i increases, dissipation due to shear Alfvén waves is reduced as $1/\Delta\beta_i$, and therefore the instability driven by L_n/L_c becomes more unstable. Also, for fixed β_i , the curvature drive does not affect the dissipations, and therefore a stable shear Alfvén wave will behave indifferently under variation of the curvature drive.

Suydam's criterion[57] is a stability criterion for finite β interchange modes in a sheared slab or in cylindrical geometry. In the shearless case, $k_{||}$ is a free parameter and can be zero without any restriction and thus there is no guarantee of stabilization. In a sheared magnetic field, this is no longer the case. By imposing magnetic shear we have a variation along the equilibrium magnetic field $\mathbf{B}_0$,

$$\mathbf{B}_0(x) = B_0(\hat{\mathbf{z}} + \frac{x - x_0}{L_s}\hat{\mathbf{y}}),$$

and this results in a constraint on $k_{||}$ which is zero only at the mode rational surface located at x_0. Thus, depending on the strength of the magnetic shear L_s, the amount of coupling to stable shear Alfvén waves is determined and the stability condition is established. Suydam's criterion, based on this shear stabilization, is formulated from one fluid MHD theory, and the condition for a stable eigenmode is

$$4\pi g \left|\frac{\partial \rho_0}{\partial x}\right| \frac{L_s^2}{B_0^2} > \frac{1}{4} \tag{4.31}$$

In our parameterization, this can be expressed as

$$\beta_i \left(\frac{L_s}{L_n}\right)^2 \left(\frac{L_n}{L_c}\right)(1+\tau) > \frac{1}{4} \tag{4.32}$$

This criterion gives us an approximate parameter regime which can be accomodated with full kinetic particle simulation parameters. The boundary between stable regions and unstable regions predicted by Suydam's criterion would be different from the prediction of a full kinetic treatment since the latter includes linear electron and ion Landau damping through the electron and ion Z-functions. But, in general, there should be an agreement between the two theories when the parameter regime is well inside of the stable or unstable region, i.e., well away from the marginally stable boundary, since kinetic effects would modify this boundary.

4.4 Linear Analysis of Finite β Collisional Interchange Modes

Linear analyses for the finite beta collisional interchange modes are carried out by means of the linear numerical scheme described in Section 4.2 . From the analyses of Chapter3 and of the proceeding subsections, the parameters contributing to destabilize the eigenmodes are L_n/L_c, ν_{ei}, and β_i , where L_n/L_c must exceed $(L_n/L_c)_c$. In this section the relationship among these three parameters and their effects on the stability problem are studied systematically. Two main parameter varaiations are carried out. One is the ν_{ei} variation with fixed β_i to see the effect of collisionality in finite beta plasmas, for comparison with the electrostatic case. The other is the β_i variation for the collisionless and collisional plasmas. These two parameter variations are carried out for two values of L_n/L_c. We noted in Section 4.3 that there is a threshold which distinguishes stable drift waves and unstable drift-interchange modes in the finite beta variations. Thus, it is a logical step to carry out the analysis of collisional electromagnetic modes for cases below $(L_n/L_c)_c$ and above the threshold $(L_n/L_c)_c$. The corresponding L_n/L_c values are L_n/L_c=0.1, which shows a drift type character, and L_n/L_c=0.26, which has an interchange mode character.

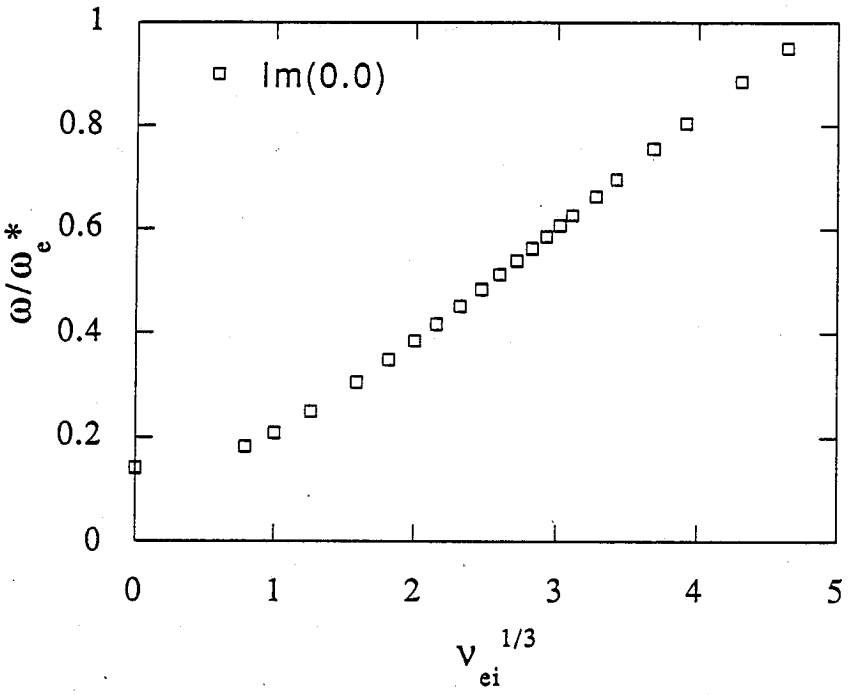

Figure 4.14: Collisional electrostatic mode following $\nu_{ei}^{1/3}$ scale

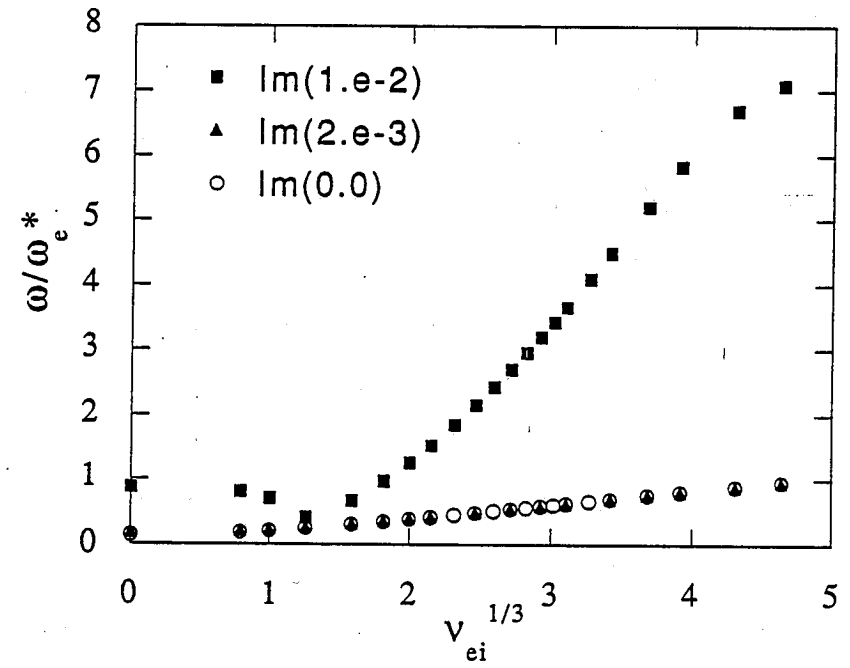

Figure 4.15: Collisional electromagnetic mode following $\nu_{ei}^{1/3}$ scale with β_i=0.002 and 0.01

4.4.1 Parameter variations with L_n/L_c=0.26

Collisionality or ν_{ei} variations with two values of β_i are first carried out, and also the electrostatic case(β_i=0.) is performed as a reference. Two β_i values are selected, β_i=2. $\times 10^{-3}$, which is slightly above the mass ratio (m_e/m_i =1/1836) but less than $(m_e/m_i)^{1/2}$, and β_i=0.01, which is close to $(m_e/m_i)^{1/2}$. The other parameters are T_e/T_i =1.0, $k_y\rho_i$=0.25, and L_s/L_n =16. As a reference, the growth rate scaling of the electrostatic case is shown in Fig.4-14, and the growth rate scaling of two finite beta cases are shown for this reference case in Fig.4.15. In Fig.4.15 we can see that the β_i=0.01 mode follows the same scaling as that of the electrostatic case, but with an order of magnitude larger growth rate, in the strong collisionality regime. In nearly collisionless and semi-collisional regimes, the behavior of the eigenmode is different. In this regime, as ν_{ei} increases, the growth rates decrease till ν_{ei}= 4 $\sim$ 5 ω_e^* . After passing this regime, for collisionality nearly 10 ω_e^* , the growth rate exhibits the typical $\gamma \sim \nu_{ei}^{1/3}$ scaling. The β_i=0.002 case shows almost no difference with the electrostatic case. It has a slightly larger growth rate, but without noticeable difference. The eigenmode spectrum for β_i=0.002 is shown compared to the electrostatic case in Fig.4.16. In Fig.4.16, the real frequency behavior of the finite beta case is different from its electrostatic counterpart in the low collisionality regime. Real eigenfrequency comparisons for three β_i cases are shown in Fig.4.17. In the β_i=0.01 case, the real frequency goes to a negative frequency, which is nearly 10 ω_e^* when ν_{ei} is increased to 50 ω_e^* , whereas in the low beta case, the frequency remains almost zero, as for the electrostatic case. To clarify this picture, β_i scans for the case of collisionless, semi-collisional and collisional regimes are performed. The corresponding collision frequencies which have β_i variation are 0, 0.5, 1, 4, 10, 20, and 40 ω_e^* . As a reference, the

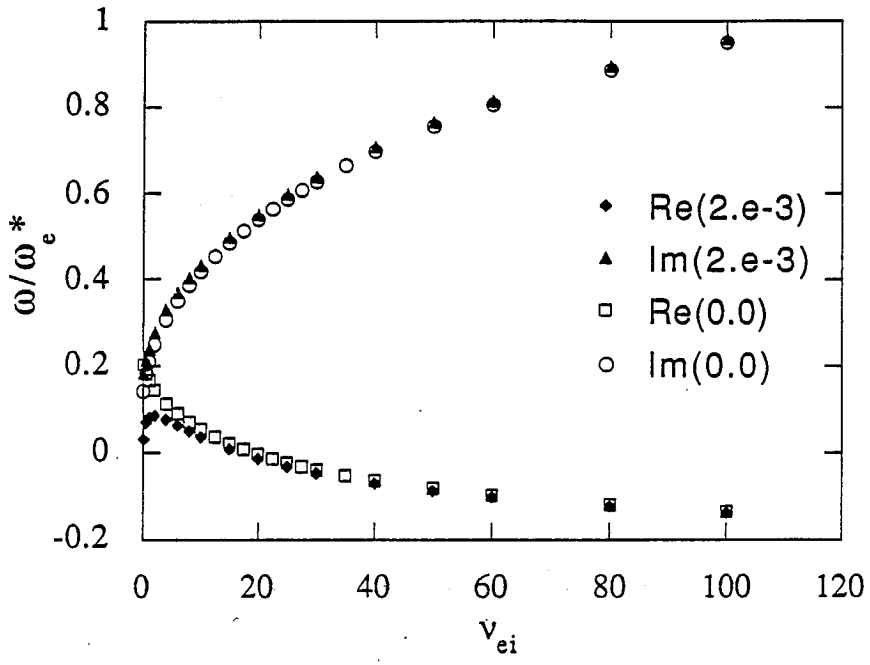

Figure 4.16: Eigenmode spectrum under variation of ν_{ei} with β_i=0.002 and 0.0

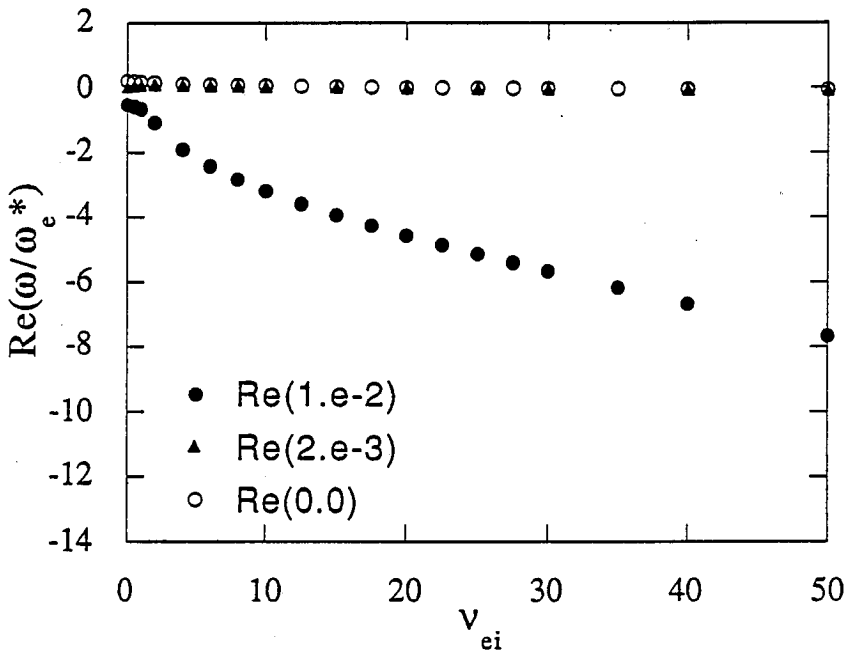

Figure 4.17: Collisional electromagnetic mode real eigenfrequency spectrum of β_i=0.002 and 0.01 with comparison of electrostatic case.

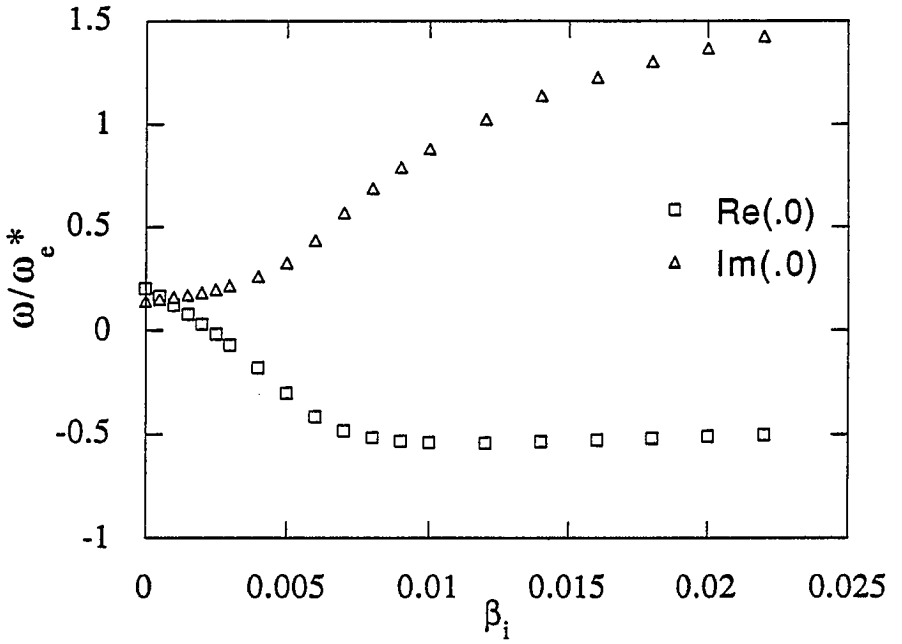

Figure 4.18: Eigenmode spectrum of collisionless mode under the variation of with β_i.

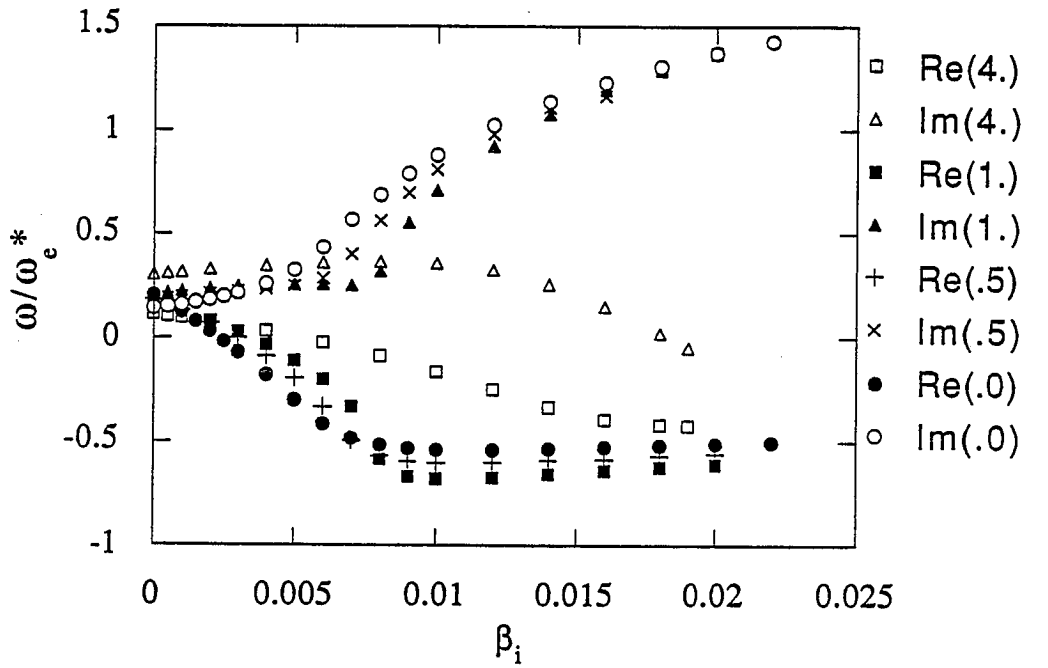

Figure 4.19: Eigenmode spectrum of near collisionless and semi-collisional mode under the variation of β_i.

β_i variation for the collisionless mode is carried out. The result of this variation is shown in Fig. 4.18. As β_i increases the growth rate starts to increase from below ω_e^* and then exceeds above ω_e^* when β_i is close to $(m_e/m_i)^{1/2}$, while the real eigenfrequency asymptotes to $-0.5\ \omega_e^*$ after passing $\beta_i \sim 0.075$. Since in the ν_{ei} variations, deviation from the typical collisional eigenfrequency spectrum is seen near the collisionless or semi-collisional regime, analyses with β_i variation are concentrated in this regime and later on compared with the collisional case. Analyses are carried out with a collisionality of ν_{ei}= 0.5, 1.0, and 4.0 by varying β_i and are compared with the ν_{ei}=0. case. The results are shown in Fig.4.19. At low β_i less than m_e/m_i , the growth rates with finite resistivity are slightly larger than those for zero collisionality. When β_i passes m_e/m_i , growth rates become smaller than the zero resistivity ones. In particular the growth rate for ν_{ei}=4 ω_e^* is damped out when β_i reaches $(m_e/m_i)^{1/2}$. The real eigenfrequencies asymptote to $-0.5\ \omega_e^*$ as β_i increases for all four of the values of ν_{ei} that were tested. These eigenfrequency spectra are now compared with the spectra for the high collisionality cases. Analyses of β_i variation with collisionality of 10, 20, 40 ω_e^* are carried out. Growth rates compared for ν_{ei}=0 and 4 ω_e^* are compared in Fig. 4.20 . From this picture, we notice that the growth rates with strong collisionality have almost a neutral response to the finite beta effect, compared with the nearly collisionless regime. There is a very small increment of the growth rate as β_i increases from zero to $(m_e/m_i)^{1/2}$. A full comparison of the eigenmode spectrum for highly collisional cases and weakly collisional cases in finite beta plasmas is shown in Fig. 4.21. The real eigenfrequency spectrum of the high collisionality mode slightly deviates from the positive side of the typical electrostatic zero frequency mode to the negative side of zero frequency as β_i increases to $(m_e/m_i)^{1/2}$. This plot tells us that the kinetic resistive drift interchange mode in the regime which follows the typical $\nu_{ei}^{1/3}$

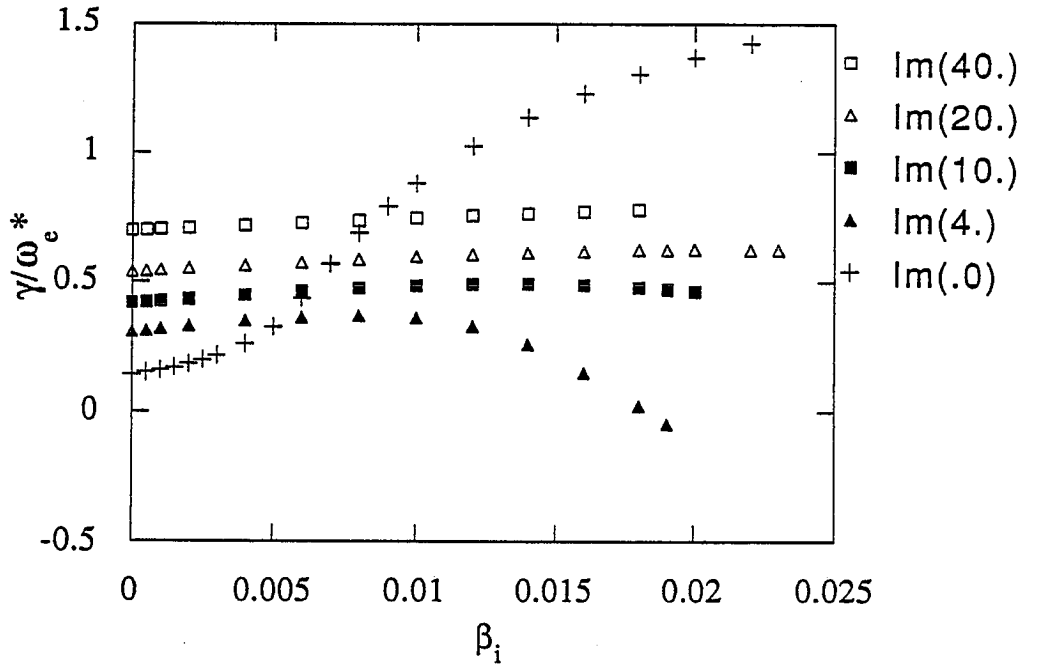

Figure 4.20: Growth rate comparison of collisonless, semi-collisional and collisional mode under variation of β_i .

scale is predominantly an electrostatic mode.

4.4.2 Parameter variations with L_n/L_c=0.1

As prescribed in subsection 4.3.2, with curvature as weak as L_n/L_c=0.1, which is below the threshold $(L_n/L_c)_c$, the mode is stable in the electrostatic limit, and finite beta effects on this mode are also stabilizing. In general, convergence for stable modes is numerically poor in the shooting code. Thus, a full parameter scan is difficult to achieve, unlike in the unstable cases. Also, stable modes are not the ones of most interest here. Therefore in this subsection, only numerically feasible parameter scans, which give us well converged numerical solutions, are presented in order to complete the linear analysis. Our analysis shows that stable electrostatic modes with L_n/L_c below $(L_n/L_c)_c$ become more stable due to collisional damping as ν_{ei} increases (Fig.4.22).

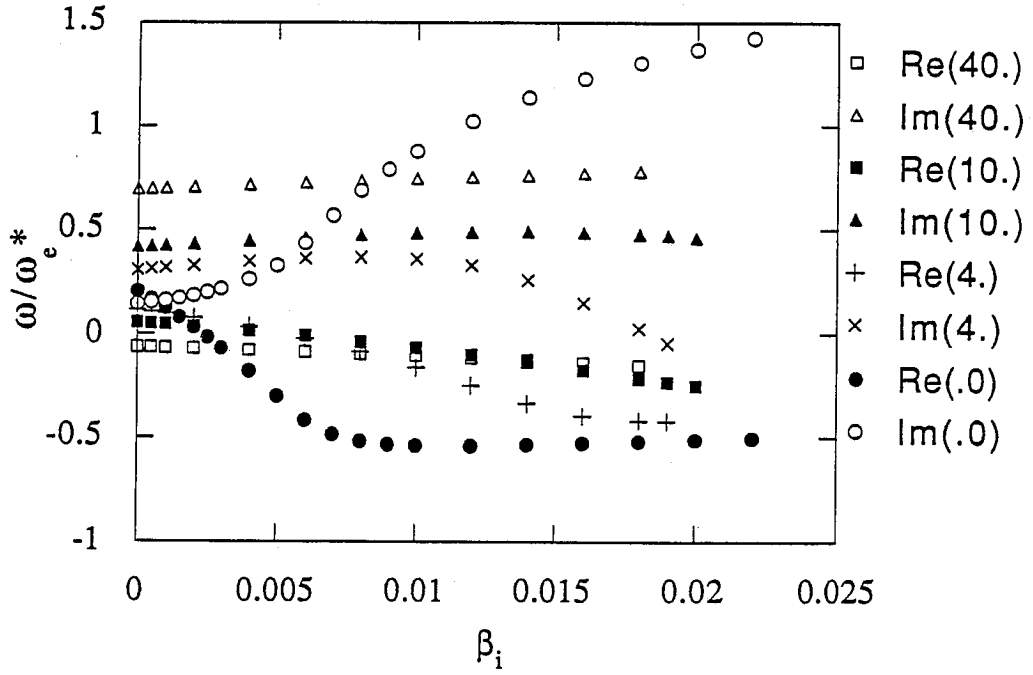

Figure 4.21: Eigenmode spectrum of collisonless, semi-collisional and collisional mode under variation of β_i .

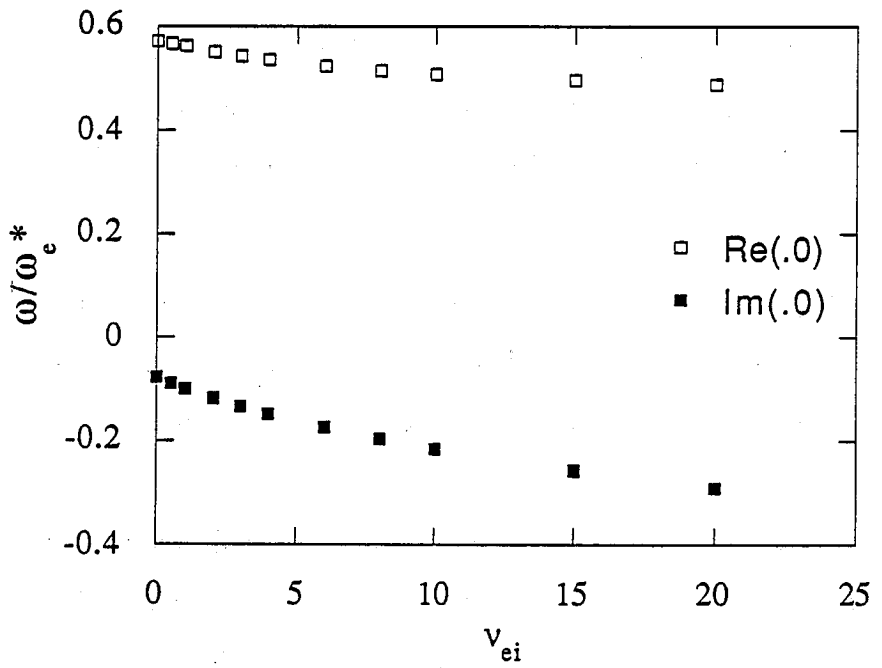

Figure 4.22: Eigenmode spectrum of electrostatic mode under variation of ν_{ei} .

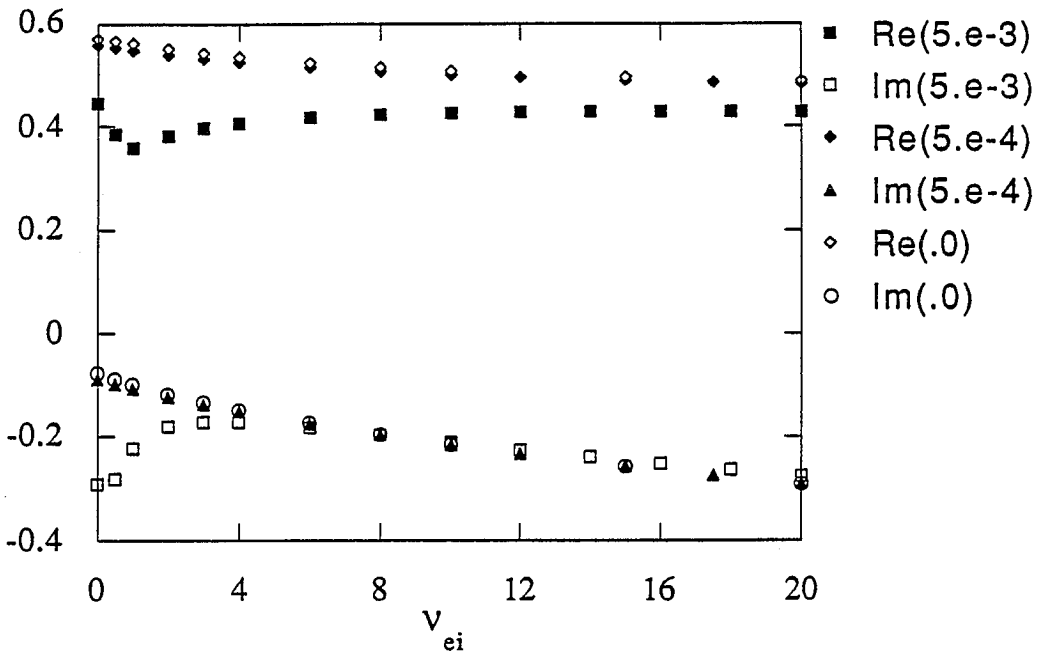

Figure 4.23: Eigenmode spectrum of electromagnetic mode compared with electrostatic mode under variation of ν_{ei} .

With β_i=5.$\times 10^{-4}$ and β_i=5.$\times 10^{-3}$, the ν_{ei} variation is carried out and compared with the electrostatic case in Fig.4.23. Except for the low collisonality limit for the three tested β_i values, the growth rates converge to the electrostatic case as ν_{ei} increases. The stable mode has a positive real frequency that is opposite to the unstable mode, which has a negative real frequency.

To complete the linear analysis, β_i scans with fixed ν_{ei} are performed. In this analysis, there again exists a limitation for the parameter scan due to the stable nature of the eigenmode. With ν_{ei} varying from collisionless to collisional, the eigenmode spectrum of the stable modes under the variation of β_i is shown in Fig.4-24. The behavior of the collisionless mode and the collisional mode under β_i variation are opposite. The collisionless mode becomes more stable, whereas the collisional mode is less stable, as β_i increases. Nevertheless, both modes are stable for all values of β_i which are less than $(m_e/m_i)^{1/2}$.

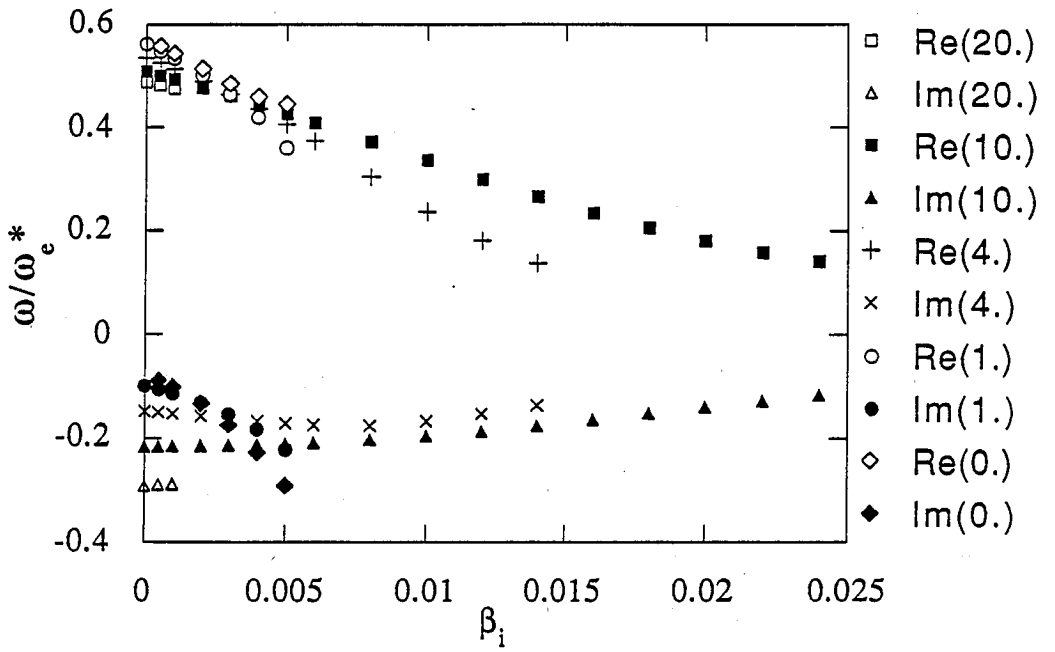

Figure 4.24: Eigenmode spectrum of collisionless, semi-collisional and collisional mode under variation of β_i .

4.5 Collisionless Electromagnetic Interchange Mode Simulation

4.5.1 Simulation Configuration and Suydam Parameter Test

Particle simulations of collisionless electromagnetic interchange modes are performed by implementing the Darwin model algorithm which has an elaborate electromagnetic field solver in $2-\frac{1}{2}$D sheared slab geometry. The simulation configuration is the same as the electrostatic interchange mode simulations performed in Chapter 3(Fig. 3.12). As shown earlier by linear analysis of electromagnetic interchange modes in the last subsections, the eigenmode associated with $A_{||}$ is radially much broader than its coupled eigenmode ϕ . Thus the simulation system size should be expanded radially to accomodate $A_{||}$ when the size of the eigenmode in $A_{||}$ exceeds the radial size of the simulation system in certain parameter regimes. This requires huge amounts of computer time

and restricts computation flexibility quite severely due to the increased number of particles, which in turn affects the memory and CPU time required to calculate particle quantities and associated field quantities in the simulations.

Before we simulate electromagnetic interchange modes with a set of accessible parameters obtained from linear eigenmode analysis, we need to go through one more stringent test of the simulation model and algorithm based on the well known stability criterion for electromagnetic interchange modes in sheared slab geometry, namely, Suydam's criterion. Simulations are performed in two cases with stable and unstable parameters obtained from linear kinetic theory, both well away from the marginally stable boundary. In Suydam criterion tests, as manifested by Eq.(4.32), the most effective parameter that distinguishes whether mode is stable or unstable is the magnetic shear length L_s when the same density gradient scale length L_n is held fixed. Parameters which give a stable eigenmode are $L_x \times L_y = 64\Delta \times 32\Delta, a_x = a_y = 1.5\Delta, \omega_{ci} = 0.025$, $\omega_e^* = 3.436 \times 10^{-4} m\omega_{pe}^{-1}$, m_e/m_i =1/100, $k_y\rho_i$=0.39, L_s/L_n =7.0, L_n/L_c=0.089, T_e/T_i =1.0, β_i=5×10^{-3}, particle density $n_0 = 16/\Delta^2$, $y-$direction grid stretching parameter=2.0, and total run time($n\Delta t$)= $4000 \times 4\omega_{pe}^{-1} = 400\omega_{ci}^{-1}$. The unstable set of parameters is the same as in the stable case, except for L_s/L_n =14.0 . In Fig. 4.25 the results of testing the Suydam stable parameters are shown ; there is no sign of instabilities with respect to density profile flattening, magnetic island formation, or linear growth rates. On the other hand, with an unstable parameter set, as shown by Fig. 4.26, density profile modification, magnetic island formation, and linear growth associated with instability are observed.

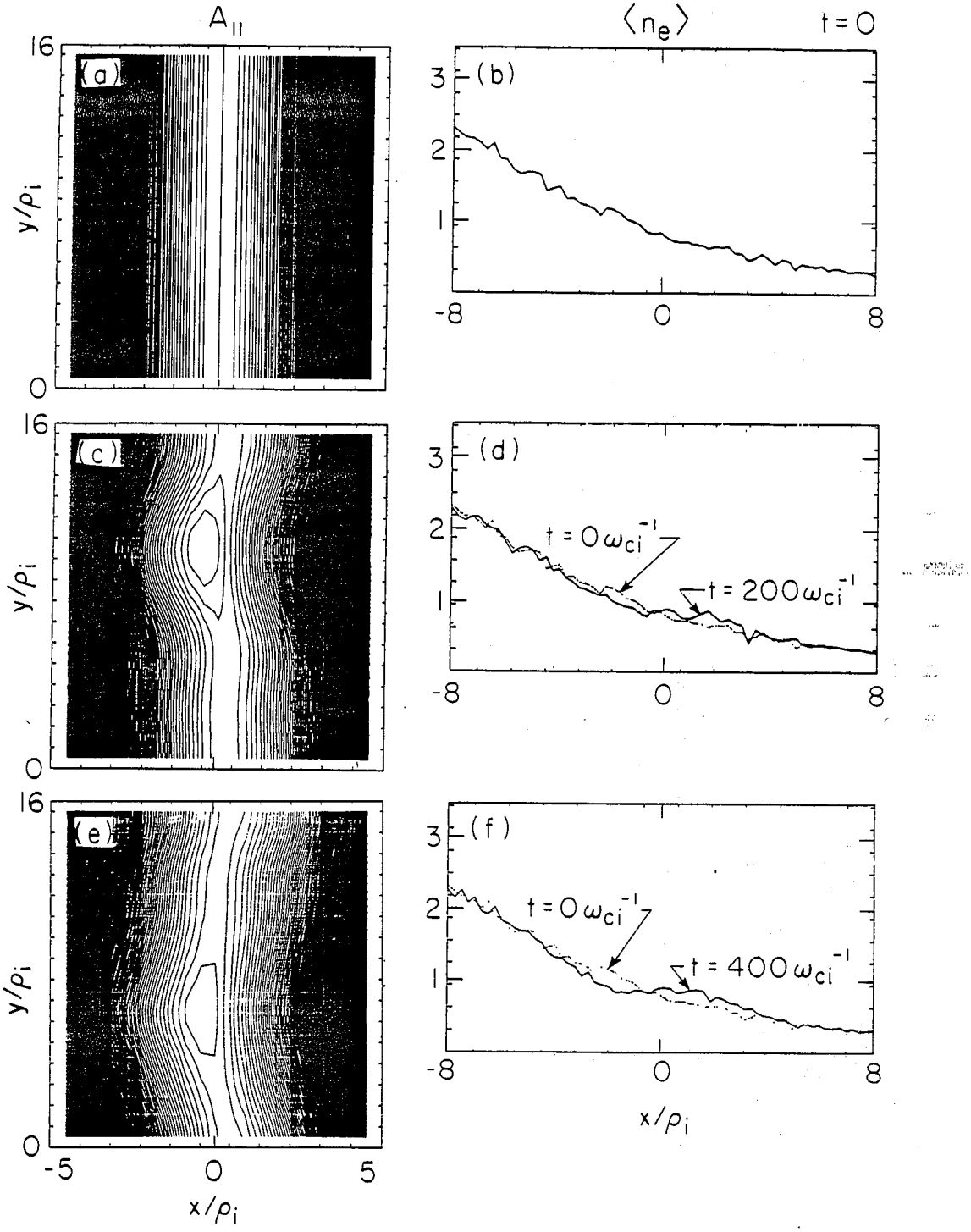

Figure 4.25: Simulation of Suydam unstable parameter results. Magnetic island formation around mode rational surface and electron density profile relaxation at $t = 0, 200, 400\omega_{ci}^{-1}$.

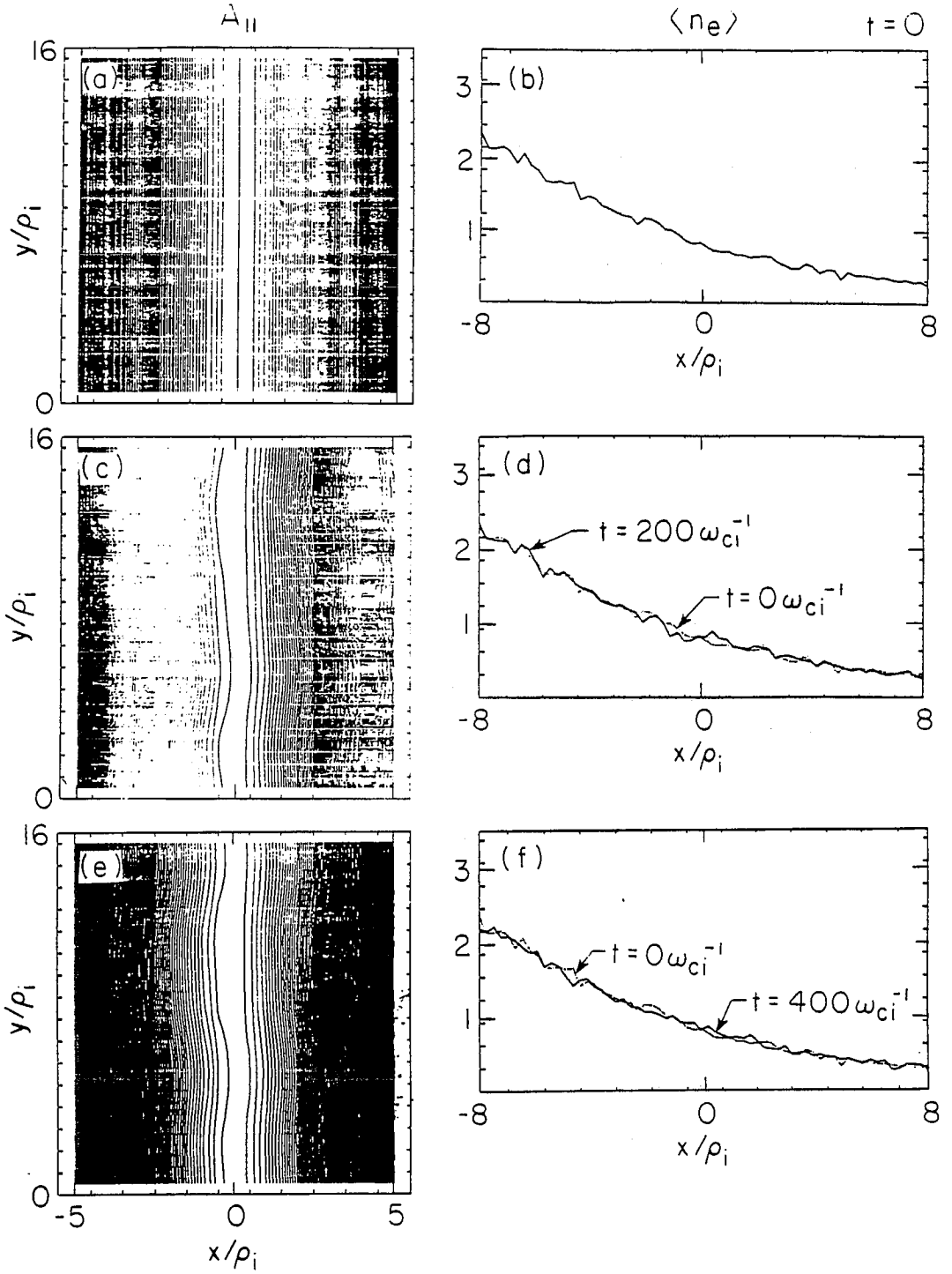

Figure 4.26: Simulation of Suydam stable parameter results. Magnetic field line around mode rational surface and electron density profile at $t = 0, 200, 400\omega_{ci}^{-1}$.

4.5.2 Collisionless Electromagnetic Interchange Mode Simulation Results

Scaling studies of the linear growth rate and the saturation level of the electromagnetic field quantities with respect to the parameter β_i are carried out. The dynamical aspects of collisionless finite β interchange modes are shown in terms of quasilinear density profiles flattening, and phase relations between particle and field quantities, especially for the perturbed magnetic field. Magnetic island widths associated with radial magnetic fluctuations are measured. Also the time variation of thermal quantities such as the modification of the parallel electron and parallel ion temperature profile are also observed.

Simulation parameters are m_e/m_i =100, L_s/L_n =14, T_e/T_i =1, ρ_i=4.0, L_n/L_c=0.2, ω_{ci} = 0.025, $k_y\rho_i$=0.39m, and ω_e^*=3.436 $\times$ $10^{-4}m\omega_{pe}^{-1}$. The system size was varied from $L_x \times L_y = 64\Delta \times 32\Delta$ to $L_x \times L_y = 128\Delta \times 32\Delta$ depending on the $A_{||}$ mode width, $a_x = a_y = 1.5\Delta$, with β_i varies from 0.0025 to 0.05. Linear growth rates are measured from the electrostatic potential ϕ (m=1) and compared with linear kinetic theory calculations (Fig. 4.27). The associated linear eigenmode structure for ϕ and $A_{||}$ measured from simulations are compared with linear theory results (Fig. 4.28). There is reasonable agreement between simulation and theory for the growth rate and for the eigenmode structure in the linear phase. In Fig. 4.28, the eigenfrequency obtained from a linear shooting code is ω/ω_e^*=$(-0.446, 0.904)$ and the real eigenfrequency measured from a simulation interferogram is $-0.814\ \omega_e^*$. The saturation level of ϕ , when measured and compared with the mixing length estimate, and shows a similar trend, but with an order of magnitude difference (Fig. 4.29). As β_i increases from zero to near m_e/m_i , the level of magnetic fluctuations, as measured by B_r, which is B_x in sheared slab geometry, increases by an order of

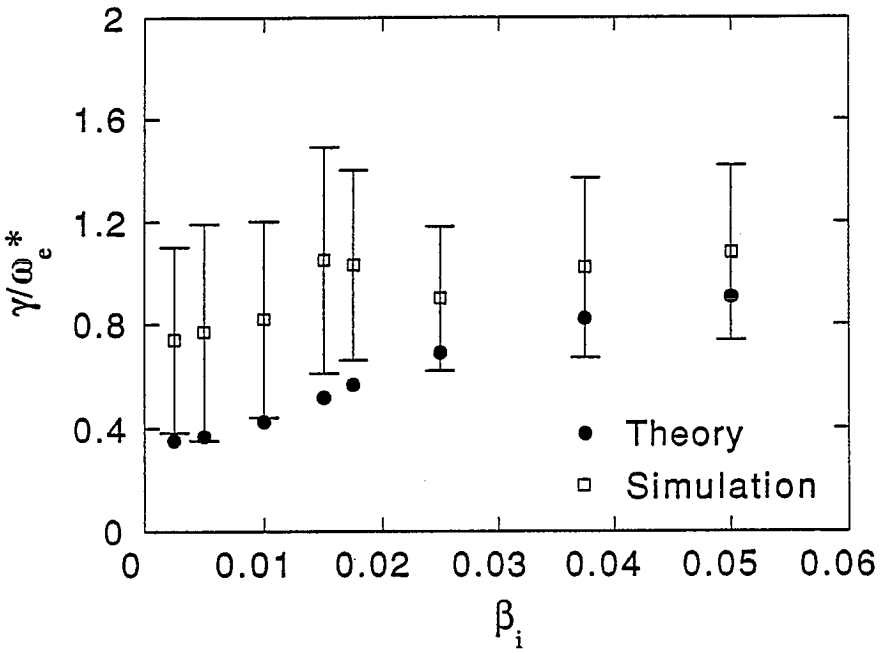

Figure 4.27: Growth rate of $m = 1$ mode comparison with linear kinetic theory.

magnitude and tends to saturate as β_i increases further. The ϕ saturation level also increases but the increment is less than an order of magnitude as β_i increases (Fig. 4.30). In Fig. 4.30, ϕ and B_r are measured at the peak saturation level of the m=1 mode. Also, the measured B_r/B_0 levels are compared with the quasilinear estimate of B_r/B_0 in terms of the measured $e\phi/T_e$ (Ref.49),

$$\frac{B_r}{B_0} \simeq i\tau\beta_i(k_y\rho_i)\frac{L_s}{L_n}\frac{\rho_i}{\Delta}\frac{e\phi}{T_e} \qquad (4.33)$$

and shows fairly good agreement. The magnetic island width, Δ_I is measured under the variation of β_i (Fig. 4.31). The measured island width is of the order of ρ_i , for β_i above the mass ratio m_e/m_i . Magnetic island formation around the mode rational surface at the saturated phase is shown in Fig. 4.32. The magnetic island width becomes broadened as β_i increases.

The ϕ and n_e fluctuation amplitude saturation measured at the location of the mode rational surface (x=x_0=$128\Delta/2$) are shown in Fig. 4.33 and

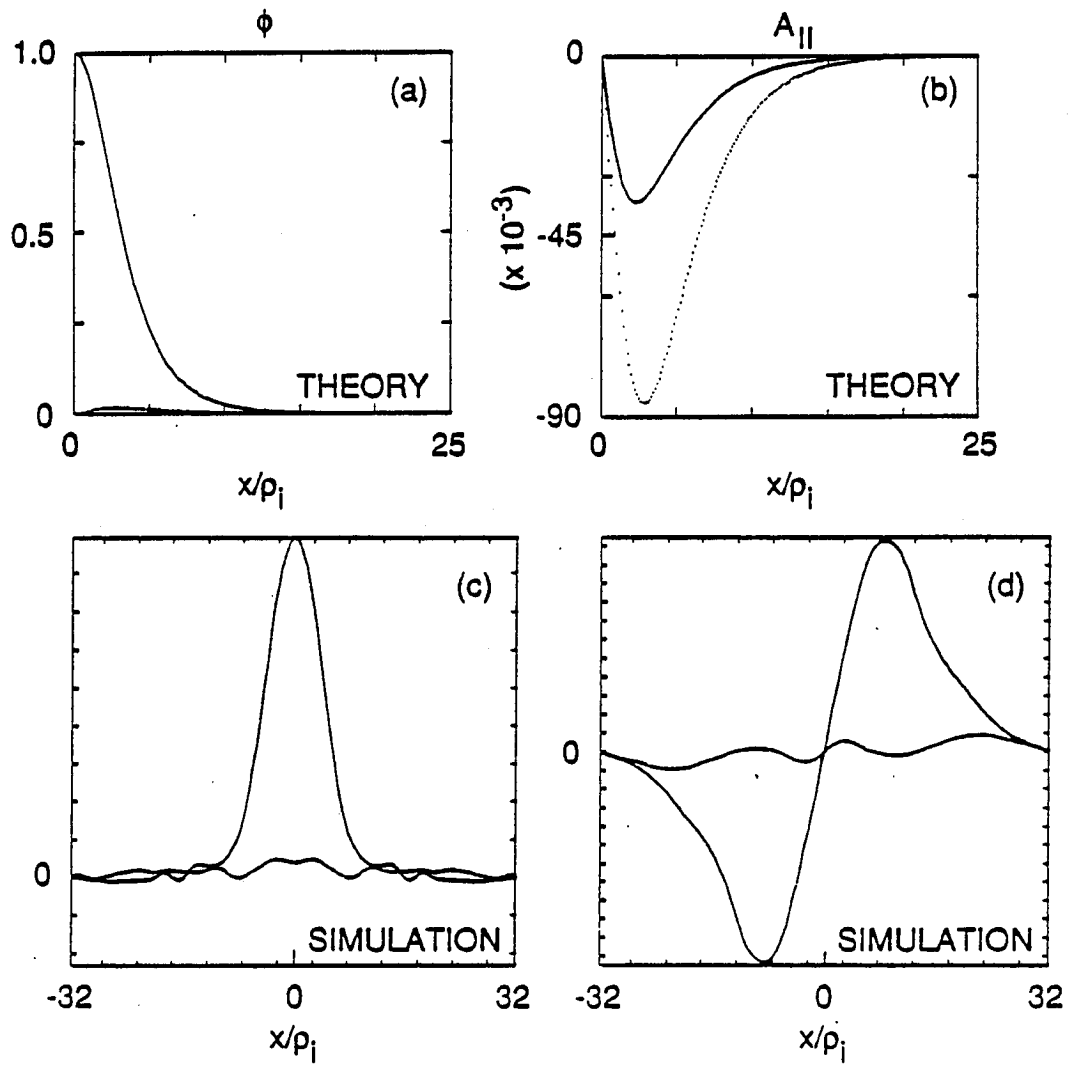

Figure 4.28: Eigenmode structure of ϕ and $A_{||}$ Parameters used are $\tau = 1$, m_e/m_i =0.01, β_i=0.05 L_n/L_c=0.2, $k_y\rho_i$=0.39.

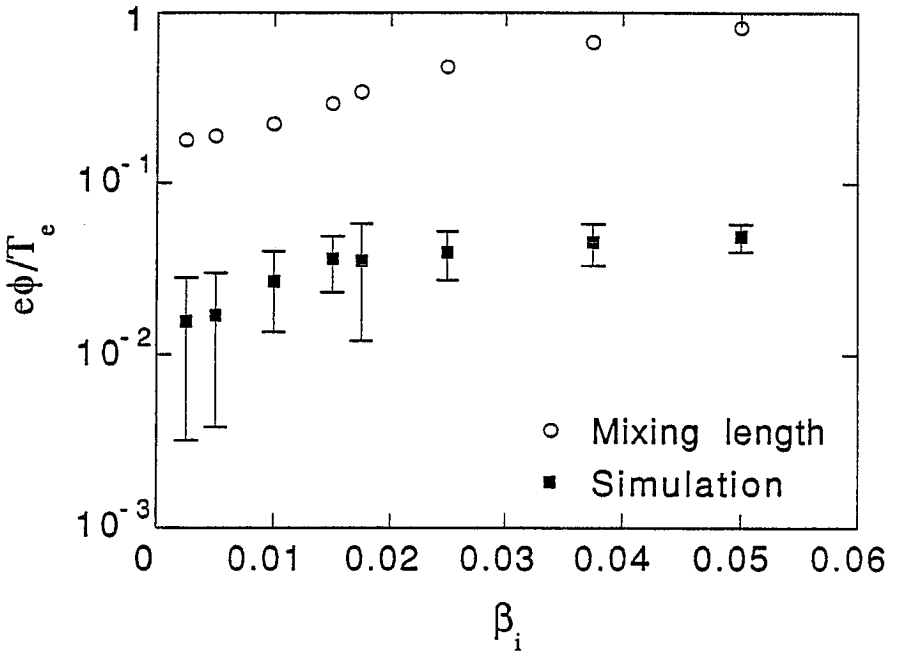

Figure 4.29: ϕ saturation level comparison with mixing length theory estimation.

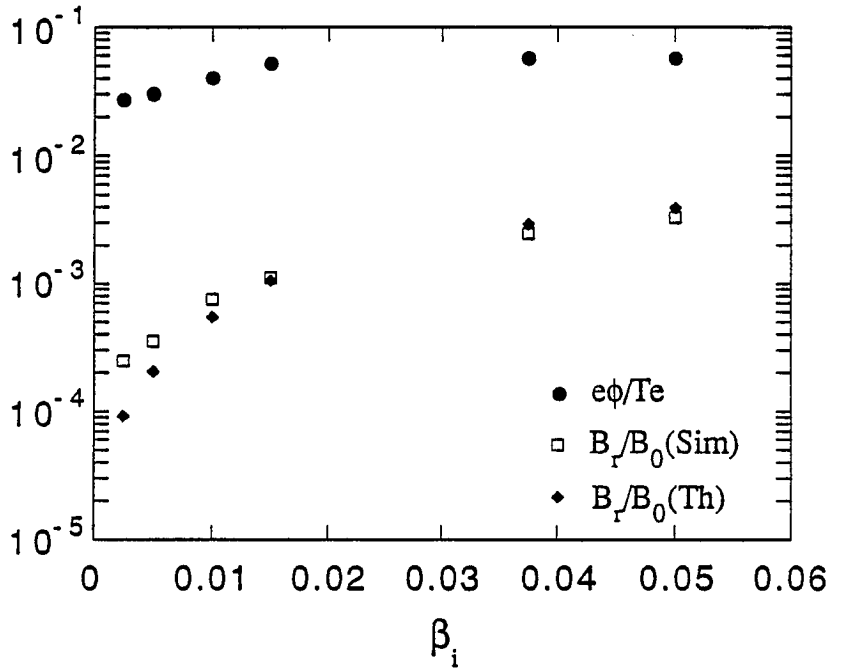

Figure 4.30: ϕ saturation level and B_r saturation level compared with quasi-linear theory estimation.

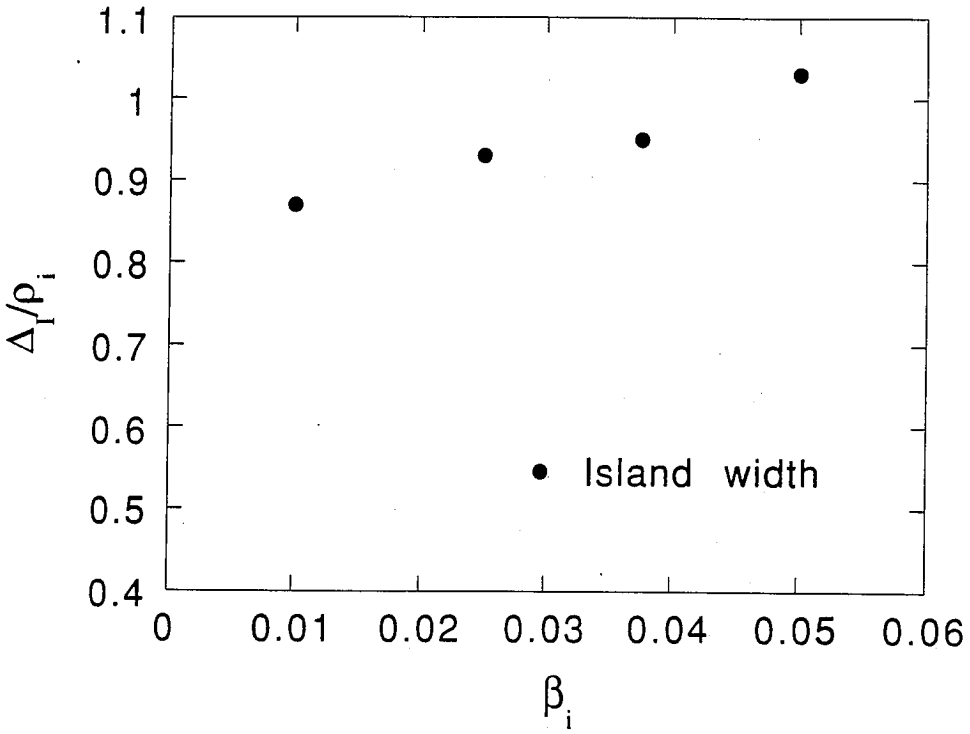

Figure 4.31: Magnetic island width measurement under the variation of β_i .

show a similar saturation trend. At the mode rational surface $A_{||}$,which is A_z in our simulation system, is zero due to its parity, and its amplitude reaches a maximum near the middle point located midway between the mode rational surface and the boundary. The time variation of the A_z and n_e fluctuation amplitudes is measured at the point $x = x_0 + L_x/4$ (Fig. 4.34) and shows that n_e and A_z saturate in a similar way. Measurements of n_e, ϕ , and A_z at saturation tell us that n_e fluctuations are correlated strongly with ϕ at the mode rational surface, although they are dominated mostly by the electromagnetic eigenmode A_z, which has a broad eigenmode structure in the region away from the mode rational surface, especially after the saturation stage is reached. This picture can be seen from electron phase space plots(Fig. 4.35) Fig. 4.35 shows that the electron response is also dominated by the electromagnetic eigenmode in the region away from the mode rational surface in the linear phase. The spatial mode structures of ϕ , n_e, n_i, and B_x, which corresponds to B_r, are studied by

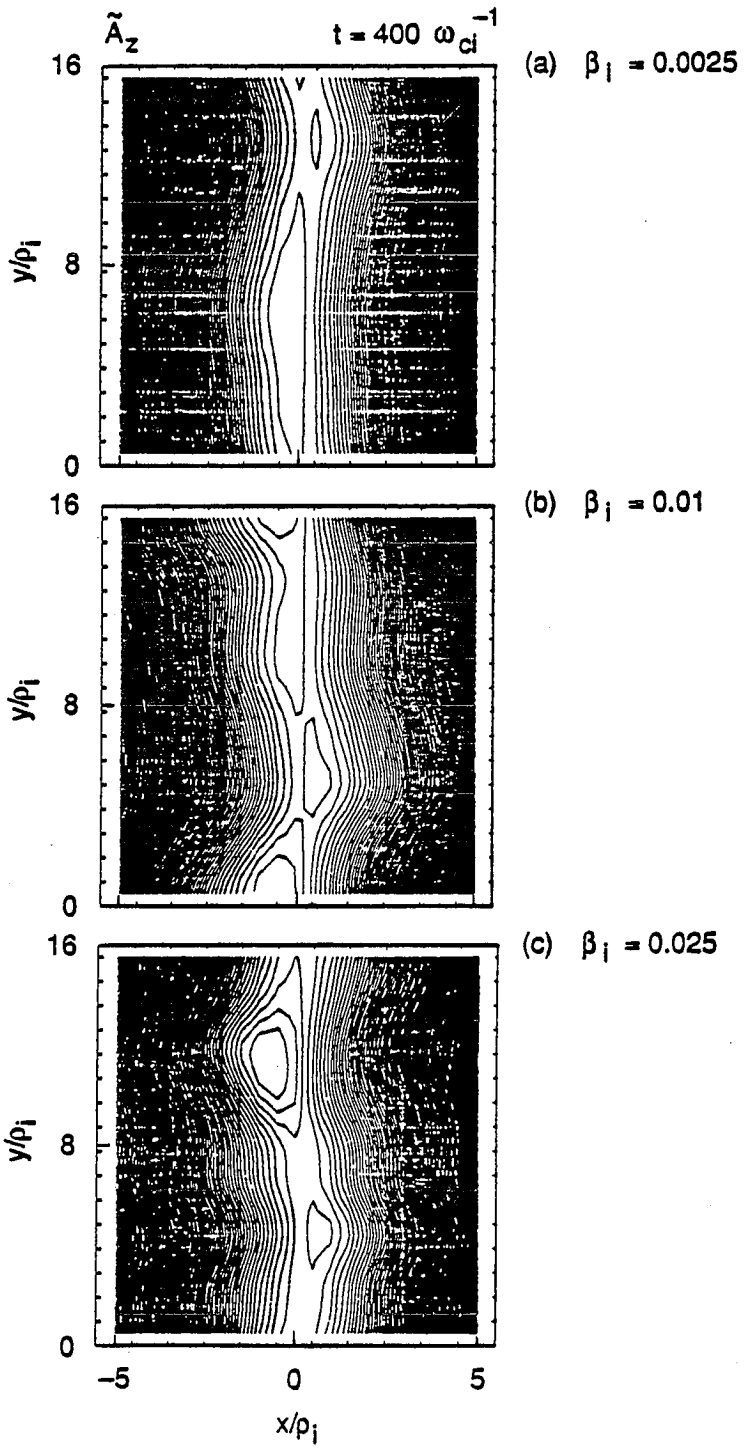

Figure 4.32: Magnetic island formation around the mode rational surface for the case of β_i= 0.0025, 0.01, 0.025 at $t = 400\omega_{ci}^{-1}$.

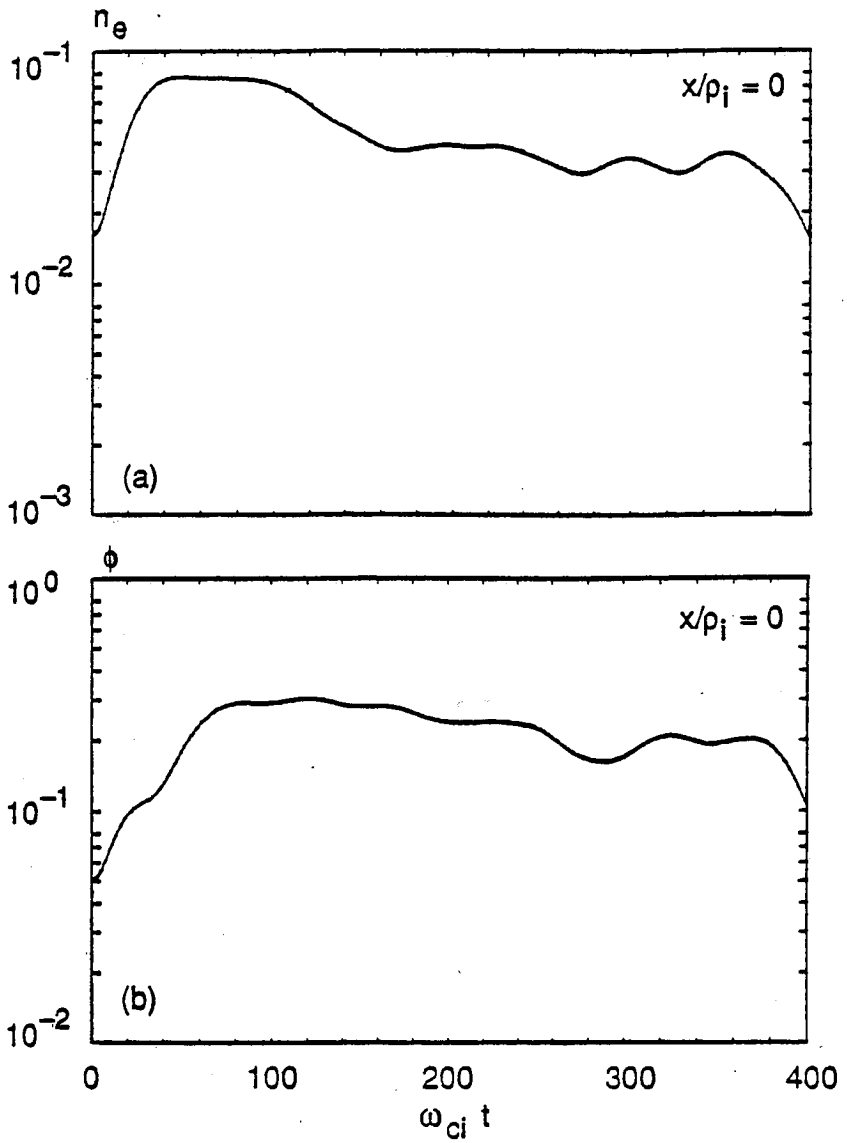

Figure 4.33: ϕ and n_e fluctuation amplitude saturation measured at the mode rational surface $x = x_0$.

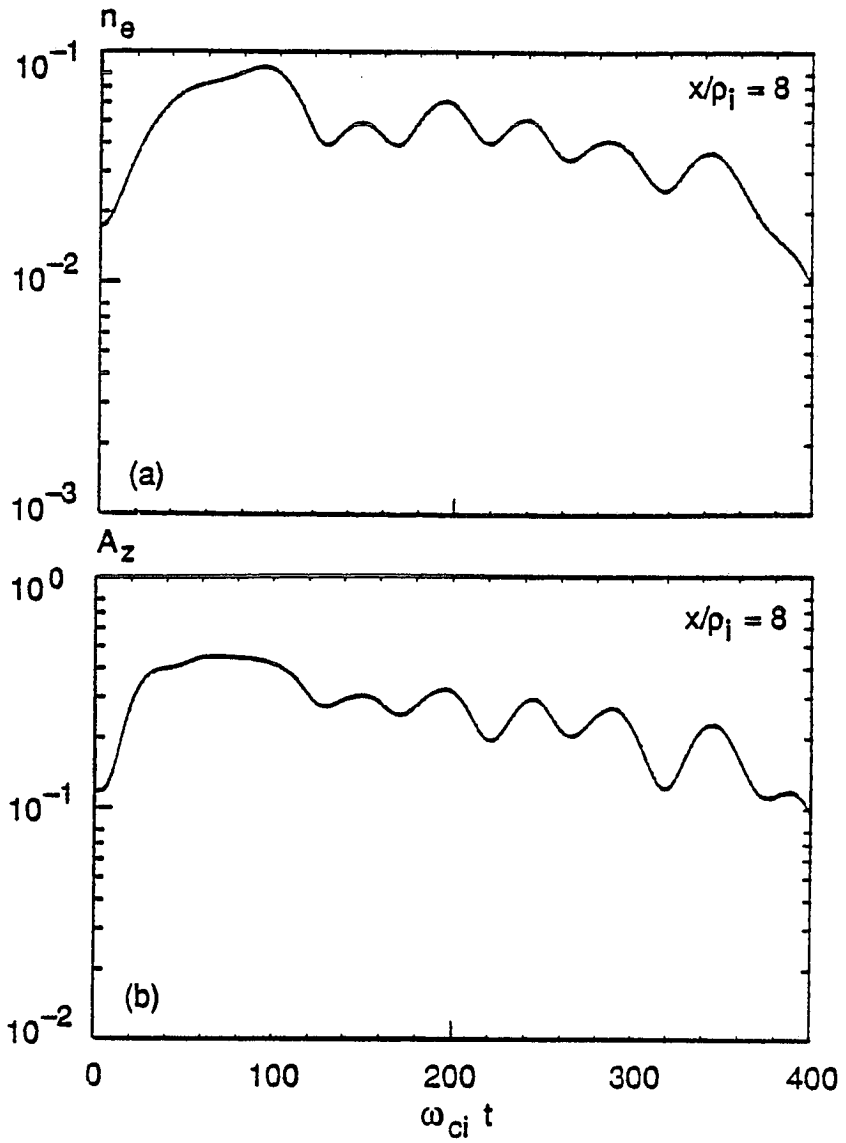

Figure 4.34: n_e and A_z fluctuation amplitude saturation measured at the location $x = x_0 + 4\rho_i$.

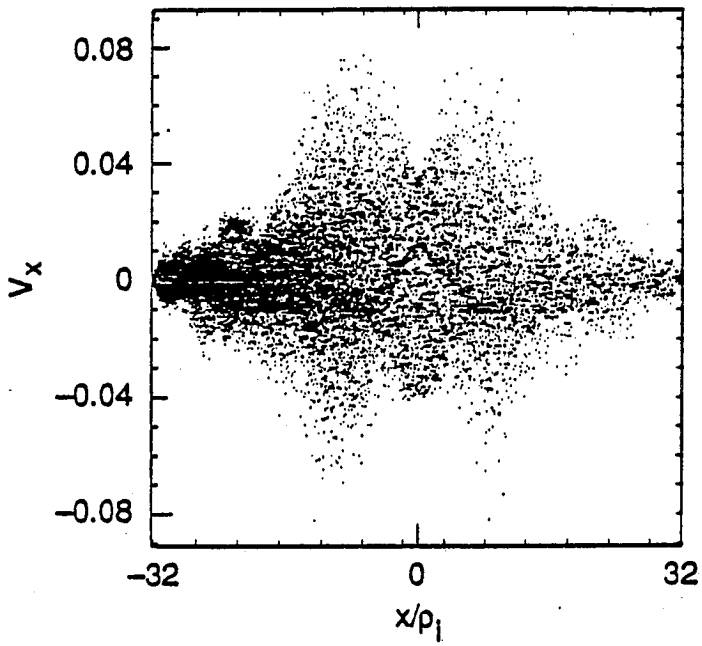

Figure 4.35: Electron phase space(v_x, x) plot at the linear phase $t = 60\omega_{ci}^{-1}$.

contour plots and mode structure snapshots taken in the linear and saturation phases. Pictures are taken close to the end of the linear phase ($t = 60, 80\omega_{ci}^{-1}$) ; and for the study of the fully saturated phase, two snapshots are taken at $t = 200\omega_{ci}^{-1}$ and $t = 400\omega_{ci}^{-1}$. Observations are made concerning the mode width of each fluctuation and the relative phase relations. At $t = 60\omega_{ci}^{-1}$, as shown by Fig. 4.36, n_e and n_i satisfy quasi-neutrality, with a broad eigenmode width of $\sim 20\rho_i$, which is comparable to the mode width of B_x since ϕ has a width of $\sim 10\rho_i$. The approximate phase difference at the mode rational surface between ϕ and n_e is $\pi/4$. The phase difference observed between n_e and B_x is nearly $\pi/2$. Snapshots for n_e, ϕ, and A_z are shown in Fig. 4.37. At the mode rational surface, there is an amplitude decrease within a width which is comparable to the width of ϕ in the electron density response n_e. Overall , the electron density mode width is comparable to the mode width of A_z. At

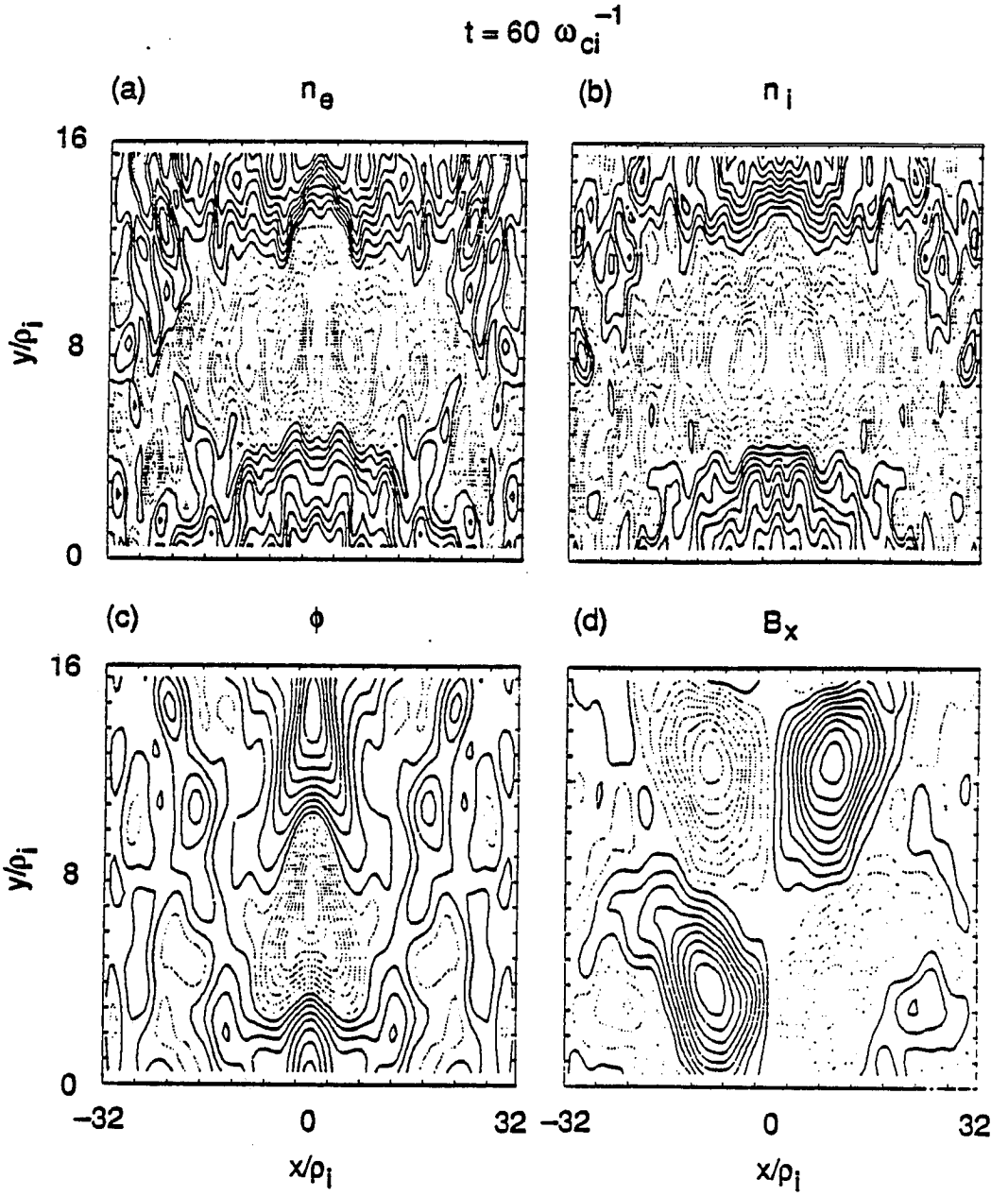

Figure 4.36: Contour plot of n_e, n_i, ϕ, and B_x at $t = 60\omega_{ci}^{-1}$

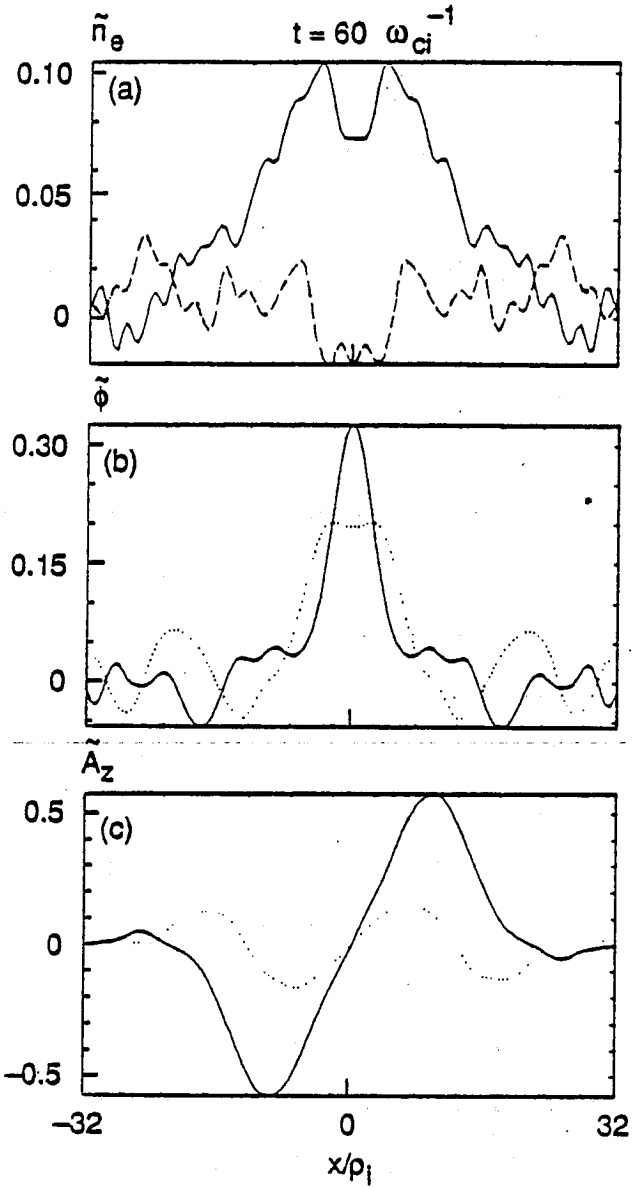

Figure 4.37: Snapshot of n_e, ϕ, and A_z at $t = 60\omega_{ci}^{-1}$

$t = 80\omega_{ci}^{-1}$, which is near the beginning of the saturation stage, as shown by Fig. 4.38, n_e and ϕ have a phase difference of $\sim \pi/8$, while n_e and B_x have a phase difference of $\pi/2$. At the mode rational surface, the electron response is strongly coupled within the spatial mode width of ϕ , and ϕ and n_e have a broader radial response at the mode rational surface. The global electron density mode width is comparable to the width of the magnetic perturbation away from the mode rational surface. In the snapshots of n_e and ϕ ,an electron density hole, whose width corresponds to the mode width of ϕ , is observed (Fig. 4.39). In the saturation phase at $t = 200\omega_{ci}^{-1}$, n_e and ϕ are in phase(Fig. 4.40). B_x and ϕ hold their phase difference at $\pi/2$. Snapshops of ϕ show that ϕ is slightly narrowed at the half width of the mode but is overall less localized (Fig. 4.41). The mode structure of n_e has a broader hole structure, which also matches with the broadened mode structure of ϕ . At $t = 400\omega_{ci}^{-1}$, the saturation level is severely damped and the associated radial mode structure of n_e, and ϕ shows a damped eigenmode structure (Fig. 4.42). At this moment n_e and ϕ are well in phase, and the phase difference of n_e and B_x is $\pi/2$. Snapshots of n_e, ϕ, and A_z also show the wiggly damped eigenmode structure, but the coherent structure of n_e and ϕ at the mode rational surface is still observed (Fig. 4.43). Coherent response between n_e and ϕ is observed both in the linear phase and in the nonlinear saturation stages, as shown by the contour plots of n_e and ϕ and by the radial mode structure snapshots of n_e and ϕ . Also the electron response is coupled strongly with the magnetic perturbation in the region outside the mode rational surface, both in the linear and the nonlinear phases.

As a typical quasilinear behavior resulting from linear instability, density profile flattening is observed. Unlike the collisionless electrosatic case, both in the linear and saturated phases ambipolarity holds between electrons and

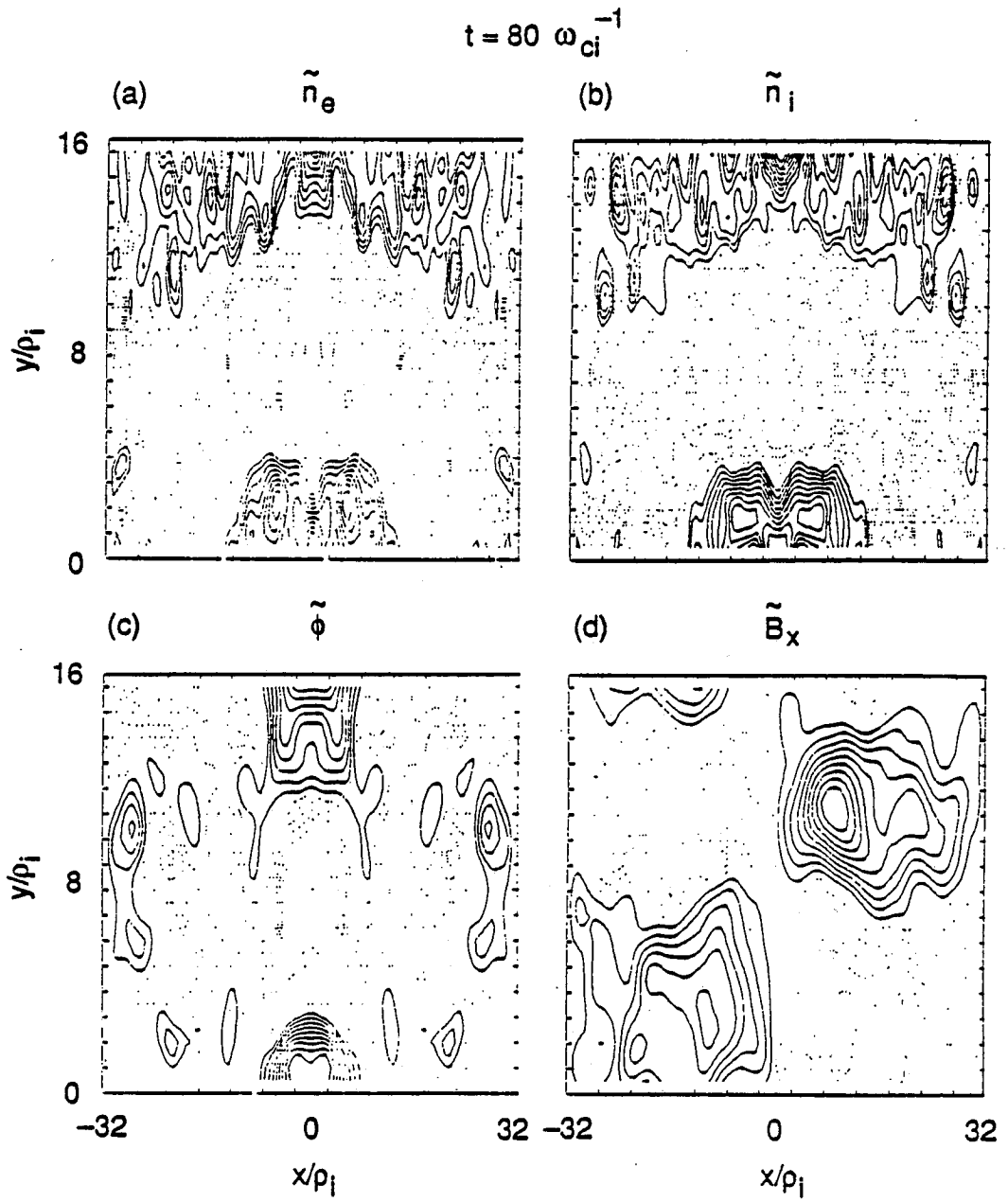

Figure 4.38: Contour plot of n_e, n_i, ϕ, and B_x at $t = 80\omega_{ci}^{-1}$

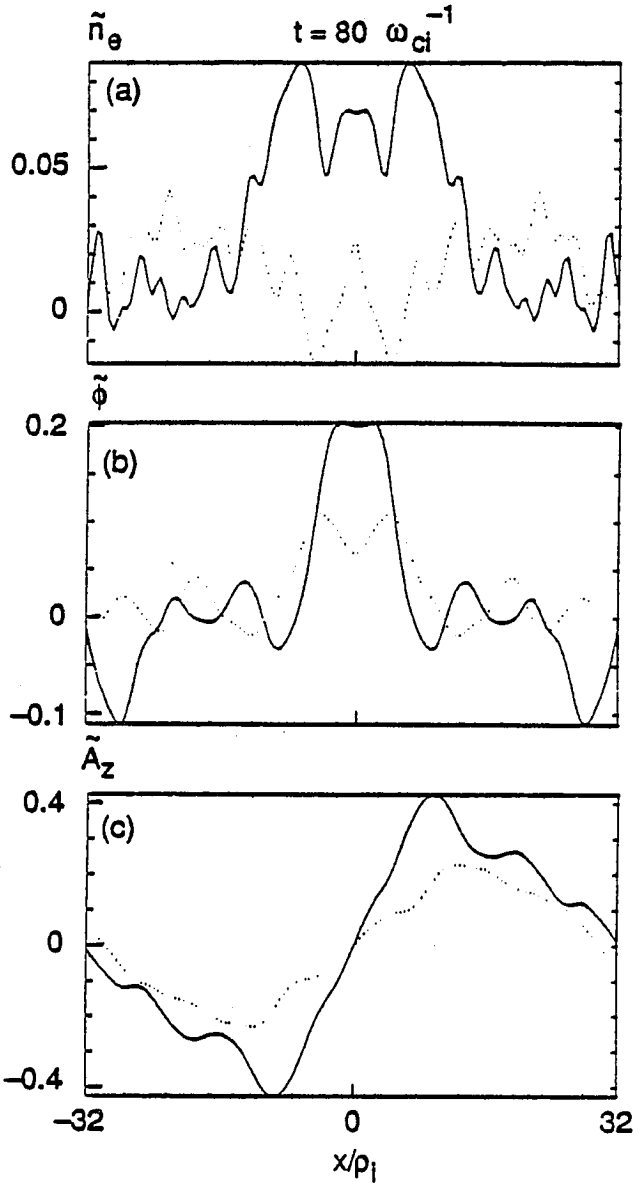

Figure 4.39: Snapshot of n_e, ϕ, and A_z at $t = 80\omega_{ci}^{-1}$

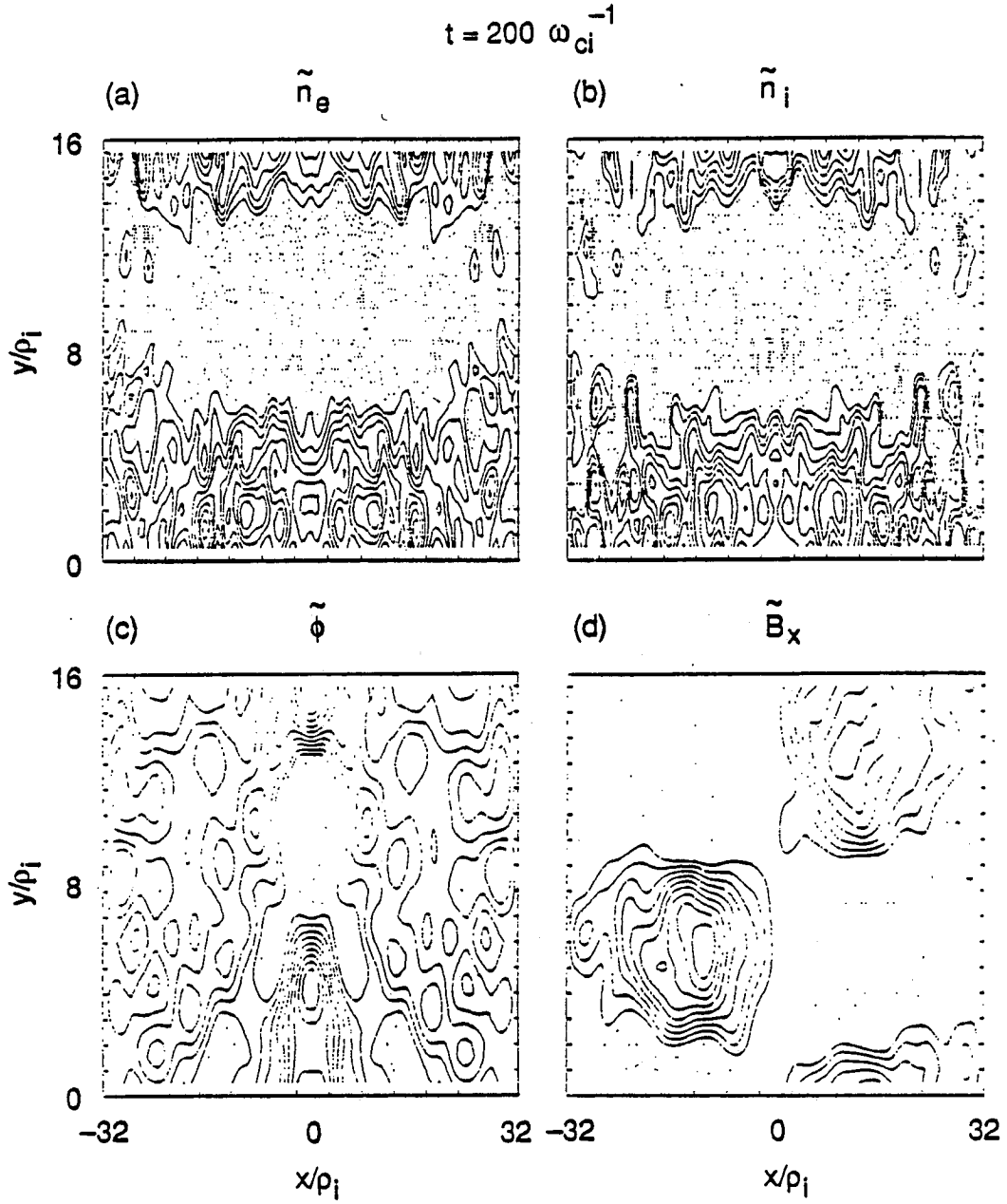

Figure 4.40: Contour plot of n_e, n_i, ϕ, and B_x at $t = 200\omega_{ci}^{-1}$

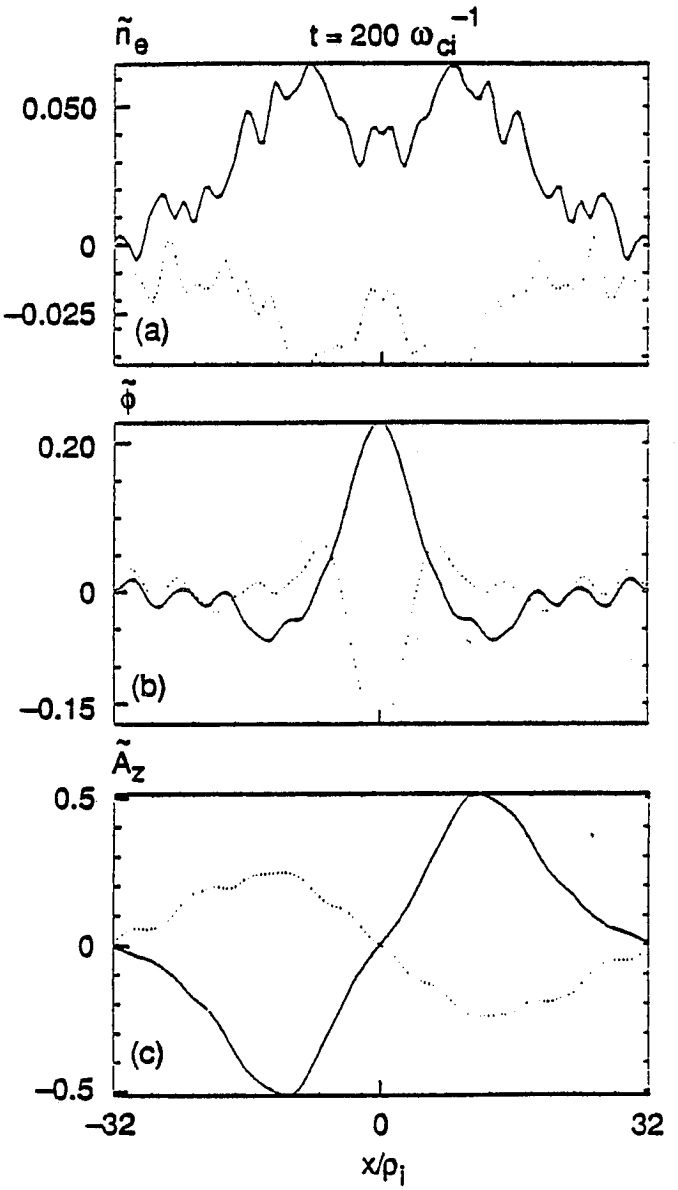

Figure 4.41: Snapshot of n_e, ϕ, and A_z at $t = 200\omega_{ci}^{-1}$

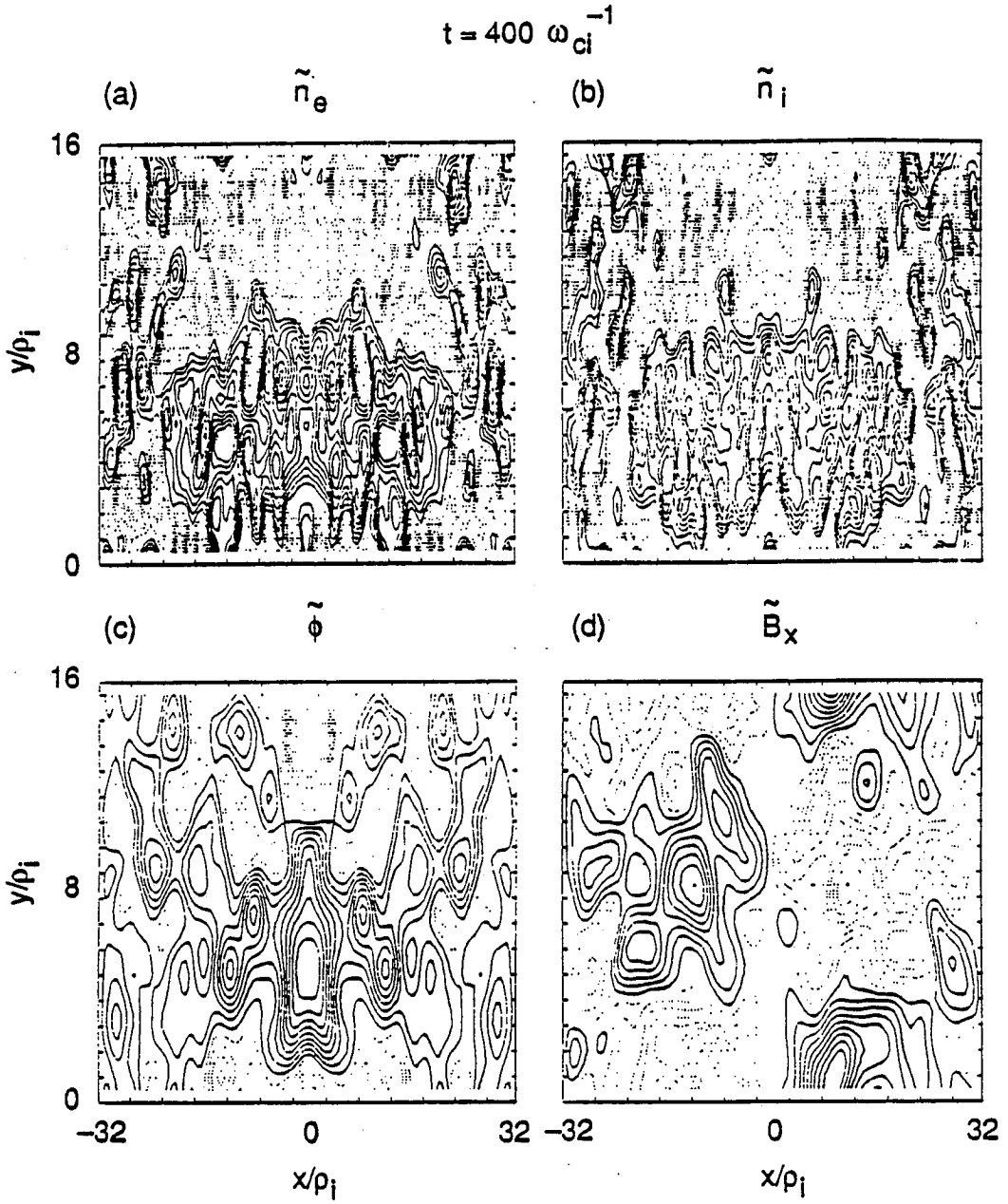

Figure 4.42: Contour plot of n_e, n_i, ϕ, and B_x at $t = 400\omega_{ci}^{-1}$

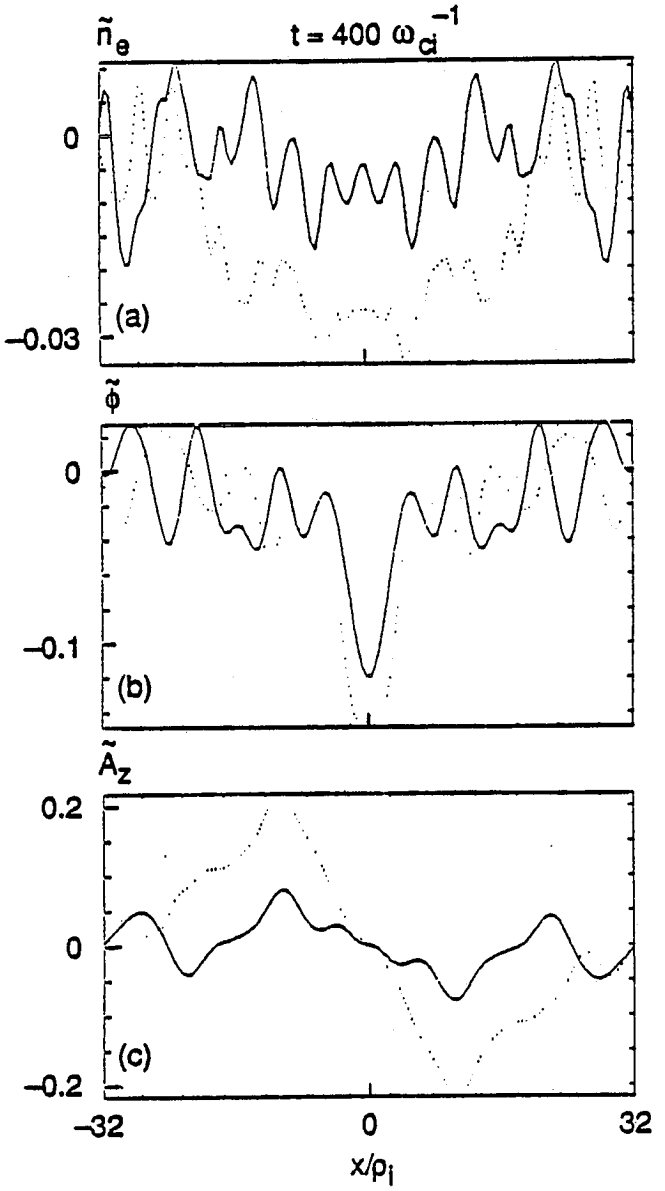

Figure 4.43: Snapshot of n_e, ϕ, and A_z at $t = 400\omega_{ci}^{-1}$

ions as density plateau formation occurs (Figs. 4. 44,45). A parallel electron temperature profile modification associated with an electron velocity distribution deformation near the mode rational surface is observed (Fig. 4.46). A small amount of parallel electron heating occurs on the high density side of the electron density profile($x \sim x_0 - 2\rho_i$). At the saturated phase, the peak of temperature profile diffuses radially inward towards the mode rational surface. The parallel ion temperature profile distortion is negligible both in the linear phase and in the saturated phase(Fig. 4.47).

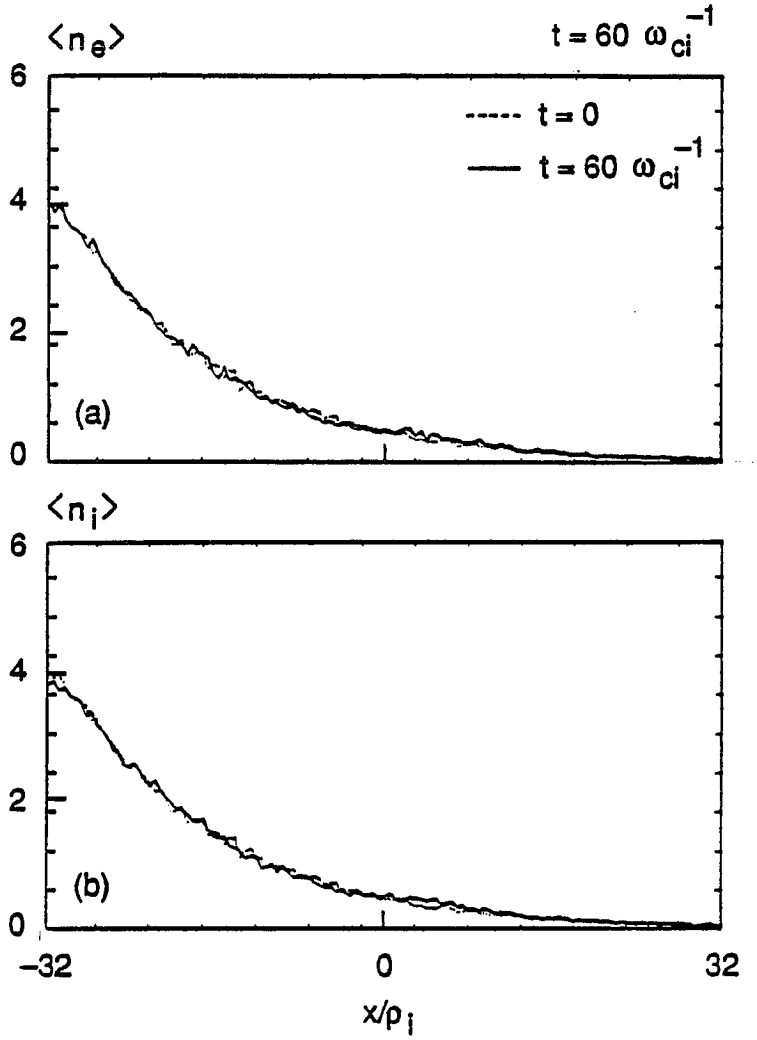

Figure 4.44: Electron and ion density profile relaxation measured at $t = 60\omega_{ci}^{-1}$

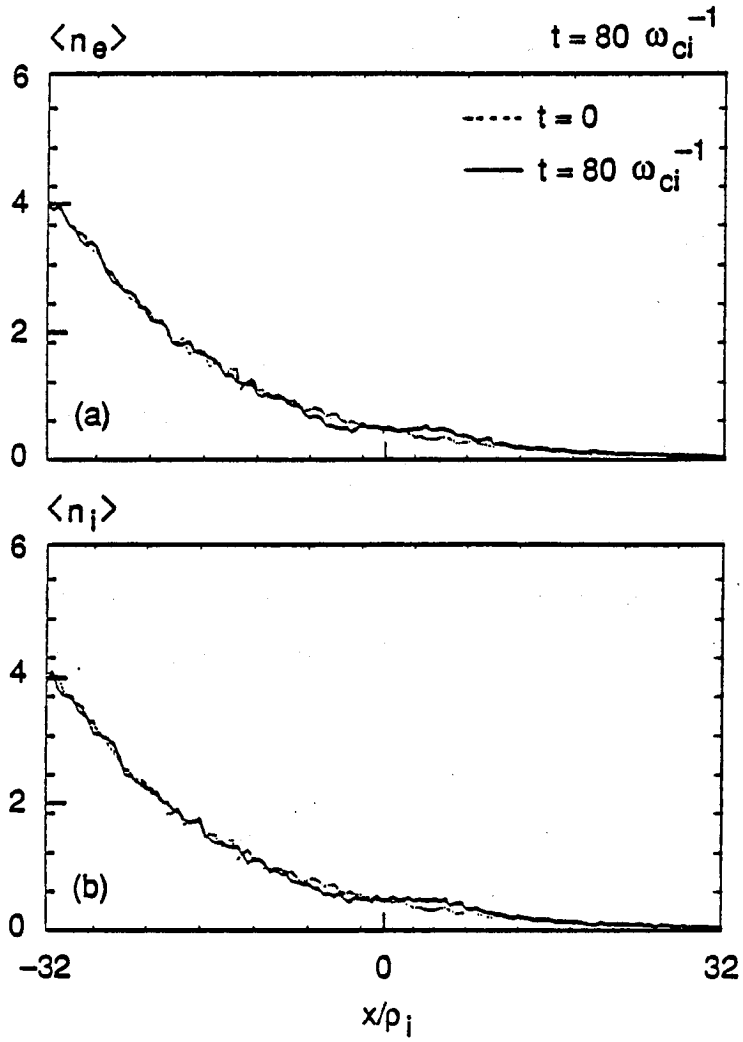

Figure 4.45: Electron and ion density profile relaxation measured at $t = 80\omega_{ci}^{-1}$

4.6 Collisional Electromagnetic Interchange Mode Simulation

4.6.1 Introduction

Simulations of collisional electromagnetic interchange modes are performed in two respects. The first part consists of a scaling study of the relevant physical pictures in the linear and nonlinear stages. In the linear stage, the linear growth rate and linear eigenmode width are measured with respect to variations of the relevant parameters. In the nonlinear stage, measurements of the saturation level for the relevant particle and field quantity fluctuations are made. In the second part, relevant measurements and observations of the dynamical and statistical quantities related to the evolution of the field and particle fluctuations are made. The simulation configuration is the same as for the previous electrostatic and collisionless electromagnetic simulations. As mentioned before in Chapter 3, the collisional slow interchange mode requires extending the grid in the y direction up to four times to accomodate acceptable low m numbers. This already requires extra amounts of particles in the simulation system and, as a result, consumes a comparable amount of computing time for the electrostatic simulation to that required by the collisionless electromagnetic simulations. Thus, for the collisional electromagneticit interchange modes is a formidable task to run the simulation code with the extended grid in the y direction, as was done for the electrostatic interchange modes in Chapter 3.

4.6.2 Scaling studies in linear and nonlinear phases

Scaling studies are carried out for the most interesting parameters, which are the electron-ion collision frequency. ν_{ei} and β_i , as mentioned ear-

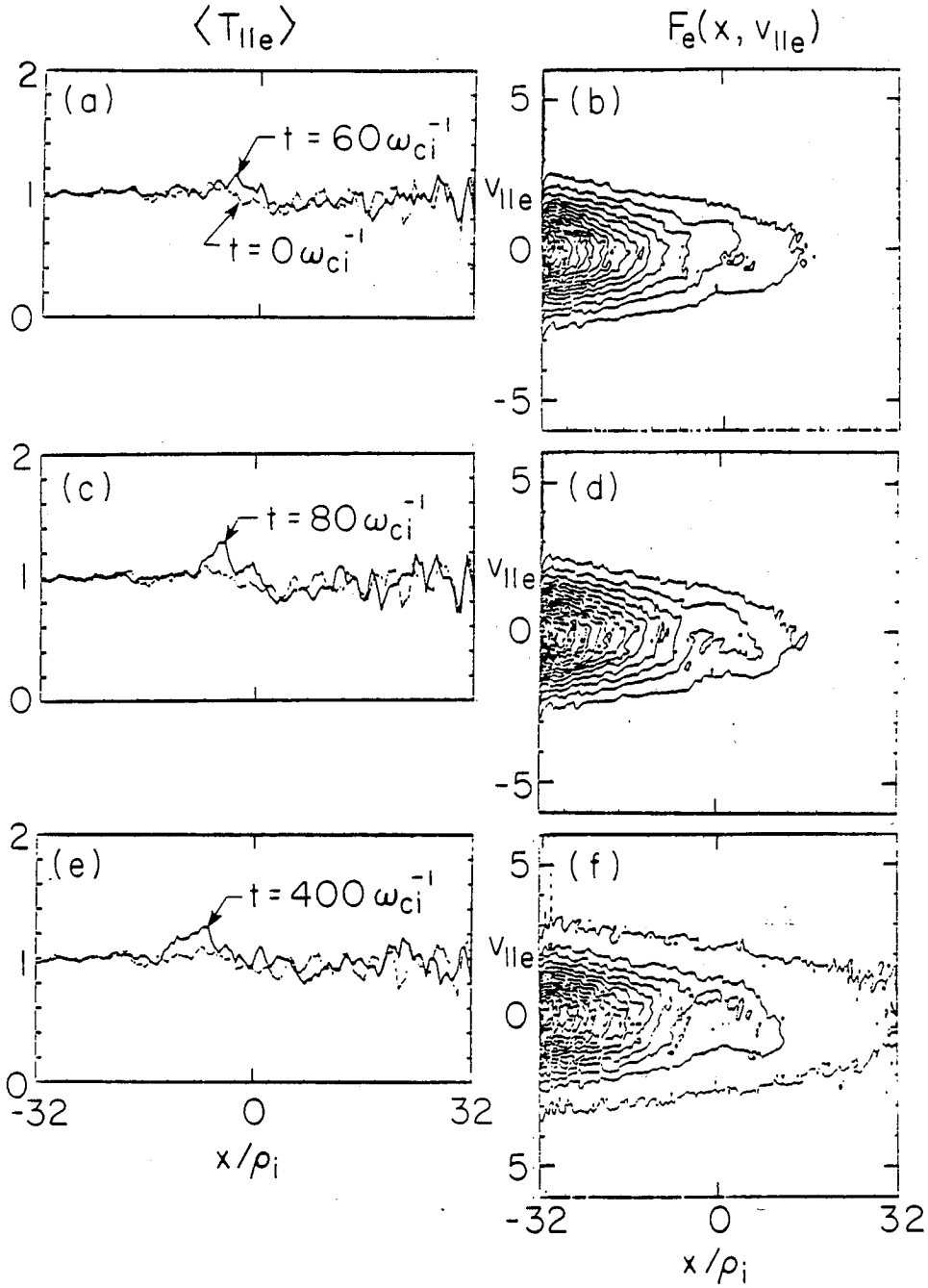

Figure 4.46: Parallel electron temperature profile and parallel electron velocity distribution contour in $(x, v_{||})$ phase space measured at $t = 60, 80, 400\omega_{ci}^{-1}$

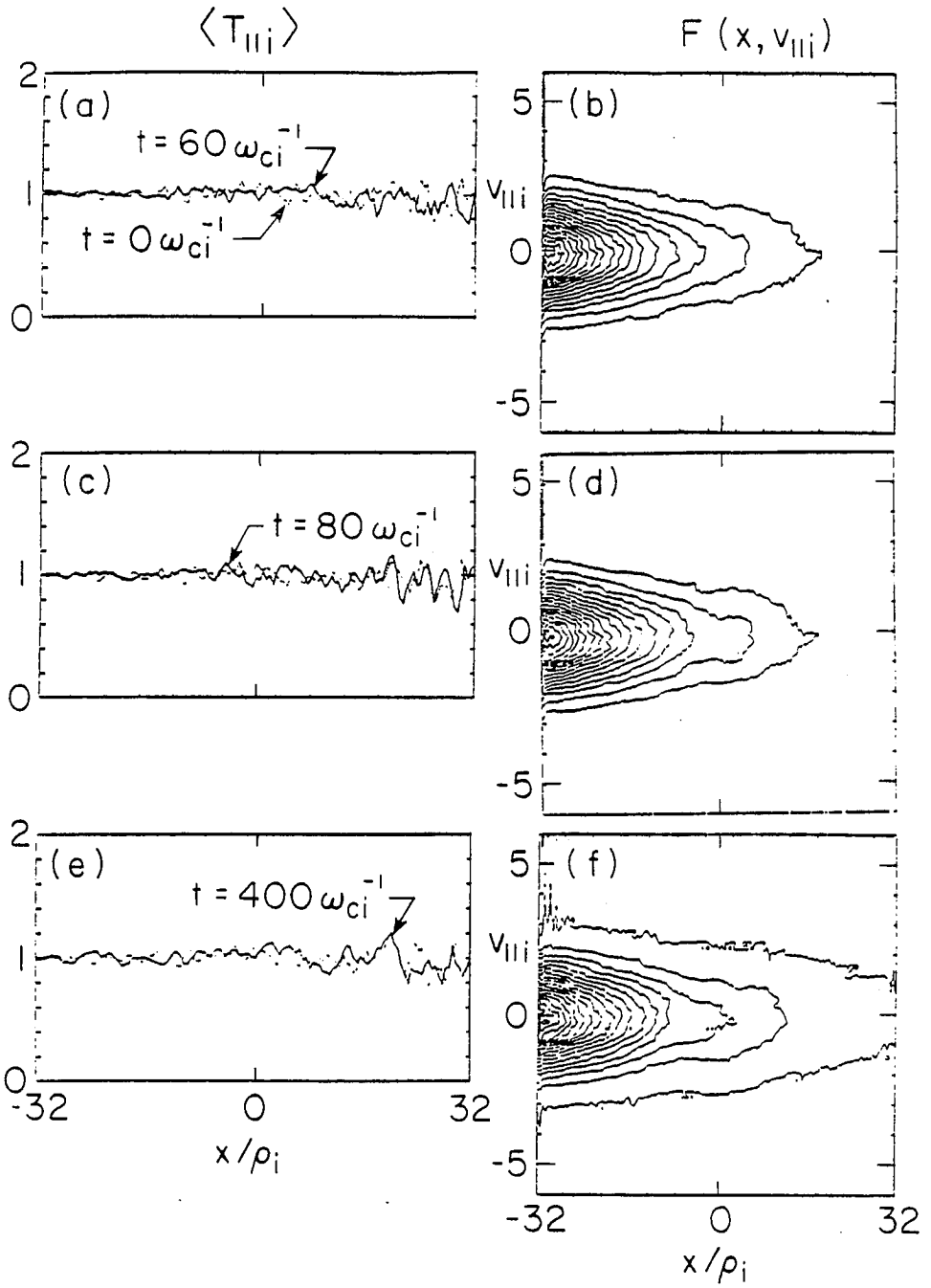

Figure 4.47: Parallel ion temperature profile and parallel ion velocity distribution contour in $(x, v_{||})$ phase space measured at $t = 60, 80, 400\omega_{ci}^{-1}$

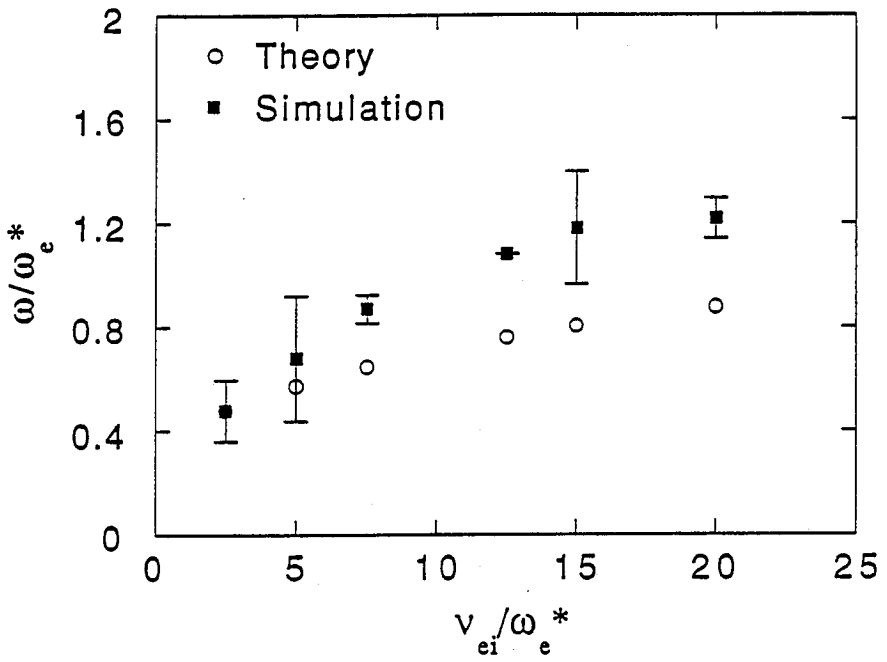

Figure 4.48: Growth rate comparison of ϕ (m=1) eigenmode with linear kinetic theory.

lier in Section 4.4. Measurements of the relevant quantities are carried out in the linear and nonlinear phases with respect to the parameter ν_{ei} . As a first step, the linear growth rates measured from the m=1 ϕ mode in the simulation are compared to linear theory with respect to ν_{ei} variations (Fig. 4.48). There is resonable agreement between simulation and theory. The linear eigenmodes of ϕ and $A_{||}$ are also compared and show good agreement in terms of mode width and mode structure (Fig. 4.49). The parameters used in this calculation are m_e/m_i =400, L_s/L_n =14, T_e/T_i =1, ρ_i=2.5, L_n/L_c=0.26, $\omega_{ci} = 0.02$, $k_y\rho_i$=0.245m, ω_e^*=4.295 $\times 10^{-4}\omega_{pe}^m$, β_i=3.08 $\times 10^{-3}$, the system size is $L_x \times L_y = 128\Delta \times 32\Delta$, $a_x = a_y = 1.5\Delta$ and ν_{ei} varies from 2.5 to 20 ω_e^* . The total run time is $n\Delta t = 4000 \times 10\ \omega_{pe}^{-1} = 800\ \omega_{ci}^{-1}$.

In the nonlinear stage, the ϕ and B_r fluctuation levels are measured as ν_{ei} is varied. As ν_{ei} increases, the ϕ fluctuation level and the B_r fluctuation

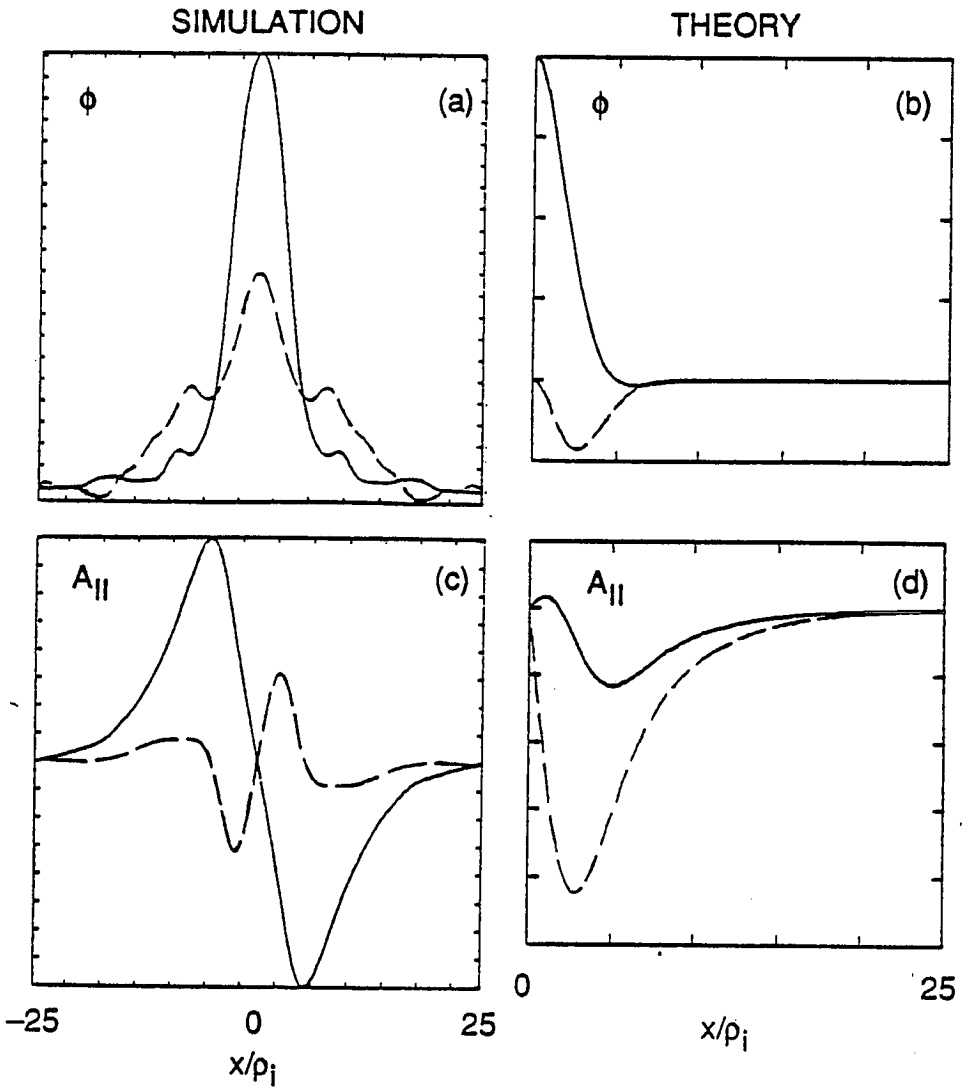

Figure 4.49: Eigenmode structure of ϕ and $A_{||}$ Parameters used are τ=1, m_e/m_i =1/400, β_i=3.08 $\times$ 10^{-3}, L_n/L_c=0.26, ν_{ei}=12.5 ω_e^* , and $k_y\rho_i$=0.245.

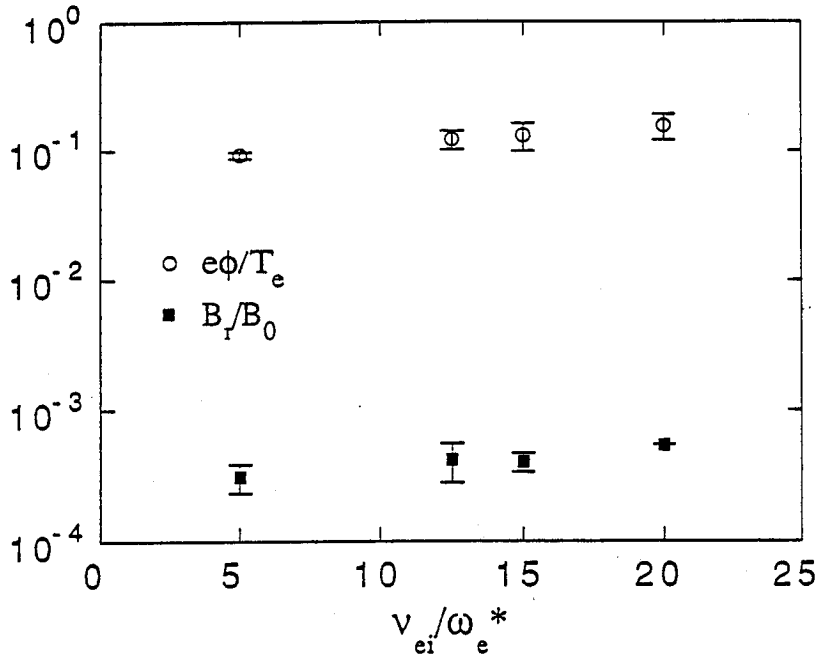

Figure 4.50: ϕ saturation level and B_r saturation level measurements for ν_{ei}=5, 12.5, 15, 20 ω_e^* .

level also increase with a similar trend (Fig. 4.50). Also, the ϕ saturation levels are compared with the mixing length estimate, which in this case is an upper bound(Fig. 4.51). Both measurement and estimate are showing a similar trend.

After passing the linear stage and nearing saturation, modification of the quasilinear density profile and parallel ion temperature profile are also observed. For both electrons and ions, ambipolarity holds during density gradient profile flattening at the mode rational surface. The density gradient flattening size is comparable to the eigenmode width. As the collisionality ν_{ei} is increased, the amount of flattening is also increased for both electrons and ions. A parallel ion temperature profile modification associated with density profile flattening is observed (Fig. 4.52), although there is a no change in the parallel electron temperature profile (Fig. 4.53). newpage The parallel ion temperature profile

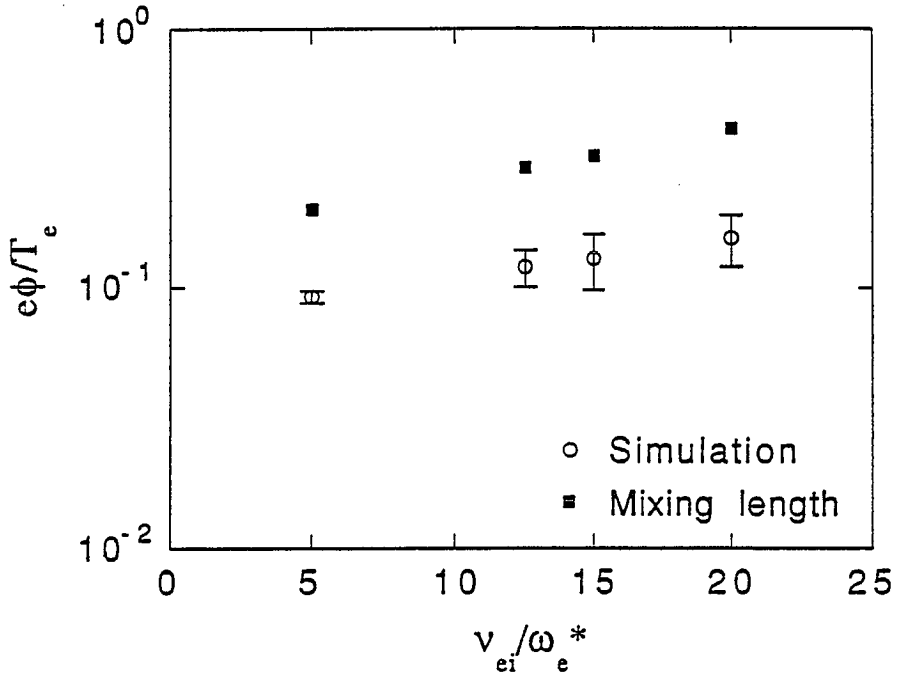

Figure 4.51: ϕ saturation level comparison with the mixing length theory estimation.

modification occurs only when collision frequencies are such as to be in the strongly collisional regime. At $t = 800\omega_{ci}^{-1}$, with β_i=3.08 $\times$ 10^{-3}, significant parallel ion temperature heating occurs on the high density side of the ion density profile for ν_{ei}=15 and 20 ω_e^* , whereas there are minimal temperature profile changes for the ν_{ei}=5 ω_e^* case (Fig. 4.52). Figure 4.52 as well as other simulations carried out with ν_{ei}=12.5, 30ω_e^* with the same simulation parameters, which are used in the simulations of Fig. 4.52 except for ν_{ei} , show that the extent of the temperature profile modification is proportional to ν_{ei} .

Since the parallel temperature profile modification is only observed in collisional finite β plasmas and since the amount of profile modification is proportional to ν_{ei} , it is a logical step to check the relation between temperature profile modification and β_i when the collision frequency ν_{ei} is fixed. As an initial survey, simulations are carried out with fixed ν_{ei}=20ω_e^* for β_i=3.08 $\times$

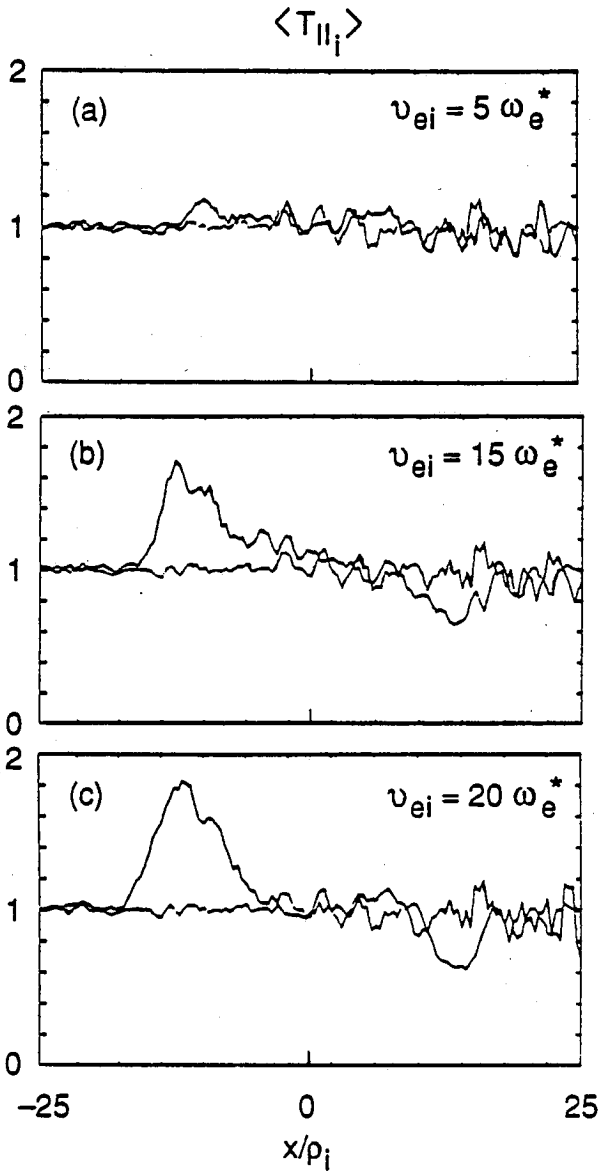

Figure 4.52: Parallel ion temperature profile modifications observed for the case of ν_{ei}=5, 15, 20 ω_e^* with β_i=3.08×10^{-3}.

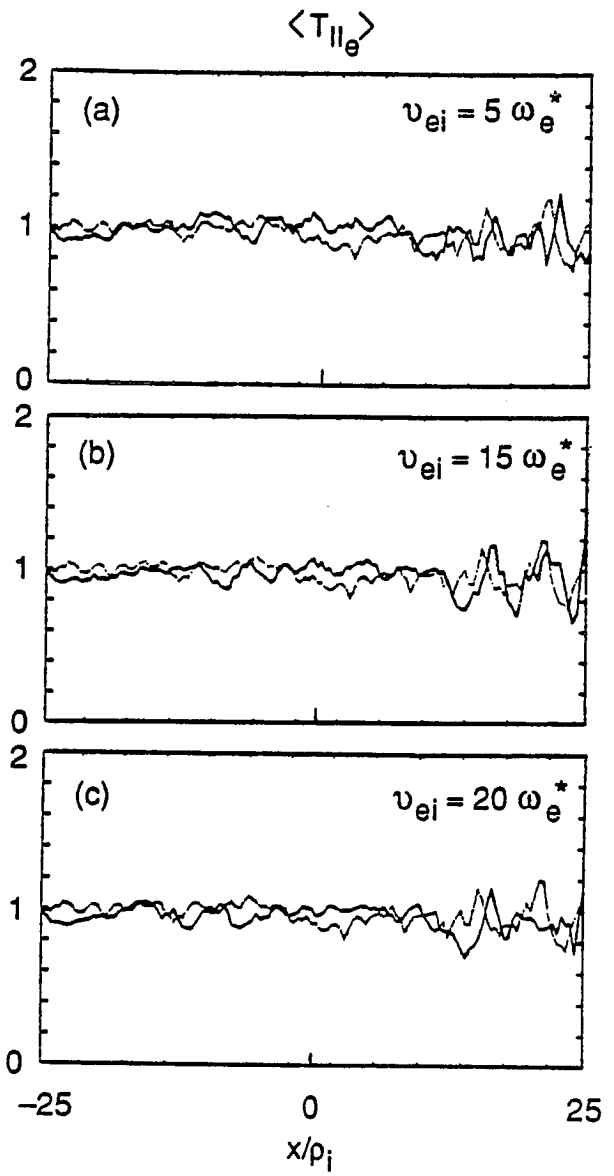

Figure 4.53: Parallel electron temperature profile with the same parmeters of Fig. 4.52.

10^{-5}, which is almost the electrostatic limit and for β_i=3.08 $\times$ 10^{-3}. The first noticeable difference between the finite beta plasma and its electrostatic limit is the fluctuation level of the electrostatic field and the perturbed magnetic fields (Fig. 4.54).

Also in the finite beta plasma case, a noticeable amount of damping occurs after the peak saturation phase in the electrostatic field energy fluctuations, whereas only a small amount of damping is observed in the electrostatic limit (Fig. 4.54). At the final saturation(or damping) stage ($t = 800\omega_{ci}^{-1}$) of the finite β case, density gradient flattening is quite severe compared to the electrostatic case (Fig. 4.56). In both cases ambipolarity holds between electrons and ions. There is a slight distortion of the parallel electron temperature profile while the parallel ion temperature profile is not affected in the electrostatic limit. In the finite beta case the trend is reversed. Although the parallel electron temperature profile changes little, the parallel ion temperature profile is severely modified (Fig. 4.57).

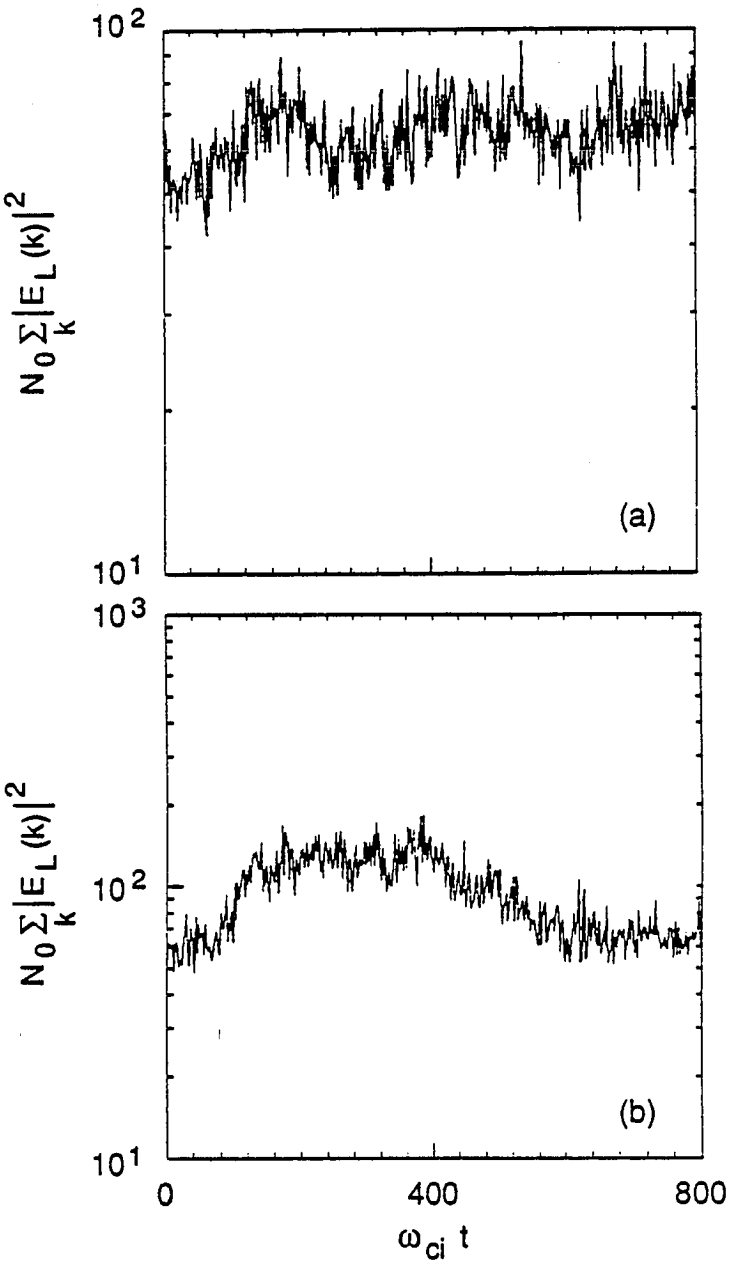

Figure 4.54: Electrostatic field energy fluctuation levels for β_i=3.08 $\times 10^{-5}$ and for β_i=3.08 $\times 10^{-3}$. N_o is total number of particles in the simulation system.

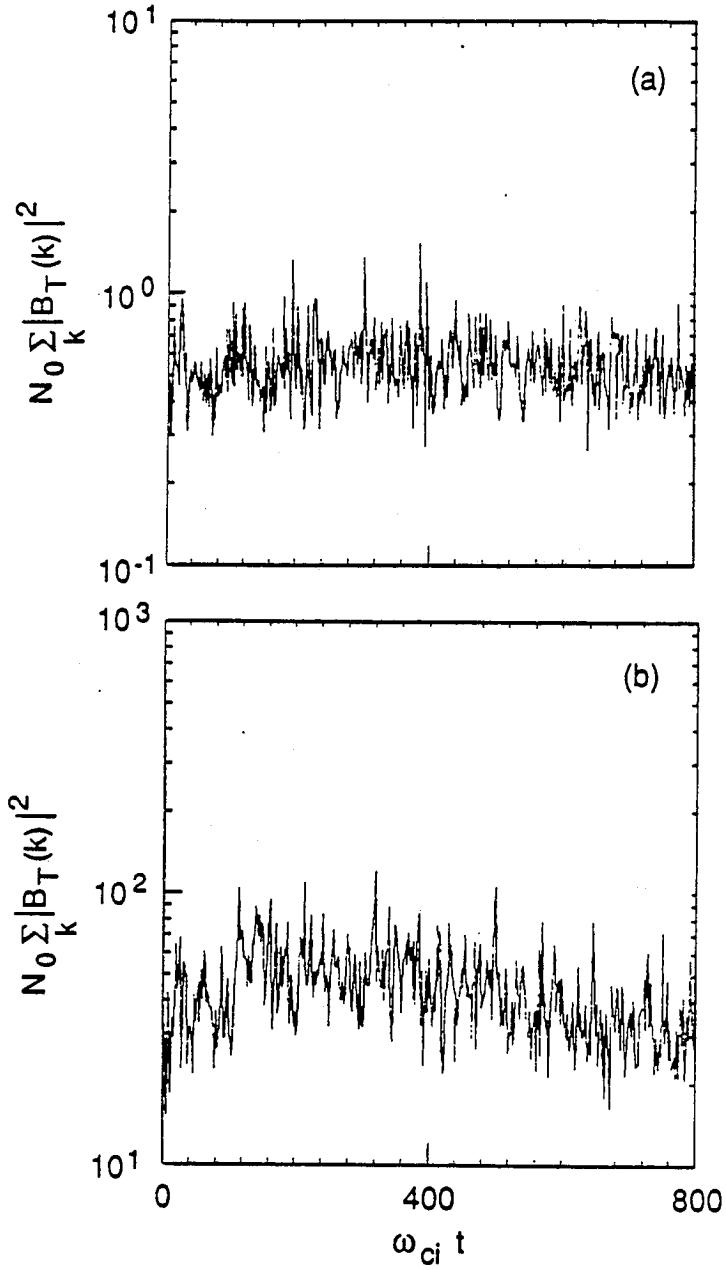

Figure 4.55: Magnetic field energy fluctuation levels for β_i=3.08 $\times 10^{-5}$ and for β_i=3.08 $\times 10^{-3}$. N_o is total number of particles in the simulation system.

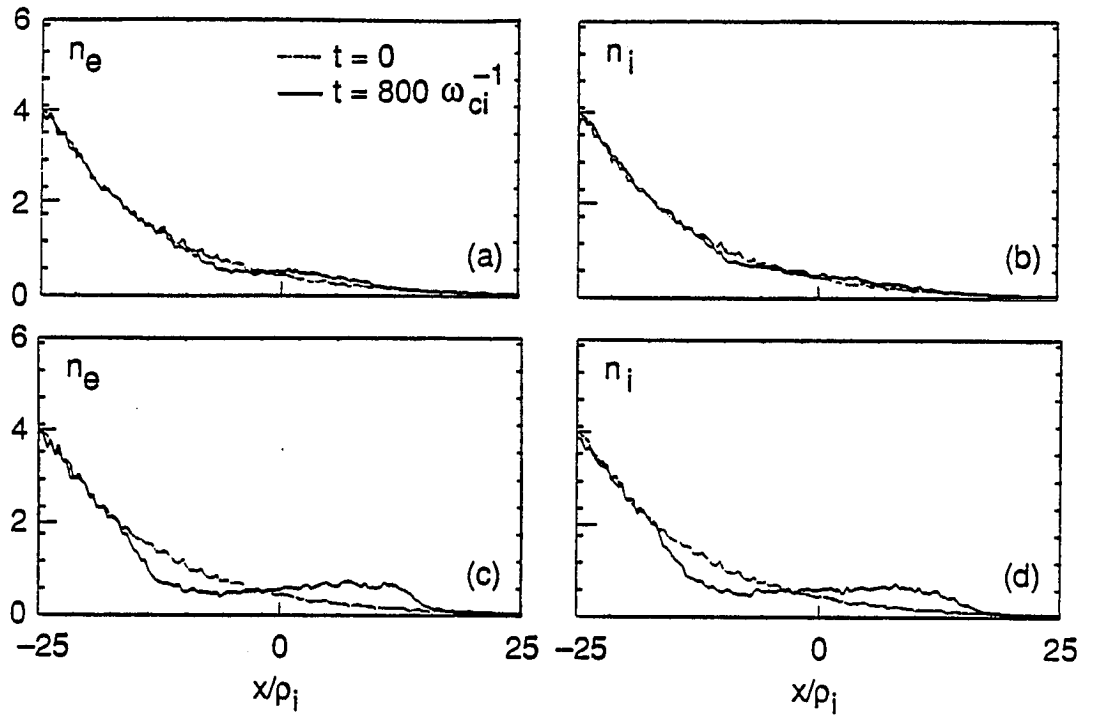

Figure 4.56: Electron and ion density gradient flattening observed for the case of β_i=3.08 $\times$ 10^{-5} and for β_i=3.08 $\times$ 10^{-3}.

To understand the parallel ion temperature profile modification caused by the two parameters β_i and ν_{ei} , a set of simulations are performed by varying β_i with fixed ν_{ei}=30 ω_e^* , which boosts the instability even more. The selected β_i values are 0.001, 0.0025, and 0.003 , which correspond to below the mass ratio, at the mass ratio, and above the mass ratio. The rest of the simulation parameters are the same as for the previous cases. As an initial survey, the saturated fluctuation levels of ϕ, n_e, and B_r are measured (Fig. 4.58). The saturation levels of all three quantities increase as β_i increases. In particular, there is a noticeable amount of increase, which is close to an order of magnitude, in the magnetic fluctuation level. For the ϕ fluctuation level, a simple mixing length estimate is made to check the tendency of the fluctuations to increase with β_i (Fig. 4.59). The mixing length estimate has a flat response to β_i , since the linear growth rate and linear mode width have no dependence on β_i according to the linear eigenmode analysis calculations (Sec. 4.4). The parallel ion temperature profile modification due to β_i shows that there exists no direct proportionality between $T_{||}$ and β_i . The amount of parallel ion heating reaches its maximum at β_i=0.0025 (Fig. 4.60).

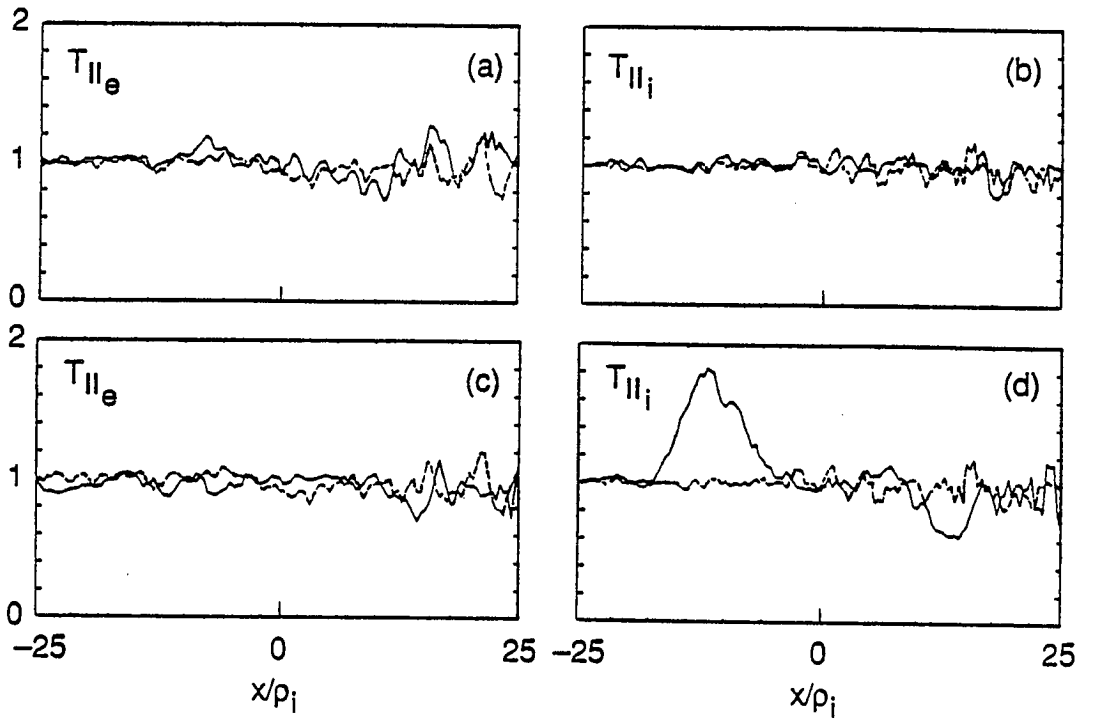

Figure 4.57: Parallel electron and ion temperature profile at $t = 800\omega_{ci}^{-1}$ for the case of β_i=3.08 $\times$ 10^{-5} and for β_i=3.08 $\times$ 10^{-3}.

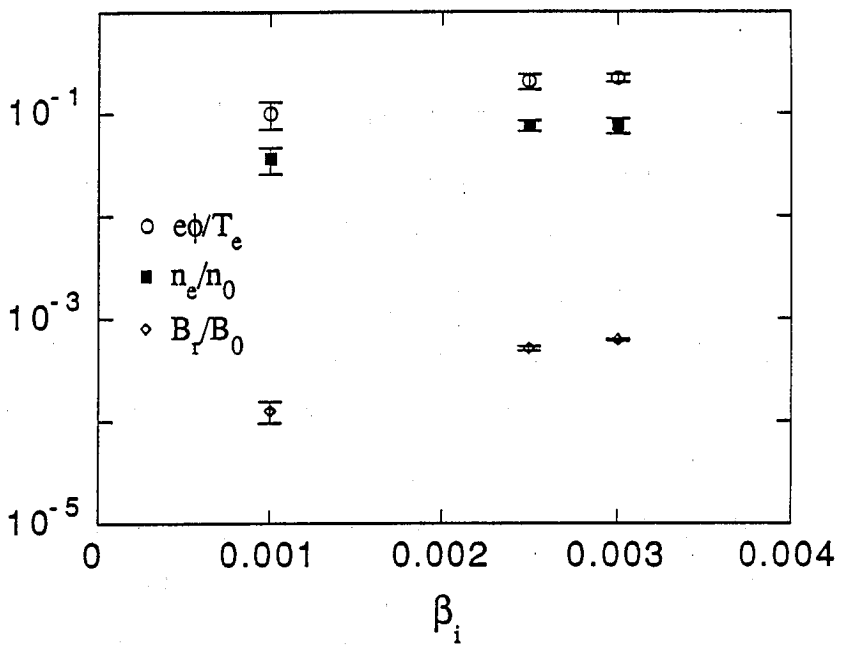

Figure 4.58: ϕ, n_e, and B_r saturation level for β_i=0.001, 0.0025, 0.003 .

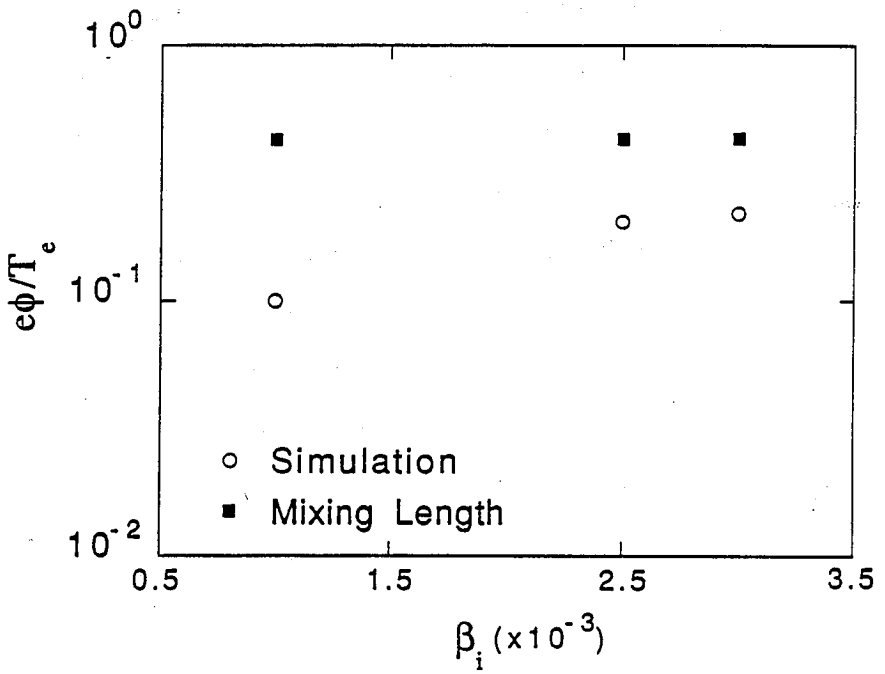

Figure 4.59: ϕ saturation level compared with mixing length estimation for β_i=0.001, 0.0025, 0.003.

4.6.3 Time evolution of the collisional electromagnetic interchange mode

To have a glimpse of the dynamical picture for the finite beta collisional interchange mode and resulting physical phenomena, elaborate diagnostic procedures are performed at the spot of interest in the time evolution of field and particle quantity fluctuations. The spots of interest are chosen from the time evolution of the ϕ energy plot (Fig. 4.61). Parameters used in this run are β_i=0.003 and ν_{ei}=30 ω_e^* . The time evolution of the electrostatic potential energy is separated into four stages : linear phase, saturated phase, damping stage, and final damped stage. Four spots in the same time sequence, which correspond to the linear phase ($t = 80\omega_{ci}^{-1}$), saturated phase ($t = 240\omega_{ci}^{-1}$), damping stage($t = 440\omega_{ci}^{-1}$), and final damped stage($t = 800\omega_{ci}^{-1}$), are selected. At each spot, the density profiles, parallel temperature profiles, and parallel velocity distribution functions for the electrons and ions are monitored. Also, snapshots of the radial mode structure of the n_e, n_i, ϕ , and B_x perturbations are taken to measure the phase and the size of the perturbation around the mode rational surface, which corresponds to the approximate eigenmode width. The time evolution of the density profile relaxation is shown in Fig. 4.62. At the saturated stage, a quasilinear plateau is established and continues to diffuse radially till the final damped stage is reached. Ambipolarity holds between electrons and ions throughout the time evolution of the density profile. The time evolution plots of the parallel ion temperature profile show that the parallel ion temperature profile modifications are associated with the quasilinear density profile relaxations (Fig. 4.63).

At the saturated phase, $t = 240\omega_{ci}^{-1}$, a noticeable amount of temperature profile modification is observed along with density plateau formation. In

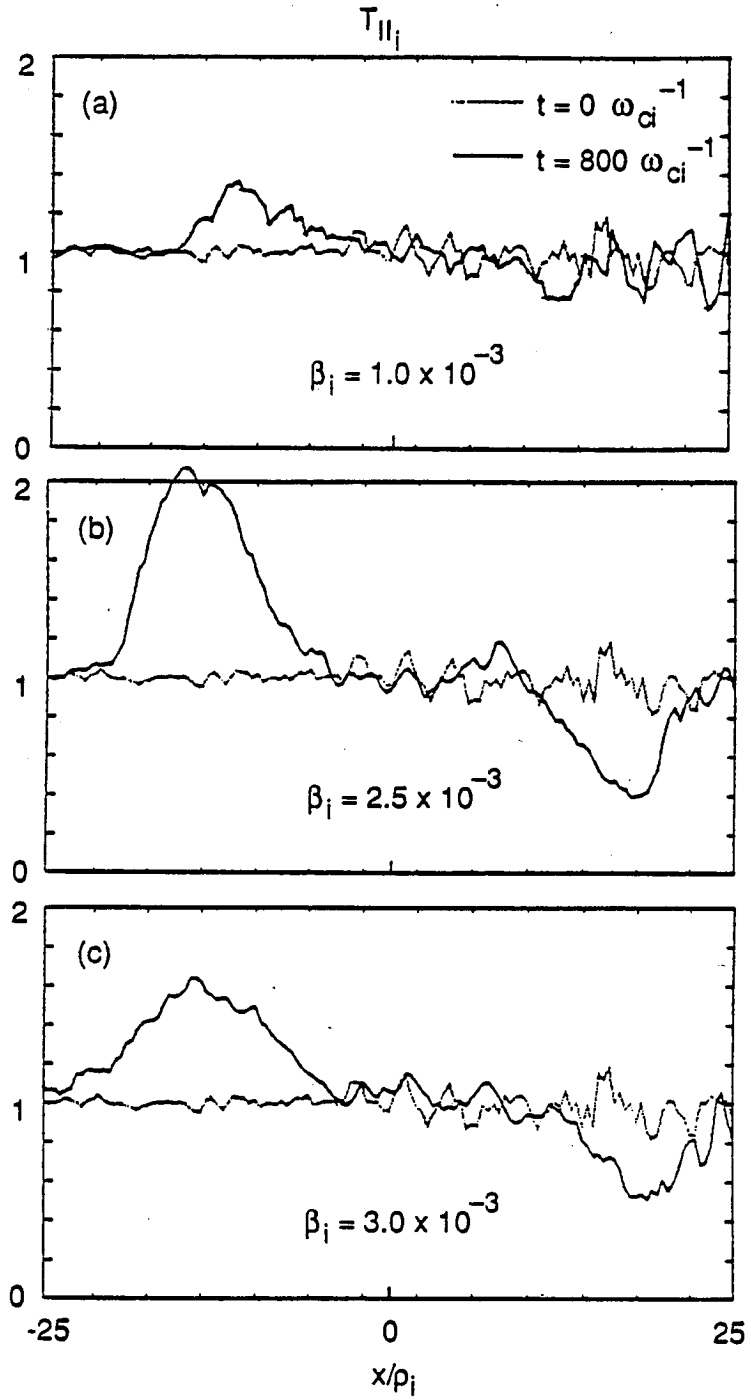

Figure 4.60: $T_{||i}$ profile for the case of β_i=0.001, 0.0025, 0.003 .

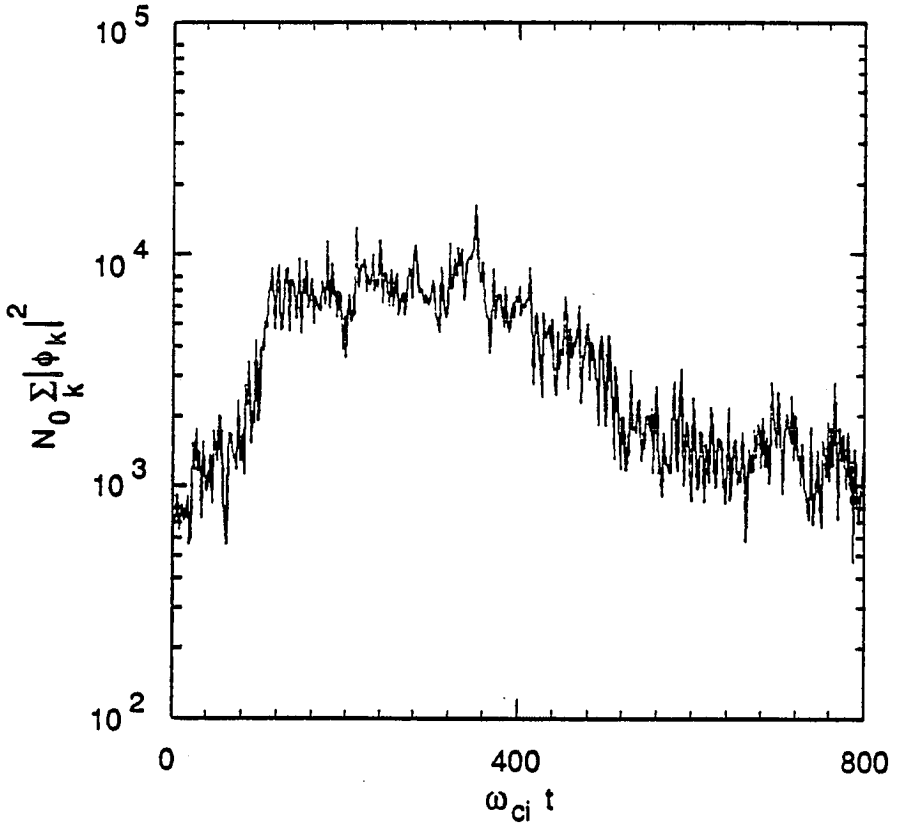

Figure 4.61: Time evolution of electrostatic potential energy with parameters β_i=0.003 and ν_{ei}=30 ω_e^* .

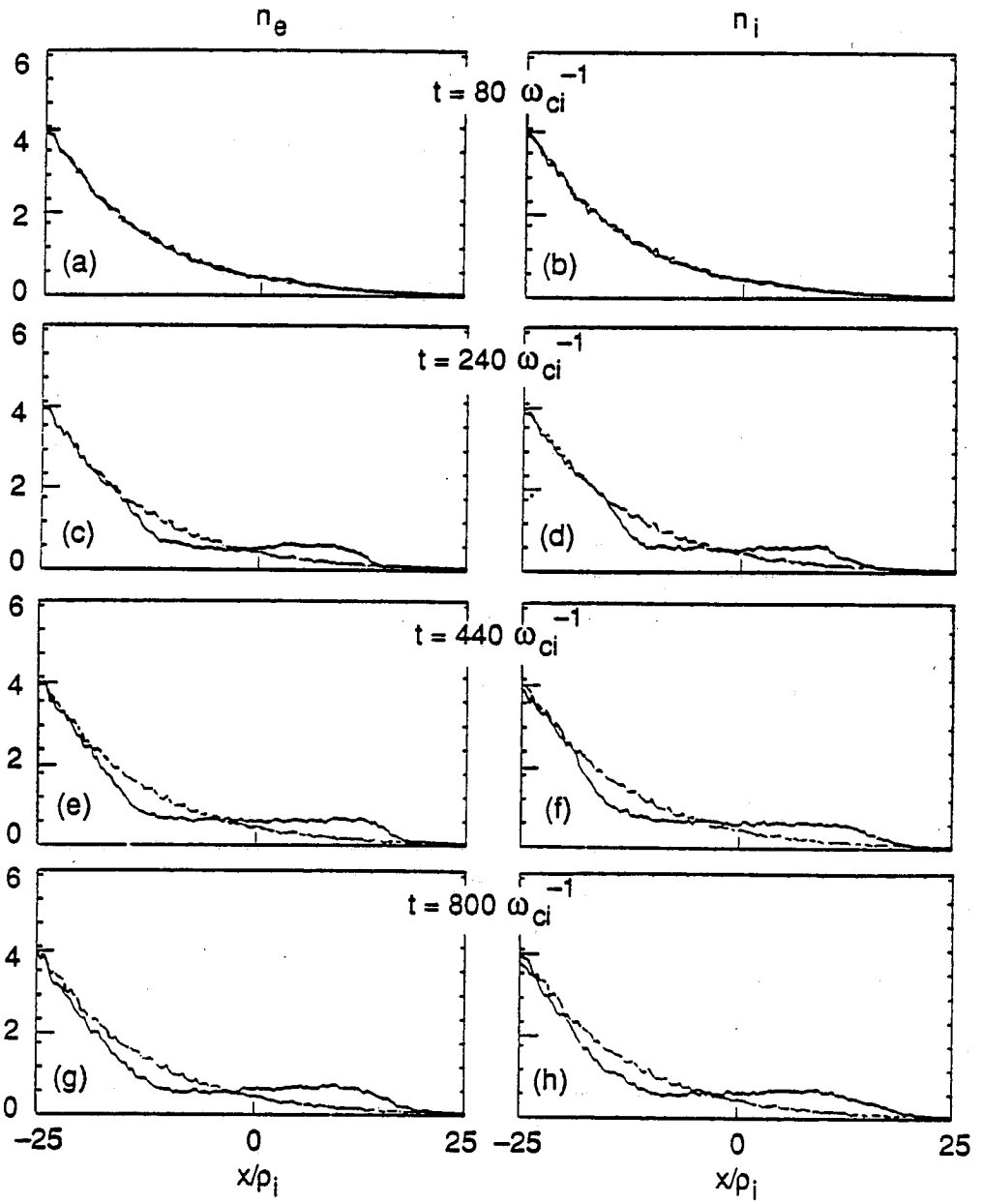

Figure 4.62: Time evolution of electron and ion density profile observed at $t = 80, 240, 440, 800\omega_{ci}^{-1}$.

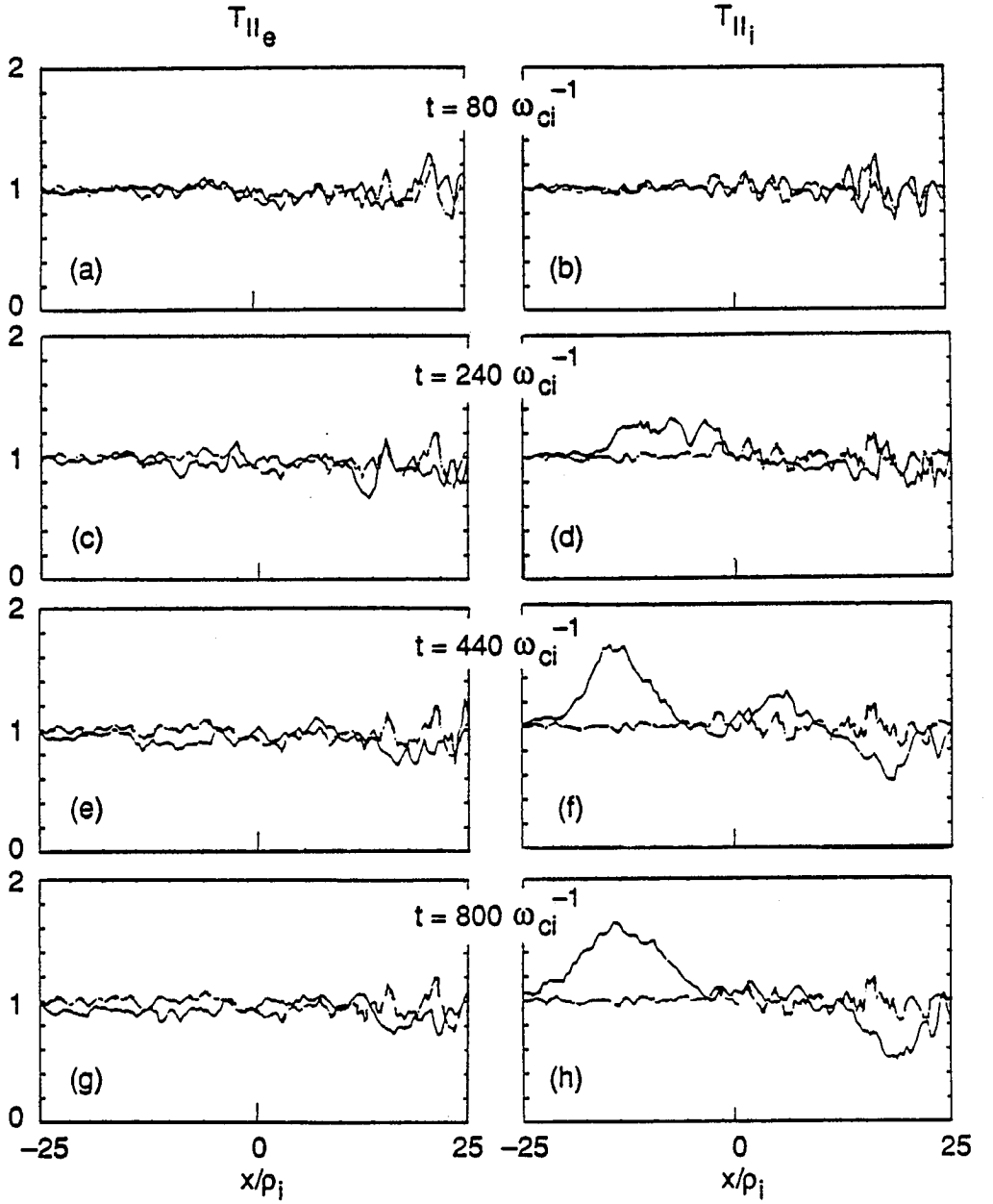

Figure 4.63: Time evolution of parallel electron and ion temperature profiles observed at $t = 80, 240, 440, 800\omega_{ci}^{-1}$.

the area located on the dense part of the electron profile, which has an approximate radial extent of $10\rho_i$, a noticeable amount of ion heating is observed. In the middle of the damping stage($t = 240\omega_{ci}^{-1}$), the amount increases and peaks at $x \sim 10\rho_i$, away from the mode rational surface located at $x = x_0$. At the final damped stage, the peaked temperature profile is slightly broadened radially. No significant profile modification is observed for the parallel electron temperature. Parallel ion Maxwellian velocity deformations associated with temperature profile modifications are compared with the parallel electron Maxwellian in Fig. 4.64. Whereas the electron velocity distribution has only a modification due to quasilinear density profile relaxation, the ion thermal velocity distribution is severely distorted. Three dimensional plots of parallel electron and ion velocity distibutions are also shown in Fig.4.65. Clear deformation of the parallel ion velocity distribution is observed at the place where ion heating has occured.

As a next step for the study of the dynamical picture of the collisional electromagnetic interchange mode, snapshots of the spatial structure of n_e, n_i, ϕ, and B_x are taken at each time spot described before. At the linear stage($t = 80\omega_{ci}^{-1}$), there are clear phase differences, among n_e, ϕ, and B_x, which drive instability (Fig. 4.66). Electron and ion density fluctuations have a broader response than the potential fluctuations. The size of the density fluctuations at the mode rational surface is comparable to the size of the potential fluctuations. In the region away from the mode rational surface, density fluctuations come under the influence of the magnetic fluctuation B_x, which has a wider eigenmode structure than the potential fluctuation ϕ. At the saturated phase($t = 240\omega_{ci}^{-1}$), the electrostatic potential response becomes broadened at the mode rational surface. We observe a close correlation between the density responses n_e and n_i and the magnetic fluctuation B_x by comparing the fluctuation widths and their contour shapes at the mode rational surface(Fig. 4.67).

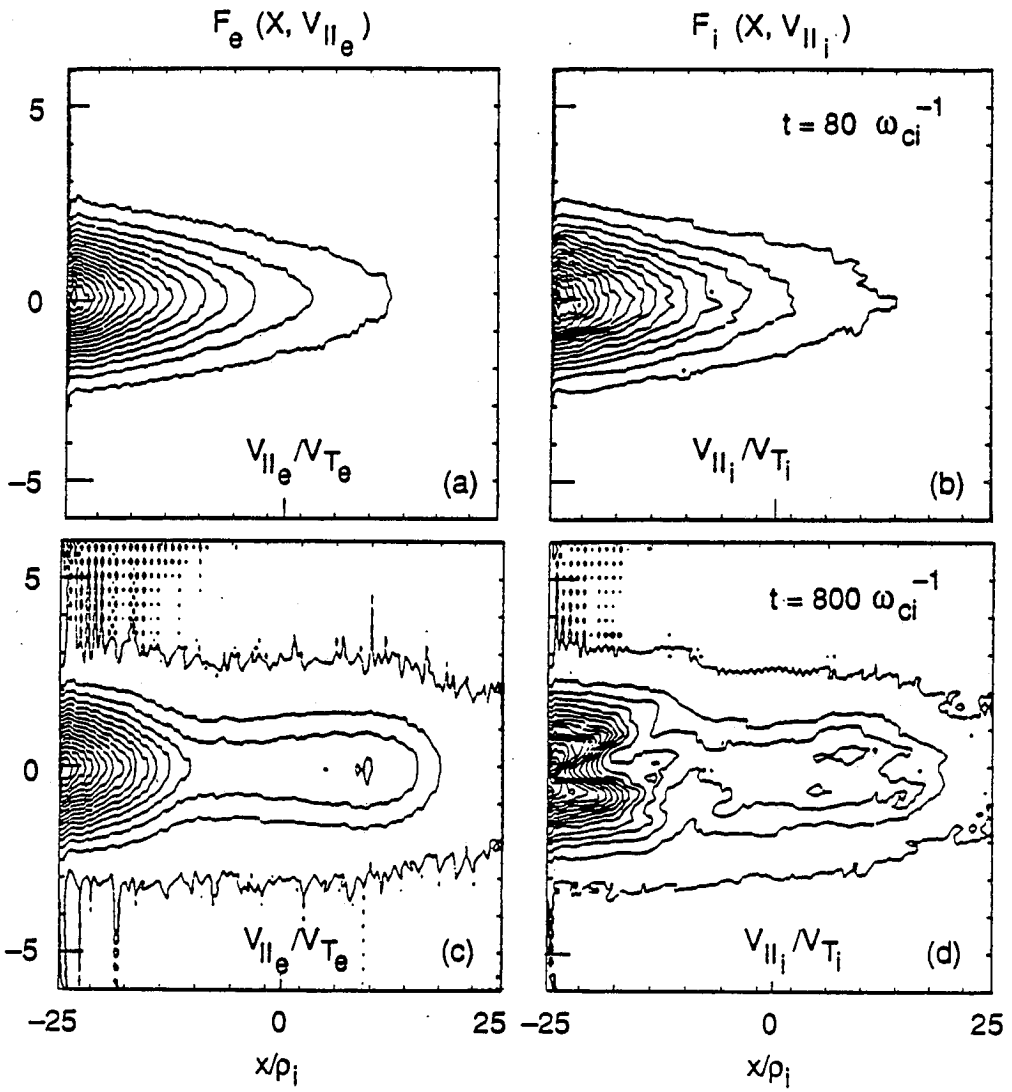

Figure 4.64: Parallel electron and ion velocity distributions, observed at $t = 80, 800\omega_{ci}^{-1}$.

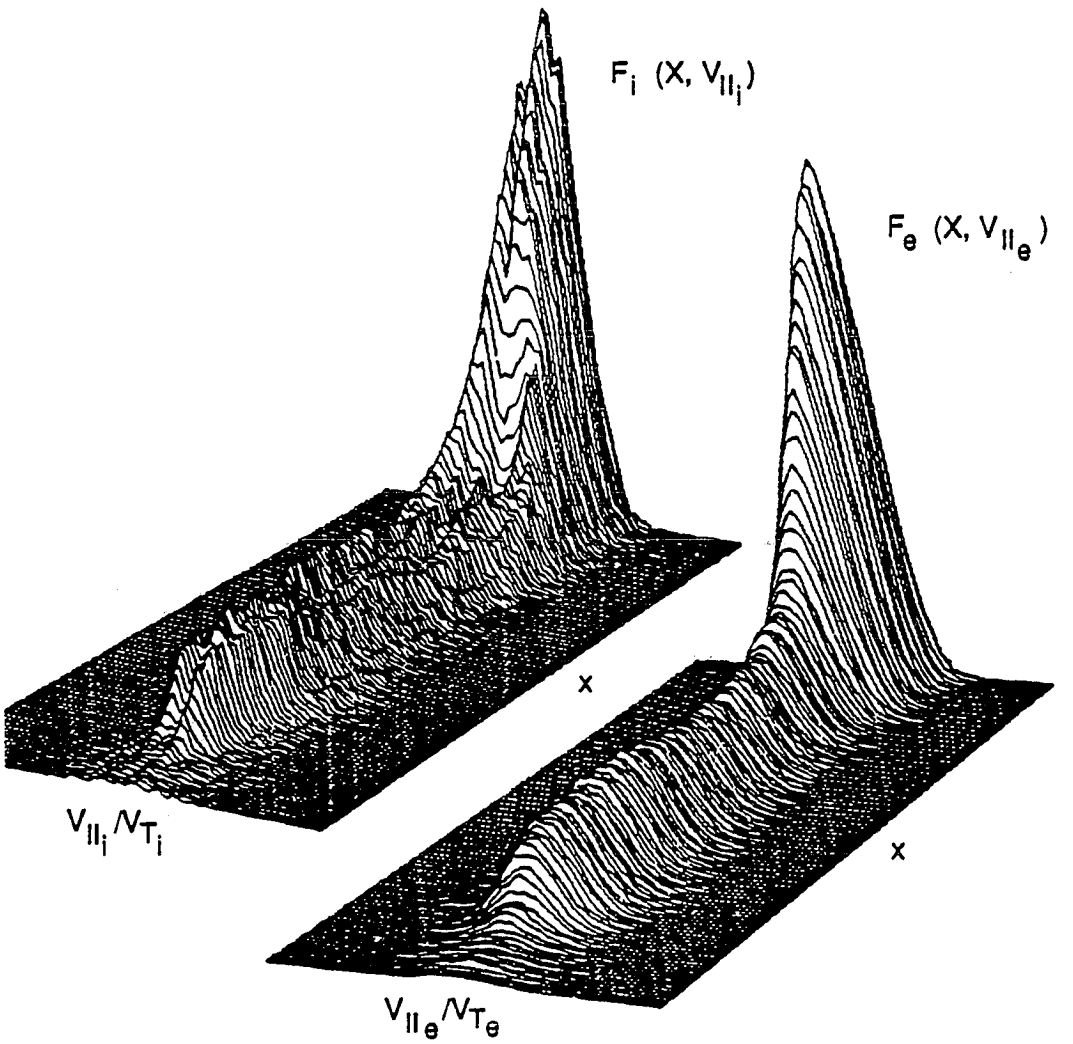

Figure 4.65: 3D plot of the parallel electron and ion velocity distributions at $t = 800\omega_{ci}^{-1}$.

At this stage ϕ and n_e are nearly in phase, while B_x and n_e have a phase difference of nearly $\pi/2$. The width of the density fluctuation is very close to the size of the magnetic fluctuation contour. In the middle of the saturation damping phase ($t = 440\omega_{ci}^{-1}$), ϕ and n_e have a phase difference of $\pi/2$, while ϕ and B_x have a phase difference of π (Fig. 4.68). Also n_e and B_x have a phase difference of $\sim \pi/2$. The widths of the fluctuations for n_e, n_i, ϕ, and B_x at the mode rational surface are nearly equal. At the boundary of the system, the density fluctuations are still dominated by the magnetic fluctuations. At the final damped state($t = 800\omega_{ci}^{-1}$), ϕ and n_e are again in phase(Fig. 4.69).

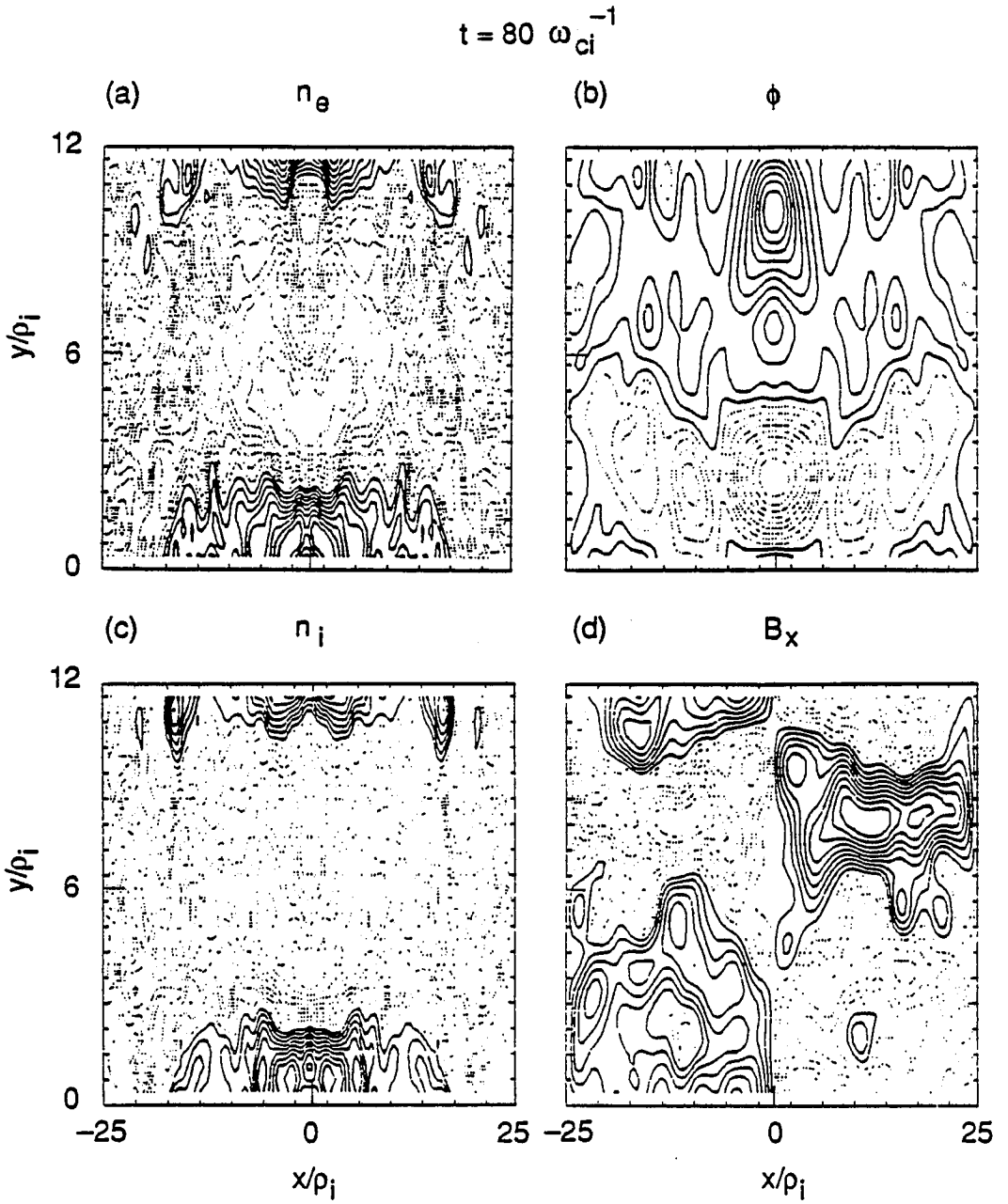

Figure 4.66: Contour plot of n_e, n_i, ϕ, and B_x at $t = 80\omega_{ci}^{-1}$.

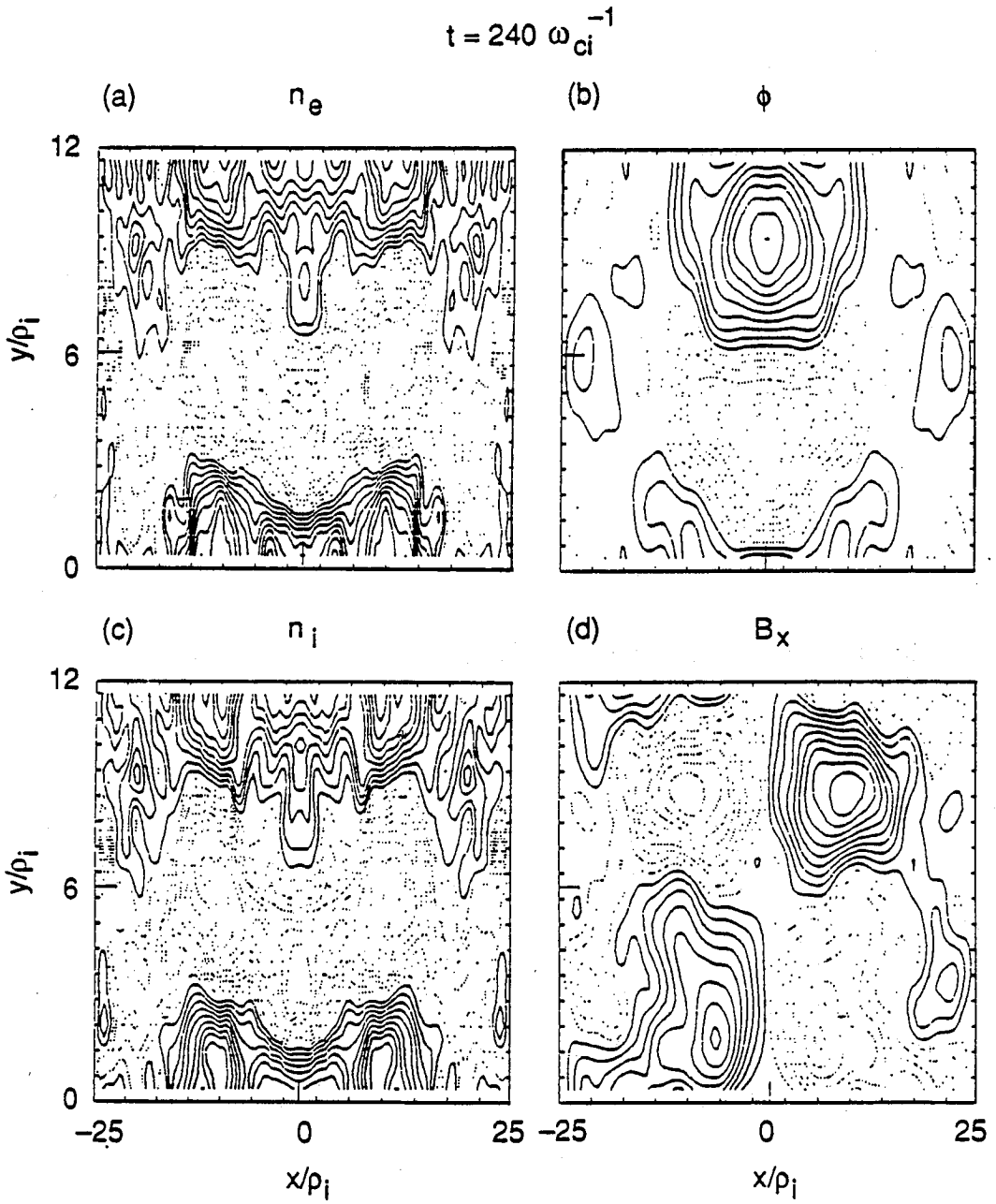

Figure 4.67: Contour plot of n_e, n_i, ϕ, and B_x at $t = 240\omega_{ci}^{-1}$.

Contour plots show that the density fluctuations are governed by ϕ , and B_x only has a minimal influence on them. As a summary, in the linear phase, n_e is driven by the electrostatic mode ϕ with a phase difference of $\pi/2$. At the saturation and at the damping phase, the electron and ion density fluctuations are governed by the magnetic fluctuation, A_z, with finite phase differences of $\sim \pi/4$ and $\pi/2$ respectively. At the final damped saturated phase, the density fluctuations are again controlled by the electrostatic component ϕ . This picture can be seen clearly from the particle phase space plots(v_x, x) taken at the same spots in the time sequence. At the initial linear stage, particles are driven by the electrostatic mode, and in the saturated stage the electromagnetic component amplitude A_z is comparable to ϕ and shows a strong coupling to the particles (Fig. 4.70). At the damping stage, phase space plots show that particle fluctuations are governed by the electromagnetic mode, and at the final stage the electrostatic component ϕ becomes dominant again (Fig. 4.71). To investigate the parallel ion temperature profile modification, another diagnostic is carried out by taking a snapshot of the parallel current fluctuations for the electrons and ions. At $t = 440\omega_{ci}^{-1}$, when significant parallel ion temperature profile modification has occured, parallel ion current fluctuations are compared with A_z fluctuations and show a strong coupling between j_i and A_z, although there is no correlation between j_e and A_z (Figs. 4.72,23). Also, the peak ion temperature heating point coincides with the point where the A_z and j_i amplitudes are maximum. Coupling of j_i and A_z is strong in the phases where the amplitude of the electromagnetic component is comparable to or larger than the amplitude of its electrostatic component (Figs. 4.70,71). Island formation associated with the perturbed A_z is observed, along with the resulting E_T^z fluctuations (Figs.4.74,75). In the linear stage, at $t = 80\omega_{ci}^{-1}$, there are minimal magnetic fluctuations along the field lines. But when the saturation stage is

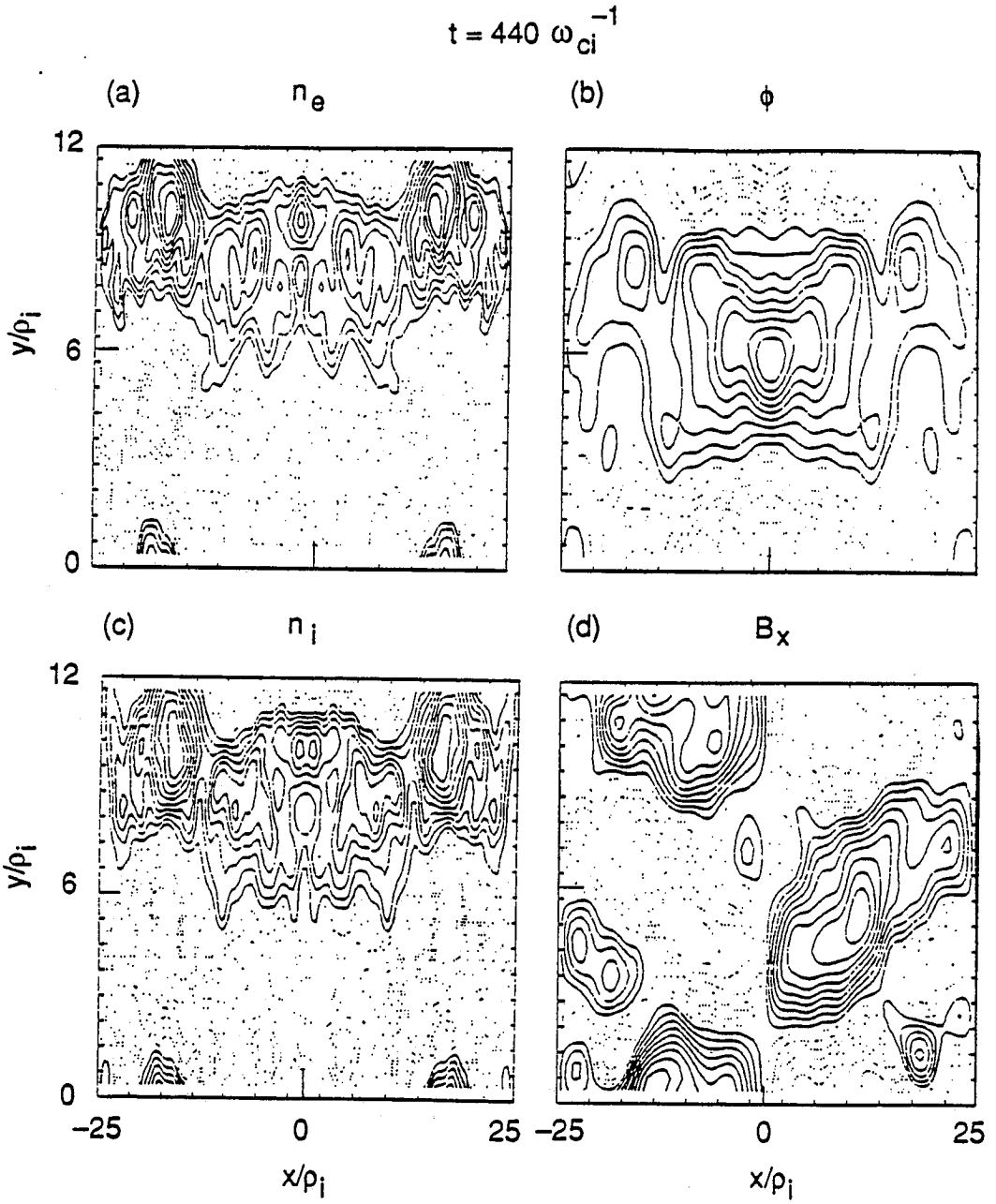

Figure 4.68: Contour plot of n_e, n_i, ϕ, and B_x at $t = 440\omega_{ci}^{-1}$.

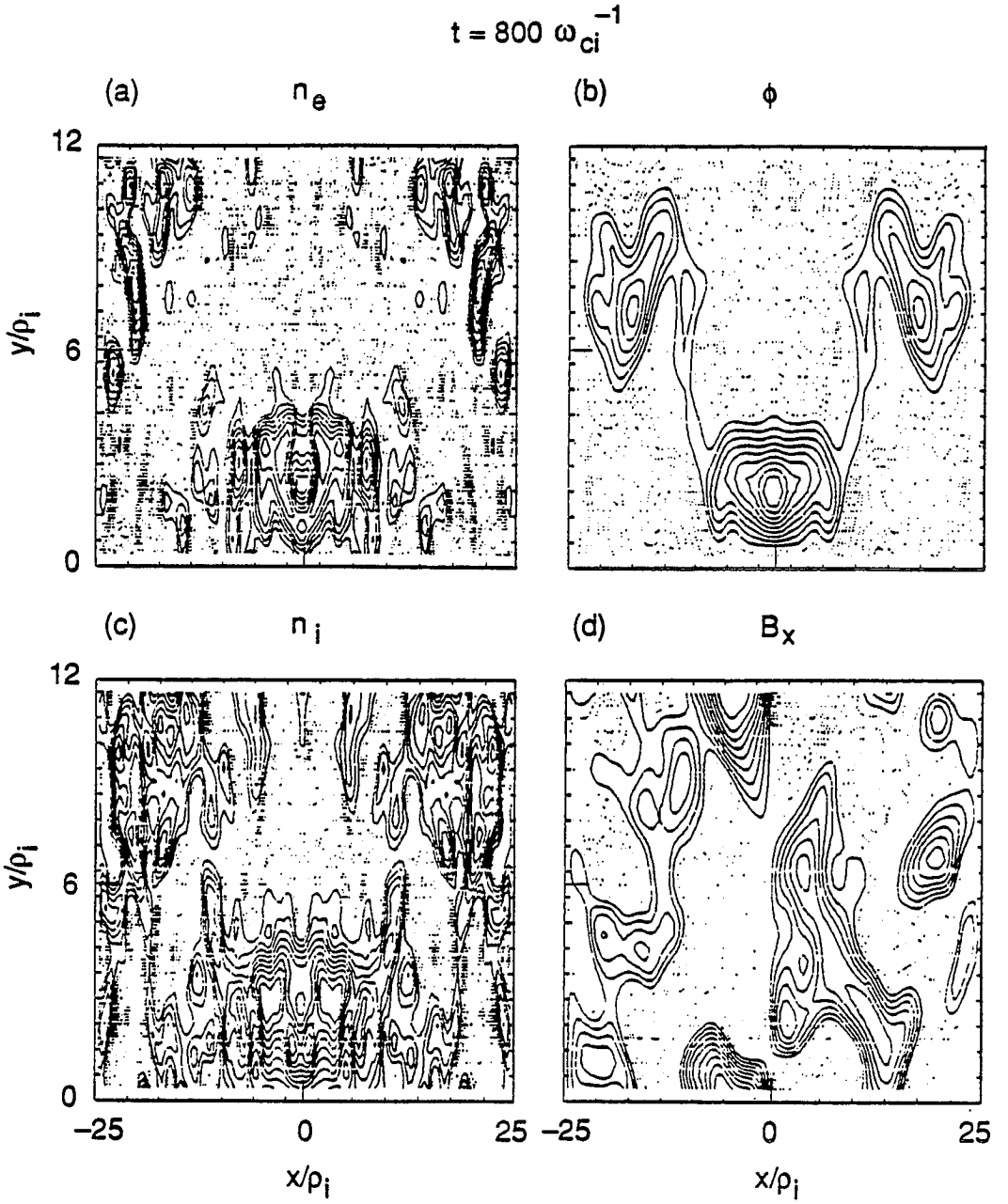

Figure 4.69: Contour plot of n_e, n_i, ϕ, and B_x at $t = 800\omega_{ci}^{-1}$.

reached at $t = 240\omega_{ci}^{-1}$, island formation with a width of $\sim 1.2\rho_i$ is observed. The island width reaches its maximum of $\sim 1.6\rho_i$ at $t = 440\omega_{ci}^{-1}$and is slightly lessened in the final damped stage. The associated E_T^z fluctuations show the same trend as the A_z fluctuations.

A summary of the collisional electromagnetic interchange mode simulation goes as follows. Both electron-ion collisional effects and finite beta effects, which are expressed in terms of ν_{ei} and β_i , respectively, enhance the fluctuation levels of ϕ and B_r in a similar fashion. Significant parallel ion temperature profile modification is observed in the nonlinear stage along with density profile flattening, while the parallel electron temperature has a negligible modification. The amount of $T_{\|i}$ profile modification is proportional to the collision frequency ν_{ei} . The largest $T_{\|i}$ profile modification is observed when β_i=0.0025. Cases with β_i=0.001 and 0.003 show a lesser degree of $T_{\|i}$ profile modification. Ion temperature profile modification occurs only when there is strong coupling between j_i and A_z fluctuations, and the amplitude of A_z is comparable to the amplitude of ϕ in the nonlinear damped saturation stage.

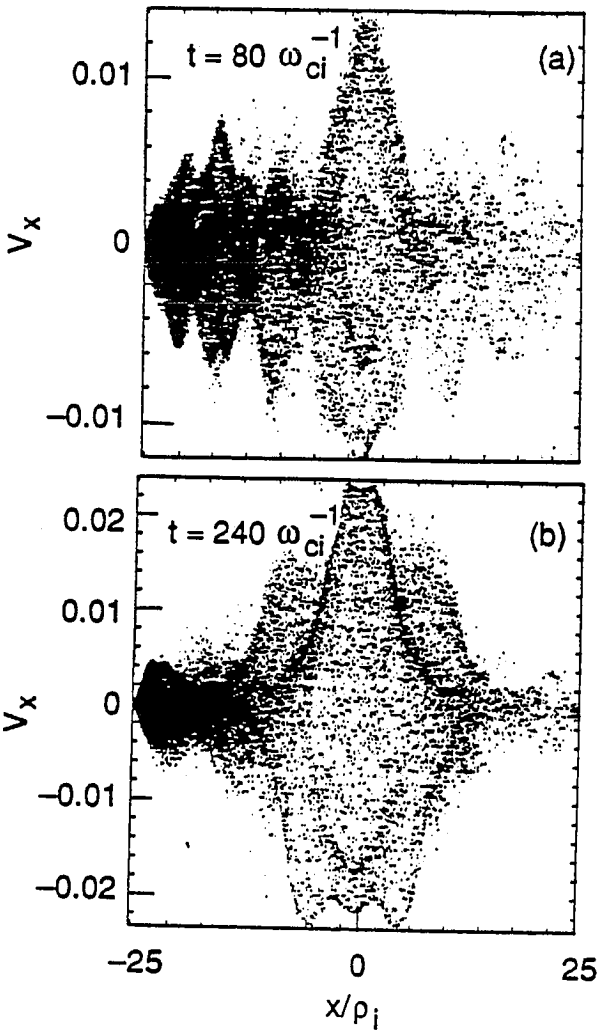

Figure 4.70: Phase space plot (v_x, x) of electrons at $t = 80, 240\omega_{ci}^{-1}$.

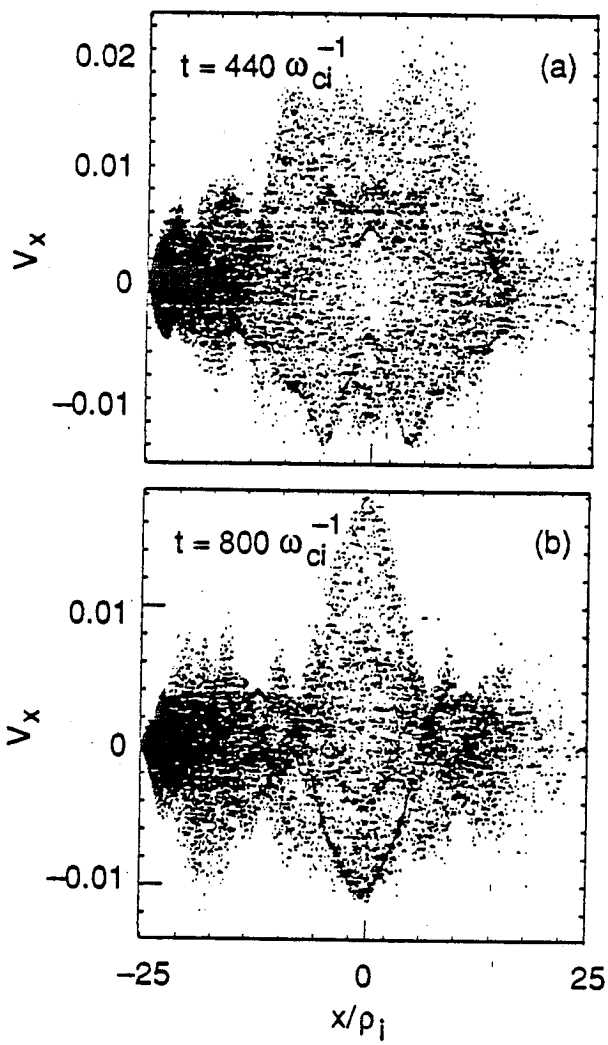

Figure 4.71: Phase space plot (v_x, x) of electrons at $t = 440, 800\omega_{ci}^{-1}$.

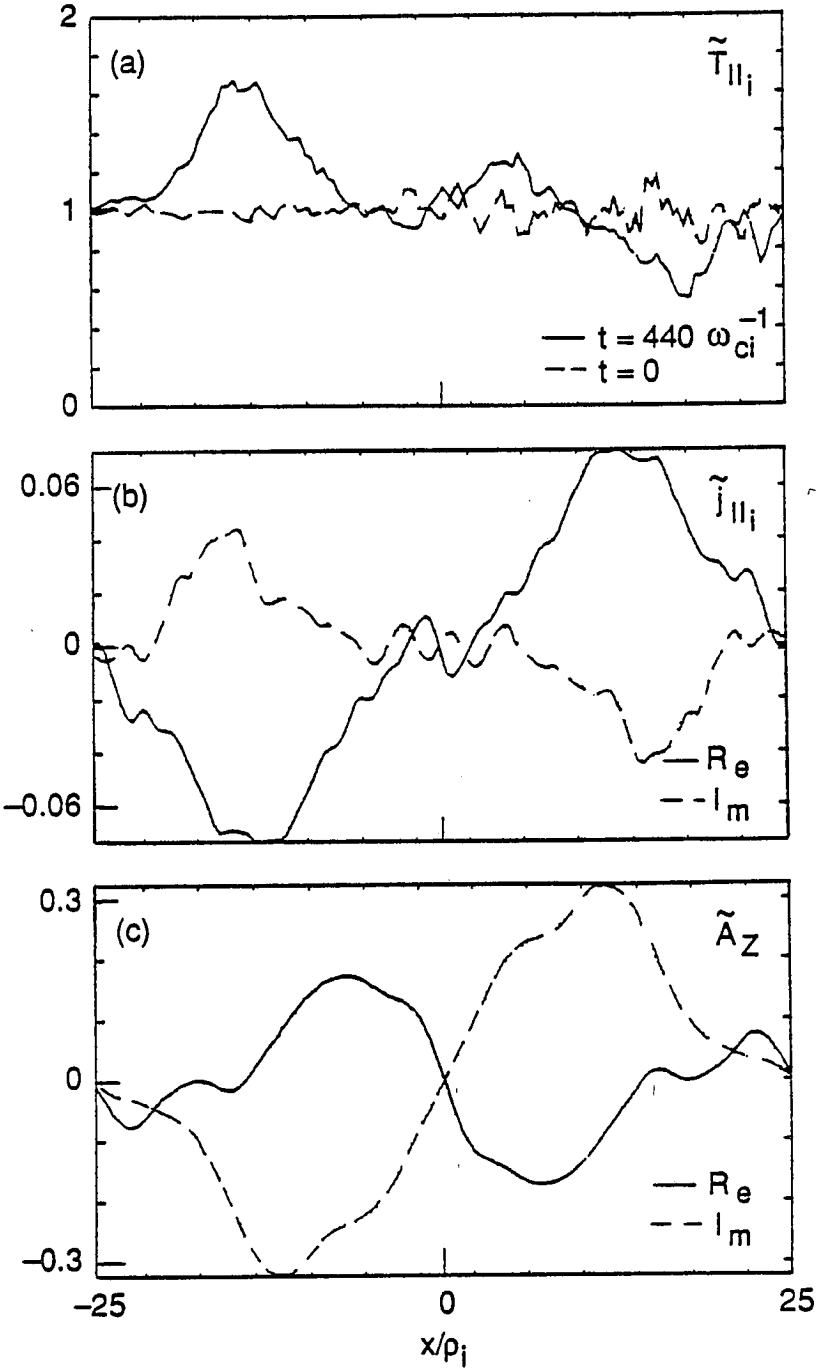

Figure 4.72: Snap shot of $T_{\|i}$ profile, A_z, and j_i at $t = 440\omega_{ci}^{-1}$.

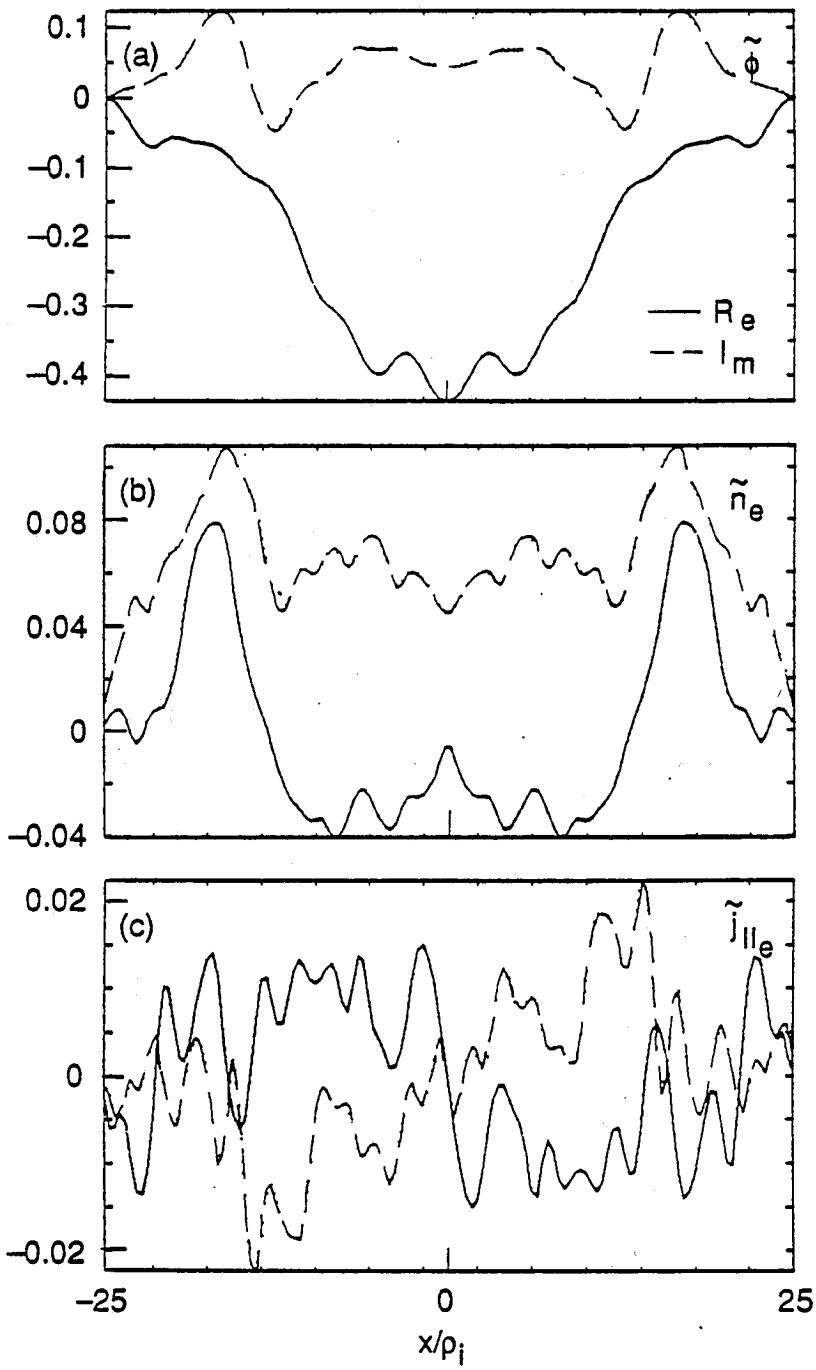

Figure 4.73: Snap shot of ϕ , n_e, and j_e at $t = 440\omega_{ci}^{-1}$.

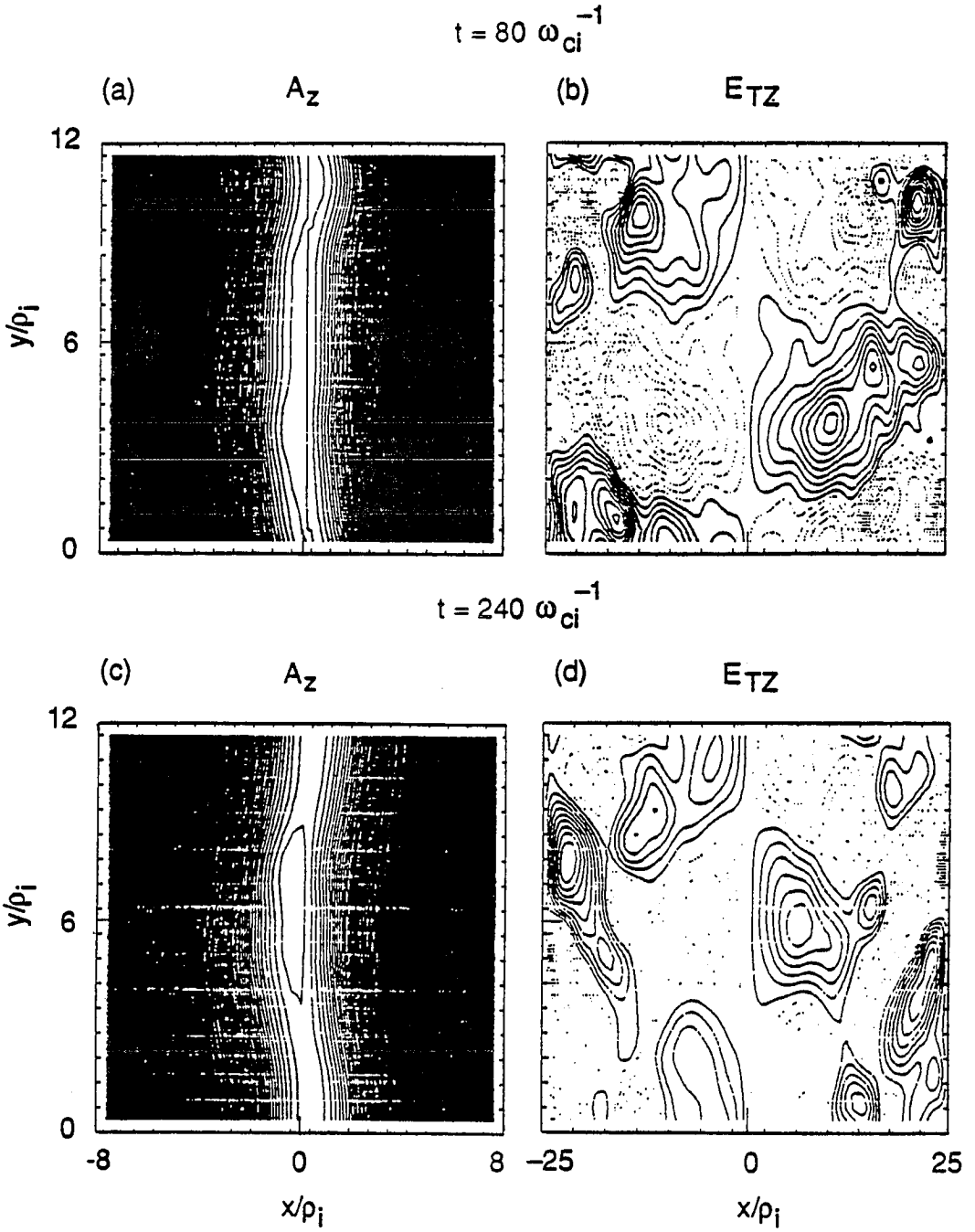

Figure 4.74: Snap shot of A_z , and E_T^z at $t = 80, 240\omega_{ci}^{-1}$.

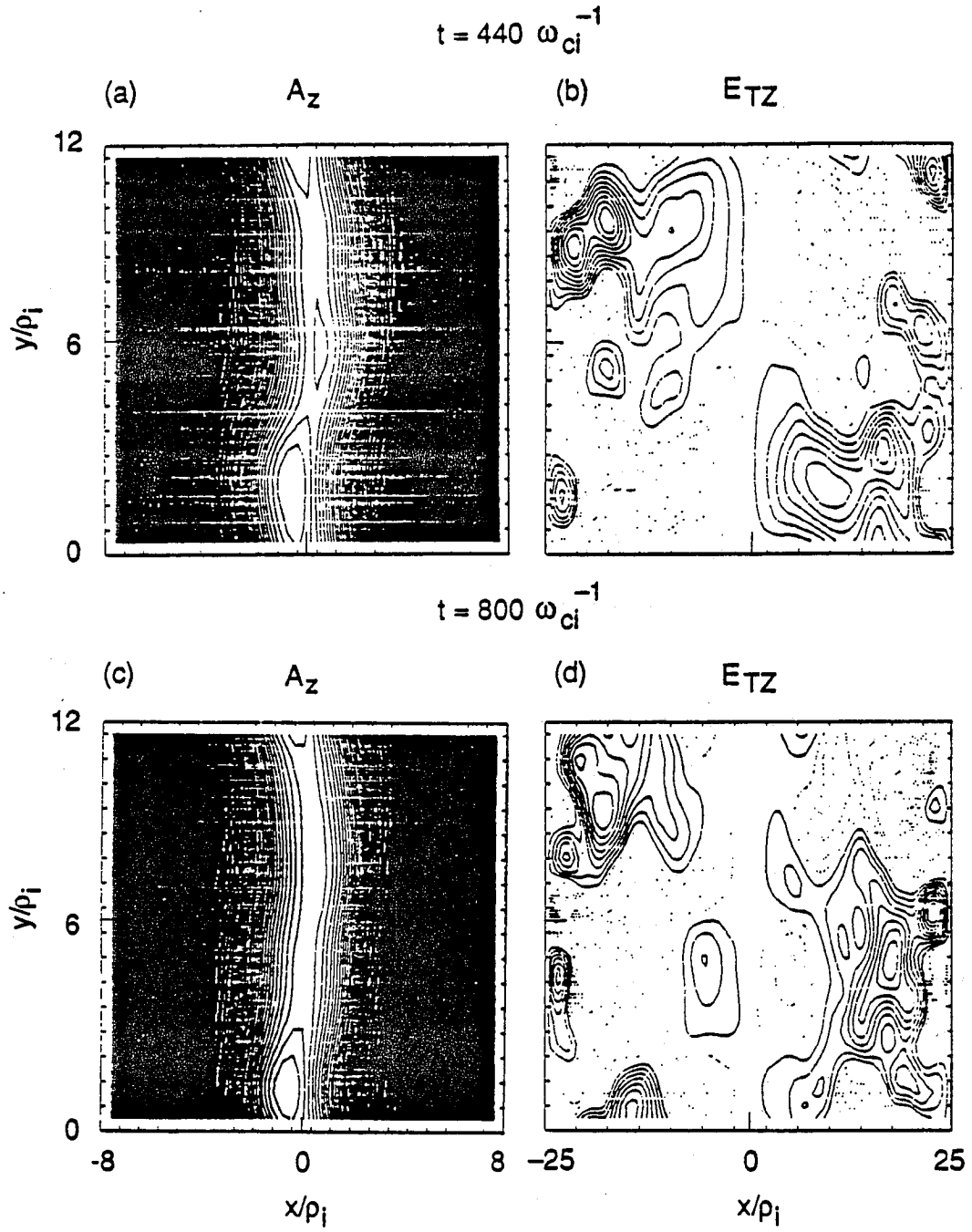

Figure 4.75: Snap shot of A_z , and E_T^z at $t = 440, 800\omega_{ci}^{-1}$.

Chapter 5

Summary and Conclusions

The work presented in this dissertation, namely, a the kinetic study of the finite β interchange modes in a sheared magnetic field, is an initial step forward to understand the fundamental mechanism of self-consistent magnetic turbulence on the basis of the knowledge of the relatively well understood electrostatic mode. Since the inherent complexity of self-consistent magnetic turbulence prohibits the feasibility of an analytical approach, particle simulations which follow the self-consistent interaction of particles and fields in space and in time is a very powerful approach to understand this difficult topic. However, the current computational environment restricts the full scale approach of using a 3D multi-helicity low frequency electromagnetic particle code. Therefore, as an alternative, a simplified $2-1/2$D version was adopted and applied to the finite β interchange modes in sheared slab geometry. The implementation of this task showed that even this simpler alternative is already a burden when we consider the present computational capabilities. In Chapter 2, a bounded $2-1/2$D magneto-inductive guiding center electron particle code, which eliminates unnecessary high frequencies above the ion plasma frequency and preserves low frequency fluctuations, is developed in sheared slab geometry as a major tool. A sophisticated algorithm, that traces the perturbed magnetic fields accurately in time and in space was developed. It was very efficienct for advancing the electromagnetic fields. To simulate the electron-ion collisions for the resistive interchange mode, the Lorentz collision operator is correctly implemented in

the guiding center electron model on the basis of the conservation of magnetic moment and energy of the particle, which are the adiabatic invariants of the guiding center electrons. (A poorly implemented Lorentz collision operator in the guiding center electron model would turn the thermal Maxwellian electron distribution into a cold electron beam after few small pictch angle scatterings by the Lorentz collision operator, since the only thermal velocity is the one electron velocity component parallel to the ambient magnetic field in the guiding center electron model.)

In Chapter 3, as ground work for the main theme of this dissertation, analyses of the electrostatic interchange modes were carried out in both the linear and nonlinear stages by the use of a second order shooting code and also with electrostatic particle codes. In the linear scaling studies, we obtained good agreement between kinetic theory calculations and computer simulations for the growth rates and mode widths under relevant parameter variations. Linear kinetic fast interchange analysis and simulations showed that the width of the low m modes is broader than that of the high m modes. Also the eigenmode with high m number grows faster than the low m number one and has a larger negative frequency through ω_i^* . For kinetic slow interchange modes, linear analysis and simulations recovered the typical $\gamma \sim \nu_{ei}^{1/3}$ scaling of the fluid limit for $\nu_{ei} \gg \omega$. There are discrepancies due to kinetic effects such as finite gyro-radius effects and Landau damping between the fluid limit calculations and the kinetic results for the growth rates, mode widths, and saturation levels. As the instability driving parameters such as the curvature drive L_n/L_c and ν_{ei} increase, quasilinear density profile modifications are also enhanced, i.e. , broader plateau formations were observed and also the electrostatic potential ϕ saturation levels increase. The increase of the saturation levels showed the same tendency as in the mixing length estimates. Phase relations between

the density fluctuation n_e and the potential ϕ were observed in the linear and saturated phases. The electrons respond non-adiabatically in the linear phase and become adiabatic in the saturated phase. For slow interchage modes, simulations with more modes showed low wave number condensation at the final saturation stage due to the nonlinear energy transfer mechanism between low wave numbers and high wave numbers.

In Chapter 4, coupled radial eigenmode equations were derived from the electron drift-kinetic equation and the ion gyro-kinetic equation, with the quasi-neutrality condition and parallel Ampére's law. Linear scaling studies showed that there is good agreement between theory calculations and simulation results in the linear phase for the growth rates, mode widths, and mode structures for both collisionless and collisional interchange modes. Besides these linear scaling studies, collisionless linear analyses showed that there exists a threshold in L_n/L_c which distinguishes stable drift waves and unstable drift-interchage modes as β_i is varied. The shear Alfvén wave, which is an another branch of the drift-Alfvén eigenmode system, shows no response to the curvature drive L_n/L_c . Also the shear Alfvén branch does not exist when β_i is below m_e/m_i , which demonstrates its electromagnetic character. Collisional linear analyses showed that finite β effects are not quite visible in the strong collisional regime on the growth rate and linear eigenmode widths. As an initial study of finite β collisionless interchange modes, Suydam parameters were tested for the collisionless electromagnetic interchange mode. A simulation with Suydam stable parameters showed no sign of instability in terms of the linear growth rate, density profile modifiaction, and magnetic island formation, whereas a simulation with unstable parameters showed definite signs of instability for the same quantities. Collisionless finite β simulations showed that as $\beta_i$increases from zero to m_e/m_i , the level of magnetic fluctuation increases

by an order of magnitude and tends to saturates as β_i increases further. The electrostatic potential ϕ saturation level also increases, but the increment is less than an order of magnitude as β_i increases. The magnetic island width becomes larger as β_i increases. There exists an algebraic relation between B_r and ϕ saturation levels. Snapshots of n_e, ϕ , and A_z revealed that the electron response is strongly coupled to ϕ around the mode rational surface, whereas in the region outside the mode rational surface, n_e is dominated by the magnetic perturbation due to its wide mode structure in linear and nonlinear phases. As a quasilinear effect, increased density profile modification was observed as β_i increases, along with parallel electron temperature profile modifications. A small amount of parallel electron heating occurs on the high density side of the electron density profile. At the saturated phase, the peak of the temperature profile diffuses radially towards the mode rational surface. The parallel ion temperature profile modification is negligible in both linear and nonlinear phases.

Collisional finite β simulations showed that electron-ion collision frequency ν_{ei} and finite β effects enhance the fluctuation levels of ϕ and B_r. Observations made by contour plots of density, electrostatic potential, and magnetic field perturbation showed that in the linear phase, the density perturbation is governed by ϕ with a phase difference, whereas in the saturation and in the damping phases, the density perturbation is dominated by the magnetic perturbation with a phase difference. At the final saturated phase, the density fluctuations are again controlled by the electrostatic component ϕ . Significant parallel ion temperature profile modification was observed in the nonlinear stage, along with density profile modification, while the parallel electron temperature has a negligible modification. The amount of ion temperature profile modification is proportional to the collision frequency ν_{ei} , but there is no clear

proportionality to β_i . Ion temperature profile modification occurs only when there is a strong coupling between $j_{\|i}$ and A_z fluctuations, and the amplitude of A_z is comparable to the amplitude of ϕ in the nonlinear damped saturation stage according to the observations made.

Overall, for collisionless and collisional cases, finite β effects increase the the saturation levels of the electrostatic and magnetic fields. Also, magnetic fluctuations control the density fluctuations in the region outside the mode rational surface, due to their extended eigenmode structure. Effects of magnetic fluctuations on collisional finite β interchange modes are quite severe in the nonlinear saturation and damping phases in terms of the saturation level, density profile modifications, and parallel ion temperature profile modifications, whereas in the linear stages there are no visible effects. Based on the linear analyses and observations made from the simulation, we conclude that magnetic fluctuations seem to strongly modify the saturation mechanism and the dynamics of particles in nonlinear stages, mainly due to the large scale of the perturbed eigenmode structure centered at the mode rational surface, as compared to the scale of the electrostatic mode, which is more localized at the mode rational surface.

In future work, the following systematic approaches will be required in order to gain understanding of the dynamics of self-consistent magnetic turbulence. The simulations performed so far could not isolate quasilinear effects from the pure nonlinear effects due to density profile relaxation. To isolate quasilinear effects, we need a fluid simulation of finite β interchange modes with a fixed density profile, with one single mode rational surface, and with the correct amount of dissipation from the kinetic effects. Moreover, fully three dimensional multi-helicity fluid simulations should be followed to have

truly strong turbulence phenomena which do not have self-consistency feedback yet. On the basis of these fluid calculation, we need to develop an algorithm which can hold the density gradient in the particle simulation, and we need to implement this algorithm for the full 3D multi-helicity particle simulation code for finite β interchange modes. Then, finally we were possibly be able to isolate the feedback of self-consistent magnetic fluctuations on anomalous electron thermal transport in the strong turbulence regime. All these procedures are extremely time consuming and will require extensive work.

In terms of future work, the following systematic approaches will be required as procedures which lead to an understanding of the dynamics of self-consistent magnetic turbulence. There exists a number of finite beta fluid models of pressure gradient turbulence or resitive g-modes which have had considerable success in probing the characteristics of (mainly) the electrostatic component of the physics (Carreras, Garcia, Diamond[58]; Lee, Carreras, Garcia[50]). We have shown in this dissertation that kinetic effects complicate the picture significantly. An interesting exercise in order to elucidate the relative importance of electron and ion kinetic effects would be to treat cases identical to the ones discussed here but with a fluid description for electrons and ions, as is done in the 3D multiple helicity fluid computations. Then, the fluid description could be upgraded by treating the electrons as guiding center particles and the ions as a fluid. This work is, in fact, in progress with the hybrid kinetic electrons-hydrodynamic ions code HIPE(Lyster and Leboeuf)[59]. In this way, a progressive view of the changes in the nonlinear effects would emerge, as more and more of the kinetics are included. More importantly, the particle simulations presented in this thesis are limited to a single rational surface and are dominated by quasilinear effects, such as density and temperature profile modifications. Profiles must be maintained and multiple rational

surfaces must be present in order to study a truly nonlinear, turbulent steady states, as is done in the 3D multiple helicity fluid calculations. To do this kinetically requires three-dimensional, finite β , δf algorithm (M. Kotchenreuther)[60] or gyro-kinetic(W. W. Lee)[61] particle codes, where only perturbations about the equilibrium profiles are followed. Fewer particles are therefore required since the equilibrium density profile does not need to be represented by the particles. This in turn would allow for increased spatial resolution for the same computer capacity, and such an approach may lead to results that are more directly comparable to the large scale 3D, multiple helicity fluid calculations.

REFERENCES

[1] A.B. Rechester and M.N. Rosenbluth, Phys. Rev. Lett. **40**, 38 (1978).

[2] T.H. Stix, Nucl. Fusion **18**, 353 (1978).

[3] M.N. Rosenbluth, R.Z. Sagdeev, J.B. Taylor, and G.M. Zaslavski, Nucl. Fusion **6**, 297 (1966).

[4] B.B. Kadomtsev, O.P. Pogutse, in plasma physics and Controlled Nucl. Fusion research (Proc. 7th Int. Conf. Vienna, 1978), Vol. 1, IAEA, Vienna, 649 (1979)

[5] J.A. Krommes, C. Oberman, and R.G. Kleva, J. Plasma Phys. **30**, 11 (1983).

[6] S.J. Zweben, C.R. Menyuk, and R.J. Taylor, Phys. Rev. Lett. **42**, 1270 (1979).

[7] S.J. Zweben, R.J. Taylor, Nucl. Fusion **21**, 193 (1981).

[8] P.C. Liewer, Nucl. Fusion **25**, 543 (1985).

[9] D.D. Schnack, J. Killeen, and R.A. Gerwin, Nucl. Fusion **21**, 1447 (1981).

[10] J.M. Finn, W.M. Manheimer, Phys. Fluids **26**, 962 (1983).

[11] T.C. Hender and D.C. Robinson, Nucl. Fusion **21**, 755 (1981).

[12] T.S. Hahm and L. Chen, Phys. Fluids **28**, 2432 (1985)

[13] T.E. Stringer, Nucl. Fusion **15**, 125 (1975).

[14] H. Furth, J. Killeen, and M.N. Rosenbluth, Phys. Fluids **18**, 875 (1975).

[15] B. Coppi, J.M. Greene, J.L. Johnson, Nucl. Fusion **6**, 101 (1966).

[16] B.A. Carreras, P.H. Diamond, Phys. Fluids B **15**, 1011 (1989).

[17] R.D. Hazeltine and J.D. Meiss, Phys. Reports, **121**, 40 (1985).

[18] C.Z. Cheng and H. Okuda, J. Comp. Phys. **25**, 133 (1977).

[19] W.W. Lee and H. Okuda, J. Comp. Phys. **26**, 139 (1978).

[20] C. G. Darwin, Phil. Mag. **39**, 403 (1983).

[21] J. Busnardo-Neto, P.L. Prichett, A.T. Lin, and J.M. Dawson, J. Comp. Phys. **23**, 300 (1977).

[22] C.W. Nielson, H.R. Lewis, in Methods in Computational Physics, Vol. 16, edited by J. Killeen (Academic Press, London, 1981).

[23] W.W. Lee, H. Okuda, and W.M. Nevins, in Proc. of the 8th Conference on Numerical Simulation of Plsmas, LLNL Report No. CONF-780614, PD. 7 (1978).

[24] J.L. Geary *et.al.*, J. Comp. Phys. **42**, 1986.

[25] P. Concus and G.H. Golub, SIAM J. Numer. Anal., **10**, 1103 (1977).

[26] K.T. Tsang, J.C. Whitson, and J. Smith, Phys. Fluids **22**, 1689 (1979).

[27] J.M. Dawson, Rev. Mod. Phys. **55**, 300 (1977).

[28] J.W. Cooley and J.W. Tuckey, Math. Comput., **19**, 297 (1965).

[29] W.L. Kruer, J.M. Dawson, and B. Rosen, J. Comp. Phys. **13**, 114 (1973).

[30] H. Naitou, S. Tokuda, and T. Kamimura, J. Comp. Phys. **33**, 86 (1979).

[31] R. Shanny, J.M. Dawson, and J.M. Greene, Phys. Fluids **10**, 1281 (1967).

[32] J.F. Federici, W.W. Lee, and W.M. Tang, Phys. Fluids **30**, 425 (1987).

[33] J.H. Han and J.N. Leboeuf, Institute for Fusion Studies Report No. 422, The University of Texas at Austin (1990).

[34] T. Kamimura, T. Wagner, and J.M. Dawson, Phys. Fluids **21**, 1151 (1978).

[35] R.C. Davidson, Handbook of Plasma Physics, Vol.1, Basic Plasma Physics I, edited by A.A. Galeev and R.N. Sudan(Elsevier,New York, 1984), p.531

[36] R.C. Davidson, Handbook of Plasma Physics, Vol.2, Basic Plasma Physics I, edited by A.A. Galeev and R.N. Sudan(Elsevier,New York, 1984), p.560

[37] A.I. Akhiezer *et.al.*, Plasma Electrodynamics, Vol.I, (Pergamon press,London, 1978), p.275

[38] T.M. Antonsen Jr. , B. Lane, Phys. Fluids **23**, 1205 (1980).

[39] P.L. Bhatnagar, E.P. Gross, and M. Krook, Phys. Rev. **94**, 511, (1954).

[40] G. Rewolt, W.M. Tang, and R.J. Hastie, Phys. Fluids **29**, 2893, (1986).

[41] P.J. Catto, W.M. Tang, and D.E. Baldwin, Plasma Phys. **23**, 639 (1981).

[42] B.D. Fried and S.D. Conte, The Plasma Dispersion Function(Academic Press, New York), 1961

[43] L.D. Pearlstein, H.L. Berk, Phys. Rev. Lett. **23**, 220 (1969).

[44] R.D. Sydora, J.N. Leboeuf, P.H. Diamond,Z.G. An and T. Tajima, Phys. Fluids **28**, 255 (1985).

[45] R.D. Sydora Ph.D. Thesis, Department of Physics, The University of Texas at Austin (1985); also Institute for Fusion Studies Report No. 178, The University of Texas at Austin (1985).

[46] H. Naitou, S. Tokuda, and T. Kamimura, J. Comp. Phys. **38**, 265 (1980).

[47] M.N. Rosenbluth, N.A. Krall, N. Rostoker, Nucl. Fusion Suppl. A1, 143 (1962).

[48] A.A. Galeev, R.Z. Sagdeev, Handbook of Plasma Physics, Vol.2, Basic Plasma Physics II, edited by A.A. Galeev and R.N. Sudan(Elsevier,New York, 1984), p.687

[49] W. Horton, Handbook of Plasma Physics, Vol.2, Basic Plasma Physics II, edited by A.A. Galeev and R.N. Sudan(Elsevier,New York, 1984).

[50] G.S. Lee, B.A. Carreras, and L. Garcia, Phys. Fluids **1**, 119 (1989).

[51] P.J. Catto, A.M. El Nadi, C.S. Liu, M.N. Rosenbluth, Nucl. Fusion **14**, 405 (1974).

[52] B. B. Kadomtsev, Plasma Turbulence, Academic Press, London(1965).

[53] K.T. Tsang, J.C. Whitson, J.D. Callen, P.J. Catto, and J. Smith, Phys. Rev. Lett. **41**, 557 (1978).

[54] W.M. Tang, Nucl. Fusion **18**, 1089 (1978).

[55] S.P. Hirshman, K. Molvig, Phys. Rev. Lett. **42**, 648 (1979).

[56] Y.C. Lee, L. Chen, Phys. Rev. Lett. **42**, 708 (1979).

[57] B.R. Suydam, 2nd Int. Conf. Peaceful Uses At. Energy(Proc. Conf. Geneva, 1958) **31**, 157 (1958).

[58] B.A. Carreras, L. Garcia, and P.H. Diamond, Phys. Fluids **30**, 1388 (1987).

[59] P.M. Lyster and J.N. Leboeuf, Institute for Fusion Studies Report No. 337, The University of Texas at Austin (1988).

[60] M. Kotschenreuther, Institute for Fusion Studies Report No. 360, The University of Texas at Austin (1989).

[61] W. W. Lee, J. Comp. Phys. **72**, 243 (1987).